

# **Advanced Characterisation of Silicon Wafers and Solar Cells under Different Operating Conditions**

**Shuai Nie**

A thesis in fulfilment of the requirements for the degree of

Doctor of Philosophy



**UNSW**  
SYDNEY

School of Photovoltaic and Renewable Energy Engineering

Faculty of Engineering

January 2022



## Thesis submission for the degree of Doctor of Philosophy

Thesis Title and Abstract

Declarations

Inclusion of Publications  
Statement

Corrected Thesis and  
Responses

### ORIGINALITY STATEMENT

☒ I hereby declare that this submission is my own work and to the best of my knowledge it contains no materials previously published or written by another person, or substantial proportions of material which have been accepted for the award of any other degree or diploma at UNSW or any other educational institution, except where due acknowledgement is made in the thesis. Any contribution made to the research by others, with whom I have worked at UNSW or elsewhere, is explicitly acknowledged in the thesis. I also declare that the intellectual content of this thesis is the product of my own work, except to the extent that assistance from others in the project's design and conception or in style, presentation and linguistic expression is acknowledged.

### COPYRIGHT STATEMENT

☒ I hereby grant the University of New South Wales or its agents a non-exclusive licence to archive and to make available (including to members of the public) my thesis or dissertation in whole or part in the University libraries in all forms of media, now or here after known. I acknowledge that I retain all intellectual property rights which subsist in my thesis or dissertation, such as copyright and patent rights, subject to applicable law. I also retain the right to use all or part of my thesis or dissertation in future works (such as articles or books).

For any substantial portions of copyright material used in this thesis, written permission for use has been obtained, or the copyright material is removed from the final public version of the thesis.

### AUTHENTICITY STATEMENT

☒ I certify that the Library deposit digital copy is a direct equivalent of the final officially approved version of my thesis.

## Thesis submission for the degree of Doctor of Philosophy

Thesis Title and Abstract

Declarations

Inclusion of Publications  
Statement

Corrected Thesis and  
Responses

UNSW is supportive of candidates publishing their research results during their candidature as detailed in the UNSW Thesis Examination Procedure.

Publications can be used in the candidate's thesis in lieu of a Chapter provided:

- The candidate contributed **greater than 50%** of the content in the publication and are the "primary author", i.e. they were responsible primarily for the planning, execution and preparation of the work for publication.
- The candidate has obtained approval to include the publication in their thesis in lieu of a Chapter from their Supervisor and Postgraduate Coordinator.
- The publication is not subject to any obligations or contractual agreements with a third party that would constrain its inclusion in the thesis.

☒ The candidate has declared that **some of the work described in their thesis has been published and has been documented in the relevant Chapters with acknowledgement**.

A short statement on where this work appears in the thesis and how this work is acknowledged within chapter/s:

Chapter 3 contains the results from the Paper "Photoluminescence-based spatially resolved temperature coefficient maps of silicon wafers and solar cells" published in IEEE Journal of Photovoltaics.

Chapter 4 contains the results from the Paper "Temperature sensitivity maps of silicon wafers from photoluminescence imaging: The effect of gettering and hydrogenation," submitted to Progress in Photovoltaics: Research and Applications on 21/11/2021. It is currently under review.

Chapter 5 contains the results from the Paper "Advanced photoluminescence imaging using non-uniform excitation" published in Progress in Photovoltaics: Research and Applications.

Chapter 6 contains the results from the Paper "Unravelling the silicon-silicon dioxide interface under different operating conditions" published in Solar Energy Materials and Solar Cells.

For the journal papers mentioned above, I am the first author and the corresponding author. The contributions of the other authors have been clarified in the acknowledgement section.

### Candidate's Declaration



I declare that I have complied with the Thesis Examination Procedure.

# Abstract

The continuing push for higher energy conversion efficiencies and reduced cost-per-watt of photovoltaic solar cells results in the need for improved characterisation methods. Generally, the characterisation of photovoltaic devices is conducted under standard test conditions of 25 °C at an irradiance of 1000 W·m<sup>-2</sup>. However, photovoltaic device operating temperature and irradiance deviate significantly from the standard test conditions. This results in a considerable knowledge gap regarding their performance under realistic operating conditions, along with the challenge related to the lack of suitable characterisation methods. Therefore, this thesis aims to develop innovative characterisation methods to expand the knowledge about the electrical properties of silicon wafers and cells under different operating conditions.

The temperature coefficient is an important figure of merit for quantifying the impact of operating temperatures on the photovoltaic devices' performance. In this thesis, a method for measuring the spatially resolved temperature coefficient of silicon wafers and cells is developed. Using this method, broad studies on the local temperature-dependent behaviours of regions with varying electrical quality are carried out. The local temperature coefficient is compared at different ingot positions, between different materials, as well as after implementing different solar cell fabrication processes. As a result, a wealth of temperature coefficient information is generated — information that was previously unavailable through conventional global measurements — and thus, allows more accurate modelling of photovoltaic energy yield.

Charge carrier lifetime is an essential parameter of photovoltaic devices as it empirically quantifies various recombination processes occurring simultaneously in the devices. It directly relates to the performance of photovoltaic devices. In this thesis, an advanced photoluminescence imaging method using non-uniform excitation is developed to accurately determine the carrier lifetime images of silicon samples with spatially inhomogeneous electrical properties at different operating conditions. A contactless approach for quantifying surface recombination and extracting interface defect

parameters from temperature- and injection-dependent lifetime measurements is also developed. This approach is successfully applied to investigate the silicon-silicon dioxide interface at various temperatures and injection levels. The associated interface defect parameters and the temperature dependence of the capture cross-sections are determined.

The methods developed in this thesis combine to promote targeted improvements to photovoltaic device characterisation — and thus, photovoltaic device design and efficiency — by enabling detailed individual assessment of surface and bulk electrical properties under different operating conditions that typically occur in the field.

# Acknowledgement

It has been a thrilling and incredible journey, and I am finally presenting this thesis. Many thanks to all the wonderful people who accompanied, supported, and encouraged me along this way.

I would like to express my deepest gratitude to my primary supervisor, Ziv Hameiri, for the constant support throughout my Taste of Research, my undergraduate thesis, and most importantly, my PhD. You are more than a supervisor to me. Thank you so much for your patience, guidance, and motivation which helped me grow as a researcher. I have learned so much from you, and you are always a great inspiration to me. I would also like to offer my appreciation to my joint supervisor Thorsten Trupke for your advice and knowledge, and for establishing a powerful PL imaging technique. Your insightful suggestions have always motivated me to think more deeply to improve the quality of my work.

I would like to say a big thank you to my colleagues: Robert Dumbrell, Kyung Kim, Carlos Vargas, Jack Colwell, Raghavi Bhoopathy, Saman Jafari, Yoann Buratti, Anh Le, Simon Zhang, Zubair Abdullah-Vetter, Yan Zhu, and Robert ( $\mu$ Rob) Lee Chin, Arman Mahboubi Soufiani, Johannes Seif, Nino Borojevic, Priya Dwivedi, John Rodriguez, Oliver Kunz, Appu Paduthol, Henner Kampwerth, Germain Rey, Mattias Juhl, Rhett Evans, Iskra Zafirovska, the entire ACDC team, and the whole PL group for all of the valuable feedback at the group meetings, for the numerous discussions, and for being such inspiring people to work with. My sincere gratitude goes to Oliver, Yan, and  $\mu$ Rob, whom I worked closely with during my PhD. Oliver, I appreciate all the discussions, practical skills, and critical feedback you have provided to me. Yan, thank you for training me and accelerating my knowledge of the carrier lifetime.  $\mu$ Rob, I am grateful for having you as my  $\mu$ PL teacher and English mentor, as well as for all our useful and useless conversations. I also want to thank the people who have spent the time to proofread my journal papers, conference papers, and thesis chapters, thank you  $\mu$ Rob, John, Oliver, Yan,

Arman, Saman, Simon, and Zubair. Many thanks to Ziv, Saman, Arman, and the Solar Industrial Research Facility (SIRF) team for helping with sample processing.

My heartfelt appreciation goes to all my collaborators: Simone Bernardini and Mariana Bertoni from Arizona State University, Sissel Tind Kristensen and Rune Strandberg from the University of Agder, Sebastian Bonilla from the University of Oxford, Torbjørn Mehl from Norwegian University of Life Sciences, Felix Theska, Nima Haghdadi, Sophie Primig, and Catherine Chan from the University of New South Wales. Sissel, thank you for accompanying me in the lab during my first year and for countless fruitful discussions and skype calls. Sebastian, many thanks for deepening my understanding of surface recombination, and for providing the sample in Chapter 6. Torbjørn, thank you for helping with the hyperspectral PL measurements. Felix, Nima, and Sophie, thank you for helping me with the EBSD and APT measurements. Catherine, thank you for providing the sample in Chapter 4.

I would like to thank the members of my review panel: Ivan Perez-Wurfl, Alison Lennon, Catherine Chan, Oliver Kunz, and Xiaojing Hao for providing your valuable feedback, and ensuring that I complete my PhD in a timely manner. I am grateful to SPREE lab development and operation team and the administrative team for ensuring an enjoyable and productive research and study environment.

I would like to extend my thanks to all my friends and family who never failed to support me. A special thanks to my beloved parents: Mr Lixin Nie and Mrs Yuping Chen, for the endless love throughout my life. 爸爸妈妈，谢谢你们！ Your constant encouragement and support have brought me to this point. I hope I have made you proud. A big thanks to my sister, thank you for taking care of dad and mom. And to Ding Zhang, my fiancé, thank you for being by my side throughout my eight years at UNSW, for doing the majority of the housework, for lending your shoulder to cry on, and for everything you have done for me.

Again, a huge thanks to everyone who supported and accompanied me in navigating this memorable PhD journey.

# Table of Contents

<b>Abstract</b>	<b>iii</b>
<b>Acknowledgement</b>	<b>v</b>
<b>Table of Contents</b>	<b>vii</b>
<b>Abbreviations and Symbols</b>	<b>xi</b>
<b>Publication List</b>	<b>xix</b>
<b>Chapter 1 Introduction</b>	<b>1</b>
1.1 Thesis Motivation and Objectives	2
1.2 Thesis Outline	3
<b>Chapter 2 Review: Theoretical Background and Literature</b>	<b>5</b>
2.1 Recombination and Carrier Lifetime	5
2.1.1 Intrinsic Recombination	6
2.1.2 Defects and Extrinsic Recombination	7
2.1.3 Effective Lifetime	10
2.2 Characterising Recombination in Silicon	10
2.2.1 Lifetime Measurement Principle	10
2.2.2 Photoconductance Measurement	12
2.2.3 Photoluminescence Measurement	15
2.2.4 Photoluminescence Imaging	17
2.3 Temperature Dependence of the Bandgap and Intrinsic Carriers	19
2.3.1 Bandgap Energy	19
2.3.2 Intrinsic Carrier Density	21
2.4 Chapter Summary	22
<b>Chapter 3 Spatially Resolved Temperature-Dependent Characterisation of Silicon Wafers and Cells</b>	<b>25</b>
3.1 Temperature Coefficients of Solar Cells	26
3.2 Method	28
3.2.1 Experimental Setup	28
3.2.2 Calibration Procedure	30
3.2.3 Sample Preparation	33
3.3 Results and Discussion	33
3.3.1 Spatially Resolved Results	33

3.3.2 Impact of Ingot Height·····	36
3.3.3 Temperature Coefficient of Dislocation Clusters·····	40
3.4 Chapter Summary ·····	43
<b>Chapter 4 Impacts of Gettering and Hydrogenation on Silicon Wafer Temperature Sensitivity ·····</b>	<b>45</b>
4.1 Gettering and Hydrogenation ·····	46
4.1.1 Gettering·····	46
4.1.2 Hydrogenation ·····	47
4.2 Method·····	49
4.2.1 Sample Preparation ·····	49
4.2.2 Characterisation Methods ·····	49
4.3 Results and Discussion ·····	51
4.3.1 Spatially Resolved Analysis ·····	51
4.3.2 Variation Along Ingot Position ·····	55
4.3.3 Temperature-Dependent Performance at the Cell Level·····	58
4.3.4 Temperature Sensitivity of Crystallographic Defects·····	59
4.4 Chapter Summary ·····	66
<b>Chapter 5 Advanced Photoluminescence Imaging Using Non-Uniform Excitation·····</b>	<b>69</b>
5.1 Photoluminescence Imaging Using Uniform Excitation·····	70
5.2 Photoluminescence Imaging Using Non-Uniform Excitation·····	70
5.2.1 System Development and Optimisation ·····	71
5.2.2 Measurement Procedure ·····	78
5.2.3 Calibration Procedure·····	80
5.3 Proof of Concept Measurements·····	82
5.3.1 Application to Non-Diffused Sample ·····	82
5.3.2 Application to Diffused Sample ·····	85
5.4 Limitations and Future Improvements ·····	89
5.4.1 Limitations ·····	89
5.4.2 General Improvements·····	90
5.4.3 Temperature-Dependent Measurements in Reflection Mode ·····	91
5.5 Chapter Summary ·····	92
<b>Chapter 6 Characterisation of the Silicon-Silicon Dioxide Interface under Various Operating Conditions·····</b>	<b>95</b>
6.1 Characterisation of the Silicon-Silicon Dioxide Interface ·····	96
6.2 Method·····	97
6.2.1 Sample Preparation ·····	97
6.2.2 Characterisation Setup ·····	98
6.2.3 Modelling ·····	98

6.3 Results and Discussion .....	103
6.3.1 Temperature- and Injection-Dependent Lifetime Measurements .....	103
6.3.2 Stability of Hydrogen Passivation and Corona Charge at High Temperatures .....	105
6.3.3 Modelling Lifetime Measurements .....	108
6.4 Chapter Summary .....	114
<b>Chapter 7 Summary and Future Work .....</b>	<b>117</b>
7.1 Summary of Contributions .....	118
7.2 Future Work .....	121
<b>Appendix A .....</b>	<b>123</b>
<b>Reference .....</b>	<b>125</b>



# Abbreviations and Symbols

## Abbreviations:

---

---

AHP	Advanced hydrogenation process
Al	Aluminium
AlO <sub>x</sub>	Aluminium oxide
AM1.5G	Air mass 1.5 Global
APT	Atom probe tomography
As	Arsenic
B	Boron
BB	Band to band
BGN	Bandgap narrowing
C	Carbon
CCD	Charge-coupled device
CMOS	Complementary metal-oxide-semiconductor
Co	Cobalt
CO <sub>2</sub>	Carbon dioxide
Cr	Chromium
CT	Charging time
Cu	Copper
CV	Coefficient of variation
Cz	Czochralski
DLTS	Deep level transient spectroscopy
DPSS	Defect parameter solution surface
DRM	Depletion region modulation
EBSD	Electron backscatter diffraction

EQE	External quantum efficiency
Fe	Iron
FGA	Forming gas anneal
FZ	Float-zone
H	Hydrogen
HD	High dislocation density
IBC	Interdigitated back contact
IDLS	Injection-dependent lifetime spectroscopy
InGaAs	Indium gallium arsenide
LCD	Liquid-crystal display
LCOE	Levelised cost of energy
LD	Low dislocation density
LED	Light-emitting diode
mc-Si	Multi-crystalline silicon
MOS	Metal-oxide-semiconductor
N	Nitrogen
Ni	Nickel
NIR	Near-infrared
O	Oxygen
P	Phosphorus
PC	Photoconductance
PDG	Phosphorus diffusion gettering
PERC	Passivated emitter rear cells
PERT	Passivated emitter and rear totally diffused
PFIB	Plasma focused ion beam
PL	Photoluminescence
$\mu$ PL	Microscopic photoluminescence
PSF	Point-spread function
PV	Photovoltaics
QSS	Quasi-steady-state

RF	Radio frequency
ROI	Region of interest
Sb	Antimony
SEM	Scanning electron microscope
SHJ	Silicon heterojunction
Si	Silicon
SiN <sub>x</sub>	Silicon nitride
SiO <sub>2</sub>	Silicon dioxide
Sn	Tin
SRH	Shockley-Read-Hall
STC	Standard test conditions
STD	Standard deviation
TC	Temperature coefficient
TIDLS	Temperature- and injection-dependent lifetime spectroscopy
TOPCon	Tunnel oxide passivated contact
Zn	Zinc

---

**Symbols:**

---

$A$	Area	[cm <sup>2</sup> ]
$a$	Quadratic calibration constant of PC coil	[siemens·V <sup>-2</sup> ]
$B_{\text{rad}}$	Radiative recombination coefficient	[cm <sup>3</sup> ·s <sup>-1</sup> ]
$b$	Linear calibration constant of PC coil	[siemens·V <sup>-1</sup> ]
$C_n$	Auger recombination coefficient for two electrons and one hole	[cm <sup>6</sup> ·s <sup>-1</sup> ]
$C_p$	Auger recombination coefficient for two holes and one electron	[cm <sup>6</sup> ·s <sup>-1</sup> ]

$D$	Diffusivity	$[\text{cm}^2 \cdot \text{s}^{-1}]$
$D_{\text{it}}$	Interface state density	$[\text{cm}^{-2} \cdot \text{eV}^{-1}]$
$D_{\text{it,a}}$	Acceptor-like interface state density	$[\text{cm}^{-2} \cdot \text{eV}^{-1}]$
$D_{\text{it,d}}$	Donor-like interface state density	$[\text{cm}^{-2} \cdot \text{eV}^{-1}]$
$D_{\text{it}_C}$	Interface state density at the conduction band edge	$[\text{cm}^{-2} \cdot \text{eV}^{-1}]$
$D_{\text{it\_mg}}$	Interface state density at mid bandgap	$[\text{cm}^{-2} \cdot \text{eV}^{-1}]$
$D_{\text{it}_V}$	Interface state density at the valence band edge	$[\text{cm}^{-2} \cdot \text{eV}^{-1}]$
$E_0$	Bandgap energy at 0 K	$[\text{eV}]$
$E_a$	Activation energy	$[\text{eV}]$
$E_C$	Conduction band edge	$[\text{eV}]$
$E_g$	Bandgap	$[\text{eV}]$
$E_{g0}$	Bandgap energy linearly extrapolated to 0 K	$[\text{eV}]$
$E_i$	Intrinsic Fermi level	$[\text{eV}]$
$E_t$	Defect energy level	$[\text{eV}]$
$E_V$	Valence band edge	$[\text{eV}]$
$E_\infty$	Energy barrier for the exponential temperature dependence of capture cross-section	$[\text{eV}]$
$FF$	Fill factor	
$F_{\text{PL}}$	Calibration factor for photoluminescence	$[\text{cm}^3 \cdot \text{s} \cdot \text{V}]$
$F_{\text{PLi}}$	Calibration constant for photoluminescence imaging	$[\text{cm}^3 \cdot \text{s}]$
$f_{\text{sample}}$	Sample-dependent calibration factor for generation rate	$[\text{cm}^{-1}]$
$f_{\text{system}}$	System-dependent calibration factor for generation rate	$[\text{cm}^{-2} \cdot \text{s}^{-1} \cdot \text{V}^{-1}]$
$G$	Carrier generation rate	$[\text{cm}^{-3} \cdot \text{s}^{-1}]$
$g_{eeh}$	Auger enhancement factor for two electrons and one hole	
$g_{ehh}$	Auger enhancement factor for two holes and one electron	
$I_{\text{PL}}$	Photoluminescence intensity	
$I_{\text{SC}}$	Short-circuit current	$[\text{A}]$
$iV_{\text{OC}}$	Implied open-circuit voltage	$[\text{mV}]$
$J_0$	Diode saturation current density	$[\text{A} \cdot \text{cm}^{-2}]$

$k$	Ratio of electron and hole capture cross-sections	
$k_B$	Boltzmann constant	[eV·K <sup>-1</sup> ]
$N_a$	Acceptor concentration	[cm <sup>-3</sup> ]
$N_C$	Effective density of states in the conduction band	[cm <sup>-3</sup> ]
$N_d$	Donor concentration	[cm <sup>-3</sup> ]
$N_{\text{dop}}$	Doping density	[cm <sup>-3</sup> ]
$N_{\text{st}}$	Surface state density for a specific energy level	[cm <sup>-2</sup> ]
$N_t$	Defect density in silicon bulk	[cm <sup>-3</sup> ]
$N_V$	Effective density of states in the valence band	[cm <sup>-3</sup> ]
$n$	Electron concentration	[cm <sup>-3</sup> ]
$n_0$	Electron concentration under thermal equilibrium	[cm <sup>-3</sup> ]
$n_1$	Electron Shockley-Read-Hall concentration	[cm <sup>-3</sup> ]
$n_i$	Intrinsic carrier concentration	[cm <sup>-3</sup> ]
$n_s$	Electron concentration at the surface	[cm <sup>-3</sup> ]
$\Delta n$	Excess carrier concentration	[cm <sup>-3</sup> ]
$\Delta n_{\text{PC}}$	Excess carrier concentration obtained from photoconductance measurements	[cm <sup>-3</sup> ]
$\Delta n_{\text{PL}}$	Excess carrier concentration obtained from photoluminescence measurements	[cm <sup>-3</sup> ]
$\Delta n_s$	excess carrier concentration at the surface	[cm <sup>-3</sup> ]
$\text{PL}_0$	Defect-related photoluminescence as the temperature approaches 0 K	
$\text{PL}_{\text{BB}}$	Band-to-band photoluminescence	
$\text{PL}_{\text{defect}}$	Defect-related photoluminescence	
$p$	Hole concentration	[cm <sup>-3</sup> ]
$p_0$	Hole concentration under thermal equilibrium	[cm <sup>-3</sup> ]
$p_1$	Hole Shockley-Read-Hall concentration	[cm <sup>-3</sup> ]
$p_s$	Hole concentration at the surface	[cm <sup>-3</sup> ]
$Q_f$	Fixed charge in the dielectric layer	[q·cm <sup>-2</sup> ]
$Q_g$	Charge on the gate electrode	[q·cm <sup>-2</sup> ]
$Q_{\text{it}}$	Charge in the interface states	[q·cm <sup>-2</sup> ]

$Q_{Si}$	Charge induced in the silicon	$[q \cdot cm^{-2}]$
$q$	elementary charge	$[A \cdot s]$
$R$	reflectance	
$r$	radius	$[mm]$
$S$	Surface recombination velocity	$[cm \cdot s^{-1}]$
$S_{n0}$	Surface recombination velocity for electrons	$[cm \cdot s^{-1}]$
$S_{p0}$	Surface recombination velocity for holes	$[cm \cdot s^{-1}]$
$S_r$	Radial sensitivity of photoconductance coil	
$T$	Temperature	$[K]$
$TC(iV_{OC})$	Temperature coefficient of implied open-circuit voltage	$[mV \cdot K^{-1}]$
$TC(V_{OC})$	Temperature coefficient of open-circuit voltage	$[mV \cdot K^{-1}]$
$\Delta TC(iV_{OC})$	Percentage difference in temperature coefficient of implied open-circuit voltage	
$t$	Time	$[sec]$
$U$	Recombination rate	$[cm^{-3} \cdot s^{-1}]$
$U_{Auger}$	Auger recombination rate	$[cm^{-3} \cdot s^{-1}]$
$U_{rad}$	Radiative recombination rate	$[cm^{-3} \cdot s^{-1}]$
$U_s$	Surface recombination rate	$[cm^{-2} \cdot s^{-1}]$
$U_{SRH \text{ bulk}}$	Shockley-Read-Hall bulk recombination rate	$[cm^{-3} \cdot s^{-1}]$
$V_{cal}$	Output voltage of amplifier connected to calibration photodiode	$[V]$
$V_{OC}$	Open-circuit voltage	$[mV]$
$V_{PC\_air}$	Output voltage of photoconductance coil without the sample in the dark	$[V]$
$V_{PC\_cal}$	Output voltage of photoconductance coil with calibration sample in the dark	$[V]$
$V_{PC\_dark}$	Output voltage of photoconductance coil with the sample in the dark	$[V]$
$V_{PC\_light}$	Output voltage of photoconductance coil with the sample after excitation	$[V]$
$V_{PL}$	Output voltage of amplifier connected to photoluminescence detector	$[V]$

$V_{\text{ref}}$	Output voltage of reference cell	[V]
$v_{\text{thn}}$	Thermal velocity of electrons	[cm·s <sup>-1</sup> ]
$v_{\text{thp}}$	Thermal velocity of holes	[cm·s <sup>-1</sup> ]
$W$	sample thickness	[cm]
$\gamma$	Temperature dependences of the parameters determining the diode saturation current density	
$\varepsilon$	Damping factor for photoluminescence imaging using non-uniform excitation	
$\epsilon_{\text{Si}}$	Relative permittivity of silicon	
$\epsilon_0$	Vacuum permittivity	[F·cm <sup>-1</sup> ]
$\lambda$	Wavelength	[nm]
$\mu_{\text{n}}$	Mobility of electrons	[cm <sup>2</sup> ·V <sup>-1</sup> ·s <sup>-1</sup> ]
$\mu_{\text{p}}$	Mobility of holes	[cm <sup>2</sup> ·V <sup>-1</sup> ·s <sup>-1</sup> ]
$\sigma_{\text{cal}}$	Dark conductance of the calibration sample	[siemens]
$\sigma_{\text{n}}$	Electron capture cross-section of bulk defect	[cm <sup>2</sup> ]
$\sigma_{\text{n\_s0}}$	Pre-factors for electron capture cross-section with exponential temperature dependency	[cm <sup>2</sup> ]
$\sigma_{\text{ns}}$	Electron capture cross-section of surface defect	[cm <sup>2</sup> ]
$\sigma_{\text{p}}$	Hole capture cross-section of bulk defect	[cm <sup>2</sup> ]
$\sigma_{\text{p\_s0}}$	Pre-factors for hole capture cross-section with exponential temperature dependency	[cm <sup>2</sup> ]
$\sigma_{\text{ps}}$	Hole capture cross-section of surface defect	[cm <sup>2</sup> ]
$\Delta\sigma$	Photoconductance	[siemens]
$\tau$	Carrier lifetime	[s]
$\tau_0$	Initial lifetime (before degradation)	[s]
$\tau_{\text{Auger}}$	Auger lifetime	[s]
$\tau_{\text{bulk}}$	Bulk lifetime	[s]
$\tau_{\text{charged}}$	Lifetime of the corona charged sample	[s]
$\tau_{\text{eff}}$	Effective lifetime	[s]
$\tau_{\text{fitted}}$	Fitted lifetime	[s]
$\tau_{\text{measured}}$	Measured lifetime	[s]

$\tau_{n0}$	Electron capture time constant	[s]
$\tau_{p0}$	Hole capture time constant	[s]
$\tau_{\text{rad}}$	Radiative lifetime	[s]
$\tau_s$	Surface lifetime	[s]
$\tau_{\text{SRH bulk}}$	Shockley-Read-Hall bulk lifetime	[s]
$\tau_{\text{uncharged}}$	Lifetime of the sample without corona charge	[s]
$\Delta\tau$	Lifetime difference	[s]
$\Phi$	Photon flux	[cm <sup>-2</sup> ·s <sup>-1</sup> ]
$\Phi_n$	Quasi-Fermi potential for electrons	[V]
$\Phi_p$	Quasi-Fermi potential for holes	[V]
$\Psi_s$	Surface potential	[V]

---

# Publication List

## Peer-reviewed journal publications:

\* Corresponding author

† Publications included in this thesis

1. C. Vargas, S. Nie\*, D. Chen, C. Chan, B. Hallam, G. Coletti, and Z. Hameiri, "Degradation and recovery of n-type multi-crystalline silicon under illuminated and dark annealing conditions at moderate temperatures," *IEEE J. Photovoltaics*, vol. 9, pp. 355-363, 2019. **(Equal contribution with C. Vargas)**
2. C. Berthod, S. T. Kristensen, R. Strandberg, J. O. Odden, S. Nie, Z. Hameiri, and T. O. Sætre, "Temperature sensitivity of multicrystalline silicon solar cells," *IEEE J. Photovoltaics*, vol. 9, pp. 957-964, 2019.
3. † S. Nie\*, S. T. Kristensen, A. Gu, R. L. Chin, T. Trupke, and Z. Hameiri, "Photoluminescence-based spatially resolved temperature coefficient maps of silicon wafers and solar cells," *IEEE J. Photovoltaics*, vol. 10, pp. 585-594, 2020.
4. S. T. Kristensen, S. Nie, C. Berthod, R. Strandberg, J. O. Odden, and Z. Hameiri, "Temperature coefficients of crystal defects in multicrystalline silicon wafers," *IEEE J. Photovoltaics*, vol. 10, pp. 449-457, 2020.
5. † S. Nie\*, R. S. Bonilla, and Z. Hameiri, "Unravelling the silicon-silicon dioxide interface under different operating conditions," *Sol. Energy Mater. Sol. Cells*, vol. 224, pp. 111021, 2021.
6. † S. Nie\*, Y. Zhu, O. Kunz, T. Trupke, and Z. Hameiri, "Advanced photoluminescence imaging using non-uniform excitation," *Prog. Photovoltaics Res. Appl.*, 2021.
7. † S. Nie\*, R. Lee Chin, A. M. Soufiani, T. Mehl, F. Theska, N. Haghdadi, S. Primig, C. Chan, T. Trupke, and Z. Hameiri, "Temperature sensitivity maps of silicon wafers

from photoluminescence imaging: The effect of gettering and hydrogenation," *Prog. Photovoltaics Res. Appl.*, accepted, 2021.

## Conference Contributions:

† Publications included in this thesis

1. S. Bernardini, **S. Nie**, Y. Zhu, Z. Hameiri, and M. Bertoni, "Surface photovoltage spectroscopy as a characterization technique for surface passivation quality assessment," in *7<sup>th</sup> World Conference on Photovoltaic Energy Conversion*, 2018.
2. S. Bernardini, Y. Zhu, **S. Nie**, Z. Hameiri, and M. Bertoni, "Analysis of SiN<sub>x</sub> SRV injection- and temperature-dependence and its degradation via TIDLS measurements," in *7<sup>th</sup> World Conference on Photovoltaic Energy Conversion*, 2018.
3. S. T. Kristensen, **S. Nie**, M. S. Wiig, H. Haug, C. Berthod, R. Strandberg, and Z. Hameiri, "A high-accuracy calibration method for temperature dependent photoluminescence imaging," in *9<sup>th</sup> International Conference on Crystalline Silicon Photovoltaics*, vol. 2147, pp. 020007, 2019.
4. † **S. Nie**, S. T. Kristensen, A. Gu, T. Trupke, and Z. Hameiri, "A novel method for characterizing temperature sensitivity of silicon wafers and cells," in *46<sup>th</sup> IEEE Photovoltaic Specialists Conference*, pp. 0813-0816, 2019. **(Won the Best Student Award)**
5. S. T. Kristensen, **S. Nie**, C. Berthod, R. Strandberg, J. O. Odden, and Z. Hameiri, "How gettering affects the temperature sensitivity of the implied open circuit voltage of multicrystalline silicon wafers," in *46<sup>th</sup> IEEE Photovoltaic Specialists Conference*, pp. 0061-0067, 2019.
6. V. Siu, **S. Nie**, Y. Zhu, and Z. Hameiri, "An incomplete ionization model for indium in silicon," in *Asia-Pacific Solar Research Conference*, 2019.
7. † **S. Nie**, Y. Zhu, O. Kunz, H. Kampwerth, T. Trupke, and Z. Hameiri, "Temperature-dependent photoluminescence imaging using non-uniform excitation," in *47<sup>th</sup> IEEE Photovoltaic Specialists Conference*, pp. 0789-0792, 2020. **(Won the Best Student Award)**

8. S. T. Kristensen, A. S. Garcia, **S. Nie**, Z. Hameiri, and R. Strandberg, "Improved temperature coefficient modelling through the recombination parameter  $\gamma$ ," in *47<sup>th</sup> IEEE Photovoltaic Specialists Conference*, pp. 0083-0087, 2020.
9. † **S. Nie**, R. S. Bonilla, and Z. Hameiri, "Temperature-dependent characterization of Si-SiO<sub>2</sub> interface passivation for corona charged oxides," in *Asia-Pacific Solar Research Conference*, 2020.
10. J. Moore, **S. Nie**, Y. Zhu, and Z. Hameiri, "Improving photoluminescence imaging using non-uniform illumination," in *Asia-Pacific Solar Research Conference*, 2020.
11. † **S. Nie**, R. L. Chin, A. M. Soufiani, C. Chan, T. Trupke, and Z. Hameiri, "Temperature-dependent performance of silicon wafers: the impact of gettering and hydrogen passivation," in *11<sup>th</sup> International Conference on Crystalline Silicon Photovoltaics*, 2021.



# Chapter 1

## Introduction

We are living in a critical time period that is characterised by an unprecedentedly increasing level of atmospheric carbon dioxide (CO<sub>2</sub>). Today, the CO<sub>2</sub> level in the atmosphere is about 49% higher than its level during the pre-industrial era [1, 2]. This poses a widespread and long-lasting crisis to our world — climate change — with a series of associated devastating consequences, such as increasing global temperature, frequent extreme weather conditions, accelerated glacier retreats, sea-level rise, species extinctions, and more. It is indisputable that immediate decarbonisation measures must be taken to stop the exacerbation of climate change. Given that the primary contributor to CO<sub>2</sub> emission is burning fossil fuels [3], a significant transition towards renewable energy sources is imperative.

Among all the renewable energy resources, solar energy has the largest reserve, far exceeding the sum of the remaining renewable energy resources by orders of magnitude [4]. Indeed, each hour, the amount of solar energy reaching our planet is sufficient to fulfil our energy demand for a year, considering the global energy consumption of ~ 20 TWy today and ~ 30 TWy by 2050 [5]. Its abundance, ubiquity, and sustainability position solar energy as the primary energy source for the zero-carbon future. Due to the huge global electricity demand with an ever-growing rate [6], a large proportion of solar energy is utilised for electricity generation via photovoltaics (PV). By directly converting solar energy into electricity, PV is expected to play a central role in electricity generation in our green future [7, 8].

Over the past decades, tremendous progress has been made in PV, resulting in a rapid cost reduction and a remarkable growth of the installed capacity [9]. In the last 12 years, there has been a ~ 20 times reduction in average PV module price from 4.12 USD/W in 2008 to 0.21 USD/W in 2020 [9, 10]. In most countries, the levelised cost of energy (LCOE) of PV is already lower than the LCOE of coal [9, 11]. Hence, PV is a viable alternative to conventional fossil fuels for electricity generation. With the global

cumulative capacity of installed PV at 756 GW by the end of 2020 [9] and 70 TW predicted by 2050 [7, 12], it is evident that PV is on its way to dominating the worldwide energy source.

## 1.1 Thesis Motivation and Objectives

Crystalline silicon (Si)-based PV technologies are the workhorses of the global PV market [9]. Their rapid development has increased module efficiency and power, enabling a rapid reduction in module prices, and thus significantly decreasing the contribution of the modules to the overall PV system cost [9, 13]. Therefore, other costs, especially the installation are becoming more important [13]. Driven by the need to optimise different expenditures of the PV systems, it is critical to further improve the module efficiency and reliability to reduce LCOE [13].

Characterisation plays a critical role in improving the efficiency and reliability of PV devices. They are greatly utilised in the development and optimisation of PV materials, processes, and device structures, as well as in the reliability assessment of PV devices. Usually, the characterisation techniques are designed to assess PV devices' properties under "standard test conditions" (STC): a standard solar spectrum AM1.5G, an irradiance of  $1000 \text{ W} \cdot \text{m}^{-2}$ , and a temperature of  $25 \text{ }^{\circ}\text{C}$  ( $\sim 298 \text{ K}$ ) [14]. This common measurement environment is chosen to allow a universal comparison of the electrical quality of wafers, cells, and modules. However, PV modules are installed all over the world and therefore work at different operating temperatures and irradiance depending on the location, season, and time of the day. For instance, solar cell operating temperature varies yearly from  $-10 \text{ }^{\circ}\text{C}$  to  $55 \text{ }^{\circ}\text{C}$  (average of  $19 \text{ }^{\circ}\text{C}$ ) in Norway while  $-5 \text{ }^{\circ}\text{C}$  to  $70 \text{ }^{\circ}\text{C}$  (average of  $37 \text{ }^{\circ}\text{C}$ ) in the USA [15]. STC cannot represent the standard operating conditions of the majority of PV devices. Since the temperature and irradiance have a significant impact on the PV devices' performance [15, 16], it is essential to develop characterisation methods under realistic operating conditions. Furthermore, many new PV devices have localised features, such as selectively diffused regions and local contacts. Some of them also suffer from non-uniformly distributed defects. Therefore, spatially resolved characterisation techniques are preferred for such devices in order to comprehend their inhomogeneous performance distribution.

Characterisation of the temperature- and injection-dependent electrical properties of PV devices in a spatially resolved manner is crucial for: (a) a better understanding of the

defects and the degradation mechanisms in PV devices, enabling the evaluation of their impacts on device efficiency and consequently devising the elimination strategies for efficiency and reliability enhancement, (b) helping future innovation of specialised PV devices with efficiency optimised for different operating conditions, and (c) accurately modelling PV energy yield in the real world conditions which are vital for designing and investing PV projects. From the above aspects, the need for a better understanding of temperature- and injection-dependent electrical properties of Si wafers and cells has emerged, along with challenges related to the lack of suitable characterisation methods. Therefore, this thesis aims to develop advanced characterisation methods and use these methods to further the understanding of the electrical properties of Si wafers and solar cells, with attention to:

- Develop a temperature-dependent spatially resolved characterisation system to probe the temperature coefficient (TC) maps of Si wafers and cells;
- Investigate the spatially resolved TC of multi-crystalline silicon (mc-Si) wafers and cells from different ingot heights;
- Assess the impacts of different solar cell fabrication steps on the spatially resolved TC of cast-mono Si wafers;
- Develop an advanced carrier lifetime imaging technique for accurate quantification and investigation of local recombination activities of non-uniformly distributed defects within Si;
- Develop an accurate method to examine the interface recombination and its temperature and injection dependence;
- Apply the above method to investigate carrier recombination at the Si-SiO<sub>2</sub> (silicon-silicon dioxide) interface, considering a wide range of variables including dielectric charge, temperature, and injection levels.

## **1.2 Thesis Outline**

Chapter 2 reviews the basic concepts of different recombination mechanisms and carrier lifetime which is essential for understanding the work in the following chapters. Moreover, the commonly used characterisation techniques for quantifying carrier recombination are introduced.

Chapter 3 presents the temperature- and injection-dependent photoluminescence (PL) imaging system developed during this thesis, which allows resolving the electrical properties of Si wafers and cells spatially under different operating conditions. Its advantages are demonstrated by investigating the TC of various regions across mc-Si wafers and cells from different ingot heights. The proposed method unveils valuable information that cannot be easily accessed by the common global characterisation techniques.

Chapter 4 further extends the application of the temperature-dependent PL imaging method proposed in Chapter 3 to explore the spatially resolved temperature sensitivity of cast-mono Si wafers and cells. Their local temperature-dependent behaviours are compared at different ingot positions as well as after implementing different solar cell fabrication processes, thus, providing a wealth of information that has not been reported previously.

Chapter 5 elaborates an advanced PL imaging method that overcomes the limitations of the conventional PL imaging systems with uniform illumination, including (a) lateral carrier flows caused by the non-uniformities of the measured samples, which affect the acquired images and result in inaccurate lifetime analysis and image blurring, (b) locally different injection levels at which samples' spatial non-uniformities are measured. The feasibility and advantages of the proposed method are demonstrated using both non-diffused and diffused Si wafers. This approach presents a significant improvement in spatial lifetime accuracy and image sharpness compared to the conventional PL imaging techniques.

Chapter 6 introduces a method to quantify surface recombination under different operating conditions which allows individual assessment of surface and bulk quality. This proposed method is employed to investigate the recombination at the Si-SiO<sub>2</sub> interface by varying the temperature, illumination intensity, and dielectric charge. Most importantly, using this method, the defect parameters associated with this interface are extracted, together with the temperature dependence of the capture-cross sections.

Chapter 7 summarises the main findings of this thesis. Future outlooks for improving the proposed methods and expanding their applications are also outlined in this chapter.

## Chapter 2

### Review: Theoretical Background and Literature

To assist the readers to understand the innovative work in this thesis, this chapter describes the theoretical background that is relevant to the entire thesis and reviews the conventional characterisation techniques and their associated limitations. Specifically, Section 2.1 provides a summary regarding different recombination mechanisms and carrier lifetime. Following that, Section 2.2 introduces the characterisation techniques that are commonly used to probe the carrier recombination in Si PV devices. Section 2.3 provides the temperature-dependent intrinsic properties of Si.

It should be noted that in each of the following chapters, a more detailed literature review related to the content of each chapter is provided.

#### 2.1 Recombination and Carrier Lifetime

The electricity generation of Si solar cells relies on creating electron-hole pairs, which usually is accomplished by the absorption of photons with energy greater than the bandgap of Si [17]. The inverse process of generation is known as recombination whereby electron-hole pairs are annihilated and their released energy can be emitted via photons, phonons or both [17]. Since recombination leads to a loss of photo-generated carriers, it limits the performance of solar cells.

Generally, recombination is classified as intrinsic or extrinsic recombination [17]. Intrinsic recombination is an unavoidable process that occurs even in a perfect Si crystal [17, 18]. Extrinsic recombination is a defect-mediated process that occurs via defect levels within the bandgap, induced by impurities, lattice imperfections or surface dangling bonds [17, 18]. Often, recombination is empirically parameterised by carrier lifetime ( $\tau$ ), which is defined as the average time that a photo-generated carrier can exist before being annihilated by recombination with the opposite charge carrier. It is expressed as the ratio between the excess carrier density ( $\Delta n$ ) and the recombination rate ( $U$ ) [19]:

$$\tau = \frac{\Delta n}{U} \quad 2.1$$

Experimentally, the carrier lifetime measured is the effective lifetime ( $\tau_{\text{eff}}$ ), resulting from different recombination processes occurring simultaneously within the Si bulk and at the surfaces.

As the main topic of this thesis is the characterisation of the electrical properties of Si wafers and cells which highly depends on carrier recombination, the following sections provide a detailed explanation of the different recombination mechanisms and their associated carrier lifetimes.

### ***2.1.1 Intrinsic Recombination***

Intrinsic recombination in Si is categorised as radiative recombination [20] and Auger recombination [21]. Radiative recombination is the reverse process of the optical generation of solar cells. It involves the transition of a free electron from the conduction band to an unoccupied state in the valence band, and releasing its excess energy in the form of a photon [20]. Therefore, the radiative recombination rate ( $U_{\text{rad}}$ ) is proportional to the concentrations of free holes and free electrons, which is given by [17]:

$$U_{\text{rad}} = B_{\text{rad}}(np - n_i^2) \quad 2.2$$

where  $n$  and  $p$  are the electron and hole concentrations, respectively.  $n_i$  is the intrinsic carrier concentration.  $B_{\text{rad}}$  is the radiative recombination coefficient, which is known to be enhanced by Coulomb attraction and affected by charge carrier density and temperature [20, 22-27].  $B_{\text{rad}}n_i^2$  represents the radiative recombination of thermally generated carriers, which is often ignored, as the photo-generated carrier concentration is more dominant.

Photon emission via radiative recombination under illumination is known as photoluminescence — the basis of PL-based characterisation techniques — which will be described in Sections 2.2.3 and 2.2.4.

Auger recombination [21, 28-30] is a three-carrier interaction process. An electron recombines with a hole while its excess energy is transferred to a third electron or hole, which is later released to the crystal as phonons [31]. The rate of Auger recombination depends on the product of the density of each particle involved and is defined as [18]:

$$U_{\text{Auger}} = C_n(n^2p - n_0^2p_0) + C_p(np^2 - n_0p_0^2) \quad 2.3$$

where  $n_0$  and  $p_0$  represent electron and hole density under thermal equilibrium.  $C_n$  and  $C_p$  are Auger coefficients for  $eeh$  (two electrons and one hole) process and  $ehh$  (two holes and one electron) process.

It should be noted that Coulombic interaction between electrons and holes [32] affects Auger recombination. This interaction was used to explain the deviation from the ideal relationship between doping concentration and Auger lifetime [33]. To account for this Coulombic interaction, the enhancement factors  $g_{eeh}$  and  $g_{ehh}$  were introduced and the new expression of  $U_{\text{Auger}}$  is given by [34]:

$$U_{\text{Auger}} = C_n g_{eeh}(n^2p - n_0^2p_0) + C_p g_{ehh}(np^2 - n_0p_0^2) \quad 2.4$$

Besides Coulomb-enhancement, Auger recombination can be affected by other factors [35-37], such as phonon participation [36], presence of particular defects to assist Auger recombination [35]. The temperature impact on Auger recombination has been experimentally accessed by Wang and Macdonald [38], where a reducing Auger coefficient has been reported between 243 K and 303 K. However, their simple model has not been confirmed on samples with different doping densities and did not consider Coulomb-enhancement. Unfortunately, all the other existing empirical parameterisations of Auger recombination [34, 39-42] do not account for the temperature dependence of the Auger coefficients.

### 2.1.2 Defects and Extrinsic Recombination

There are several types of defects appearing in Si: point defects (e.g., vacancies, self-interstitials, interstitial and substitutional impurities), line defects (e.g., dislocations), area defects (e.g., grain boundaries), and volume defects (e.g., precipitates) [43]. As previously mentioned, the presence of defects can create energy states within the Si bandgap, and subsequently facilitate extrinsic recombination. Since defects can appear in the Si bulk, and also at the surfaces, extrinsic recombination can be further categorised into bulk and surface recombination [19].

In 1952, a formula was proposed by Shockley and Read [44] and Hall [45] (SRH) from statistical considerations to describe recombination through the bulk defect with a single defect level,  $U_{\text{SRHbulk}}$ :

$$U_{\text{SRH bulk}} = \frac{np - n_i^2}{\tau_{p0}(n + n_1) + \tau_{n0}(p + p_1)} \quad 2.5$$

where  $\tau_{n0}$  and  $\tau_{p0}$  are capture time constants of electrons and holes which are related to the capture cross-sections ( $\sigma_n$  and  $\sigma_p$ ), defect density ( $N_t$ ) and thermal velocities ( $v_{\text{thn}}$  and  $v_{\text{thp}}$ ):

$$\tau_{n0} = \frac{1}{\sigma_n v_{\text{thn}} N_t}, \quad \tau_{p0} = \frac{1}{\sigma_p v_{\text{thp}} N_t} \quad 2.6$$

SRH densities  $n_1$  and  $p_1$  are given by:

$$n_1 = n_i e^{\left(\frac{E_t - E_i}{k_B T}\right)}, \quad p_1 = n_i e^{\left(\frac{E_i - E_t}{k_B T}\right)} \quad 2.7$$

where  $k_B$  is the Boltzmann constant,  $T$  is the temperature,  $E_i$  is the intrinsic Fermi level, and  $E_t$  is the defect's energy level.

It should be noted that there are a few requirements for using Equation 2.5 [46, 47]. Firstly, it is restricted to defects with a single energy level and only two charge states, i.e. the defect cannot be a multivalent defect [48]. Secondly, Equation 2.5 is valid only if the geometry of the defect does not affect the carrier distribution near the defect and thus its recombination, such as point defects. Thirdly, when extracting carrier lifetime of defects with a strong trapping-behaviour, the asymmetric excess electron and hole concentrations need to be considered [49]. If the above requirements are satisfied, the correlation between defects' electrical properties and carrier lifetime follows the SRH equation. Therefore, it can be used to extract defect parameters from measured carrier lifetime, which is known as injection-dependent lifetime spectroscopy (IDLS) or temperature- and injection-dependent lifetime spectroscopy (TIDLS). A more detailed explanation of lifetime spectroscopy is given in [46, 47, 50].

Surface recombination is usually analysed by the extended SRH equation. The surface recombination rate per unit surface area for a single level is given by [18]:

$$U_s = \frac{(n_s p_s - n_i^2)}{\frac{(n_s + n_1)}{S_{p0}} + \frac{(p_s + p_1)}{S_{n0}}} \quad 2.8$$

where  $n_s$  and  $p_s$  are the carrier concentrations at the surface.  $S_{n0}$  and  $S_{p0}$  are surface recombination velocities of electrons and holes which are related to the surface states for a specific energy level ( $N_{st}$ ) and capture cross-sections ( $\sigma_{ns}$  and  $\sigma_{ps}$ ),

$$S_{n0} = \sigma_{ns} v_{thn} N_{st}, \quad S_{p0} = \sigma_{ps} v_{thp} N_{st} \quad 2.9$$

It should be noted that the Si surface features abrupt discontinuation in the crystal lattice structure. This results in a large density of states and numerous defect levels being present within the bandgap [18]. Therefore, instead of using  $N_{st}$  for a particular energy level, surface recombination rate should be calculated by using surface state density at each energy [ $D_{it}(E)$ ] and integrating over all the energy levels [18], see Equation 6.2 in Chapter 6.

Surface recombination velocity ( $S$ ) is often used to quantify the recombination at surfaces, and it is defined as [18]:

$$S = \frac{U_s}{\Delta n_s} \quad 2.10$$

where  $\Delta n_s$  is the excess carrier concentration at the surface.

The undesirable surface recombination is reduced by surface passivation [51]. This is commonly achieved by the combination of two approaches, referred to as “chemical passivation” and “field-effect passivation”. As pointed out by Cuevas *et al.* [52, 53], the term “field-effect passivation” is misleading, as the electric field cannot repel excess minority carriers away from the surface, and instead modifies the surface carrier concentration to reduce recombination rates. Hence, this approach can be referred to as charge-assisted population control [52, 53]. Chemical passivation is obtained by reducing  $D_{it}$  and lowering the capture probabilities, while charge-assisted population control is achieved by the deposition of charge to reduce the concentration of one type of carriers available at the surface [18]. Often a dielectric layer is used to simultaneously reduce  $D_{it}$  and provide a fixed charge density ( $Q_f$ ) [18]. An in-depth investigation of Si-SiO<sub>2</sub> interface recombination occurring at different temperatures and illumination intensities can be found in Chapter 6.

### 2.1.3 Effective Lifetime

As the mentioned recombination mechanisms occur simultaneously,  $\tau_{\text{eff}}$  can be calculated as:

$$\frac{1}{\tau_{\text{eff}}} = \frac{U_{\text{rad}} + U_{\text{Auger}} + U_{\text{SRH bulk}} + U_{\text{s}}}{\Delta n} \quad 2.11$$

Generally,  $U_{\text{SRH bulk}}$  and  $U_{\text{s}}$  dominate the overall recombination rate in Si solar cells.  $U_{\text{Auger}}$  dominates the high injection level and heavily doped Si due to the cubic correlation with carrier concentration [54].  $U_{\text{rad}}$  is less dominant as Si has an in-direct bandgap [55]. Lifetime due to different recombination mechanisms can be separated to radiative ( $\tau_{\text{rad}}$ ), Auger ( $\tau_{\text{Auger}}$ ), SRH bulk ( $\tau_{\text{SRH bulk}}$ ) and surface ( $\tau_{\text{s}}$ ) lifetime [56]:

$$\frac{1}{\tau_{\text{eff}}} = \frac{1}{\tau_{\text{rad}}} + \frac{1}{\tau_{\text{Auger}}} + \frac{1}{\tau_{\text{SRH bulk}}} + \frac{1}{\tau_{\text{s}}} \quad 2.12$$

Note that symmetric lifetime samples with identical dielectric film on both sides are of interest in this thesis. For such samples with sufficiently low surface recombination,  $\tau_{\text{eff}}$  can also be expressed as [57]:

$$\frac{1}{\tau_{\text{eff}}} = \frac{1}{\tau_{\text{rad}}} + \frac{1}{\tau_{\text{Auger}}} + \frac{1}{\tau_{\text{SRH bulk}}} + \frac{2S}{W} \quad 2.13$$

where  $S$  has to be lower than  $\frac{D}{4W}$  [57],  $W$  is the sample thickness, and  $D$  is the diffusion coefficient.

## 2.2 Characterising Recombination in Silicon

Experimentally, recombination rates can be quantified by carrier lifetime. In this section, lifetime measurement principles are firstly reviewed, followed by a detailed description of the commonly used measurement techniques.

### 2.2.1 Lifetime Measurement Principle

Assuming excess carrier distribution is uniform throughout a Si sample, the excess carrier concentration follows the continuity equation [19]:

$$\frac{d\Delta n}{dt} = G - U \quad 2.14$$

where  $G$  is the generation rate. Combined with Equation 2.1, Equation 2.14 can be rearranged as [58]:

$$\tau_{\text{eff}} = \frac{\Delta n}{G - \frac{d\Delta n}{dt}} \quad 2.15$$

As Equation 2.15 implies,  $\tau_{\text{eff}}$  can be acquired by measuring the time-dependent  $\Delta n$  and generation rate. Depending on the time-dependence of the excitation,  $\tau_{\text{eff}}$  can be measured under steady state, transient and quasi-steady-state (QSS) conditions.

If a constant (or steady state) illumination is applied to the sample,  $\Delta n$  remains constant, Equation 2.15 can be simplified to:

$$\tau_{\text{eff}} = \frac{\Delta n}{G} \quad 2.16$$

This is referred to as the steady state condition where the generation rate is constant and equivalent to the total recombination rate. Since steady state illumination can heat the sample, and only lifetime at a single injection level is obtained in one measurement, this measurement condition is often not preferred for acquiring injection-dependent lifetime measurements.

If a very fast pulse of light is subjected to the sample, the decay of  $\Delta n$  is measured after the light is off and hence is only affected by the recombination. This means Equation 2.15 can be simplified to:

$$\tau_{\text{eff}} = \frac{\Delta n}{-\frac{d\Delta n}{dt}} \quad 2.17$$

This is known as the transient condition. To obtain reliable measurements in this condition, the sample's lifetime should be significantly longer than the turn-off time of the light such that there is a significant excess carrier population after the light is off. Practically, the transient condition is recommended for samples with carrier lifetime  $> 100 \mu\text{s}$  [59]. Since the measured lifetime in this condition is independent of the generation rate, it is often preferable to use this measurement condition to reduce the uncertainty in the determination of the generation rate [60].

If a long and slowly-decaying pulse of light is used such that the excitation is close to steady state, the generalised Equation 2.15 should be used. This measurement condition is known as QSS. In this condition, the absolute value of the generation rate is required for computing the lifetime. Compared to the steady state condition, QSS condition gives lifetime values across a wide range of  $\Delta n$  in one measurement. Compared to the transient condition, QSS condition is less prone to noise and can be used to measure low-lifetime samples.

### 2.2.2 Photoconductance Measurement

Photoconductance (PC) is a contactless and non-destructive characterisation technique for the carrier lifetime measurement [61, 62] that was popularised by *Sinton Instruments* [63]. It has been used in PV research labs and production lines worldwide for testing sample quality, monitoring, and optimising fabrication processes.

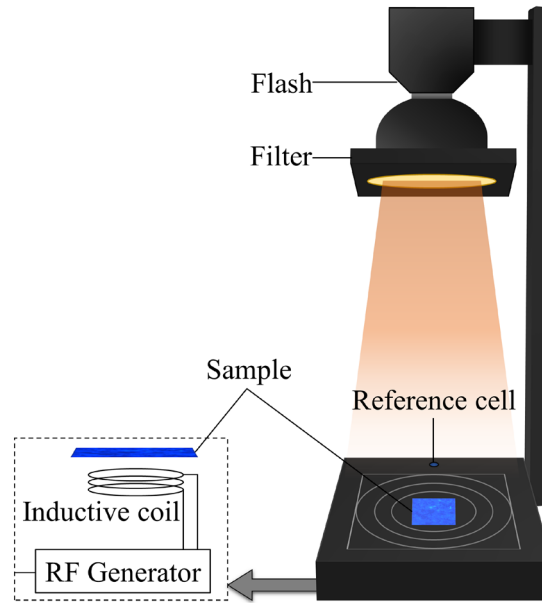


Figure 2.1 Schematic diagram of the PC setup.

As shown in Figure 2.1, in commercial PC-based lifetime testers (such as *Sinton WCT-120*) [59], a xenon photograph flash lamp with a controllable decay rate is used as the excitation source, accompanied by a long pass filter to cut off the short-wavelength part of the flash spectrum. This allows a more uniform generation profile across the sample depth. An inductive coil is positioned underneath the sample to sense its conductance. Simultaneously, the photon flux of the flash is recorded by a reference cell. Such measurements can be subsequently converted to the time-dependent excess carrier

concentration and generation rate, from which the injection-dependent  $\tau_{\text{eff}}$  can be extracted. The detailed calibration procedure from PC to carrier lifetime will be explained later.

### 2.2.2.1 Calibration of the Excess Carrier Concentration

In PC measurements, a magnetic field is generated by a radio frequency (RF) alternating current passing through the coil. This induces eddy currents and an associated magnetic field in the sample, resulting in increasing impedance of the PC coil and thus affecting the measured PC coil voltage ( $V_{\text{PC}}$ ). By establishing the absolute correlation between measured  $V_{\text{PC}}$  and sample conductance,  $\Delta n$  can be determined based on the following equation [62]:

$$\Delta n = \frac{\Delta \sigma}{qW[\mu_n(\Delta n) + \mu_p(\Delta n)]} \quad 2.18$$

where  $q$  is the elementary charge, and  $\mu_n$  ( $\mu_p$ ) is the mobility of electrons (holes) which depends on  $\Delta n$ . An iterative procedure is used to obtain self-consistent mobility and  $\Delta n$ .  $\Delta \sigma$  denotes the PC (i.e. change of the sample's conductance due to illumination), which can be calculated by [47]:

$$\Delta \sigma = (aV_{\text{PC\_light}}^2 + bV_{\text{PC\_light}}) - (aV_{\text{PC\_dark}}^2 + bV_{\text{PC\_dark}}) \quad 2.19$$

where  $V_{\text{PC\_light}}$  is the PC coil voltage recorded after excitation when  $\Delta n > 0$ ,  $V_{\text{PC\_dark}}$  is the PC coil voltage measured in the dark, and  $a$  and  $b$  are the calibration constants that can be determined by calibrating against samples with known conductance [64]. In this thesis, five calibration wafers were used, and their conductance ( $\sigma_{\text{cal}}$ ) was measured by the four-point probe technique. For each wafer, two PC coil voltage measurements were taken in the dark, with ( $V_{\text{PC\_cal}}$ ) and without ( $V_{\text{PC\_air}}$ ) the sample. The calibration constants  $a$  and  $b$  can then be determined by fitting the following quadratic equation [47]:

$$\sigma_{\text{cal}} = a(V_{\text{PC\_cal}}^2 - V_{\text{PC\_air}}^2) + b(V_{\text{PC\_cal}} - V_{\text{PC\_air}}) \quad 2.20$$

It should be noted that Equation 2.18 assumes that the excess electron concentration equals the excess hole concentration. This assumption is true for most cases unless the defects have a carrier trapping behaviour. Carrier trapping causes  $\Delta n$  calculated from Equation 2.18 to deviate from the true minority carrier concentration, resulting in a higher apparent  $\tau_{\text{eff}}$  [65, 66]. Besides carrier trapping, the artificially high apparent  $\tau_{\text{eff}}$  at low

injection levels extracted from PC measurements can be caused by the depletion region modulation (DRM) [67]. It often occurs in Si samples featuring a  $p$ - $n$  junction or an inversion-layer emitter due to the dielectric layer [67].

### 2.2.2.2 Calibration of the Generation Rate

Accurate determination of the generation rate is important for the QSS  $\tau_{\text{eff}}$  measurement. This requires the conversion from the measured output of the reference cell ( $V_{\text{ref}}$ ) to the generation rate by using the following equation:

$$G = f_{\text{sample}}\Phi = f_{\text{sample}}(f_{\text{system}}V_{\text{ref}}) \quad 2.21$$

where  $f_{\text{sample}}$  is a sample-dependent calibration factor that relates to the light source spectrum and sample's optical properties, and  $f_{\text{system}}$  is a system-dependent calibration factor that is associated with the optical path and measurement system.  $\Phi$  is the incident photon flux at the sample plane.

For xenon flash-based measurements,  $f_{\text{system}}$  is provided by *Sinton Instruments* [59].  $f_{\text{sample}}$  can be estimated by using optical models or by checking the *Sinton* manual where  $f_{\text{sample}}$  for Si samples with different substrate thicknesses and various dielectric properties are provided [59].

If other illumination sources are used, such as light-emitting diode (LED) or laser,  $f_{\text{system}}$  and  $f_{\text{sample}}$  can be determined using the method described in Section 2.2.3.2.

Alternatively,  $f_{\text{sample}}$  can be obtained by matching the QSS  $\tau_{\text{eff}}$  with the transient  $\tau_{\text{eff}}$  measurements [68]. As previously explained, the transient measurement is independent of the generation rate. By adjusting  $f_{\text{sample}}$  until QSS and transient  $\tau_{\text{eff}}$  curves are overlapped, the correct  $f_{\text{sample}}$  can be obtained. The advantage of this approach is that neither the measurements of the flash spectrum nor the sample reflectance is required. Moreover, it can compensate the uncertainty in the known  $f_{\text{system}}$ . This approach can directly obtain the product,  $f_{\text{system}}f_{\text{sample}}$ , therefore even if the known  $f_{\text{system}}$  is not accurate, the  $f_{\text{sample}}$  obtained from this approach can offset the error in  $f_{\text{system}}$ . It should be noted that this approach is limited to high lifetime samples which can be accurately measured in the transient condition.

### 2.2.3 Photoluminescence Measurement

PL is another method to obtain injection-dependent  $\tau_{\text{eff}}$ . In a typical PL setup [47], the sample is illuminated using an LED or a laser, and its emitted PL signal is detected by a photodiode (named PL detector) positioning underneath the sample, as shown in Figure 2.2. A long-pass optical filter is placed between the sample and the PL detector to avoid the detection of illumination light. An additional Si photodiode (named reference photodiode) is used to record the photon flux of excitation light. Both PL detector and reference photodiode are connected to transimpedance preamplifiers, and their associated voltage outputs are recorded by a data acquisition card (not shown in Figure 2.2).

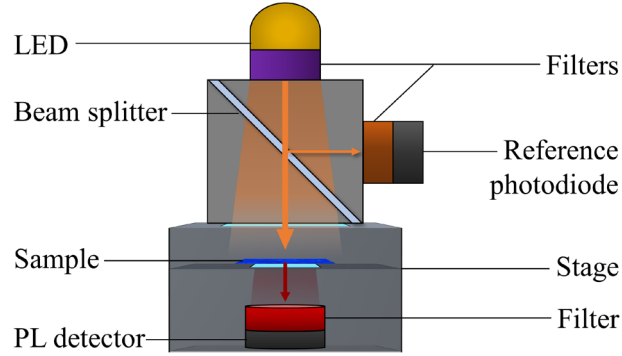


Figure 2.2 Schematic diagram of the PL setup using LED as the excitation source. Note that the optical path for the laser is similar to the LED.

Compared with PC measurement, PL-based measurement is less susceptible to carrier trapping [65], as the measured PL signal is proportional to the product of the minority and majority carriers. As long as the trap-like defect density is much lower than the doping concentration which is true for most cases, the trapping effect can usually be negligible. Therefore, PL is beneficial for obtaining the true lifetime at low injection levels. In addition, PL-based measurements are not affected by DRM as they measure the quasi-fermi level splitting in the sample directly [65]. These serve as the two main advantages for carrying out PL-based lifetime measurements.

#### 2.2.3.1 Calibration of the Excess Carrier Concentration

In PL-based measurements,  $\Delta n$  is extracted from the voltage output of the preamplifier connected to the PL detector ( $V_{\text{PL}}$ ) by using the following equation:

$$V_{\text{PL}} = F_{\text{PL}} B_{\text{rad}}(\Delta n)(N_{\text{dop}} + \Delta n)\Delta n \quad 2.22$$

Where  $N_{\text{dop}}$  is doping density and  $F_{\text{PL}}$  is the calibration factor that depends on both the sample optics and the measurement system.

Two methods are mainly used in this thesis to determine the calibration constant  $F_{\text{PL}}$ . Firstly,  $F_{\text{PL}}$  can be adjusted until the PL lifetime curve matches the PC lifetime curve. In cases of carrier trapping or DRM, PC and PL lifetime measurements need to be matched at high injection levels where the PC measurement is unaffected by carrier trapping and DRM. Secondly, the self-consistent calibration method proposed by Trupke *et al.* [69] can be applied. In this method, a symmetric illumination pulse (such as a sinusoid function) is used. The true  $F_{\text{PL}}$  can be acquired when the two halves of the lifetime curve (corresponding to the rising and falling parts of the modulated pulse) are overlapped. Note that the mismatch of the two halves of the lifetime curve could occur due to the inaccurate  $F_{\text{PL}}$  or inaccurate doping density. This can be checked by remeasuring the doping density or using another calibration approach for PL which is proposed by Giesecke *et al.* [70, 71] and does not require the information of the sample's doping density. Moreover, care needs to be taken when using the self-consistent calibration method for low lifetime samples, due to the reduced accuracy of the detection system's time response, particularly, the photodiode and the preamplifier [72, 73].

### 2.2.3.2 Calibration of the Generation Rate

For LED and laser excitation, the conversion from the measured voltage by the reference photodiode ( $V_{\text{ref}}$ ) to photon flux requires separate calibration measurements. A Si photodiode (named calibration photodiode) with known external quantum efficiency (EQE) is placed in the sample plane and connected to a preamplifier, its associated voltage output is referred to as  $V_{\text{cal}}$ . By varying the light intensity,  $V_{\text{cal}}$  and  $V_{\text{ref}}$  are recorded simultaneously. The calibration factor  $f_{\text{system}}$  can be obtained from the slope of the linear fit of the photon flux and  $V_{\text{ref}}$ :

$$\Phi = V_{\text{ref}} \cdot f_{\text{system}} \quad 2.23$$

where the photon flux  $\Phi$  is calculated from  $V_{\text{cal}}$  using the following equation:

$$\Phi = \frac{V_{\text{cal}}}{q \cdot A \cdot \text{EQE}(\lambda) \cdot g_a} \quad 2.24$$

where  $A$  is the detected area of the calibration photodiode,  $g_a$  represents the amplification factor (gain) of the preamplifier that is connected to the calibration photodiode.

For LED and laser excitation with narrow spectra,  $f_{\text{sample}}$  can be calculated by:

$$f_{\text{sample}} = \frac{1 - R(\lambda)}{W} \quad 2.25$$

where  $R$  is the reflectance of the measured sample at wavelength  $\lambda$ , in this thesis, 810 nm and 808 nm for LED and laser excitation, respectively.

With the determined  $f_{\text{system}}$  and  $f_{\text{sample}}$ , the generation rate can be calculated using Equation 2.21.

#### 2.2.4 Photoluminescence Imaging

PL imaging [74] has proven to be a powerful characterisation technique. Due to its fast, contactless, and spatially resolved nature, it has been widely used in PV research laboratories and production lines to inspect the quality of Si bricks [75], wafers [76-78], cells [79, 80], and modules [81, 82]. Based on the direct relationship between PL emission and  $\Delta n$ , PL images can provide valuable spatially resolved information regarding key electrical parameters such as  $\tau_{\text{eff}}$  [83], implied open-circuit voltage ( $iV_{\text{OC}}$ ) [84, 85], fill factor ( $FF$ ) [86], recombination saturation current [80, 87], and many others [88-90].

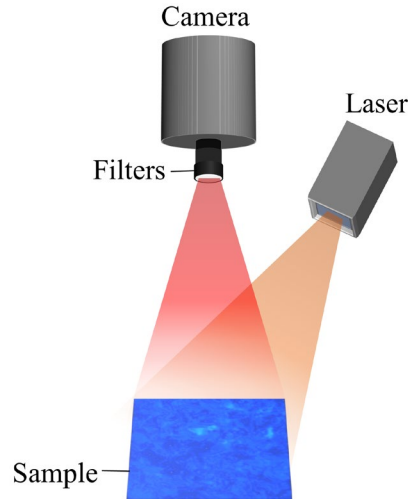


Figure 2.3 Schematic of a conventional PL imaging setup.

As shown in Figure 2.3, the conventional PL imaging systems [74] consist of a spatially uniform illumination source and an infrared camera that collects the emitted PL signal from the sample. A long-pass filter is placed between the sample and the camera to avoid the detection of reflected illumination light by the camera. In addition, a short-pass filter could be added to reduce the photon scattering of the Si sample [91] and the Si

CCD (charge-coupled device) detector of the camera [92, 93], to improve the image quality. However, adding a short-pass filter could result in increased exposure time for getting desirable PL signals. It is also important to perform image post-process including background noise correction, flat-field correction, and point spread function (PSF) correction, to improve the image quality.

The collected PL signal at pixel (x,y) is given by:

$$I_{\text{PL}(x,y)} = F_{\text{PLi}} B_{\text{rad}} (N_{\text{dop}} + \Delta n_{(x,y)}) \Delta n_{(x,y)} \quad 2.26$$

where  $F_{\text{PLi}}$  denotes a calibration constant depending on both the sample optics and the measurement system. In the captured PL images, regions with higher counts (higher  $I_{\text{PL}}$ ) represent areas with larger  $\Delta n$ . With a spatially uniform excitation, larger  $\Delta n$  indicates higher carrier lifetime and  $iV_{\text{OC}}$ . Since PL images alone provide only qualitative information, they are often converted to the minority carrier lifetime images to allow quantitative analysis. The calibration of the PL image to the lifetime image is often achieved by comparing with other lifetime measurement techniques such as QSS PC or QSS PL measurements [78, 83, 94-96].

In contrast to QSS PL and PC lifetime measurements which provide area-averaged assessments of sample quality, PL-based lifetime image is capable of providing spatially resolved information regarding the sample quality. Therefore, it is particularly useful for studying samples with spatially inhomogeneous electrical properties and defects with spatially non-uniform distributions. For instance, combined with the SRH statistics, lifetime images can be used to obtain images of metastable defects [97-99]. However, fundamentally, conventional PL imaging measurements are affected by lateral carrier flows whereby carriers can move laterally from high-quality regions to low-quality regions via diffusion and drift [100, 101]. This results in image blurring and inaccurate lifetime analysis for non-uniform samples [100, 101]. It is very challenging to accurately account for these lateral carrier flows, especially for devices with junctions where the lateral carrier flows are driven by both drift and diffusion. This carrier smearing effect of the conventional PL images will be further discussed in Chapter 5, followed by a newly proposed approach to solve this limitation.

## 2.3 Temperature Dependence of the Bandgap and Intrinsic Carriers

The dominating effect for the temperature dependence of Si solar cells is the change of bandgap energy ( $E_g$ ) with temperature [102]. It is known that Si features a reduction of  $E_g$  with the increasing temperature [103, 104], resulting in an increased short-circuit current ( $I_{SC}$ ) due to higher absorption and a reduced open-circuit voltage ( $V_{OC}$ ) due to increasing  $n_i$  [17]. For Si solar cells, the temperature sensitivity of the efficiency mainly arises from the variation of  $V_{OC}$  with temperature [105]. Besides the changes in  $E_g$  and  $n_i$  as a function of temperature, electron-hole concentration product ( $np$  product), which depends on the type and magnitude of the recombination processes, is another key parameter that determines  $V_{OC}$ , and thus, its temperature dependence [105]. Different recombination processes are reviewed in Section 2.1. In the following sections, the temperature dependence of Si intrinsic properties including  $E_g$  and  $n_i$  is explained. This knowledge is essential for studying the temperature sensitivity of Si solar cells which will be the main topic of Chapter 3 and Chapter 4.

### 2.3.1 Bandgap Energy

$E_g$  is defined as the energy gap between the valence band and the conduction band. With increasing temperature,  $E_g$  of Si decreases, as shown in Figure 2.4. This characteristic is attributed to a change in the relative position of the valence band and the conduction band mainly due to a temperature-dependent electron lattice interaction, as well as the temperature-dependent dilatation of the lattice [106]. An expression for the temperature-dependence of  $E_g$  was proposed with a linear asymptote in a high temperature range [106]:

$$E_g(T) = E_0 - \frac{\alpha T^2}{T + \beta} \quad 2.27$$

where  $E_0$  is the bandgap energy at 0 K, and  $\alpha$  and  $\beta$  are constants.

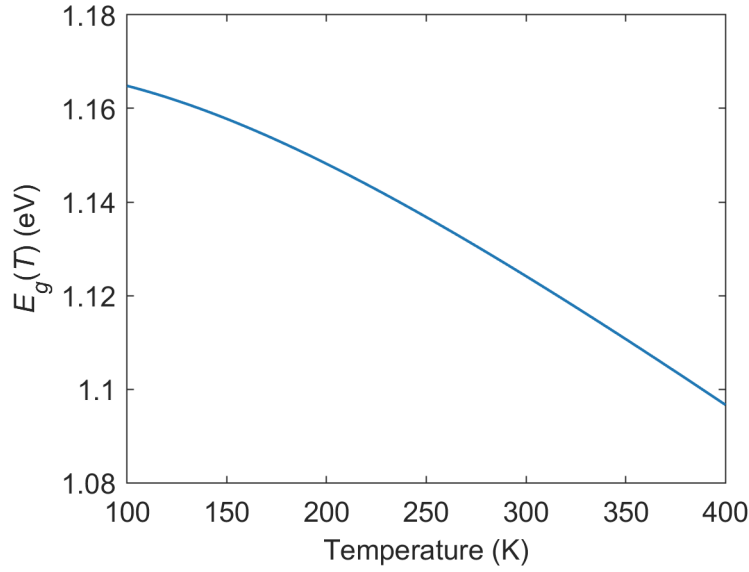


Figure 2.4 Si  $E_g$  as a function of temperature, computed from Pässler's model [103].

Based on experimental data from References [107, 108], a temperature-dependent  $E_g$  model was parameterised by Thurmond [109] and Alex *et al.* [104] using Varshni's formula (Equation 2.27), and later by Pässler [103] using a different expression (Equation 2.28). The extracted parameters of Si  $E_g$  are provided in Table 2-1. As discussed in [103, 110, 111], parameter sets obtained with Varshni's formula are associated with a high degree of arbitrariness, as well as cause systematic deviations between measured and calculated temperature dependences especially in the cryogenic temperature range. In this thesis, Pässler's model [103] is used due to its higher precision.

Table 2-1 Parameters for temperature-dependent  $E_g$  models.

	Thurmond [109]	Alex <i>et al.</i> [104]	Pässler [103]
$E_0$ (eV)	1.17	1.1692	1.17
$\alpha$ (eVK <sup>-1</sup> )	$4.73 \times 10^{-4}$	$4.9 \times 10^{-4}$	$3.23 \times 10^{-4}$
$\beta$ (K)	636	655	-
$\Theta$ (K)	-	-	446
$\Delta$	-	-	0.51

$$E_g(T) = E_0 - \alpha\theta \left\{ \frac{1 - 3\Delta^2}{e^{\frac{\theta}{T}} - 1} + \frac{3\Delta^2}{2} \left( 1 + \frac{\pi^2}{3(1 + \Delta^2)} \left( \frac{2T}{\theta} \right)^2 + \frac{3\Delta^2 - 1}{4} \left( \frac{2T}{\theta} \right)^3 + \frac{8}{3} \left( \frac{2T}{\theta} \right)^4 + \left( \frac{2T}{\theta} \right)^6 \right)^{\frac{1}{6}} - 1 \right\} \quad 2.28$$

### 2.3.2 Intrinsic Carrier Density

$n_i$  is defined as the concentration of the carriers created by the thermal excitation of electrons from the valence band to the conduction band. The temperature dependence of  $n_i$  can be deduced by the following equation:

$$n_i^2 = N_C(T)N_V(T)e^{-\frac{E_g}{k_B T}} \quad 2.29$$

where the effective densities of states in the conduction and valence bands ( $N_C$  and  $N_V$ ) are also temperature-dependent.

There are several semi-empirical models available for computing  $n_i$  in Si, including Green [112], Sproul and Green [113, 114], Misiakos [115], and Couderc *et al.* [116]. All these models use the following expression to describe the temperature dependence of  $n_i$ :

$$n_i = C_A T^{C_B} e^{-\frac{C_C}{T}} \quad 2.30$$

where coefficients  $C_A$ ,  $C_B$ ,  $C_C$  for different semi-empirical models [112-116] and their valid temperature range are summarised in Table 2-2. As mentioned in [116], Green used a generic model for the carriers' mobilities instead of the actual measurements of the samples to parameterise the temperature dependence  $n_i$  in Si, and thus it is less accurate. Later, Sproul and Misiakos used measurements with sufficient precision, however, their interpretation needs to be improved. As pointed out in [116], Sproul's model did not consider the bandgap narrowing (BGN) effect as the available models at that time suggested no BGN effect for the used samples. By using Sproul's data and including Schenk's BGN model [117], Couderc *et al.* [116] reassessed the temperature dependence of  $n_i$  (see Figure 2.5). Note that Couderc *et al.* [116] also compared different  $E_g$  models and suggested that Pässler's model is the most accurate one to use. Therefore, in this thesis,  $n_i$  model from Couderc *et al.* and  $E_g$  model from Pässler are used.

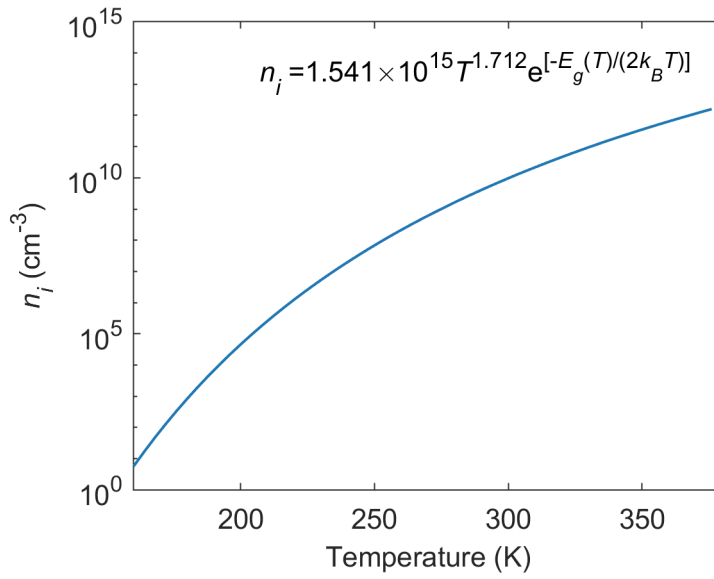


Figure 2.5  $n_i$  in Si as a function of temperature, computed from Couderc's model [116].

Table 2-2 Parameters for different semi-empirical models of  $n_i$  and their valid temperature range.

	<b>Green</b> [112]	<b>Sproul</b> [113]	<b>Sproul</b> [114]	<b>Misiakos</b> [115]	<b>Couderc</b> [116]
$C_A \times 10^{14}$	16.8	10.2	16.4	0.27	15.41
$C_B$	1.715	2	1.706	2.54	1.712
$C_C$	$E_g(T)/2k_B$	6880	$E_g(T)/2k_B$	6726	$E_g(T)/2k_B$
<b><math>T</math> range (K)</b>	200–500	275–375	77–300	78–340	77–375

## 2.4 Chapter Summary

This chapter reviewed the fundamental concepts of recombination mechanisms, including intrinsic recombination such as Auger recombination and radiative recombination, and extrinsic recombination through defects within the Si bulk and at the surfaces. These different recombination processes occur in parallel and can be experimentally quantified by  $\tau_{\text{eff}}$ . Different characterisation techniques for extracting the  $\tau_{\text{eff}}$  have been introduced. However, most of these techniques are designed for conducting measurements at room temperature. Therefore, it highlights the need for improving the characterisation of temperature-dependent electrical properties of Si wafers and cells. As the main topic of this thesis is the effect of temperature on solar cell performance, the temperature dependence of the intrinsic properties of Si, i.e., the change of  $E_g$  and  $n_i$  with temperature,

was also reviewed. Note that this chapter is the basis for the following chapters, a more detailed literature review related to the content of each chapter is provided later in the following chapters.



## Chapter 3

# Spatially Resolved Temperature-Dependent Characterisation of Silicon Wafers and Cells\*

The performance of solar cells is typically measured under STC of 25 °C. However, solar cells' field operating temperatures are often higher than 25 °C, with high temperatures being known to have a detrimental impact on solar cell performance. This impact is often quantified by the TC which is reported as a global value across the entire cell. However, the TC is not expected to be uniform across a solar cell with spatially inhomogeneous distributions of defects. Therefore, this chapter introduces an innovative temperature- and injection-dependent PL imaging method to spatially resolve the TC map of inhomogeneous materials (e.g., mc-Si). In this method, the fast and contactless nature of PL imaging is paired with a temperature-controlled stage enabling the capture of high-quality images at different temperatures. The raw PL images are then calibrated using the front detection QSS PL technique [118], resulting in temperature-dependent  $iV_{OC}$  images. This technique avoids the issues of carrier trapping [65] and DRM [67] known to impact PC-based measurements and can be applied to both non-metallised and metallised samples.

Using the developed method, it is possible to determine the local TC of regions with varying quality (i.e., different defects) and compare them at different ingot positions as well as different Si materials, thus, providing a wealth of material information that was

---

\* This chapter is based on:

**S. Nie**, S. T. Kristensen, A. Gu, R. L. Chin, T. Trupke, and Z. Hameiri, "Photoluminescence-based spatially resolved temperature coefficient maps of silicon wafers and solar cells," *IEEE J. Photovoltaics*, vol. 10, pp. 585-594, 2020.

**S. Nie**, S. T. Kristensen, A. Gu, T. Trupke, and Z. Hameiri, "A novel method for characterizing temperature sensitivity of silicon wafers and cells," in *46<sup>th</sup> IEEE Photovoltaic Specialists Conference*, pp. 0813-0816, 2019 — Won the Best Student Award.

previously not available from the global measurements. By expanding the utility of PL imaging into temperature-dependent measurements, this method is expected to improve energy yield prediction and facilitate future innovations in the optimisation of solar cells for true operating conditions.

Section 3.1 reviews previous studies on the temperature dependence of Si solar cells. Section 3.2 then describes the temperature- and injection-dependent PL imaging system that was developed and utilised in this chapter, together with the details about the calibration method using front detection QSS PL. This method is then employed to study the TC of mc-Si wafers and cells from two ingots of different dislocation densities. The results are summarised and discussed in Section 3.3.

### 3.1 Temperature Coefficients of Solar Cells

Solar cells are typically characterised under the following STC specifications: an AM 1.5G solar spectrum, an irradiance of  $1000 \text{ W} \cdot \text{m}^{-2}$ , and a temperature of 298 K [14]. However, the actual operating conditions of PV devices in the field often significantly deviate from STC [119]. With increasing temperature, parameters such as  $V_{OC}$ ,  $FF$ , and maximum power output decrease [120]. However, variation in  $I_{SC}$  with temperature depends on the absorber layer. For instance,  $I_{SC}$  increases with increasing temperature in Si [121], whereas it decreases in metal halide perovskites [122]. Consequently, the instantaneous output of solar cells can be strongly affected by the operating temperature [123, 124]. In order to allow PV users to accurately predict energy production and PV companies to optimise their cells for true operating conditions, TC, which quantify the impact of temperature on the electrical properties of solar cells, is of particular importance.

For Si solar cells, the temperature sensitivity of the efficiency mainly arises from the variation of  $V_{OC}$  with temperature [105]. Besides the changes of  $E_g$  and  $n_i$  at elevated temperatures that are discussed in Chapter 2, the  $np$  product, which depends on the type and magnitude of the recombination processes, is also a key parameter determining  $V_{OC}$ , and thus, the temperature dependence of Si solar cells [105]. The analytical expression of the temperature coefficient of  $V_{OC}$  [ $TC(V_{OC})$ ] is given by [15]:

$$TC(V_{OC}) = \frac{dV_{OC}}{dT} = - \frac{\frac{E_{g0}}{q} - V_{OC} + \frac{\gamma k_B T}{q}}{T} \quad 3.1$$

where  $E_{g0}$  is the bandgap energy of the semiconductor material linearly extrapolated to 0 K.  $\gamma$  represents the temperature dependences of several parameters determining the diode saturation current density  $J_0$  [15, 17]. The parameter  $\gamma$  also contains information regarding the dominant recombination mechanisms in the material [15]. According to Green [17],  $\gamma$  commonly has values between one and four.

The derivation of Equation 3.1 is explained by Dupré *et al.* [15] using three methods, including the use of the single-diode model,  $np$  product, and external radiative efficiency. Equation 3.1 predicts an approximately linear reduction of  $V_{OC}$  with increasing temperature over a limited temperature range [15, 105], resulting in negative  $TC(V_{OC})$  values. Moreover, a reduction in the absolute temperature sensitivity of  $V_{OC}$  is expected with increasing  $V_{OC}$  [15, 105]. In this thesis, a reduction in  $TC(V_{OC})$  or  $TC(iV_{OC})$  refers to a **lower** temperature sensitivity [i.e., less negative  $TC(V_{OC})$  or  $TC(iV_{OC})$ ].

The temperature dependence of solar cells is normally reported as an average value for the entire cell [120, 121, 125-130]. For instance, the study of Berthod *et al.* [127] into TCs of compensated mc-Si solar cells identified variations in TCs for different cell positions along the ingots with high and medium blend-in-ratio. A less negative TC towards the top of the ingot has been reported, however, the origin of this lower temperature sensitivity has not been clarified. Follow-up studies investigated the TC of passivated emitter rear cells (PERC) fabricated from compensated mc-Si ingots with different targeted resistivities [129, 131]. The authors concluded that a lower resistivity is beneficial for the PERC cells' temperature sensitivity, as a higher net doping leads to a larger  $V_{OC}$ , thus, confirming the theoretical prediction of a reduced temperature sensitivity with increasing  $V_{OC}$ . In addition, the thermal behaviour of tunnel oxide passivated contact (TOPCon) solar cells has been examined using the current-voltage ( $I$ - $V$ ) measurements [132].  $V_{OC}$  drop has been found to be the main limiting factor for TOPCon's performance at elevated operating temperatures. Although an enhanced surface passivation quality has been observed with increasing temperatures, it does not have a noticeable influence on  $TC(V_{OC})$ . Recently, Zhang *et al.* [126] assessed the TC and their illumination dependence of Si solar cells with various structures including PERC, PERT (passivated emitter and rear totally diffused), SHJ (Si heterojunction), and TOPCon. Under 1 Sun illumination, SHJ cell features the least negative TC among all the examined cells. Particularly for  $V_{OC}$ , more negative TCs with decreasing illumination intensity were obtained for all the cells, and their TCs becomes almost identical at the lowest illumination intensity of 0.01 Suns.

Note that the shift of TC to more negative values is expected due to dropping  $V_{OC}$  at lower illumination, but the reason for similar TC of different cell structures at very low illumination is not clear yet.

There has been growing, but limited, research into the spatially resolved temperature sensitivity across wafers and solar cells [133-137]. Existing studies show a large variation in the TC across wafers and cells. Eberle *et al.* [134] have reported a more negative TC, particularly for  $V_{OC}$ , at cell areas with a high concentration of impurities, such as the edge of the cells. Later, Haug *et al.* [133] obtained the spatial distributions of the lifetime and the corresponding TC maps of compensated Si wafers. Positive TC of the lifetime was determined for the entire wafers, with higher TC correlated to low lifetime areas and lower TC observed at high lifetime areas. Eberle *et al.* also further investigated the local temperature-dependent behaviour of mc-Si wafers and cells [137]. They identified a reduction in temperature sensitivity of  $V_{OC}$  in regions that contain dislocation clusters. However, the origin of low temperature sensitivity has not been found. It has been suggested that the low temperature sensitivity of dislocated regions may be caused by the presence of impurities in the dislocation clusters and thus affected by temperature-dependent SRH recombination.

Many of the studies analyse the TC of solar cells and its dependence on the material itself via global single-value measurements. However, for non-uniform materials, such as mc-Si where the concentration and distribution of impurities and crystallographic defects vary significantly across the ingot, spatially resolved measurements can provide more meaningful information. In the following sections, a contactless method is presented that is capable of investigating the impact of temperature on the electrical performance of both metallised and non-metallised Si samples by using spatially resolved temperature-dependent PL-based measurements.

## 3.2 Method

### 3.2.1 Experimental Setup

Figure 3.1 shows a schematic of the PL-based measurement system used to obtain  $iV_{OC}$  images of wafers and cells at different temperatures. The system consists of a Si CCD camera and an 808 nm diode laser. The highest light intensity that currently can be achieved is 0.5 Suns for 6-inch samples and 8 Suns for 2-inch samples. Optical filters

(long pass filters 950 nm and 850 nm, and a short pass filter 1000 nm) are placed in front of the camera to avoid detection of any reflected excitation light. A circular temperature-controlled stage with a diameter of 15 cm (*Sinton Instruments WCT-120 TS*) is used to heat the wafers and cells to higher temperatures. The wafer temperature is monitored by a k-type thermocouple in direct contact with a sister sample when it is heated by the stage.

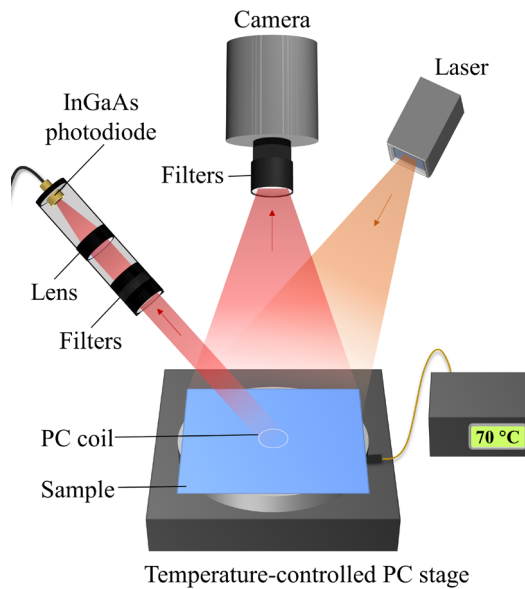


Figure 3.1 The temperature-dependent PL experimental setup (not to scale).

The obtained PL images are then calibrated using the front detection QSS PL technique [118], whereby a sinusoidal laser pulse is used. The PL emission from a selected region is focused on an indium gallium arsenide (InGaAs) photodiode with a lens. The selection of the InGaAs detector is due to its fast response time and higher sensitivity to longer wavelength signals, thus, resulting in higher accuracy for measuring low lifetime samples and metallised samples [72]. A customised filter set, including long pass 850 nm and 950 nm filters and a short pass 1250 nm filter, is attached to the lens to ensure the detection of only the band-to-band PL emission from the samples. In addition, a PC signal from a defined region of the wafer can be recorded by an inductive coil in the *Sinton WCT-120 TS* stage to improve the accuracy of the calibration procedure. Note that the position of InGaAs photodiode is adjusted such that the detected region on the sample would be the same as the sensor area of the coil for subsequent  $\tau_{\text{eff}}$  calibration. A Si photodiode is used to monitor the incident photon flux during measurements (not shown in Figure 3.1). Both photodiodes are connected to transimpedance preamplifiers (*Femto*, not shown in Figure 3.1). All signals are recorded with a *National Instrument* data

acquisition card that is connected to a computer. An additional xenon photograph flash can be used when data at higher injection levels are required.

The primary advantage of this setup is that it enables the determination of absolute  $\tau_{\text{eff}}$  and  $iV_{\text{OC}}$  for both metallised and non-metallised samples, in contrast to using only PC-based measurements [96, 136]. Moreover, this method is resilient to the effects of carrier trapping and DRM [65, 67].

### 3.2.2 Calibration Procedure

The conversion from relative PL counts to  $iV_{\text{OC}}$  maps is based on the relationship between the emitted PL intensity and the  $\Delta n$  at each pixel, which is described by Equation 2.26. The calibration of the constant  $F_{\text{PLi}}$  for PL imaging is performed using QSS PL measurements obtained under the same temperatures as those used during the PL imaging. This calibration procedure involves three main steps: (i) calibration of QSS PL measurements to  $\tau_{\text{eff}}$ ; (ii) determination of the calibration constant,  $F_{\text{PLi}}$ , for the PL imaging; and (iii) conversion of the PL images into  $iV_{\text{OC}}$  maps.

**Step (i):** The calibration of QSS PL measurements to  $\tau_{\text{eff}}$  is explained in Chapter 2 (Section 2.2.3). Two methods are available for obtaining  $\tau_{\text{eff}}$  when using QSS PL, as follows: (a) matching the PC and PL measurements (only for wafers); or (b) using the self-consistent method (for both wafers and cells). There are a few points to note for both methods:

For (a), firstly the PC and PL measurements need to be matched at high injection levels if the samples experience trapping or DRM. Secondly, although the PC and PL signals are detected from the same region on the sample, the PC signal is a weighted integral over the sensor area due to the radial sensitivity of the coil (as discussed in Chapter 5) whereas the PL signal is integrated over the detector field of view. If  $\tau_{\text{eff}}$  is not uniform over the detected sample area, a discrepancy could be attained between the PC and PL measurements due to different averaging methods. This discrepancy depends on the sample and its degree of non-uniformity. Therefore, an area with a relatively uniform lifetime distribution is recommended for carrying out the QSS PL and PC measurements.

For (b), due to the time derivative term in Equation 2.15,  $\frac{d\Delta n}{dt}$ , any error in the calibration factor will cause the disagreement of the two halves of the  $\tau_{\text{eff}}$  curve (i.e., the rising and falling parts of the curve). However, in some cases, such as using a long

illumination pulse, this self-consistent method becomes insensitive to the change of the calibration factor, whereby the rising and falling parts of  $\tau_{\text{eff}}$  always overlap, as the  $\frac{d\Delta n}{dt}$  term is no longer predominant. Therefore, short illumination pulses are preferable for obtaining an accurate calibration factor. Moreover, an accurate record of the time-dependent PL and illumination signals is essential for obtaining accurate  $\tau_{\text{eff}}$ . Although a large amplifier gain is desirable for a better signal to noise ratio, especially for low-quality samples, this can reduce the cutoff frequency of the amplifier. Therefore, measurements with different gains need to be tested to ensure similar  $\tau_{\text{eff}}$  is obtained.

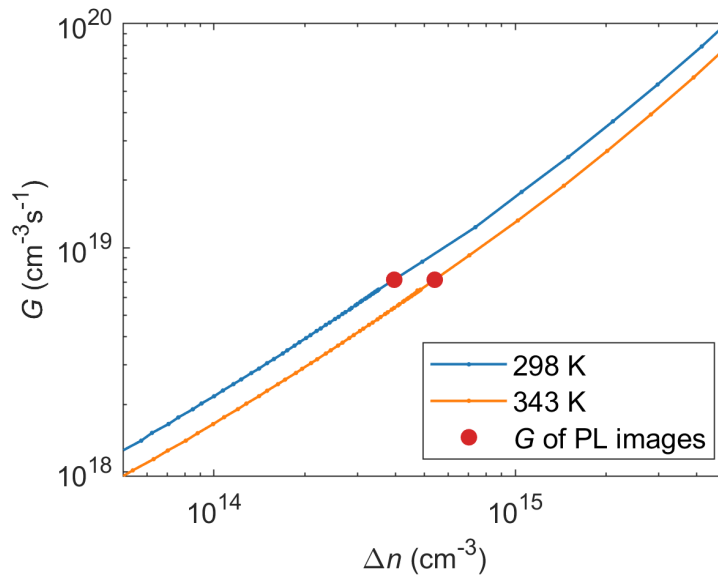


Figure 3.2 Equivalent steady-state  $G$  as a function of  $\Delta n$  extracted from QSS PL measurements at 298 and 343 K. The red point indicates the  $G$  of the PL images and the corresponding  $\Delta n$  of the PL images at the detected regions.

**Step (ii):** The calibrated  $\tau_{\text{eff}}$  from QSS PL measurement is then converted into the equivalent steady-state generation rate using  $G = \frac{\Delta n}{\tau_{\text{eff}}}$ , as shown in Figure 3.2. The obtained equivalent steady-state generation rate is then correlated to the generation rate of the PL image to determine the corresponding  $\Delta n$  that is the average  $\Delta n$  at the detected region of the PL image (the red points in Figure 3.2). Together with the averaged PL intensity across the detected area,  $\Delta n$  is used to determine the PL images' calibration constant  $F_{\text{PLi}}$  via Equation 2.26.

It is worth mentioning that the non-uniformity in the sample could induce lateral carrier flows, which affect the validity of  $\tau_{\text{eff}}$  obtained from the global PC and PL-based methods. Depending on the investigated sample and measurement condition, the impact

of lateral carrier flow can be reduced for low-quality samples (shorter diffusion lengths) as well as  $\tau_{\text{eff}}$  measurements at high injection levels (reduced mobility). Note that the mc-Si samples investigated in this chapter have low  $\tau_{\text{eff}}$ , and the highest illumination achieved by this setup is used to reduce the impact of lateral carrier flows. A new method that effectively mitigates the impact of lateral carrier flows and obtains more accurate  $\tau_{\text{eff}}$  measurements for non-uniform samples is presented in Chapter 5.

**Step (iii):**  $iV_{\text{OC}(x,y)}$  is calculated using:

$$iV_{\text{OC}(x,y)}(T) = \frac{k_{\text{B}}T}{q} \ln \left( \frac{I_{\text{PL}(x,y)}(T)}{F_{\text{PLi}}(T)B_{\text{rad}}(T)n_{\text{i}}(T)^2} \right) \quad 3.2$$

The bandgap energy model of Passler [103] combined with the effective hole mass parameterisation of Couderc *et al.* [116] are used to determine  $n_{\text{i}}$ . The radiative model from [22, 27] is used to determine  $B_{\text{rad}}$ .

The subsequent local TC( $iV_{\text{OC}(x,y)}$ ) is obtained from calibrated PL images taken at different temperatures via:

$$\text{TC } (iV_{\text{OC}})_{(x,y)} = \frac{iV_{\text{OC}(x,y)}(T_2) - iV_{\text{OC}(x,y)}(T_1)}{T_2 - T_1} \quad 3.3$$

where  $T_1$  is 298 K and  $T_2$  is 343 K. Equation 3.3 simplifies the determination of TC, as it uses only two temperatures. This simplification has been tested by taking six measurements between 298 K and 343 K at 5–10 K intervals. A linear reduction of  $iV_{\text{OC}}$  with increasing temperature is observed in this temperature range. A good agreement ( $< 2\%$ ) is found between the TC obtained from Equation 3.3 and the TC obtained from the slope of the linear fit, thus, validating the simplified approach of Equation 3.3.

The validity of the proposed method was tested by comparing the  $iV_{\text{OC}}$  images of several wafers obtained by the proposed method and by the method implemented in a commercial PL imaging tool (*BT Imaging, LIS-R3*) and the methods from [96, 136]. In addition, the  $I$ - $V$  characteristics of several solar cells were measured at the temperature range of 298–343 K using a *Wavelabs I-V* tester (*model SINUS-220*) and compared with the results obtained by the proposed method. For both wafers and cells, great agreement ( $< 5\%$ ) has been obtained. An example is presented in Section 3.3.1.

### 3.2.3 Sample Preparation

Fourteen wafers from two industrially grown *p*-type boron (B)-doped mc-Si centre ingots were used (produced in 2015). Of the seven wafers obtained from each ingot, two originate from near the top of the ingot, two from near the bottom, and the remaining three wafers from positions in between. One ingot has a high dislocation density, while the second ingot has a low dislocation density. The exact dislocation density is determined using the algorithm implemented in a commercial PL imaging tool (*BT Imaging, LIS-R3*). The resistivity of the wafers varies between  $1.5 \, \Omega \cdot \text{cm}$  and  $2.2 \, \Omega \cdot \text{cm}$ . The wafers were saw-damage etched before undergoing a phosphorus-based gettering process. After etching off the diffused layer, the wafers were recleaned before undergoing silicon nitride ( $\text{SiN}_x$ ) passivation [refractive index of 2.08 (at 632 nm) and thickness of 75 nm] using an industrial plasma-enhanced chemical vapour deposition system (*MAiA, Meyer Burger*). The stability of  $\text{SiN}_x$  passivation at elevated temperatures was tested, and no degradation was observed within the duration of the measurements. The final thickness of all the wafers was approximately  $185 \pm 10 \, \mu\text{m}$ . Please note that the wafers were not belt-furnace fired. Fourteen solar cells made from sister wafers are also included. These cells were fabricated in an industrial PERC production line.

The samples were studied using the temperature-dependent PL imaging system described in Section 3.2.1. The PL images are acquired at temperatures from 298 K to 343 K under 0.5 Suns illumination. The relative PL images are then calibrated and converted into  $iV_{\text{OC}}$  images using front detection QSS PL measurements conducted under identical conditions to those used during the PL imaging.

## 3.3 Results and Discussion

### 3.3.1 Spatially Resolved Results

An example of the various parameter images obtained by the proposed method is depicted in Figure 3.3. Two wafers from the middle of each ingot are compared (resistivity:  $1.8 \pm 0.1 \, \Omega \cdot \text{cm}$ ; high and low dislocation densities). Figure 3.3(a) and (d) shows  $iV_{\text{OC}}$  maps at 298 K. As expected, lower  $iV_{\text{OC}}$  values are observed in areas with dislocation clusters (appear as dark clusters in the PL images) and grain boundaries (dark lines). The calculated average  $iV_{\text{OC}}$  of the highly dislocated (HD) wafer is  $611 \pm 3 \, \text{mV}$ , which is 15 mV ( $\sim 2.5\%$ ) lower than the average  $iV_{\text{OC}}$  of the lowly dislocated (LD) wafer ( $626 \pm 3 \, \text{mV}$ ).

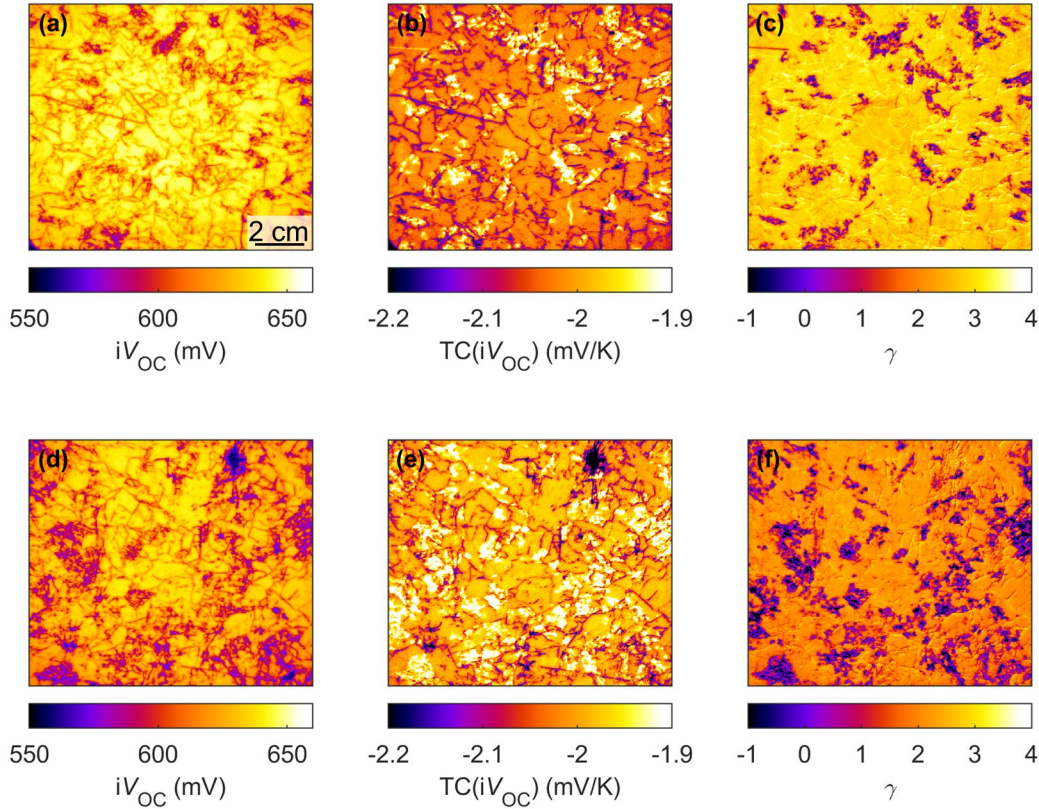


Figure 3.3 (a) and (d) Spatially resolved  $iV_{OC}$  at 298 K; (b) and (e)  $TC(iV_{OC})$ ; and (c) and (f)  $\gamma$  of two wafers with (a)–(c) low and (d)–(f) high dislocation densities under 0.5 Suns illumination. The images were cropped to present only the regions of interest.

Images of  $TC(iV_{OC})$  are displayed in Figure 3.3(b) and (e). A large variation of  $TC(iV_{OC})$  across the wafers is observed. The data shows that  $TC(iV_{OC})$  is more negative in grain boundaries and some dislocation clusters, indicating a larger reduction of  $iV_{OC}$  with increasing temperature in these regions compared to other areas across the wafer. Most of the dislocation clusters show lower temperature sensitivity. This observation contradicts the common belief that the temperature sensitivity is expected to increase with decreasing  $iV_{OC}$  [15, 120]. Recent studies have observed only low temperature sensitivity of dislocation clusters [134, 137]. However, in this investigation, dislocated regions of two tested ingots show both high and low temperature sensitivities. This discrepancy could possibly be explained by differences in the processing procedure for the investigated wafers. This is later shown by Kristensen *et al.* [77] that the gettering process can alter the  $TC(iV_{OC})$  of the dislocated region from low temperature sensitivity to high temperature sensitivity. Moreover, in Chapter 4, the impacts of different solar cell fabrication processes on the  $TC(iV_{OC})$  map of Si wafers are explored.

Figure 3.3 (c) and (f) presents  $\gamma$  maps calculated by applying Equation 3.1 to each pixel. There is a clear difference between the two ingots, with global values of 2.29 for the LD wafer and 1.35 for the HD wafer. Lower  $\gamma$  values (even negative), consequently reducing  $J_0$  [15], are observed at dislocation clusters, explaining the more uniform  $\gamma$  distribution across the LD wafer and larger average  $\gamma$ . The source for the interesting and unexpected negative  $\gamma$  is discussed in References [77, 130, 137]. Dupre *et al.* explained that global negative  $\gamma$  values of cells are mostly due to an increase of external radiative efficiency [138] at open circuit for these cells at increased temperatures [130]. However, the physics behind this negative  $\gamma$  is still unclear and requires further investigation. In Chapter 4, the implication of negative  $\gamma$  will be further explored.

To assess the validity of the proposed method at the cell level, cell measurements obtained using the proposed method are compared with  $I$ - $V$  measurements [127, 129, 133]. An example is presented here. Figure 3.4 illustrates the  $iV_{OC}$  map of a PERC cell originating from the middle of the HD ingot [sister cell of the wafer of Figure 3.3(d)–(f)] and its corresponding  $TC(iV_{OC})$  map under 0.5 Suns illumination. Note that a circular heat stage is used for the PL imaging, causing a circular pattern. Only the middle region, outlined in black, is used for subsequent analysis. The local values are harmonically averaged and compared with the results obtained from global  $I$ - $V$  measurements for the same solar cell. The harmonic average is used as it provides a better estimation of the material quality for predicting cell performance [139, 140]. Table 3-1 summarises the results. Excellent agreement within the range of 1% is found between the two measurements.

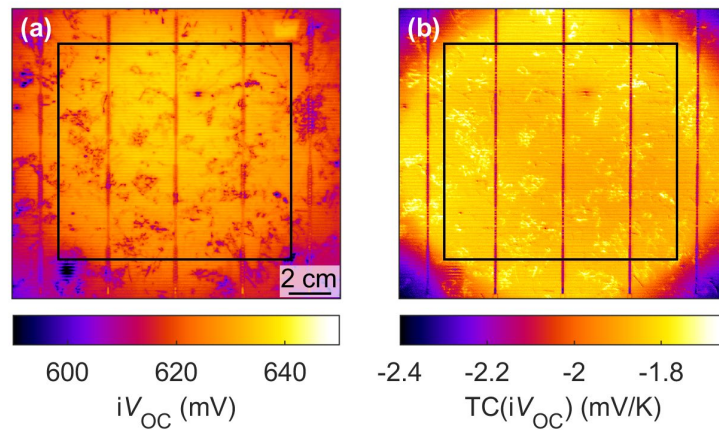


Figure 3.4 (a) Spatially resolved  $iV_{OC}$  at 298 K and (b)  $TC(iV_{OC})$  of a PERC solar cell originating from the middle of the highly dislocated ingot under 0.5 Suns illumination.

Table 3-1 Global  $iV_{OC}/V_{OC}$  and  $TC(iV_{OC}/V_{OC})$  of a PERC cell from the middle of the HD ingot.

	$iV_{OC}/V_{OC}$ at 298 K (mV)	$TC(iV_{OC}/V_{OC})$ (mV/K)
<b>PL-based method</b>	627	-1.87
<b><i>I-V</i> measurement</b>	625	-1.89

By comparing  $iV_{OC}$  maps and  $TC(iV_{OC})$  maps of the cells, the regions near the contacts (especially busbars) show higher temperature sensitivity, as expected from the higher recombination in these areas in comparison with the well-passivated regions between the contacts. Regions with lower temperature sensitivity are found to be correlated with dislocated areas. Comparing the cell with the wafer, the temperature sensitive regions across the sister wafer [such as grain boundaries and some dislocation clusters in Figure 3.3(d) and (e)] are not as easily identified on the cell maps [Figure 3.4(a) and (b)]. The difference can be explained by the lateral conduction across the cell and the incomplete fabrication process of the wafers in Figure 3.3, specifically the lack of firing.

### 3.3.2 Impact of Ingot Height

Figure 3.5(a) shows the harmonically averaged  $iV_{OC}$  at 298 K extracted from calibrated PL images of the wafers from both the HD and LD ingots. As expected, the LD ingot has a higher  $iV_{OC}$  compared to the HD ingot. For both ingots, the highest  $iV_{OC}$  is observed in the middle of the ingot; the  $iV_{OC}$  declines gradually towards the bottom and top of the ingot. This trend follows the variation of material quality with ingot height, where the top and bottom parts of the ingot contain a higher impurity concentration due to segregation from the liquid-to-solid phase and diffusion from the crucible [141, 142]. A similar trend has been observed in Reference [142]. The global  $V_{OC}$  values of the sister cells measured using a temperature-dependent *I-V* tester are presented in Figure 3.5(b). The variation of  $V_{OC}$  along the ingot is less obvious compared to the wafers, however, the  $V_{OC}$  of top and bottom cells are still lower than those of the more centrally located cells. The cells exhibit higher voltage compared to the sister wafers; this is more pronounced for cells at the bottom of the ingot. This can be explained by the lack of the firing process for the wafers, which is known to passivate large fractions of the grain boundaries [142-144].

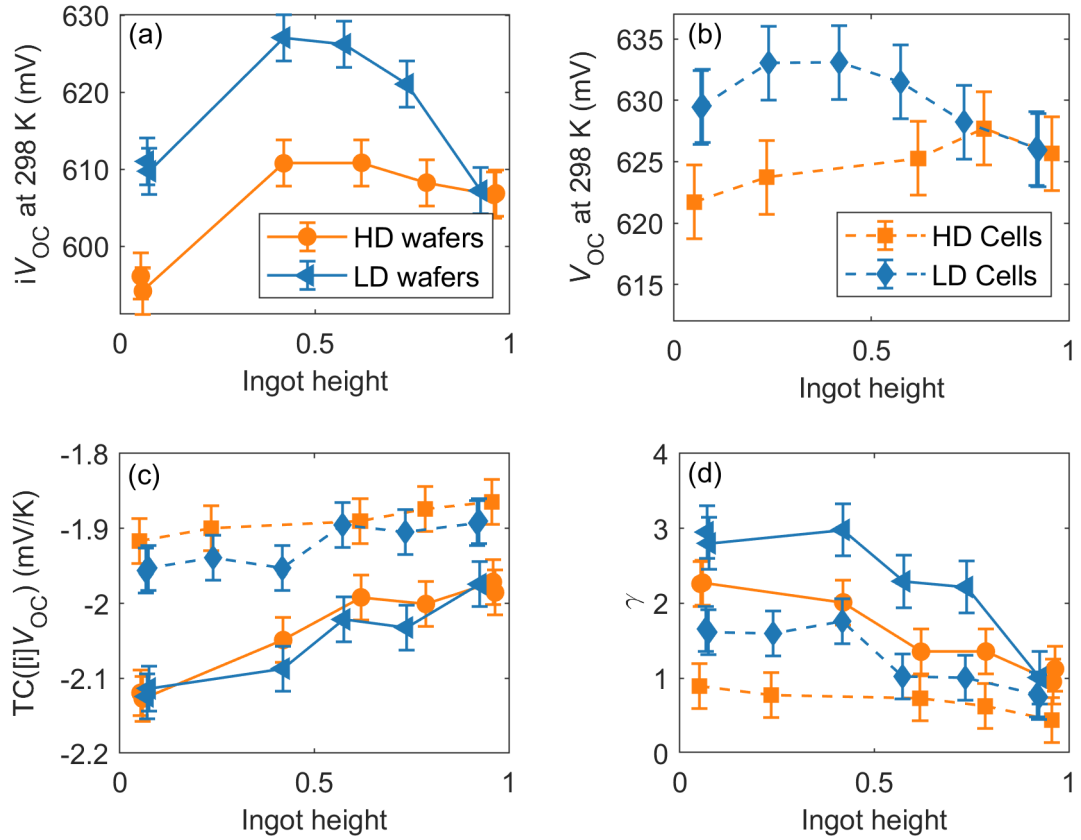


Figure 3.5 Global results of wafers and sister cells with low and high dislocation densities as a function of ingot height under 0.5 Suns illumination: (a)  $iV_{OC}$  at 298 K; (b)  $V_{OC}$  at 298 K; (c)  $TC(iV_{OC})$  and  $TC(V_{OC})$ ; and (d)  $\gamma$ . The error bars represent the measurement uncertainties.

Figure 3.5(c) shows the average  $TC(iV_{OC})$  extracted from calibrated PL images of the wafers and global  $TC(V_{OC})$  for the cells as a function of ingot height.  $TC(iV_{OC})$  of the investigated wafers are found to be less negative with increasing ingot height (from  $-2.15$  mV/K to  $-1.95$  mV/K), although the top wafers show reduced  $iV_{OC}$  values. The improved TCs of the top wafers can be explained by an increasing  $TC(\tau_{eff})$  towards the top of the ingot, as discussed in Reference [133]. Moreover, the increasing density of dislocation clusters with low temperature sensitivity towards the top of the ingot (see Figure 3.7) could also contribute to the overall less negative TC of the top wafers and cells. This is likely due to the increased concentration of impurities causing low temperature sensitivity [137]. The cells exhibit a similar trend, but with lower temperature sensitivity and less variation along the ingot. This is in agreement with previous studies [127, 129, 133]. When considering the measurement uncertainty as represented by the error bars, there is no clear difference in the global temperature sensitivity between the two ingots, for both wafers and cells. It is difficult to pinpoint the impact of dislocation

density on the global TC values since dislocation clusters show both high and low  $TC(iV_{OC})$  as demonstrated in Figure 3.3.

Figure 3.5(d) shows the average  $\gamma$  values of the cells and wafers (calculated using Equation 3.1) as a function of ingot height. Like the cells, the wafers exhibit a decreasing  $\gamma$  with increasing ingot height. Berthod *et al.* observed a similar trend on compensated materials [129]. Interestingly, the wafers exhibit larger  $\gamma$  values compared to the cells and stronger variation along the ingot, indicating a more significant change in the recombination rate from the bottom to the top of the ingot.

Figure 3.6 shows the pixel-level  $TC(iV_{OC})$  as a function of  $iV_{OC}$  at 298 K under 0.5 Suns illumination. The colour represents the data density normalised to unity ('1' represents the highest density). As expected theoretically from Equation 3.1, the temperature sensitivity tends to decrease with increasing  $iV_{OC}$ . However, it is very interesting to observe that regions with similar  $iV_{OC}$  (at 298 K) show a large spread, up to 40%, in  $TC(iV_{OC})$ , suggesting that temperature sensitivity can only be well understood by spatially resolved measurements.

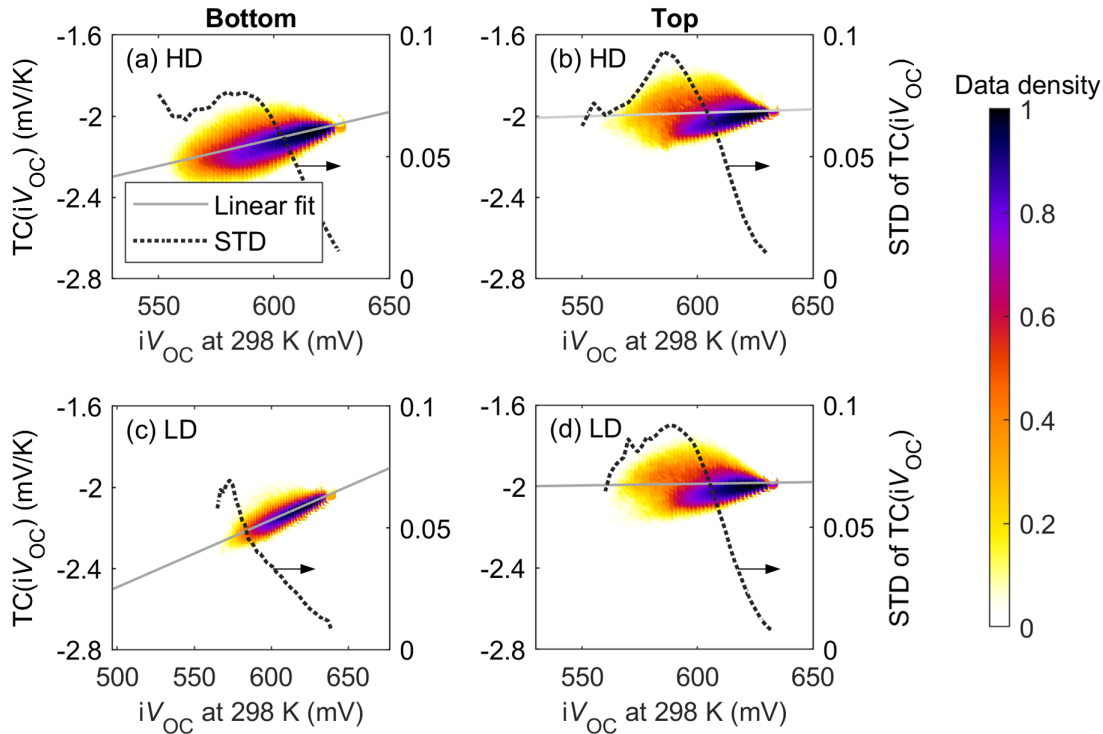


Figure 3.6 Density scatter plot of  $TC(iV_{OC})$  as a function of  $iV_{OC}$  at 298 K of HD and LD wafers from bottom and top of the ingots under 0.5 Suns illumination, with the line of best linear fit (grey) and  $TC(iV_{OC})$  standard deviation (black) overlaid. The standard deviation shown is for  $iV_{OC}$  bins of 2 mV.

The spread of  $TC(iV_{OC})$  across the wafers in the  $iV_{OC}$  domain is quantitatively determined as standard deviation (STD) of  $TC(iV_{OC})$  at different  $iV_{OC}$  bins. For all wafers, low STD occurs at high  $iV_{OC}$ , while the medium to low  $iV_{OC}$  range shows high STD. A shift of  $TC(iV_{OC})$  towards less negative values is noticeable for the top wafers. This is consistent with the previous observation [see Figure 3.5(c)] that the average temperature sensitivity reduces with increasing ingot height.

A linear fit of  $TC(iV_{OC})$  as a function of  $iV_{OC}$  at 298 K is also included in Figure 3.6. A clear trend of less-negative TC for increasing  $iV_{OC}$  is observed for the bottom wafers of both ingots. However, a flatter trendline is observed for the top wafers, in addition to a larger spread of TC across these wafers at medium to low  $iV_{OC}$  (as indicated by the larger STD values).

Figure 3.7 presents maps of  $iV_{OC}$  at 298 K,  $TC(iV_{OC})$ , and the resulting  $\gamma$  of two wafers originating from the bottom (a)–(c) and top (d)–(f) of the HD ingot. As expected, small grains and a large fraction of grain boundaries can be observed in the bottom wafer. It seems that for the bottom wafer, almost all the low-quality regions (grain boundaries and dislocated regions) show a higher temperature sensitivity compared to the intra-grain regions. In contrast, the difference between these regions appears less significant in the top wafer, where most of the dislocation clusters show low temperature sensitivity. In general, it seems that wafers from the top of the ingot are less sensitive to temperature variations compared to wafers from the bottom (see global TC values in Figure 3.5). This could be attributed to the impact of a higher density of grain boundaries and different impurities in the bottom wafer. It is possible that the dislocation clusters are decorated by different impurities with different impacts on the temperature sensitivity of the wafers. This will be discussed in the next section.

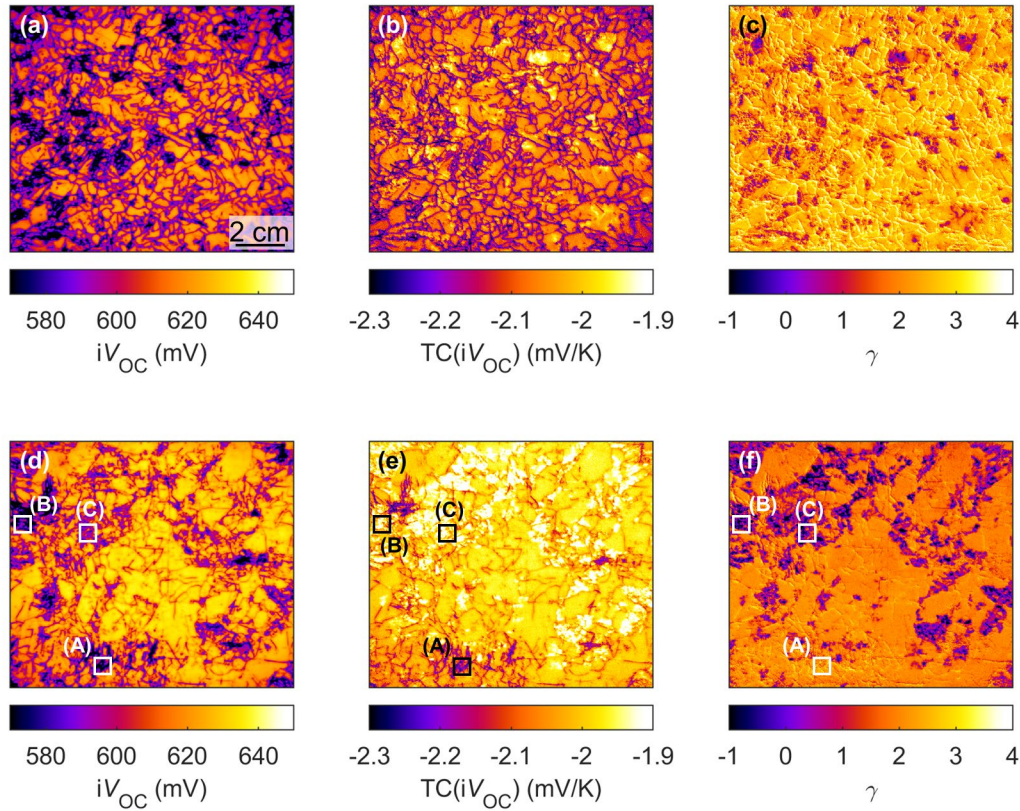


Figure 3.7 Spatially resolved  $iV_{OC}$  at 298 K,  $TC(iV_{OC})$ , and  $\gamma$  of two HD wafers from (a)–(c) the bottom and (d)–(f) the top of the ingot under 0.5 Suns illumination. The images were cropped to present only the regions of interest.

### 3.3.3 Temperature Coefficient of Dislocation Clusters

To investigate the source of the large variation in the  $TC(iV_{OC})$  of dislocation clusters, dislocated areas with different TCs were selected for further investigation. Three different regions of interest (ROIs) are defined in Figure 3.7(d)–(f), labelled (A), (B), and (C). Table 3-2 summarises the obtained parameters for these regions.

Table 3-2  $iV_{OC}$ ,  $TC(iV_{OC})$ , and  $\gamma$  of different ROIs across a highly dislocated wafer from the top of the ingot.

	$iV_{OC}$ at 298 K (mV)	$TC(iV_{OC})$ (mV/K)	$\gamma$
ROI (A)	584	-2.14	2
ROI (B)	580	-1.95	-0.32
ROI (C)	594	-1.95	0.19

All three ROIs are low-quality regions containing dislocation clusters. ROIs (A) and (B) have a similar  $iV_{OC}$  at 298 K, but different TC; whereas ROIs (B) and (C) have a similar TC, but different  $iV_{OC}$ . Compared to ROI (A) with  $\gamma$  of 2, the  $\gamma$  values of ROIs (B) and (C) are much smaller than one (and even negative); a lower  $\gamma$  is shown to contribute to less negative TC( $iV_{OC}$ ). This indicates that different recombination rates limit the performance of these three regions, and a lower  $\gamma$  leads to a reduced recombination rate at higher temperatures, thus, a more favourable TC( $iV_{OC}$ ).

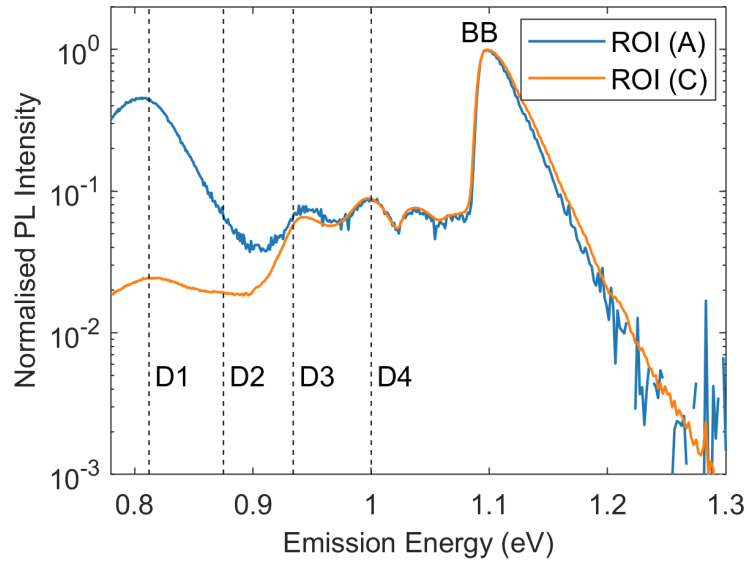


Figure 3.8 PL spectra of ROIs (A) and (C) of a highly dislocated wafer from the top of the ingot at  $122 \pm 7$  K (actual sample temperature) under 20 Suns.

These regions were examined by micro-PL ( $\mu$ PL) spectroscopy [43]. Figure 3.8 shows the PL spectra of ROIs (A) and (C) at an actual sample temperature of  $122 \pm 7$  K (the actual sample temperature is obtained by modelling the band to band (BB) peak [145]). Low temperatures are chosen for the investigation, as defect peaks are strongly temperature-quenched and therefore more noticeable at lower temperatures. The four dislocation-related lines are labelled as D1 (0.812 eV), D2 (0.875 eV), D3 (0.934 eV), and D4 (1.000 eV) [146, 147]. D1, D2 (very weak), D3, and D4 can be identified in both regions, indicating that both regions are highly dislocated. From previous studies [146, 148-150], D1 and D2 are found to be associated with defects and impurities decorating the dislocations, whereas D3 and D4 have been correlated with the intrinsic properties of the dislocation cores.

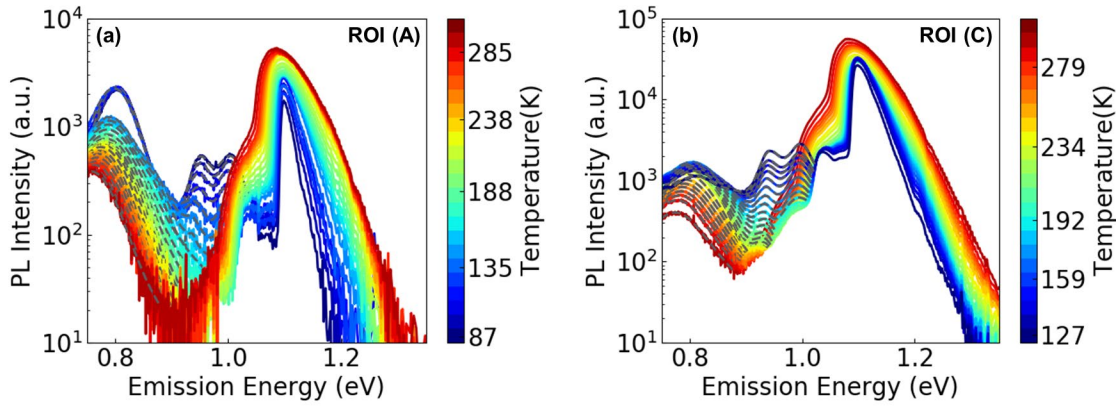


Figure 3.9 PL spectra under 20 Suns of: (a) ROI (A) at a sample temperature range from 87–304 K; and (b) ROI (C) at a sample temperature range from 127–302 K.

To distinguish between these regions, temperature-dependent  $\mu$ PL measurements were performed at a wide temperature range from 87 K to 304 K for ROI (A) and from 127 K to 302 K for ROI (C) and shown in Figure 3.9. For both ROIs, the D1 peak can be observed even at medium to high temperatures, while D3 and D4 cannot be observed above 200 K. Each defect peak is then fitted using the Voigt function [151] and the fits are shown in Figure 3.9 as grey dot lines. Since the D1 peak can be observed across the entire temperature range (even at high temperatures), this suggests that the D1 emission is a good indicator of the recombination activity at these dislocated regions [148]. The activation energies ( $E_a$ ) of D1-associated defects are extracted at both ROIs by using an Arrhenius plot to fit the spectrally integrated defect PL (see Figure 3.10).

In order to extract  $E_a$  of the D1-associated defects, the spectrally integrated defect PL,  $PL_{\text{defect}}(T, \Delta n)$ , is fitted to the equation below (the derivation of this equation is given in Appendix A) [152]:

$$PL_{\text{defect}}(T, \Delta n) = \frac{PL_0}{1 + \frac{C}{\Delta n(T)} T^{1.5} \exp\left[-\frac{E_a}{k_B T}\right]} \quad 3.4$$

where  $PL_0$  and  $C$  are positive constants.  $PL_0$  represents  $PL_{\text{defect}}$  as the temperature approaches 0 K.  $\Delta n(T)$  is calculated relatively using the spectrally integrated BB PL ( $PL_{\text{BB}}$ ) and the ionised acceptors ( $N_a^-$ ) [153] as  $\Delta n(T) \propto [PL_{\text{BB}}(T)]/[B_{\text{rad}}(T) \times N_a^-(T)]$ . The measurement is assumed to be at low injection based on the extrapolated lifetime curves. This assumption is also confirmed using a PC1D simulation [154] of the sample using the maximum observed bulk lifetime of 30  $\mu$ s, yielding a maximum excess carrier

concentration that is only twice the doping density. This assumption should become even more valid at lower temperatures, as the lifetime decreases with decreasing temperature. For ROI (C), similar to Reference [147], the measurement cannot be well fitted at low temperatures. The reason for this has not been provided in Reference [147] although it is stated that this type of behaviour seems not to be an effect characteristic of dislocation clusters.

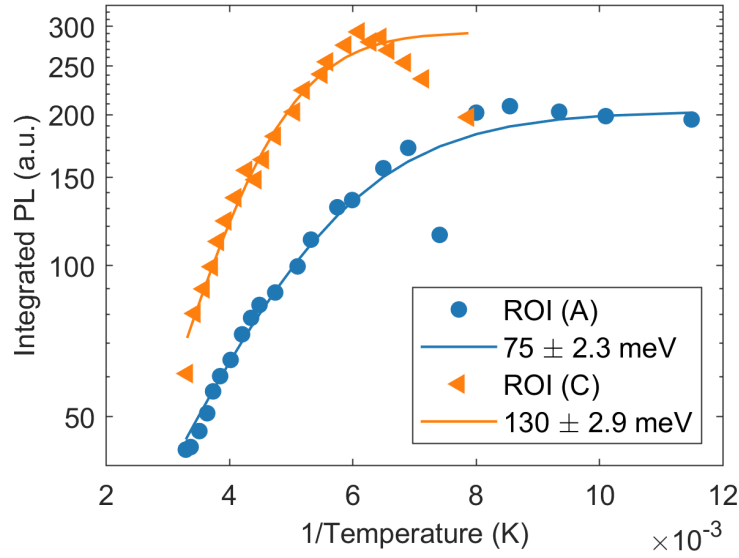


Figure 3.10 Arrhenius plots for ROIs (A) and (C) with their respective best fit.

The two different extracted values of  $E_a$  are  $75 \pm 2.3$  meV for ROI (A) and  $130 \pm 2.9$  meV for ROI (C). This may indicate that different impurities occupy these two regions. Compared to ROI (A), ROI (C) shows a stronger reduction of  $PL_{\text{defect}}$  with increasing temperature (Figure 3.10), indicating that recombination strongly decreases with temperature. This suppresses the effect of the temperature dependence of  $n_i$  which reduces the magnitude of the decrease of  $iV_{OC}$  with increasing temperature. As a result, the temperature sensitivity at ROI (C) is lower.

### 3.4 Chapter Summary

This chapter presents a method for measuring temperature-dependent  $iV_{OC}$  images on metallised and non-metallised samples without the impact of carrier trapping and DRM, by combining PL imaging and front detection QSS PL measurements. These spatially resolved measurements allow for the assessment of both local and global temperature

characteristics of wafers and cells, providing more detailed information regarding the material properties than conventional global measurements.

The TCs of wafers and cells from different ingot heights with different dislocation densities were studied using the developed technique. The local results demonstrate that dislocated areas on wafers show both high and low temperature sensitivity, compared to intra-grain regions. Moreover,  $\gamma$  is found to exhibit low values (even negative) in some areas of dislocation clusters, with low temperature sensitivity.

Global TC( $iV_{OC}$ ) values of the investigated wafers and cells are found to be less negative with increasing ingot height. Furthermore, the wafers from the top of the ingots show a larger spread of localised TC( $iV_{OC}$ ) towards less negative values which is particularly evident at a medium to low  $iV_{OC}$  range, likely due to less temperature-sensitive dislocation clusters. This suggests that cells made from the top of the ingot, although having higher defect concentrations, suffer relatively less degradation when performing at higher temperatures.  $\mu$ PL measurements were performed at dislocated regions with different TC values.  $E_a$  is found to be  $130 \pm 2.9$  meV and  $75 \pm 2.3$  meV for the dislocation clusters with low and high temperature sensitivity, respectively, which may indicate that different impurities occupy these two regions, thereby resulting in different TC values.

This chapter demonstrates the advantages and feasibility of the proposed approach and expands the utility of PL imaging into temperature-dependent measurements. Besides the results presented in this chapter, this proposed method was also used to study the local temperature sensitivity of crystal defects of compensated mc-Si materials, see References [77, 155]. Furthermore, this approach is used to investigate the impact of different solar cell fabrication processes on the TC of cast-mono Si, which is presented in the next chapter. In general, this method is expected to be beneficial for improving the understanding of the thermal behaviour of non-uniform PV materials and optimising solar cell and wafer performance under non-STC.

## Chapter 4

# Impacts of Gettering and Hydrogenation on Silicon Wafer Temperature Sensitivity<sup>†</sup>

In Chapter 3, a temperature-dependent PL imaging method which enables spatially resolved TC( $iV_{OC}$ ) maps of Si wafers and cells was introduced. It was shown that TC( $iV_{OC}$ ) is non-uniform across the wafers and cells due to the presence of non-uniformly distributed defects. Gettering and hydrogenation modify the recombination activity of the defects in PV devices and are expected to affect the temperature sensitivity of Si wafers and cells. This chapter assesses the influence of gettering, firing, and advanced hydrogenation on the spatially resolved TC( $iV_{OC}$ ) of cast-mono Si wafers, using the method presented in Chapter 3. Most regions containing crystallographic defects are characterised by low temperature sensitivity and are further investigated using hyperspectral PL imaging and atom probe tomography. The combination of three advanced characterisation methods, from the nanoscale to the milliscale, provides an in-depth understanding of the temperature-dependent recombination activity in cast-mono Si.

Section 4.1 briefly reviews the gettering and hydrogenation processes. Section 4.2 describes sample preparation and the various characterisation techniques used in this chapter. Section 4.3 explores the correlation between local and global TC, ingot height and different fabrication processes, followed by a detailed investigation of the low temperature sensitivity at defective regions.

---

<sup>†</sup> This chapter is based on:

**S. Nie**, R. Lee Chin, A. M. Soufiani, T. Mehl, F. Theska, N. Haghdadi, S. Primig, C. Chan, T. Trupke, and Z. Hameiri, "Temperature sensitivity maps of silicon wafers from photoluminescence imaging: The effect of gettering and hydrogenation," *Prog. Photovoltaics Res. Appl.*, under review, 2021.

**S. Nie**, R. Lee Chin, A. M. Soufiani, C. Chan, T. Trupke, and Z. Hameiri, "Temperature-dependent performance of silicon wafers: the impact of gettering and hydrogen passivation," in *11<sup>th</sup> International Conference on Crystalline Silicon Photovoltaics*, 2021.

## 4.1 Gettering and Hydrogenation

The efficiency of Si solar cells is affected by defects introduced during crystal growth and in the fabrication processes [17]. Especially for advanced, high-efficiency cells, their efficiency is more sensitive to impurities. Gettering and hydrogenation that occurs during solar cell fabrication play key roles in the performance enhancement of Si solar cells [156, 157]. In this section, a brief review of getting and hydrogenation is provided.

### 4.1.1 Gettering

Gettering involves removing or relocating impurities to regions in the device that are less detrimental to the overall performance [157-159]. It is often integrated into the existing fabrication processes, such as dielectric deposition [160], formation of the  $p$ - $n$  junction [161], metal contacts [162], and passivating contacts [163]. Often, gettering is described as a three-step process: release, diffusion, and capture [159]. The first step is to release the impurities from the precipitates and dissolve them into mobile states [157]. This step is particularly important for cast-grown Si materials, such as cast-mono Si and mc-Si, as the majority of the metal contaminants are present in the form of precipitates [141, 164-166]. When the metal-containing precipitates are heated and their solubility limits are raised above the concentrations of the dissolved impurities, the metal precipitates dissolve. In the second step, the dissolved impurities diffuse towards the gettering region (or gettering sites) [157]. This step relies on the diffusivity of the impurities. For instance, under the common gettering conditions, interstitial metal impurities such as copper (Cu), nickel (Ni), iron (Fe), chromium (Cr), and cobalt (Co) have high to moderate diffusivity [167], whereas substitutional impurities including arsenic (As), antimony (Sb), tin (Sn), and zinc (Zn) have low diffusivity [167, 168]. Often, higher temperatures are used to improve the diffusivity of impurities. In the third step, the impurities are captured and become immobilised [157]. Depending on where the impurities are captured, this process can be categorised into internal and external gettering. In the former case, defective regions such as dislocations and grain boundaries act as efficient gettering sites [169, 170], whereas in the latter case, a heavily doped layer, an aluminium (Al) layer, or a dielectric film acts as the gettering sink [157]. Different from the first two steps, low temperatures are preferred in the third step to improve the capture efficacy. In response to the trade-off of optimal temperature between three steps, variable temperature gettering strategies have been developed and shown to enhance the gettering effects [171-173].

The commonly used gettering technique is phosphorus diffusion gettering (PDG). It is often used in Si solar cell fabrication to create electron collectors [169]. This process induces both external gettering of impurities to the heavily doped surface layer and internal gettering to the crystallographic defects. The effects of PDG on the electrical properties of Si have been studied in the past [142-144, 159, 168, 173-179]. An improved overall lifetime after PDG was reported in References [144, 168, 174-176]. In particular, spatially resolved results indicate that a significant lifetime enhancement is exhibited at the regions with a high initial lifetime and low density of crystallographic defects [142-144, 177]. However, for regions containing large fractions of crystallographic defects, such as grain boundaries and dislocations, lifetime often does not improve and even drops upon PDG [142-144, 177]. This worsening of the lifetime is mostly related to the redistribution of impurities as well as impurities trapped and precipitated at crystallographic defects during PDG [143, 176, 180]. Additionally, the fast cooling after phosphorus diffusion potentially freezes the small precipitates, whose recombination activity is typically stronger than large precipitates formed during ingot cooling [143]. In general, it can be concluded that the effects of gettering rely on the changes in concentration and distribution of the recombination centres, involving dissolved and precipitated metal impurities, dislocations, and grain boundaries.

#### **4.1.2 Hydrogenation**

Hydrogen passivation utilises atomic hydrogen to passivate defects, in contrast to the gettering process which removes or relocates impurities. Normally, hydrogen passivation is incorporated into Si solar cell processing via a thermal diffusion of hydrogen from hydrogen-rich dielectric layers to the bulk during the metallisation firing process [156, 181-183]. The impacts of different firing conditions and various hydrogen-containing dielectric layers on hydrogen passivation efficacy have been discussed in Reference [182]. The optimum thermal condition for hydrogen passivation relates to the diffusivity of hydrogen and the mass density of the dielectric layers [181, 184, 185] which controls the balance between in- and out-diffusion of hydrogen during firing [182].

For effective hydrogen passivation of defects, the charge states of interstitial hydrogen have been identified as critical factors. In Si, atomic hydrogen can exist in three charge states — negative ( $H^-$ ), neutral ( $H^0$ ), and positive ( $H^+$ ) — which have different diffusivity and bonding mechanisms [186-188]. Among the three charge states,  $H^0$  has been

identified as a more effective charge state for passivating certain defects in Si, as it has high reactivity and can diffuse freely without being affected by charge effects and electric fields in Si [189, 190]. However,  $H^0$  is always present in a much lower concentration compared to  $H^-$  and  $H^+$  [191]. The dominant charge state of hydrogen is  $H^+$  for *p*-type Si samples and  $H^-$  (at low temperatures) for *n*-type Si samples [192, 193].

The impacts of hydrogenation on the electrical properties of Si have been investigated considerably, however, some conflicting results have been reported. With respect to its beneficial effect, several studies showed that hydrogenation can reduce the recombination strength of some defects, such as metallic impurities, precipitates, and crystallographic defects [142, 144, 182, 183, 194-198]. Particularly for mc-Si, notable hydrogen passivation has been observed in the intra-grain regions and at the grain boundaries whose recombination activity are newly activated by gettering [142, 143, 182]. It has been estimated that hydrogenation can reduce the efficiency loss due to recombination at crystallographic defects from  $> 1.5\%_{\text{abs}}$  to  $< 0.5\%_{\text{abs}}$  for industrial mc-Si PERC [199]. On the other hand, the effectiveness of hydrogen passivation of defects in Si has been questioned [200]. For example, it has been reported that significant concentrations of Fe can be passivated by hydrogen [196-198], however, this result was not supported by others [201, 202], where Fe has been found to be gettered by the dielectric layers during this thermal process [201]. In addition, hydrogenation has been found to be ineffective for passivating some dislocations and grain-boundaries [143, 156, 182, 203, 204]. The ineffectiveness could be due to different reasons, such as non-optimal processing conditions, the insufficient concentration of atomic hydrogen transported from the dielectric layers into the bulk, the thermal dissociation of hydrogen-defect complexes, or the atomic hydrogen preferentially occupying low-mobility and low-reactivity charge states [143, 156, 182].

Recent studies have demonstrated that illumination or electrical minority carrier injection at elevated temperatures, known as an advanced hydrogenation process (AHP), can improve the effectiveness of hydrogen passivation by manipulating the charge state of atomic hydrogen [156, 205, 206]. It has been shown that some “stubborn” defects, such as boron-oxygen (BO) complexes, can be deactivated by an AHP [156, 207], thus leading to  $\sim 1\%_{\text{abs}}$  improvement in cell efficiency [208]. In addition, an AHP at moderate temperature has been reported to benefit the dislocated regions in cast-mono Si, with efficiency enhancements of up to  $2\%_{\text{abs}}$  [209, 210].

Although the impacts of gettering and hydrogenation on the electrical performance of Si wafers and cells have been investigated in the past, there is no study focusing on their impacts on the temperature-dependent performance of Si. This leads to the aim of this chapter, which is to investigate in detail the influence of gettering, firing, and AHP on the  $TC(iV_{OC})$  of cast-mono Si wafers.

## 4.2 Method

### 4.2.1 Sample Preparation

In this chapter, *p*-type B-doped cast-mono Si wafers from different ingot heights were used ( $1.4 \pm 0.15 \text{ } \Omega\text{-cm}$  resistivity,  $180 \pm 10 \text{ } \mu\text{m}$  thick). The wafers were saw damage etched before separate processing in the following groups:

- (i) Un-gettered: The wafers were passivated with 75 nm of  $\text{SiN}_x$  using an industrial plasma-enhanced chemical vapour deposition system (*MAiA* from *Meyer Burger*) at a deposition temperature of 673 K.
- (ii) Gettered: Sister wafers were gettered by a phosphorus diffusion at a peak temperature of 1123 K using a *Tempress* tube furnace, resulting in sheet resistance of  $\sim 40 \text{ } \Omega/\text{sq}$ . The diffused layers were then removed, and the wafers were passivated using identical  $\text{SiN}_x$  layers as used for the un-gettered Group (i) samples.
- (iii) Fired: The gettered (and passivated) wafers were fired in ambient air at a peak temperature of 1128 K using a *Schmid* commercial belt furnace.
- (iv) AHP: Tokens from each of the fired wafers were hydrogenated on a temperature-controlled stage at 573 K for 780 sec using 980 nm laser illumination of  $\sim 56 \text{ kW}\cdot\text{m}^{-2}$ .

### 4.2.2 Characterisation Methods

**PL Imaging:** After each process step, the wafers were characterised using the custom-built temperature-dependent PL imaging system [78, 85] described in Chapter 3. The PL images were acquired at an illumination intensity of 0.5 Suns and varying temperatures in the range of 298–353 K (for un-gettered and gettered wafers) and 298–323 K (for fired and hydrogenated wafers). The temperature range was reduced for the fired and hydrogenated wafers to avoid temperature-induced degradation. After the elevated

temperature measurements, the samples were remeasured at 298 K to ensure that no changes were induced during the PL measurements.

Charge-carrier trapping effects were observed in PC measurements carried out on these wafers. Therefore, the PL images were calibrated into  $iV_{OC}$  images using the QSS PL front detection method [78, 118] described in Chapter 3. The local  $TC(iV_{OC})$  is obtained from the slope of a linear fit of  $iV_{OC}$  as a function of temperature for each pixel. As previously stated,  $TC(iV_{OC})$  is negative and a  $TC(iV_{OC})$  reduction refers to a lower temperature sensitivity i.e., less negative  $TC(iV_{OC})$ , in this thesis.

**Hyperspectral PL imaging:** In this chapter, a hyperspectral PL imaging system [211] was used to resolve the local spectral PL imaging of un-gettered wafers from the top of the ingot, which enables both the BB and defect (i.e., dislocation) related PL emission to be probed. The system uses an 808 nm line laser as the excitation source, with a maximum intensity equivalent to  $\sim 20$  Suns. The spectral PL emission in the wavelength range of 900–2500 nm is detected by a near-infrared (NIR) push-broom hyperspectral camera, with a mercury cadmium telluride detector and a spectral resolution of 6.3 nm (256 bands). Hyperspectral PL measurements were taken within the temperature range of 88–343 K, with a pixel size of  $165 \times 165 \mu\text{m}^2$ .

**Atom Probe Tomography (APT):** Atom probe specimens were fabricated from un-gettered wafers from the top of the ingot at selected sites. Electron backscatter diffraction (EBSD) mapping was carried out using an *EDAX Hikari Super* system with a *JEOL 7001f* scanning electron microscope (SEM).  $\text{Xe}^+$  plasma focused ion beam (PFIB) milling was then used to fabricate atom probe specimens from a low angle boundary with  $\sim 3^\circ$  misorientation using a *ThermoFisher Helios G4* PFIB system. These specimens were then run in a *Cameca LEAP 4000X Si* atom probe with a wide field of view in a laser-assisted evaporation mode with the following acquisition conditions: temperature of 50 K, laser energy of 25 pJ, pulse frequency of 200 kHz, and detection rate of 1.0%. Note that the detector efficiency of this instrument is  $\sim 57\%$ . The reconstructions were done using the *Cameca AP Suite 6.1*, based on the tip shape as captured by the SEM images. A sequence of EBSD, SEM, and PFIB images that show the workflow of the sample preparation for the atom probe measurements are given in Figure 4.1 while the range of the mass spectrum used for identified peaks is provided in Figure 4.14.

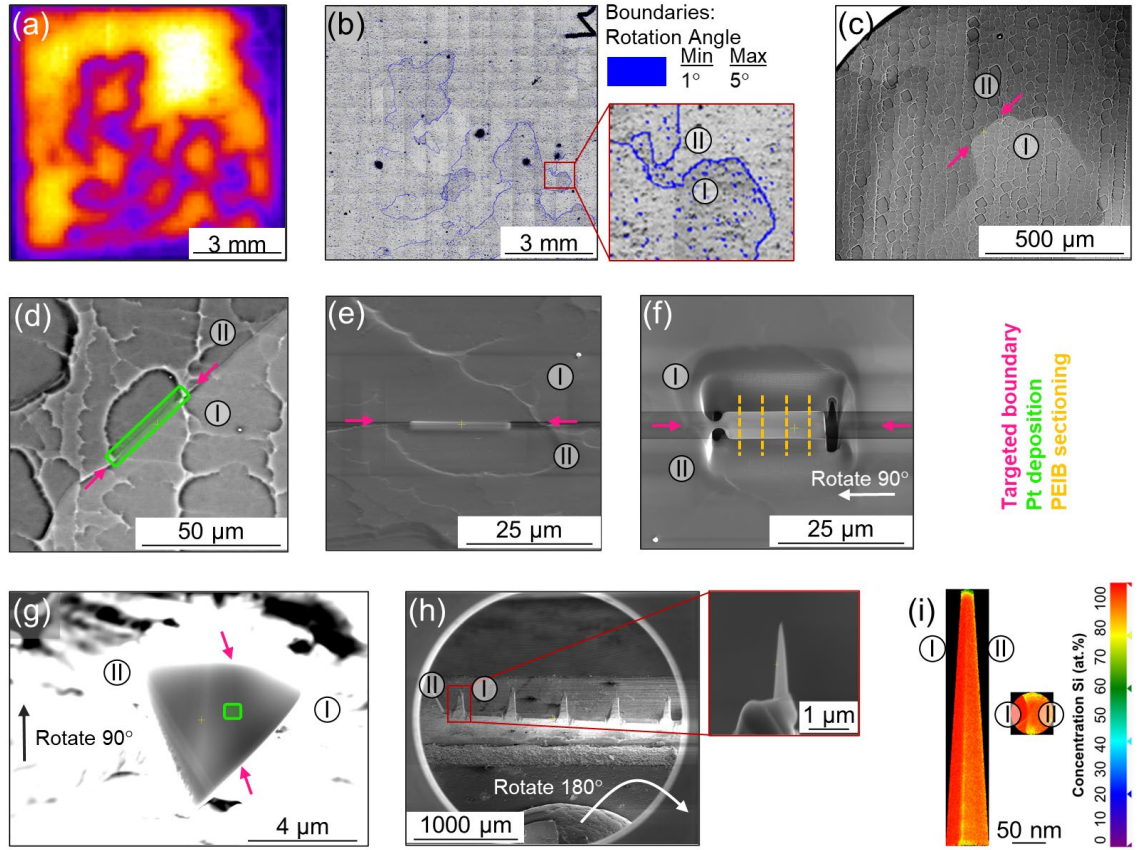


Figure 4.1 (a) PL<sub>BB</sub> image and (b) the corresponding EBSD map for a region-of-interest of a cast-mono wafer from the top of the ingot. Acquisition conditions of the EBSD measurements were an acceleration voltage of 20 kV, probe current of ‘13’, working distance of 15 mm,  $8 \times 8$  binning, 0.65 sec exposure, and 1.6 gain. The Combo scan option was used to generate  $\sim 8 \times 8 \text{ mm}^2$  large maps with a step size of 5  $\mu\text{m}$ . Note that the black marks in the EBSD map are measurement-related artefacts. A sequence of SEM and PFIB images (c)–(h) show the workflow of the sample preparation for the atom probe measurements: (c) selecting targeted boundary and (d) area for platinum (Pt) deposition, (e) after Pt deposition, (f)–(g) in-situ lift-out and annular milling, and (h) final prepared atom probe specimens. In-situ lift-out and annular milling employed acceleration voltages between 5–30 kV with currents of 0.01–4.0 nA. A final clean-up was carried out using 5 kV and 0.03 nA for 30 sec after imaging atom probe specimens. A representative APT density plot is given in (i).

## 4.3 Results and Discussion

### 4.3.1 Spatially Resolved Analysis

Figure 4.2 shows images of  $iV_{OC}$  at 298 K,  $TC(iV_{OC})$ , and  $\gamma$  of cast-mono wafers from the top of the ingot before and after gettering, after firing, and after AHP. The dark line-shaped patterns in the  $iV_{OC}$  images, Figure 4.2(a)–(d), are caused by crystallographic defects. EBSD measurements [see Figure 4.1(a)–(b)] confirmed that those features are low angle grain boundaries, which are normally formed due to the movement and aggregation of a high density of dislocations [212, 213]. The residual stress and strain

around these dislocations can naturally capture other defects and impurities, and thus, make these regions highly recombination active [214]. In the ingot casting thermal process, dislocations are generated at the seed joints [213, 215]. They then multiply rapidly along the growth direction. Therefore, substantially higher densities of crystallographic defects are observed in the wafers from the top of the ingot [212, 213].

As shown in Figure 4.2(a)–(d), crystallographic defects are highly recombination active before the gettering process. Gettering further increases the recombination strength of the crystallographic defects due to internal gettering. Similar observations were made in earlier studies on mc-Si wafers [77, 142]. No significant change is observed in the defect-free regions (referring to the regions that do not contain recombination active crystallographic defects in this chapter) after the gettering. In contrast, Reference [142] has reported that the intra-grain regions in mc-Si wafers from the top of the ingot improve after gettering. This disagreement could be in part owing to different dominant defects and the redistribution of impurities after gettering as evidenced by the change in the temperature-dependence of  $iV_{OC}$  between Figure 4.2(e) and (f). Hydrogen passivation occurring during the firing process due to hydrogen release from the dielectric layers and its subsequent diffusion into the bulk significantly reduces the recombination in the defect-free regions (with an average improvement of  $\sim 25$  mV in  $iV_{OC}$  for the cast-mono wafers investigated here). However, the crystallographic defects remain recombination active. This observation agrees with the conclusions of Bertoni *et al.* [203] indicating that the hydrogen passivation efficacy is lower in regions with high dislocation density. The low passivation efficiency can be explained by  $H^+$  with low mobility and reactivity that dominates the distributed hydrogen state within the wafers [156]. An additional AHP can increase the fractional concentration of hydrogen atoms with the desired charge states, especially  $H^0$ , allowing improved hydrogen passivation [205, 209]. As a result, the entire wafer shows improved  $iV_{OC}$  after AHP, with a greater relative improvement in regions with crystallographic defects. Hence, it can be concluded that the recombination activity of the crystallographic defects tends to increase after gettering and to reduce after AHP. However, even after AHP, these defects are still recombination active.

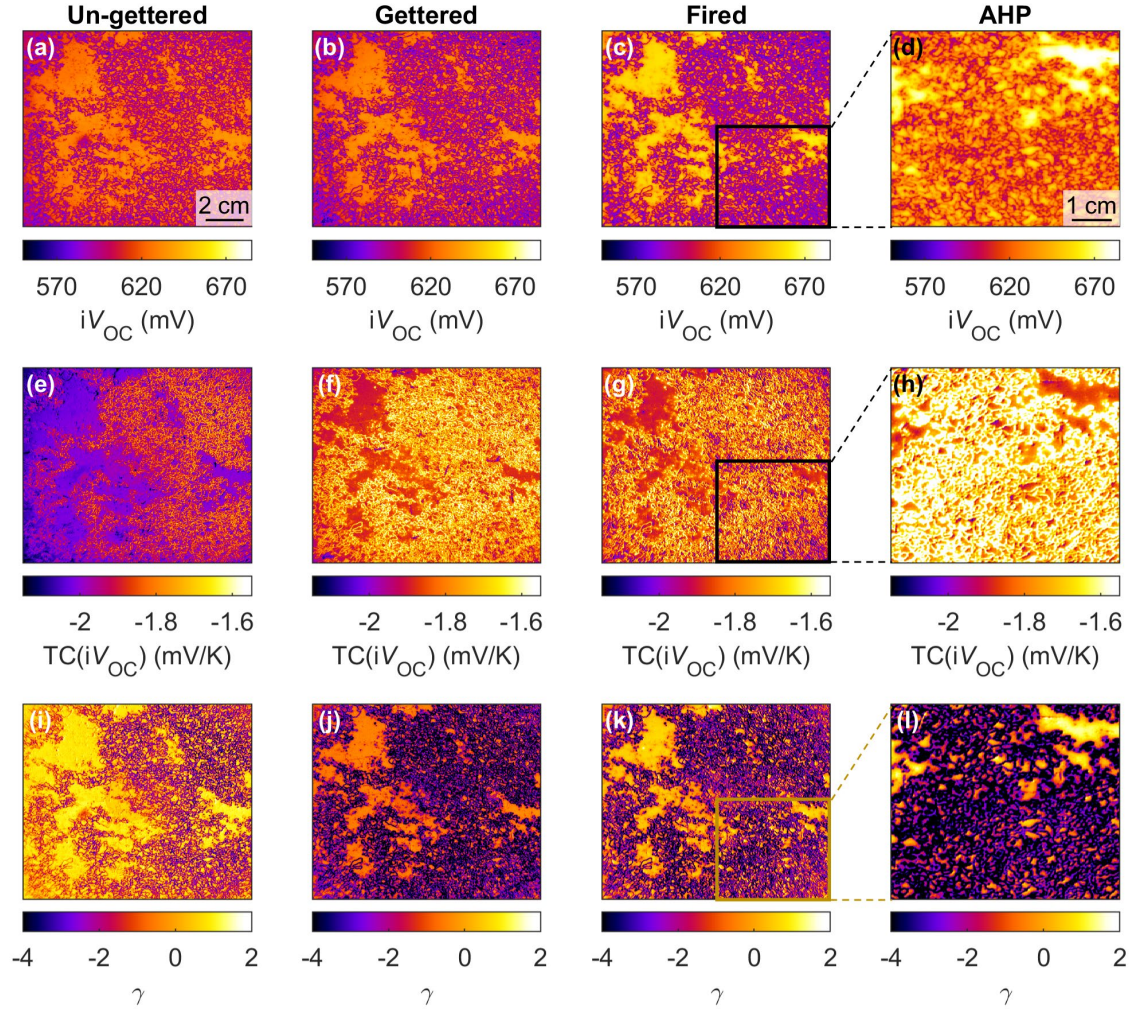


Figure 4.2 (a)–(d)  $iV_{OC}$  at 298 K, (e)–(h)  $TC(iV_{OC})$ , and (i)–(l)  $\gamma$  maps before gettering, after gettering, after firing, and after AHP for wafers from the top of the ingot.

$TC(iV_{OC})$  is determined by several components, and its material-dependent variability is acquired by the  $iV_{OC}$  at 298 K (varying according to the recombination rate) and the temperature-dependence of recombination activity which is related to  $\gamma$ . Equation 3.1 indicates that a high  $iV_{OC}$  and a small  $\gamma$  will contribute to reducing  $TC(iV_{OC})$ , and vice versa. Figure 4.2(e)–(h) presents the experimentally determined  $TC(iV_{OC})$  after each process.  $TC(iV_{OC})$  varies significantly between regions of different quality (defects). Before gettering, regions with less negative  $TC(iV_{OC})$  are correlated to areas with a high concentration of crystallographic defects. Hence, in regions that are dominated by crystallographic defects,  $iV_{OC}$  reduction rate at elevated temperatures is slower compared to the high-quality defect-free regions. The gettering process reduces the temperature sensitivity of both the defect-free regions and most of the regions containing crystallographic defects. In contrast, previous studies have indicated that gettering does

not affect the temperature sensitivity of the intragrain regions in mc-Si wafers substantially, despite the increase in material quality [77]. This discrepancy can be explained by the different temperature-dependencies of the dominant recombination as indicated by the lower  $\gamma$  in the defect-free regions of the cast-mono wafers obtained after gettering. Interestingly, the firing process does not have a prominent impact on the thermal behaviour and only a slight variation in  $TC(iV_{OC})$  can be observed. This contrasts with the expected improvement in  $TC(iV_{OC})$  in the defect-free regions, due to the improvement of  $iV_{OC}$  in those regions after the firing process. This could be explained by increasing  $\gamma$  values due to the alteration of the temperature-dependent recombination rate. Interestingly, an AHP significantly reduces the temperature sensitivity across the entire wafer.

Contrary to our expectation that low-quality areas should feature high temperature sensitivity, most regions containing crystallographic defects have low temperature sensitivity following the processing steps. Therefore, the performance difference between the defective regions and the defect-free areas would reduce at higher operating temperatures. Nevertheless, these defective regions still limit the device performance at elevated temperatures, although it is not as severe as previously expected.

Figure 4.2(i)–(l) illustrates  $\gamma$  maps after different processes. Reference [15] earlier suggested that  $\gamma = 3$  for materials that are limited by SRH recombination in the bulk and at the surfaces. This computation is based on the assumptions that the bulk and surface lifetimes are independent of temperature. Hence,  $\gamma < 3$  implies an improved carrier lifetime with increasing temperature for SRH recombination-limited materials. The maps demonstrate  $\gamma$  values below 3 for the entire wafers. This can be explained by the presence of temperature dependencies of the SRH recombination. The gettering process reduces  $\gamma$ , and therefore a faster improvement rate of the carrier lifetime at elevated temperature is expected and thus, lower  $TC(iV_{OC})$ . However, this superior behaviour is weakened by the subsequent firing process. Interestingly, reduced  $\gamma$  values are found after an AHP, particularly for the regions containing crystallographic defects. This indicates that an AHP not only improves  $iV_{OC}$  but also contributes to lower  $TC(iV_{OC})$ . In comparison to the defect-free regions, it is noticeable that most of the crystallographic defects show negative  $\gamma$ , possibly due to the temperature dependence of the recombination caused by the impurities decorating the crystallographic defects. This will be further discussed in Section 4.3.4.

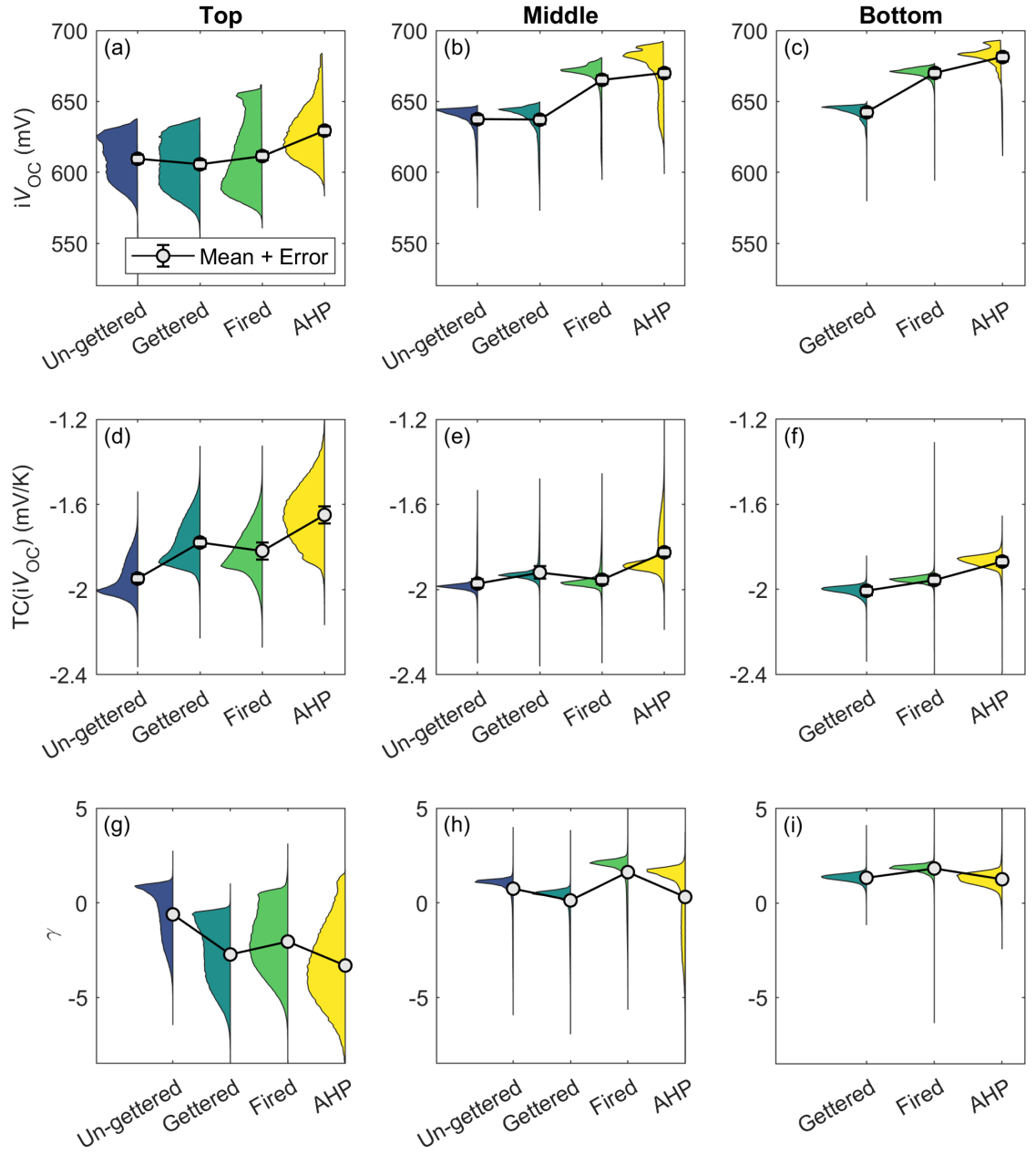


Figure 4.3  $iV_{OC}$  at 298 K (top row),  $TC(iV_{OC})$  (middle row), and  $\gamma$  (bottom row) histograms and their global values (given as symbols) for the wafers from the top, middle, and bottom of the ingot after the various processes.

#### 4.3.2 Variation Along Ingot Position

Figure 4.3(a)–(c) presents the  $iV_{OC}$  distributions and their global values for representative wafers from the top, middle, and bottom of the ingot after the various processes. The light grey dot represents the global value, while the coloured regions to the left of the dot present the distribution. Wafers from different ingot positions respond differently to the processes. Broad distributions are observed for the top wafers due to large variations in the  $iV_{OC}$  of crystallographic defects compared to the defect-free regions. Since wafers

from the bottom to the middle part of the ingot often have a considerably lower crystallographic defect concentration (see Figure 4.4), their  $iV_{OC}$  distributions are much narrower.

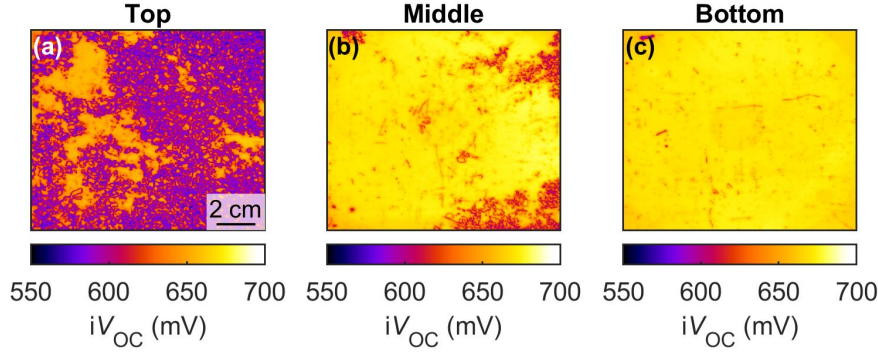


Figure 4.4  $iV_{OC}$  maps at 298 K for the wafers from the (a) top, (b) middle, and (c) bottom of the ingot after firing.

The bottom part of the ingot contains high concentrations of impurities due to their diffusion from the crucible walls during the casting process [213]. Consequently, the un-gettered bottom wafers show an inferior performance with global  $iV_{OC}$  below 540 mV and therefore the associated data are not presented in Figure 4.3(c). After gettering,  $iV_{OC}$  of the bottom wafers significantly increases, while only a negligible effect is noticed for wafers from the middle and top parts of the ingot. The firing process has previously been reported to improve the defect-free regions [144], so the observed increase of  $iV_{OC}$  for wafers from the bottom and middle positions of the ingot is not surprising. For wafers at the top of the ingot, the high  $iV_{OC}$  bins which represent defect-free regions shift to higher values, thus, resulting in a wider  $iV_{OC}$  distribution; since large parts of these wafers are affected by crystallographic defects that remain highly recombination active after the firing process, their global  $iV_{OC}$  values remain almost unchanged. It should be noted that a recent study by Sio *et al.* [144] reported a reduction in the recombination activity of crystallographic defects in cast-mono Si wafers after firing. The apparent discrepancy with the results reported here could be explained by the different hydrogen content of the dielectric layers used, and the different firing conditions [182]. The AHP results in effective passivation of the entire wafer and a substantial improvement in the  $iV_{OC}$ , regardless of ingot height. Note that the AHP is performed on quarters of the 6-inch wafers. As some of these quarters contain a larger proportion of crystallographic defects in comparison to the full wafers, the improvement after the AHP may be underestimated. The superior performance of the middle and bottom wafers after all the processes is

expected, due to the extremely low density of crystallographic defects in these wafers [213].

Figure 4.3(d)–(i) presents  $TC(iV_{OC})$  and  $\gamma$  distributions and their average values of wafers from different ingot heights after the various processing steps. Although  $iV_{OC}$  does not significantly change after the gettering process, the  $TC(iV_{OC})$  is actually less negative. This is likely caused by a change in the temperature dependence of recombination after gettering, possibly due to the redistribution of impurities as indicated by a reduction of  $\gamma$ , as shown in Figure 4.3(g)–(i). Interestingly, although the firing process enhances the  $iV_{OC}$  of all the wafers, except for the defective regions of the top wafer, it causes a weak shift of  $TC(iV_{OC})$  towards more negative values for wafers from the top and middle of the ingot, whereas the  $TC(iV_{OC})$  of wafers from the bottom of the ingot is slightly reduced (less negative). As previously discussed, a high  $iV_{OC}$  and a low  $\gamma$  value are contributing factors for a less negative  $TC(iV_{OC})$ . As  $\gamma$  is increased after the firing process for all wafers [see Figure 4.3(g)–(i)], the reduction of  $TC(iV_{OC})$  of the bottom wafers is mainly due to their  $iV_{OC}$  improvement after firing. Remarkably, the AHP not only compensates for the negative impact of the firing process but further attenuates the temperature sensitivity of all investigated wafers by reducing  $\gamma$ . It is interesting that this reduced sensitivity is larger than would be expected from just the improved  $iV_{OC}$ . This could be due to an interaction with hydrogen, resulting in changing dominant defects or defect configurations that have a lifetime with more favourable temperature sensitivity.

To differentiate the respective contributions of increased  $iV_{OC}$  and decreased  $\gamma$  to the  $TC(iV_{OC})$  of wafers after an AHP, the relative difference,  $\Delta TC(iV_{OC})$ , between the measured  $TC(iV_{OC})$  and the expected  $TC(iV_{OC})$  is analysed. The expected  $TC(iV_{OC})$  is calculated using Equation 3.1 and the  $\gamma$  maps obtained after the firing process, assuming  $TC(iV_{OC})$  variations after an AHP are solely due to  $iV_{OC}$  improvement. As shown in Figure 4.5(a)–(c), most regions of wafers from different ingot positions show negative  $\Delta TC(iV_{OC})$  values, indicating that the measured  $TC(iV_{OC})$  is lower than the expected values. On average, the reduction of  $\gamma$  by an AHP contributes around 7% to the  $TC(iV_{OC})$  reduction, with stronger impacts in the regions containing crystallographic defects. This process has an intriguing positive impact on the temperature sensitivity of the Si wafers, besides the known material quality improvement that can be achieved by an AHP.

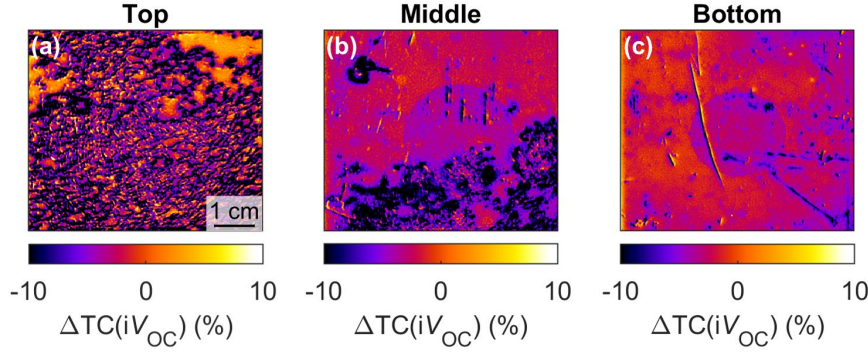


Figure 4.5 Percentage difference in TC,  $\Delta TC(iV_{OC})$ , between measured and expected temperature sensitivity for wafers from the (a) top, (b) middle, and (c) bottom of the ingot after an AHP. Negative values indicate lower temperature sensitivity than expected. Note that the circular pattern in the images is an artefact caused by the PC coil of the Sinton WCT-120TS temperature-controlled stage used for PL imaging. A 1000 nm short-pass filter was used for PL imaging to reduce the effect of stage reflection. Areas with uniform temperature and reflection are used for analysis.

#### 4.3.3 Temperature-Dependent Performance at the Cell Level

As presented in Chapter 3, the dislocation clusters in mc-Si wafers show less negative  $TC(iV_{OC})$ , resulting in lower temperature sensitivity of the wafers and cells from the top part of the ingot in comparison to bottom wafers and cells. Similar observations are made on cast-mono Si samples in this chapter. Then, the question arises whether the performance of low-quality Si solar cells can be comparable with or even better than the performance of cells with high material quality at higher operating temperatures. In this section, the performance of two representative cast-mono cells originating from the bottom and top of the ingot are compared.

Figure 4.6 displays the  $iV_{OC}$  and  $TC(iV_{OC})$  images of quarters of the 6-inch industrial PERC devices made using sister wafers of samples in Figure 4.4. Since the bottom cast-mono samples are free from crystallographic defects, this allows a more direct comparison than mc-Si samples as the bottom mc-Si samples are limited by a large density of grain boundaries. Similar to the wafers, bottom cast-mono cells show a higher  $iV_{OC}$  but more negative  $TC(iV_{OC})$  than the top cells. Figure 4.7 summarises the global  $iV_{OC}$  and efficiency of these two cells at different temperatures measured using a *Wavelabs I-V* tester. Note that symbols represent the measurements and lines represent linear interpolation to higher temperatures. Although the top cell has a lower TC, its  $iV_{OC}$  at temperatures up to 353 K is still lower than the bottom cell. Surprisingly, the overall efficiency of the top cells exceeds the efficiency of the bottom cells at temperatures above 345 K, due to the combination of more favourable TCs of  $I_{SC}$ ,  $V_{OC}$  and  $FF$ .

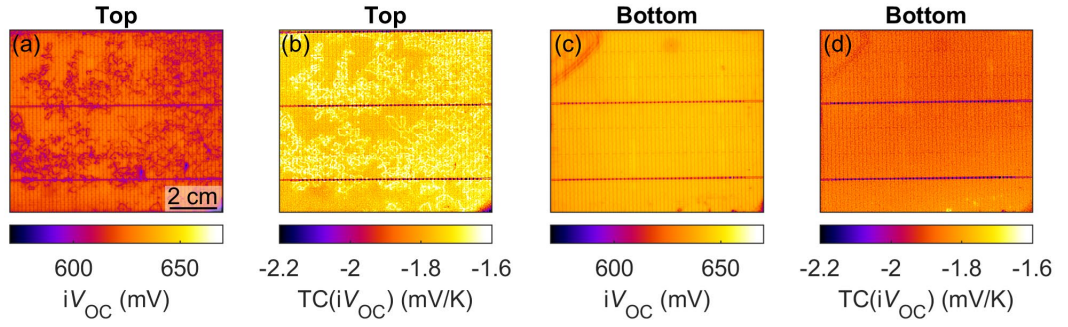


Figure 4.6  $iV_{OC}$  at 298 K and  $TC(iV_{OC})$  images of quarters of 6-inch PERC devices originating from the (a)–(b) top and (c)–(d) bottom of the cast-mono Si ingot. These measurements were obtained under 0.5 Suns illumination.

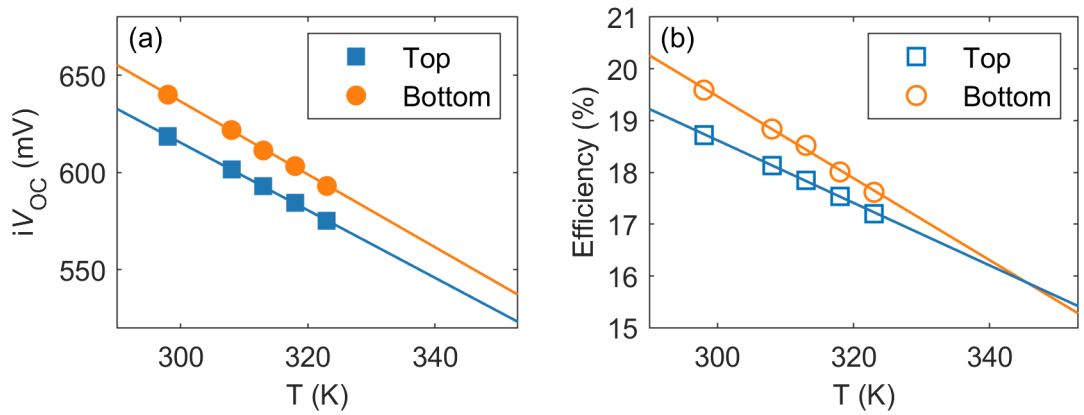


Figure 4.7 (a) Global  $iV_{OC}$  and (b) cell efficiency under 0.5 Suns illumination as a function of temperature for PERCs originating from top and bottom of the cast-mono Si ingot.

#### 4.3.4 Temperature Sensitivity of Crystallographic Defects

Temperature-dependent hyperspectral PL measurements were carried out on wafers from the top part of the ingot to investigate the temperature sensitivity of the crystallographic defects. In contrast to the temperature-dependent PL imaging system described in Chapter 3, which only acquires spectrally integrated-BB luminescence emission, a four-dimensional dataset is collected with the hyperspectral PL imaging system. The full spectrum (in the range of 0.6–1.3 eV) is obtained at each pixel in the temperature range of 88–343 K.

Figure 4.8 shows the accumulated PL spectrum over the entire sample at different temperatures. Four distinct sub-bandgap peaks at 0.81, 0.88, 0.93, and 1.00 eV are easily identified at low temperatures. As mentioned in Chapter 3, these peaks are usually correlated with the well-known D lines, defect emissions that are associated with dislocations in crystalline Si [146, 147]. The luminescence intensity of these spectral

peaks is often added in pairs (D1 together with D2, and D3 with D4) [148, 149]. D1 and D2 are commonly associated with defects and impurities decorating the dislocations and the sub-grain boundaries, whereas D3 and D4 have been correlated with the intrinsic properties of the dislocation cores and sub-grain boundaries [146, 148-150].

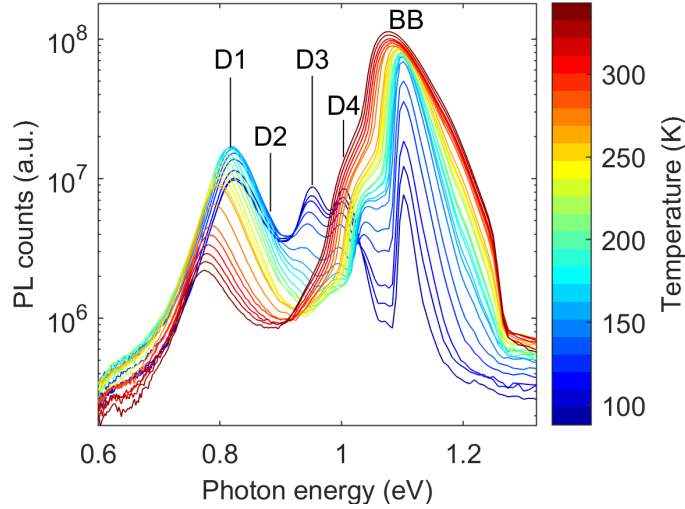


Figure 4.8 Accumulated PL spectra of a representative wafer from the top of the ingot at different temperatures, where BB emission and defect-related luminescence (D1–D4) are labelled.

To resolve the different emission signals that contribute to the defect luminescence, a multivariate curve resolution analysis [216, 217] was carried out. The spatial distributions of D1+D2 and D3+D4 luminescence ( $PL_{D1+D2}$  and  $PL_{D3+D4}$ ) at 88 K are presented in Figure 4.9, together with the  $PL_{BB}$  distribution at 88 K and 303 K. Despite the relatively strong D3 and D4 emission at 88 K, only the D1 and D2 (weak) peaks are detected at temperatures above 150 K (see Figure 4.8). For  $PL_{D3+D4}$ , an inverse correlation with  $PL_{BB}$  is observed only at temperatures below 100 K, no correlation can be identified at higher temperatures. In contrast, a clear inverse correlation is observed between  $PL_{D1+D2}$  and  $PL_{BB}$  measured at higher temperatures as demonstrated by the correlation plots at 303 K and 343 K in Figure 4.10. This suggests that the D1+D2 emission is a good indicator of the recombination activity at the crystallographic defects [148] observed and has a strong impact on the performance of the studied samples at room temperature and above. Hence, the observed low  $TC(iV_{OC})$  at the crystallographic defects is likely related to the impurities in these locations.

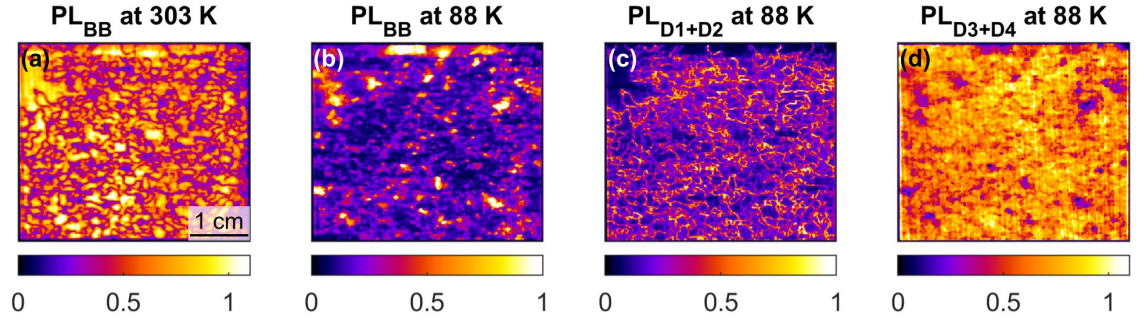


Figure 4.9 Normalised intensity map of  $PL_{BB}$  at (a) 303 K and (b) 88 K, (c) D1 + D2 at 88 K, and (d) D3 + D4 at 88 K for a representative wafer from the top part of the ingot.

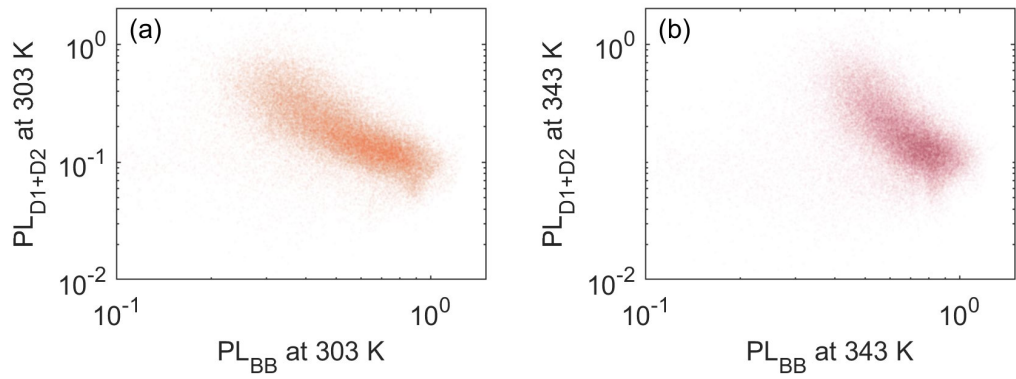


Figure 4.10 Normalised  $PL_{D1+D2}$  as a function of  $PL_{BB}$  at (a) 303 K and (b) 343 K for a representative wafer from the top of the ingot.

To further investigate this relationship, the  $E_a$  map [Figure 4.11(a)] of the D1+D2 associated defects is extracted by curve-fitting the temperature-dependence of the spectrally integrated defect PL signal at each pixel as described in Chapter 3. An example of the Arrhenius plot for extracting the  $E_a$  of a pixel containing crystallographic defects is shown in Figure 4.11(b). Note that this method is only valid at low injection levels; thus,  $E_a$  in the defect-free regions, with higher effective lifetime, may deviate from the true value.

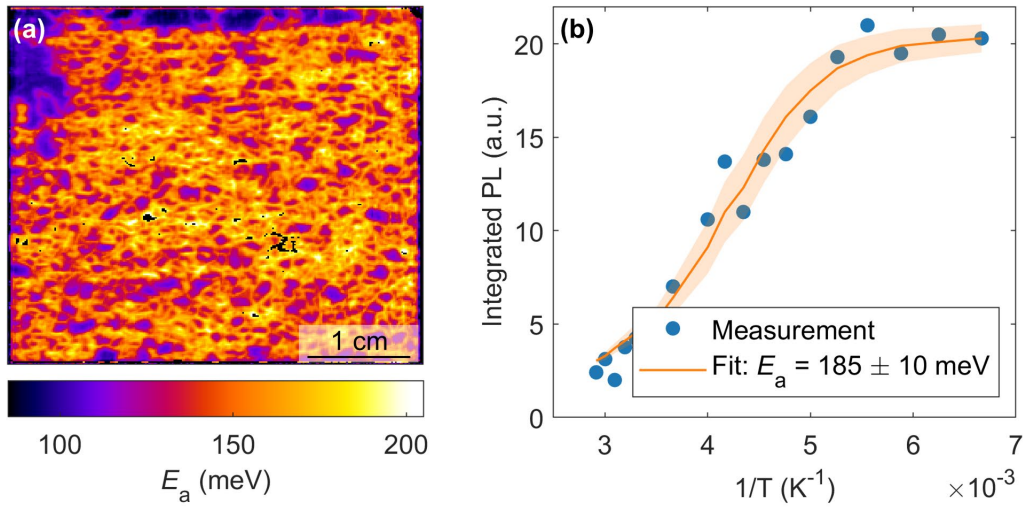


Figure 4.11 (a)  $E_a$  map of D1+D2-associated defects for a representative wafer from the top of the ingot; and (b) an Arrhenius plot for extracting the  $E_a$  of a single pixel representing crystallographic defects. Note that fits with a relative error larger than 10% were excluded in (a) and shown as black pixels.

A large value of  $E_a$  indicates a stronger reduction of the defect PL with increasing temperature, thus, the recombination decreases with rising temperatures. This can potentially compensate some of the negative impacts of  $n_i$  on  $iV_{OC}$  at elevated temperatures. Therefore,  $iV_{OC}$  reduces less at higher temperatures, resulting in low temperature sensitivity at regions containing crystallographic defects. As illustrated in Figure 4.11, regions with large  $E_a$  ( $> 120$  meV) are well correlated with the recombination-active crystallographic defects (dark lines in the  $PL_{BB}$  image). This observation agrees with results shown in Chapter 3, where an  $E_a$  of 129 meV was reported for the less temperature-sensitive dislocations in  $p$ -type mc-Si samples.

To identify the nature of impurities that decorate crystallographic defects, APT measurements were performed on selected regions containing recombination-active crystallographic defects. One representative APT reconstruction of a low angle grain boundary (indicated by a red box in the first atom map) from the top wafer is shown in Figure 4.12. Here, all elements are presented in the first map and the individual elements are displayed in the remaining maps. A significant excess of Ni, oxygen (O), and carbon (C) near the low angle grain boundary is detected, suggesting that these three impurities could play dominant roles in causing the recombination at the regions containing crystallographic defects. In addition, Fe, Cu, and Cr are also detected, but with much lower concentrations. Different concentrations of C, O, and Ni across the grain boundary indicate that segregated impurities have been accumulated along the path of motion of

such boundaries. Analogous maps for the three captured reconstructions, as well as their 1D concentration profiles across the boundaries, are provided in Figure 4.13.

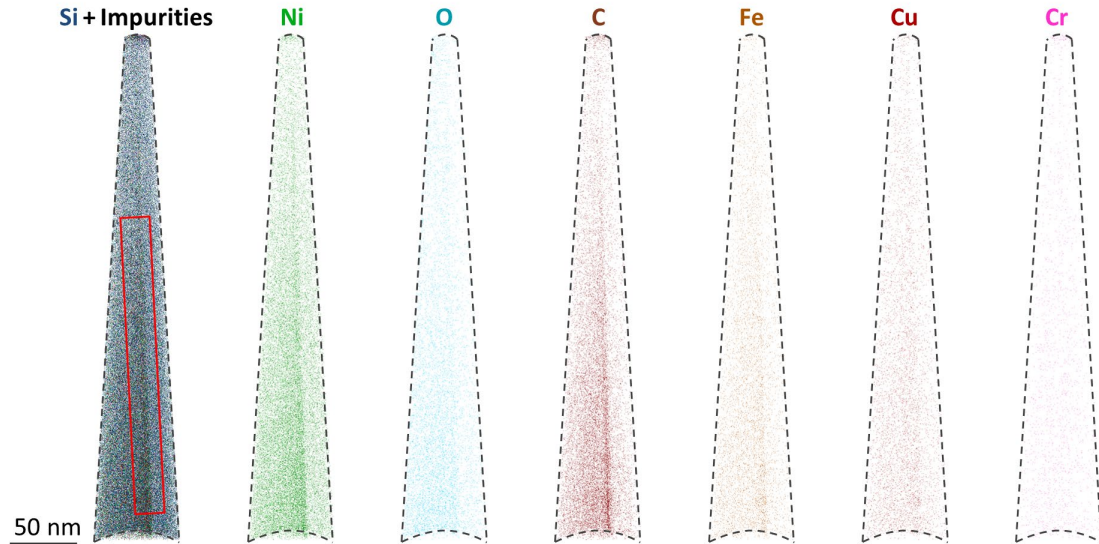


Figure 4.12 Side-view of a 3D atom probe tomographic reconstruction of a low angle grain boundary from a representative cast-mono Si wafer from the top of the ingot. The first map shows all elements and the remaining maps present individual element.

The presence of these impurities has been previously reported in cast-mono wafers [218]. Substitutional C has been shown to be another origin of the formation of low angle grain boundaries, as its concentration correlates well with the etch pit density in cast-mono wafers [215]. Moreover, Ohno *et al.* [214] found that O, Ni, and Cu atoms preferentially segregate at the grain boundaries on which arrays of dislocations exist. They, therefore, suggested that the recombination activity of the grain boundaries ( $C_{GB}$  revealed by PL imaging) can be described by the linear combination of the concentrations of O, Ni, and Cu atoms at the grain boundaries. Recently, Tweddle *et al.* [219] suggested that C and O may not be the main contributors to the recombination at grain boundaries in mc-Si wafers, whereas a direct correlation was found between the recombination rate and the concentration of nitrogen (N). However, no significant concentration of N was detected in the low angle grain boundaries investigated here. This may be due to its low concentration, below the detection limit of APT or mass-to-charge-state overlaps that obscure the presence of N. An exemplary atom probe mass spectrum is provided in Figure 4.14.

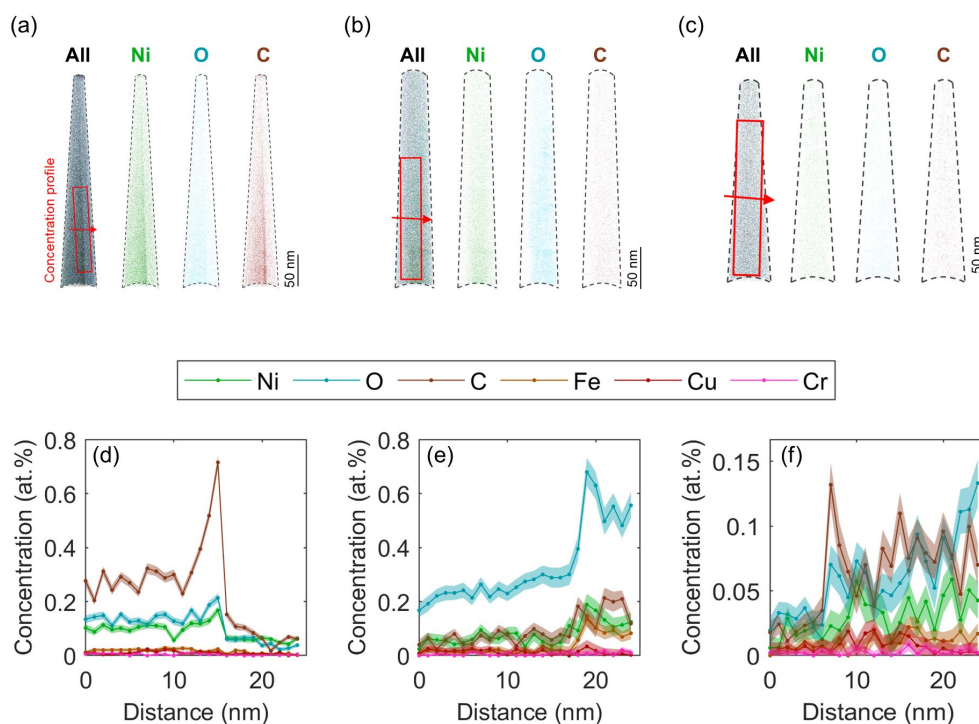


Figure 4.13 (a)–(c) Side-view of the 3D atom probe tomographic reconstructions of three captured low angle grain boundaries which are enriched by C, O, and Ni and (d)–(f) their corresponding 1D concentration profiles across the boundaries. Concentration profiles are extracted from cylindrical regions of interest in the dimensions  $150 \times 20 \times 25 \text{ nm}^3$  (highlighted by the red box while the red arrow indicates the distance from 0 nm to 25 nm), with a step size of 1 nm. All concentration profiles were decomposed into their elements and background corrected. Enrichment of C, O, and Ni are observed in the three data sets, with asymmetric levels of enrichments at left and right sides of the boundary.

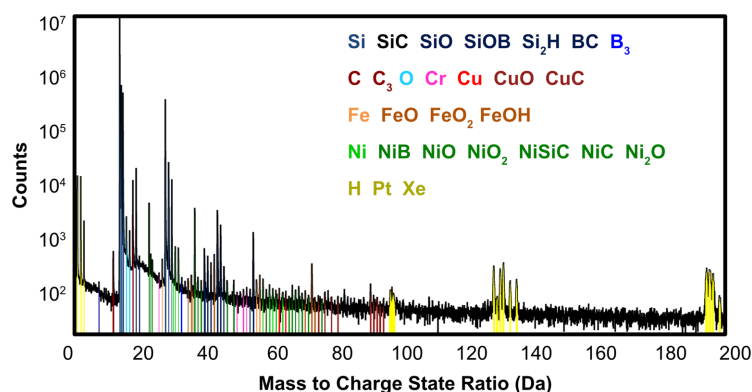


Figure 4.14 A representative atom probe mass spectrum used to identify the peaks.

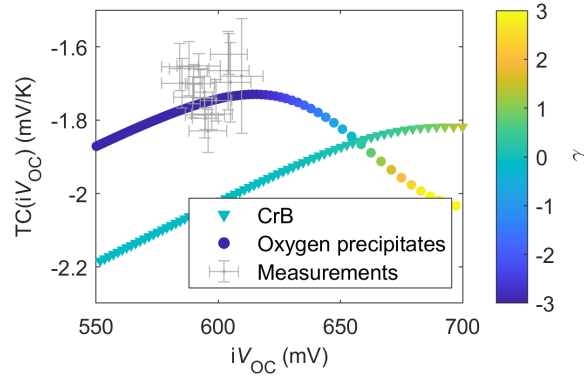


Figure 4.15 Simulated  $TC(iV_{OC})$  as a function of  $iV_{OC}$  for CrB ( $E_t = E_v + 0.27$  eV and  $\sigma_n/\sigma_p = 5.8$ ) [223] and oxygen precipitates ( $E_t = E_v + 0.22$  eV and  $\sigma_n/\sigma_p = 157$ ) [50] under 0.5 Suns illumination intensity. Note that the temperature-dependence of the capture cross-section is not considered in these simulations, as such information is not provided in the literature. The grey dots with bars represent the average measured  $TC(iV_{OC})$ - $iV_{OC}$  of randomly selected regions containing crystallographic defects and their variations within each selected region.

The temperature-dependent characteristics of the crystallographic defects are assumed to be associated with  $\gamma$ . Hence,  $\gamma$  is assumed to depend on the defect parameters, including the  $E_t$ ,  $N_t$ ,  $\sigma_n$  and  $\sigma_p$ . It has been reported that Ni [46], Cu (Cu precipitate) [220-222], Cr (CrB) [223], and O (BO and oxygen precipitates) [50, 224] show reduced recombination rates at elevated temperatures. These could contribute favourably to the  $iV_{OC}$  of crystallographic defects at elevated temperatures, leading to lower temperature sensitivity. To provide further insights, the temperature-dependent  $iV_{OC}$  at 0.5 Suns illumination intensity was simulated, based on the defect parameters available in the literature [46, 50, 220-224].  $\gamma$  was then calculated based on Equation 3.1. Figure 4.15 presents simulated  $TC(iV_{OC})$  as a function of  $iV_{OC}$  for regions dominated by CrB and oxygen precipitates, where the trace colour is mapped to  $\gamma$ . For CrB, a more negative  $TC(iV_{OC})$  is observed with decreasing  $iV_{OC}$ . This is expected due to the weak reduction of  $\gamma$ . Note that Cr is not likely to be the dominant defect, due to: (a) low concentrations were detected by APT, and (b) no significant change in lifetime was observed after applying the CrB pairs dissociation process [223]. Interestingly, oxygen precipitates show different behaviour with a stronger variation in  $\gamma$ . Above 600 mV, a declining  $\gamma$  is observed with reducing  $iV_{OC}$ , which weakens the negative impact of the low  $iV_{OC}$  on  $TC(iV_{OC})$ . Hence, in this voltage range,  $TC(iV_{OC})$  is less negative than expected towards low  $iV_{OC}$  due to lower  $\gamma$ . Although the detrimental effect of low  $iV_{OC}$  on TC prevails again at  $iV_{OC}$  below 600 mV, this increasing  $TC(iV_{OC})$  (to more negative values) considerably slows down by the negative  $\gamma$ , compared to CrB. Figure 4.15 also shows the distributions of  $TC(iV_{OC})$  as a

function of the corresponding  $iV_{OC}$  in 17 randomly selected regions that contain crystallographic defects (from Figure 4.2). The simulated  $TC(iV_{OC})$  of oxygen precipitates is within the range of the measurements. As oxygen precipitates feature especially low temperature sensitivity and their recombination activity is characterised by more negative  $\gamma$  values at low  $iV_{OC}$  ranges compared to other impurities, they are likely to be responsible for the low temperature sensitivity of the regions containing the crystallographic defects. There is little data on the temperature- and injection-dependent behaviour of C impurities, which limits the conclusions that can be made about its impact on  $TC(iV_{OC})$ .

## 4.4 Chapter Summary

This chapter highlights the importance of performing spatially-resolved analysis to assess the  $TC(iV_{OC})$  of Si wafers. This provides more detailed information about the samples' electrical properties in comparison to global single-value measurements. Results shown in this chapter imply that variations in  $TC(iV_{OC})$  in response to different processes cannot simply be explained by the intrinsic parameters of Si. It is significantly influenced by the temperature dependence of the recombination rate of the recombination active defects. Gettering is found to alter the temperature dependence of recombination, lowering  $\gamma$ , resulting in more favourable temperature sensitivity. However, this benefit is negated by the subsequent firing process. Intriguingly, performing an advanced hydrogenation process can offset the negative impact of the firing process on  $TC(iV_{OC})$  and further reduce temperature sensitivity. Although the crystallographic defects remain the most severe performance-limiting factor for cast-mono Si material for wafers from the top of the ingot, their detrimental impact is reduced at higher operating temperatures. APT results show that the regions containing crystallographic defects are enriched by Ni, O, and C. Consequently, these impurities (more feasibly oxygen precipitates) could explain the low temperature sensitivity of the regions containing high concentrations of crystallographic defects.

This chapter not only demonstrates the advantages and wide utility of the temperature-dependent PL imaging method introduced in Chapter 3, but also advances the understanding of the local thermal behaviour of cast-mono Si wafers and compares them at different ingot positions and different fabrication steps, thus, providing a wealth of information that has not been reported previously.

Although temperature-dependent PL imaging with uniform excitation has proven to be a powerful technique for probing the temperature-dependent electrical properties of Si wafers and cells in this chapter, it should be noted that it still has some limitations for lifetime imaging-based analysis. This point will be further discussed in Chapter 5, together with a newly developed PL imaging system to overcome these disadvantages.



## Chapter 5

# Advanced Photoluminescence Imaging Using Non-Uniform Excitation<sup>‡</sup>

In Chapter 3 and Chapter 4, PL imaging using uniform excitation is employed to evaluate the performance of mc-Si and cast-mono Si wafers and cells under different operating temperatures. However, for samples with inhomogeneous distributions of defects, conventional PL images obtained under uniform excitation suffer from lateral carrier flows which result in inaccurate lifetime analysis and image blurring. It is worth mentioning that lateral carrier flow is an inevitable effect during solar cell operation in the field. However, care needs to be taken when conventional PL imaging measurements are used for quantitative lifetime-based analysis, such as extracting defect parameters.

To overcome the impact of lateral carrier flows, an advanced PL imaging method using non-uniform illumination is presented in this chapter. By adaptively adjusting the light intensity at each pixel, a uniform excess carrier density across the sample is achieved, thereby eliminating lateral currents. Details regarding the proposed method are given in Section 5.2. In Section 5.3, the advantages of the proposed method are demonstrated using Si wafers with spatially non-uniform lifetimes, with and without diffusion layers. This new approach presents a significant improvement in lifetime accuracy and image sharpness compared to conventional PL imaging techniques. Practical limitations of the current setup and possible future improvements are discussed in Section 5.4.

---

<sup>‡</sup> This chapter is based on:

**S. Nie**, Y. Zhu, O. Kunz, T. Trupke, and Z. Hameiri, "Advanced photoluminescence imaging using non-uniform excitation," *Prog. Photovoltaics Res. Appl.*, 2021.

**S. Nie**, Y. Zhu, O. Kunz, H. Kampwerth, T. Trupke, and Z. Hameiri, "Temperature-dependent photoluminescence imaging using non-uniform excitation," in *47<sup>th</sup> IEEE Photovoltaic Specialists Conference*, pp. 0789-0792, 2020 — Won the Best Student Award.

## 5.1 Photoluminescence Imaging Using Uniform Excitation

As described earlier, conventional PL imaging systems consist of a spatially uniform excitation source and a camera that collects the emitted PL signal [74]. Brighter regions (higher PL counts) in conventional PL images represent areas with higher  $\Delta n$ , and thus, higher carrier lifetime. For PL imaging-based quantitative analysis, the relative PL count is converted into  $\Delta n$  using Equation 2.26 by determining the calibration factor  $F_{\text{PLi}}$  [78, 83, 94-96], see Chapter 2. Lifetime images are then calculated as the ratio between  $\Delta n$  and  $G$  [95, 96]. However, as uniform illumination is used for PL imaging, any spatial non-uniformity in the sample causes gradients in  $\Delta n$ , and thus, induces lateral carrier flows within the sample. This results in blurring of the image and inaccurate lifetime analysis as lifetime is no longer equivalent to  $\Delta n/G$ , but an additional term that quantifies the lateral carrier flows needs to be considered.

To obtain more accurate lifetime images with uniform illumination, a method has been proposed to quantify the lateral carrier diffusion and, thus, to de-smear lifetime images of non-diffused samples using Equation 5.1 [100, 101]. However, this de-smearing method is limited by measurement noise and cannot be applied to devices with junctions where the lateral carrier flows are driven by both drift and diffusion.

$$\tau_{(x,y)} = \frac{\Delta n_{(x,y)}}{G + (D\nabla^2 \Delta n_{(x,y)})} \quad 5.1$$

## 5.2 Photoluminescence Imaging Using Non-Uniform Excitation

To overcome the limitation mentioned in the previous section, Heinz *et al.* [225] introduced the principle of adaptive excitation for PL imaging via numerical simulation. Later, Zhu *et al.* [226] experimentally demonstrated this concept by developing a PL imaging system that provides uniform  $\Delta n$  images, using spatially non-uniform excitation. The obtained PL images are free from the impact of lateral carrier flows. However, the application of this method has been demonstrated only in one dimension using two “macro pixels” (two centimetre-size regions, each with a uniform lifetime). This method has not been extended to the two-dimensional pixel level and therefore, cannot be used for non-uniform materials, such as Si samples with striations [227].

This chapter presents a PL imaging method that is not affected by lateral carrier flows. The method is based on applying the above principle of non-uniform illumination at the pixel level with high spatial resolution. A steady-state inhomogeneous excitation generated by a customised liquid-crystal display (LCD)-based illumination setup is used to counteract the lateral carrier flow induced by the sample's non-uniformity (see Figure 5.1). Its ability to collect PL images with uniform  $\Delta n$  at different injection levels for both diffused and non-diffused samples allows for more accurate PL imaging-based lifetime analysis and significantly improves the image contrast and dynamic range. In addition, the capability of the proposed method is further extended to allow temperature-dependent measurements.

### ***5.2.1 System Development and Optimisation***

The concept of non-uniform illumination is essential for acquiring PL images that are inherently free from the impact of lateral carrier flows. A simple approach to generate a non-uniform illumination is using a commercially available LCD projector. The working principle of the LCD is the blocking of light, as illustrated in Figure 5.1. Specifically, an LCD panel consisting of many liquid crystal molecules is sandwiched between two polarisers. By controlling the electrical signal applied to each liquid crystal molecule, the orientation of the liquid crystal molecule and thus the polarisation of the light is modified, resulting in a change in the intensity of light passed through the polariser. Since each pixel of the LCD panel can be controlled independently, a non-uniform illumination can subsequently be generated. However, for the purpose of PL imaging, the commercially available LCD projector has two main drawbacks. The first is that the achieved maximum illumination intensity is comparatively low. By using a modified projection lens to reduce the illumination area ( $6 \times 9 \text{ cm}^2$ ), the maximum intensity obtained using a commercial projector with a high-power mercury lamp is about 0.3 Suns. The second is that a short pass filter is needed to block long-wavelength light to ensure that the camera only detects the PL signal from the sample and not the original illumination source. However, using short-wavelength illumination may cause more excess carriers generated near the illuminated surface of the sample, thus resulting in a non-uniform excess carrier profile perpendicular to the surface. Therefore, more signal is detected at the surface rather than from the bulk. To overcome these drawbacks, a straightforward method is to combine a high-power 808 nm laser with an LCD-based spatial light modulator. In the following

paragraphs, details regarding the construction and optimisation of the LCD-based illumination setup using a high-power 808 nm laser are provided.

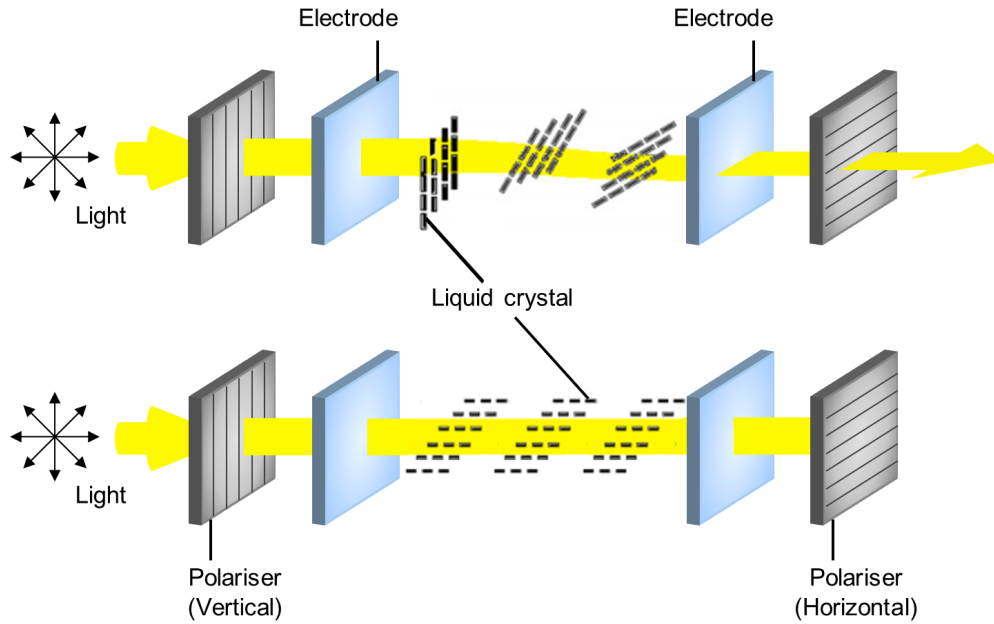


Figure 5.1 LCD operation principle.

**LCD:** The LCD is the key component in the proposed setup to generate a spatially non-uniform illumination. However, since LCDs are generally optimised for visible light applications, many of them do not perform well at 808 nm due to low contrast and transmission. In order to find a well-performing LCD at 808 nm with high resolution, contrast, and transmission, three commercially available LCD panels were tested using the setup shown in Figure 5.2. Light from an 810 nm infrared LED is first focused by an aspheric condenser lens, then passes through a bandpass filter with a centre wavelength of 810 nm to ensure the wavelength range is reduced to 805–815 nm. Two *Thorlabs* linear polarisers were placed perpendicular to each other with the LCD between them. The settings of the LCD controller were adjusted to optimise the LCD performance at 810 nm since a higher LCD drive voltage of the liquid crystal cells is needed for a longer wavelength. By adjusting the applied voltage of LCD from minimum to maximum for all the pixels, the contrast ratio between a full black illumination image and a full white illumination image was subsequently evaluated for each LCD panel. Note that the contrast depends on both the performance of the LCD panel and the two polarisers. A second test was performed to evaluate the transmission of each LCD panel at 810 nm. After removing the two polarisers, the transmission of the LCD was measured as the ratio

of the signals detected with and without LCD. All the tested results of the three LCD panels are summarised in Table 5-1. Although the *Sony LCX017* LCD has a lower resolution compared to the other two LCD panels, it has much higher transmission and contrast ratio which are the most critical parameters for PL imaging with non-uniform illumination and it was therefore selected as the most suitable option. Apart from the wavelength, the temperature is another factor that substantially affects the performance of an LCD, with higher temperatures being detrimental to the LCD contrast ratio. For instance, the contrast is reduced by a factor of  $\sim 1.35$  when the LCD is illuminated using a high-power 808 nm laser for about 20 sec. To reduce the impact of temperature, the LCD is cooled using compressed dry air and the duration of illumination is limited to less than 5 sec for one measurement.

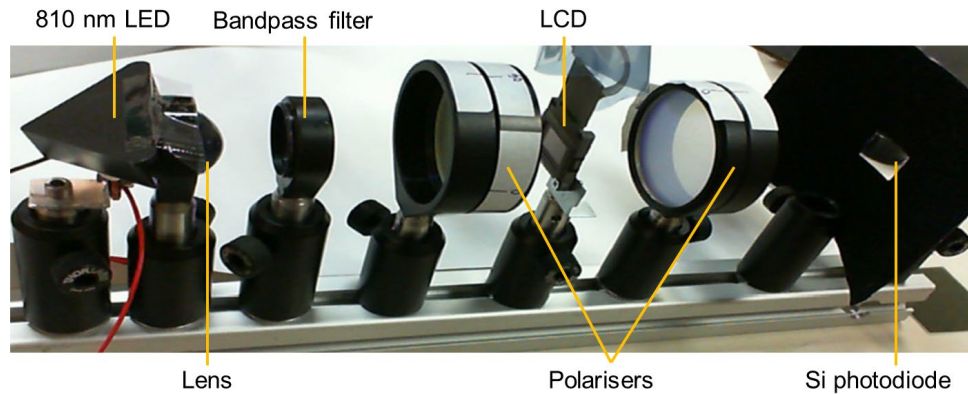


Figure 5.2 Setup used to test the performance of LCD panels.

Table 5-1 LCD panel specifications and their measured contrast and transmission for the initial screening configuration. The column highlighted in grey was the chosen model.

LCD	Epson D7	Sony LCX036BMT	Sony LCX017
Size	0.74 inch	1.8 inch	1.8 inch
Resolution	1920 × 1080	1600 × 1200	1024 × 768
Contrast ratio at 808 nm	1:50	1:43	1:92
Transmission at 808 nm	$\sim 13\%$	$\sim 38\%$	$\sim 50\%$

**Polariser:** To further improve the contrast, the *Thorlabs* linear polarisers were replaced by wire grid polarisers from *Meadowlark Optics*. These wire grid polarisers have substantially higher transmission ( $> 80\%$ ) and contrast ( $> 2000:1$ ) at 808 nm, and a very

high laser damage threshold of  $10 \text{ kW} \cdot \text{cm}^{-2}$ . The axis of the first polariser was set to  $45^\circ$ , as suggested in the instructions for the *Sony LCX017* LCD. In order to obtain the highest possible contrast ratio, four different methods of determining the axis of the second polariser were used, as follows: (i) the axis of the second polariser was adjusted until the light output was maximised when the applied voltage of the LCD is set to the maximum. The contrast is then calculated as the light output ratio when varying the applied voltage of the LCD from minimum to maximum. The other three methods were: (ii) minimising the light output when the applied voltage of the LCD is set to the maximum; (iii) maximising the light output when the applied voltage of the LCD is set to the minimum; and (iv) minimising the light output when the applied voltage of the LCD is set to the minimum. The results of all four methods are provided in Table 5-2, resulting in the best contrast being achieved by rotating the second polariser to minimise the light output when the applied voltage of the LCD is set to the minimum.

Table 5-2 Contrast optimisation for *Sony LCX017* LCD with wire grid polarisers. The column highlighted in grey was the chosen combination.

	(i)	(ii)	(iii)	(iv)
<b>Contrast</b>	1:19	1:58	1:32	1:300

The influence of the first polariser's axis was also examined since the instructions for the *Sony LCX017* LCD is mainly regarding for visible light. Figure 5.3 shows the light output as a function of the axis of the first polariser when the applied voltage of the LCD is set to minimum and maximum. Note that here, for each axis of the first polariser, the axis of the second polariser is re-adjusted to minimise the light output when the applied voltage of the LCD is set to the minimum. By increasing the axis of the first polariser from  $0^\circ$  to  $45^\circ$ , light output is increased by a factor of  $\sim 1.65$  and peaked at  $45^\circ$  for both cases. The light output ratio between maximum applied voltage and minimum applied voltage represents the contrast. Interestingly, the contrast does not vary significantly with the first polariser's axis, with a maximum change of 8%. Therefore, the axis of the first polariser was kept at  $45^\circ$  to enable a higher light output for the PL imaging system.

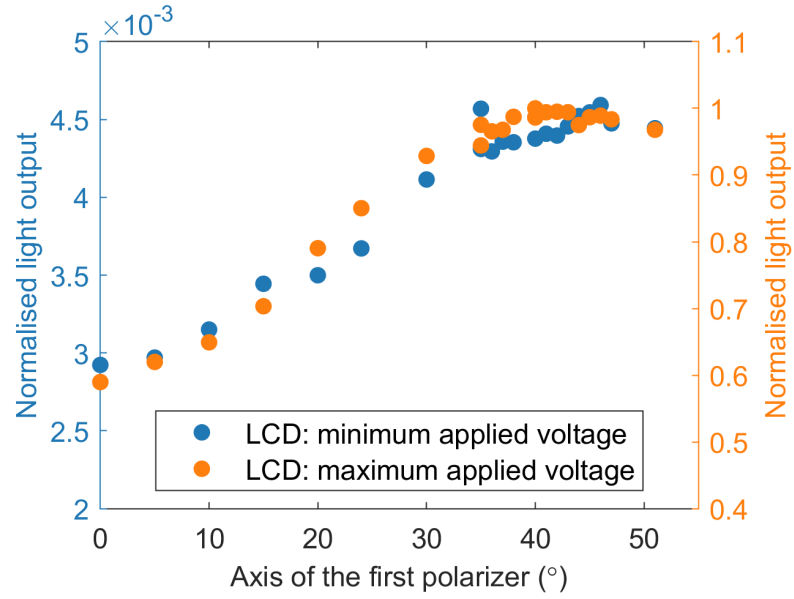


Figure 5.3 Normalised light output as a function of the axis of the first polariser when the applied voltage of the LCD is set to minimum and maximum. The light output is normalised to the maximum value obtained with maximum applied voltage.

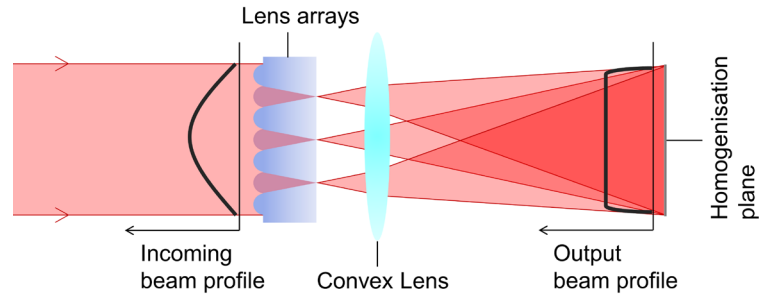


Figure 5.4 The beam shaping principle for achieving rectangular uniform illumination using optics including cross-cylindrical lens arrays and a convex lens.

**Laser Light Source:** In order to achieve a high illumination intensity, an 808 nm fibre-coupled diode laser from *Lumics* (model: *LU0808D320-D70AF*) with a peak power of 33 W was used. Since the laser beam diverges after leaving the fibre, a *Thorlabs* fibre collimation package was used to collimate the laser beam. Note that spatially uniform incoming light is required for the LCD. Therefore, to achieve this, beam shaping optics consisting of two cross-cylindrical lens arrays and a convex field lens are added to transform the circular laser beam with a Gaussian profile to a rectangular-shaped beam with a flat-top profile [228], as illustrated in Figure 5.4. Two cross-cylindrical lens arrays are placed perpendicular to each other, i.e., one shapes the beam in the  $x$ -direction and the other shapes the beam in the  $y$ -direction. These lens arrays split the incoming laser light into many beamlets, followed by a plano-convex lens which acts as a field lens,

focusing and overlapping the individual beamlets coming out of the lens arrays at the homogenisation plane. All the lenses have anti-reflection coatings to maximise the transmission at 808 nm and minimise stray light.

**Projection Lens:** A suitable lens is required to project the spatially modulated illumination generated by the LCD onto the sample plane. Initial trials were conducted using simple lenses with different focal lengths (50–75 mm) and sizes (2–3 inch), such as Bi-convex and doublet lenses, among others. These lenses were chosen to achieve a  $\sim 5 \times 5 \text{ cm}^2$  illumination area on the sample plane. However, all the projected illumination images that resulted from these simple lenses were not desirable, due to optical aberrations, in particular coma aberration and distortion aberration [229]. An example is given in Figure 5.5(a), where a 2 inch *Thorlabs* Bi-convex lens with a focal length of 60 mm is used. It was concluded that it is not possible to achieve a sharp illumination image on the sample plane using a single lens. To solve this optical aberration issue, a photographic imaging lens that consists of a series of optical elements was subsequently tried. As shown in Figure 5.5(b), the *Linos inspec.x M NIR 1.4/50* lens — used for projection here — significantly reduced the optical aberration, and a very sharp projection with minimal distortion was achieved. Moreover, this lens features an adjustable focal length (allowing change of illumination size) and an optical antireflection coating to maximise the transmission in the NIR wavelength range, ideal for the purpose of this work.

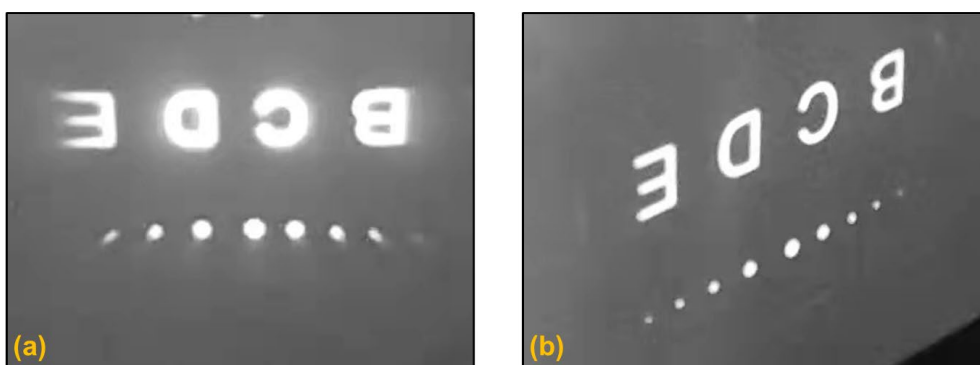


Figure 5.5 Non-uniform illumination images obtained with: (a) a *Thorlabs* Bi-convex lens; and (b) a *Linos inspec.x M NIR 1.4/50* lens. The two photos were taken from different angles.

**Final Setup:** A schematic representation of the optimised transmission-mode PL imaging system is shown in Figure 5.6. This system has been optimised to maximise the

light intensity and contrast in the sample plane and to minimise the optical aberrations of the illumination image. An 808 nm fibre-coupled diode laser with a peak power of 33 W was used as an excitation source. The laser light is firstly collimated and then passed through beam shaping optics to achieve rectangular uniform illumination. The uniform light is then polarised by the first polariser (*Meadowlark Optics*) before passing through a monochromatic LCD panel (*Sony LCX017*) and subsequently a second polariser (*Meadowlark Optics*). By controlling the electrical signal applied to each liquid crystal pixel, the orientation of the crystal is modified, enabling the continuous adjustment of the light intensity at each pixel. The illumination image is then projected onto the sample through a photographic projection lens (*Linco inspec.x M NIR 1.4/50*).

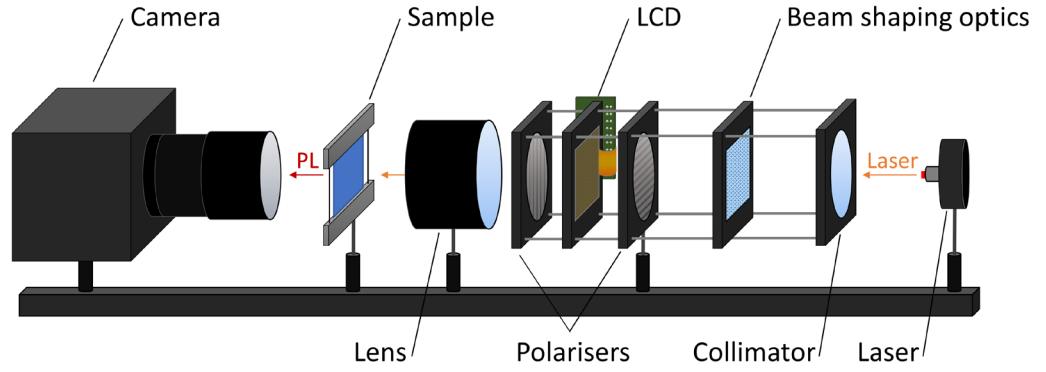


Figure 5.6 The transmission-mode PL imaging system with the customised LCD-based illumination setup.

The LCD-based illumination setup has a spatial resolution of  $1024 \times 768$  pixels with an 8-bit greyscale. The maximum illumination intensity of 1.1 Suns can be achieved for an illumination area of  $\sim 3.4 \times 4.5 \text{ cm}^2$  when the greyscale of LCD is set to 255. The pixel size of the illumination image is equivalent to a square area of  $\sim 75 \times 75 \text{ }\mu\text{m}^2$  in the sample plane. The measured contrast of this LCD-based illumination setup is up to 1:300, representing the relative intensity variation between nominally zero and maximum intensity. The achieved overall transmission is approximately 13%. Specifically, the illumination intensity is reduced by half due to the first polariser, followed by an additional  $\sim 50\%$  light reduction due to the LCD's fill factor with an active pixel area of  $70\% \times 70\%$ . The remaining  $\sim 12\%$  of light is mainly lost in the polarisers, as each polariser has a transmission of  $\sim 83\%$  at 808 nm for light that has a polarisation aligned with the polariser.

The PL emission is detected by a Si complementary metal-oxide-semiconductor (CMOS) camera with a spatial resolution of  $2048 \times 2048$  pixels. The pixel size of the camera image is equivalent to a square area of  $\sim 41 \times 41 \mu\text{m}^2$  in the sample plane. Suitable optical filtering (Long pass 850 nm, 900 nm, 975 nm) is used in front of the camera to avoid detection of the laser illumination.

### **5.2.2 Measurement Procedure**

A key requirement for achieving uniform PL images is to accurately align the illuminated pixels and the camera pixels since the illuminated pixels need to be adjusted in accordance with the measurement results via the camera. This task is complicated due to: (a) the different spatial resolution of the LCD panel and the camera; and (b) the optical aberrations of both illumination and camera images.

The straightforward pixel-alignment process is to map one LCD pixel at a time onto the corresponding pixels in the camera image by using an illumination pattern consisting of only one white pixel (greyscale value of 255; the rest of the pixels are set to the black with greyscale of 0), and then repeat one by one for all the LCD pixels. However, considering the LCD has 786432 pixels in total, this process is highly time-consuming. For time efficiency, the actual pixel-alignment process involves mapping an array of bright LCD pixels onto the corresponding pixels in the camera image. Explicitly, an illumination pattern of  $64 \times 48$  single white pixels (with a greyscale value of 255) with 16 black pixels (with a greyscale value of zero) between any two neighbouring white pixels were used. This pattern is used as it allows the maximum number of illumination pixels being mapped at a time without overlapping white pixels in the camera image. An example of this pattern is presented in Figure 5.7(a) where only a small ROI is shown. During the alignment, a paper sheet uniformly coated with ink that absorbs the 808 nm illumination and emits PL is placed on the sample stage. The corresponding image is then captured by the CMOS camera [see Figure 5.7(b)]. Note that a single pixel in the illumination image is detected as a large patch of pixels; this is due to: (a) the camera having a higher spatial resolution (smaller pixel size) than the LCD in the sample plane, and (b) the optical aberrations of the illumination. By identifying the camera pixel with the highest intensity [marked with a cross in Figure 5.7(c)] and its neighbouring pixels that have an intensity greater than half of the highest intensity [marked with black dots in Figure 5.7(c)] in the captured image, the pixels in the camera image that most closely

correspond to the illuminated (white) pixel in the illumination image are determined. By repeating this procedure with different illumination patterns that cover all the pixels of the LCD, a full alignment between the illumination and the camera pixels is obtained. Note that there is no need to repeat this alignment process unless there is a change in the measurement setup.

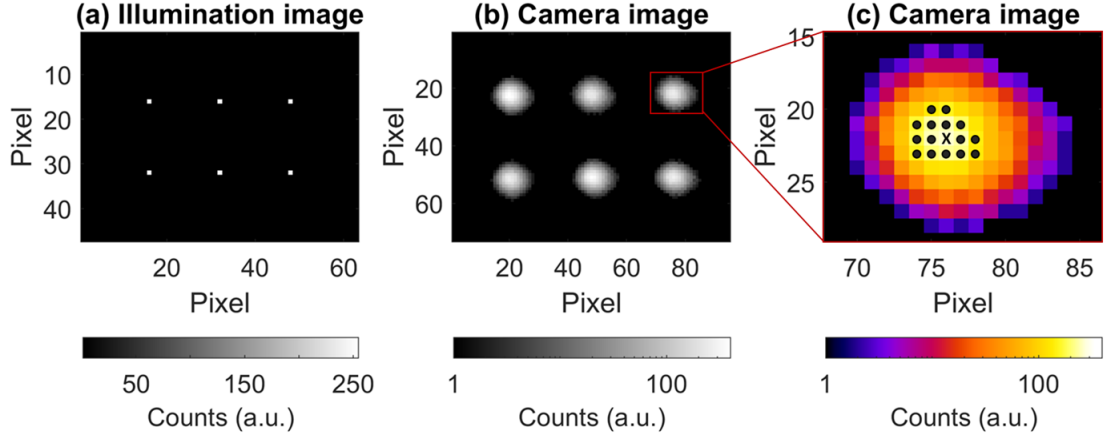


Figure 5.7 (a) Illumination pattern used for pixel-alignment (b) The corresponding camera image (c) Zoomed-in camera image of one illuminated pixel. The images are cropped and only represent a small part of the projection area.

To minimise the camera artefacts, all camera images are first flat-field corrected and then point-spread deconvolved [230] using the Lucy-Richardson method.

To achieve PL images with uniform  $\Delta n$ , the iteration procedure proposed in [225-227, 231] is used to adaptively alter the excitation intensity at each pixel of the sample. The starting point of this iteration procedure is a conventional PL image with spatially uniform excitation by setting the LCD to the highest greyscale value of 255. The pixel with the lowest PL count is then selected to be the reference pixel, where the illumination intensity is kept fixed. Based on the PL intensity of the reference pixel, the illumination intensity at all the other pixels  $(x,y)$  is modified according to:

$$\Phi_{(x,y)}^i = \Phi_{(x,y)}^{i-1} \left( \frac{I_{\text{PL(ref)}}^{i-1}}{I_{\text{PL}(x,y)}^{i-1}} \varepsilon + (1 - \varepsilon) \right) \quad 5.2$$

where  $i$  is the iteration number,  $\Phi_{(x,y)}^i$  is the illumination intensity on pixel  $(x,y)$  after the  $i^{\text{th}}$  iteration,  $I_{\text{PL}(x,y)}^{i-1}$  is the PL intensity at the pixel  $(x,y)$  after the  $(i-1)^{\text{th}}$  iteration,  $I_{\text{PL(ref)}}^{i-1}$  is the PL intensity at the reference pixel after the  $(i-1)^{\text{th}}$  iteration, and  $\varepsilon$  denotes a damping

factor that ensures convergence and has a value between 0 and 1 [225]. In this chapter,  $\varepsilon = 1$  is used to obtain a fast convergence. For samples with a stronger injection dependence of carrier lifetime, a low  $\varepsilon$  is recommended to ensure a slower but more stable convergence. Note that PL images are converted to LCD equivalent resolution based on the pixel alignment procedure described earlier to calculate the non-uniform illumination pattern required to achieve a uniform PL image.

Measuring the absolute illumination intensity in the sample plane is also essential for the iteration procedure. A power meter is used to measure the illumination intensity. Figure 5.8 shows the photon flux in the sample plane at different LCD greyscales and laser diode currents. This non-linear correlation between photon flux and LCD greyscale is used for the conversion between the illumination intensity image calculated by Equation 5.2 and the 8-bit greyscale image.

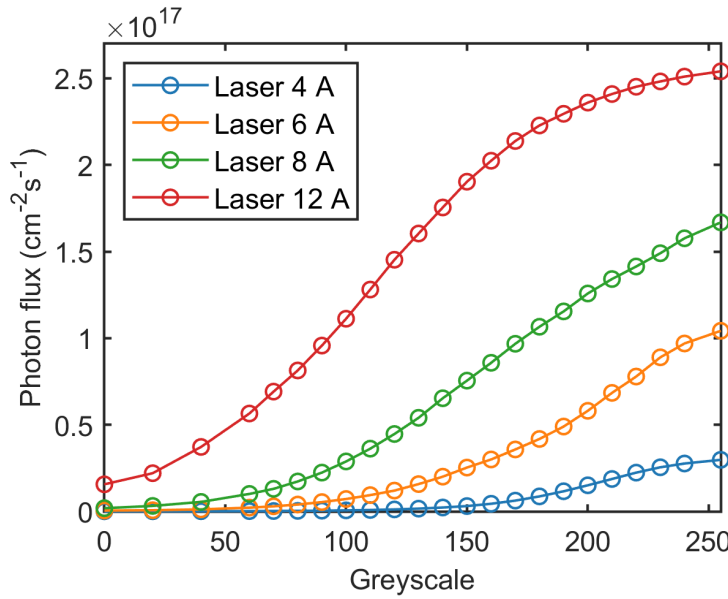


Figure 5.8 Photon flux in the sample plane as a function of LCD greyscale for four different laser intensities. The laser intensity is varied by changing the laser diode current via the laser driver.

### 5.2.3 Calibration Procedure

The calibration procedure of PL images to lifetime images requires both  $\Delta n$  and  $G$  to be quantified. For this procedure, the developed PL imaging system and a PC-based lifetime tester are used. The starting point is a conventional PL image under a steady-state uniform illumination and a steady-state PC measurement using the same illumination intensity. Parameters related to these measurements are labelled with the subscript “0”. The measured PC signal is a weighted average value over the sensed area of the sample, taking

into account the non-uniform sensitivity of the PC system. Figure 5.9 shows the radial sensitivity,  $S_r$ , of the used PC coil as a function of radius ( $r$ ) where  $r = 0$  corresponds to the centre of the PC coil.

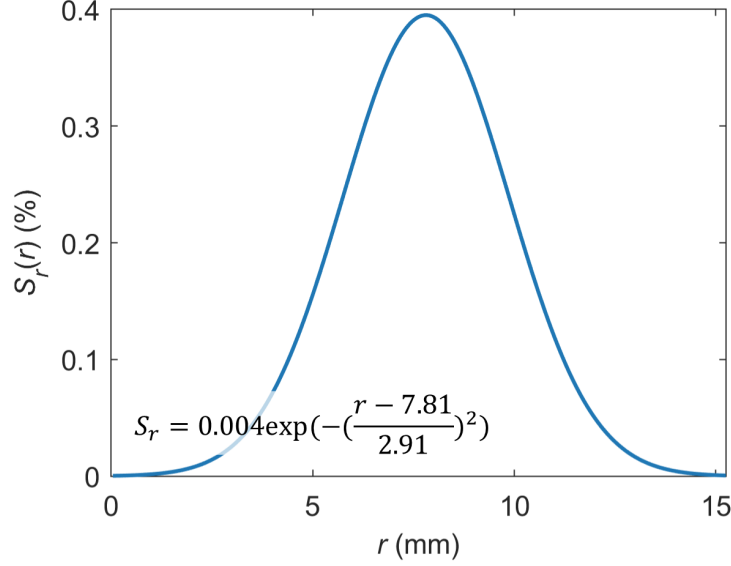


Figure 5.9 Radial sensitivity of the PC coil as a function of  $r$  for the PC lifetime tester used in this chapter;  $r = 0$  corresponds to the centre of the PC coil.

The detailed conversion from PC signal to  $\Delta n$  can be found in Chapter 2. By assuming  $\Delta n_{\text{PL}_0}$  (the weighted average  $\Delta n$  within the area that is same as the sensed area of the lifetime tester) equals  $\Delta n_{\text{PC}_0}$  (the PC-based  $\Delta n$  as measured by the lifetime tester), the calibration constant  $F_{\text{PLi}} B_{\text{rad}0}$  can be determined by solving Equations 5.3 and 5.4:

$$\Delta n_{\text{PL}_0(x,y)} = \frac{-N_{\text{dop}} + \sqrt{N_{\text{dop}}^2 + 4I_{\text{PL}_0(x,y)} / (F_{\text{PLi}} B_{\text{rad}0})}}{2} \quad 5.3$$

$$\Delta n_{\text{PC}_0} = \int_0^\infty 2\pi r S_r(r) \Delta n_{\text{avePL}_0}(r) \quad 5.4$$

where  $I_{\text{PL}_0(x,y)}$  and  $\Delta n_{\text{PL}_0(x,y)}$  represent the local PL intensity and  $\Delta n$  at pixel  $(x,y)$ , respectively.  $B_{\text{rad}0}$  is the radiative coefficient at  $\Delta n_{\text{PC}_0}$ ,  $S_r(r)$  is the radial sensitivity function of the PC coil used in this chapter at radius  $r$  (see Figure 5.9), and  $\Delta n_{\text{avePL}_0}(r)$  is the average  $\Delta n_{\text{PL}_0(x,y)}$  at radius  $r$ .

By assuming that  $F_{\text{PLi}}$  does not vary with intensity, the PL image obtained under non-uniform excitation can be calibrated to the  $\Delta n$  image by an iterative procedure until self-consistent values for  $B_{\text{rad rel}}$  and  $\Delta n_{\text{PL}}$  are achieved for each pixel  $(x,y)$ :

$$\Delta n_{\text{PL}(x,y)}^i = \frac{-N_{\text{dop}} + \sqrt{N_{\text{dop}}^2 + 4I_{\text{PL}(x,y)} / (F_{\text{PLi}} B_{\text{rad0}} B_{\text{rad rel}(x,y)}^i)}}{2} \quad 5.5$$

where  $I_{\text{PL}(x,y)}$  and  $\Delta n_{\text{PL}(x,y)}$  are the PL intensity and  $\Delta n$  at pixel  $(x,y)$  obtained from non-uniform excitation, respectively, and  $B_{\text{rad rel}(x,y)}$  is the relative change of the radiative recombination coefficient at the same pixel due to the variation of  $\Delta n$  from  $\Delta n_{\text{PC}_0}$  to  $\Delta n_{\text{PL}(x,y)}$ .  $B_{\text{rad rel}}$  is calculated based on the injection dependent radiative model from Reference [22].

Once this procedure has been carried out, lifetime images can be obtained by:

$$\tau_{(x,y)} = \frac{\Delta n_{\text{PL}(x,y)}}{G_{(x,y)}} = \frac{\Delta n_{\text{PL}(x,y)}}{\Phi_{(x,y)}(1-R)/W} \quad 5.6$$

## 5.3 Proof of Concept Measurements

### 5.3.1 Application to Non-Diffused Sample

The proposed method is firstly applied to a non-diffused  $n$ -type Czochralski (Cz) Si wafer with a resistivity of 6  $\Omega\cdot\text{cm}$ . The wafer was passivated with aluminium oxide ( $\text{AlO}_x$ ) on both sides.

PL images after each iteration (normalised to the exposure time) are shown in Figure 5.10, with the aim of producing the most uniform PL image possible by individually varying the intensity of each illumination pixel. For better visualisation of each image, different colour scales are used. Note that “Iteration 0” represents a conventional PL image obtained under uniform illumination, measured with an intensity equivalent to 0.3 Suns. The non-uniformity of the PL images after each iteration step is quantified by the coefficient of variation (CV: defined as the standard deviation divided by the mean) and is presented in Figure 5.10(l). As can be seen in this example, a uniform PL image is achieved after 10 iterations, with a relative deviation below 2.5% across the entire image. The few sudden changes of the PL intensity in Figure 5.10 (e.g., from Iteration 6 to Iteration 7) are due to the injection dependence of the lifetime. These

changes are then followed by a gentle illumination variation, resulting in a smoother transition in the next iteration (for instance, from Iteration 7 to Iteration 8).

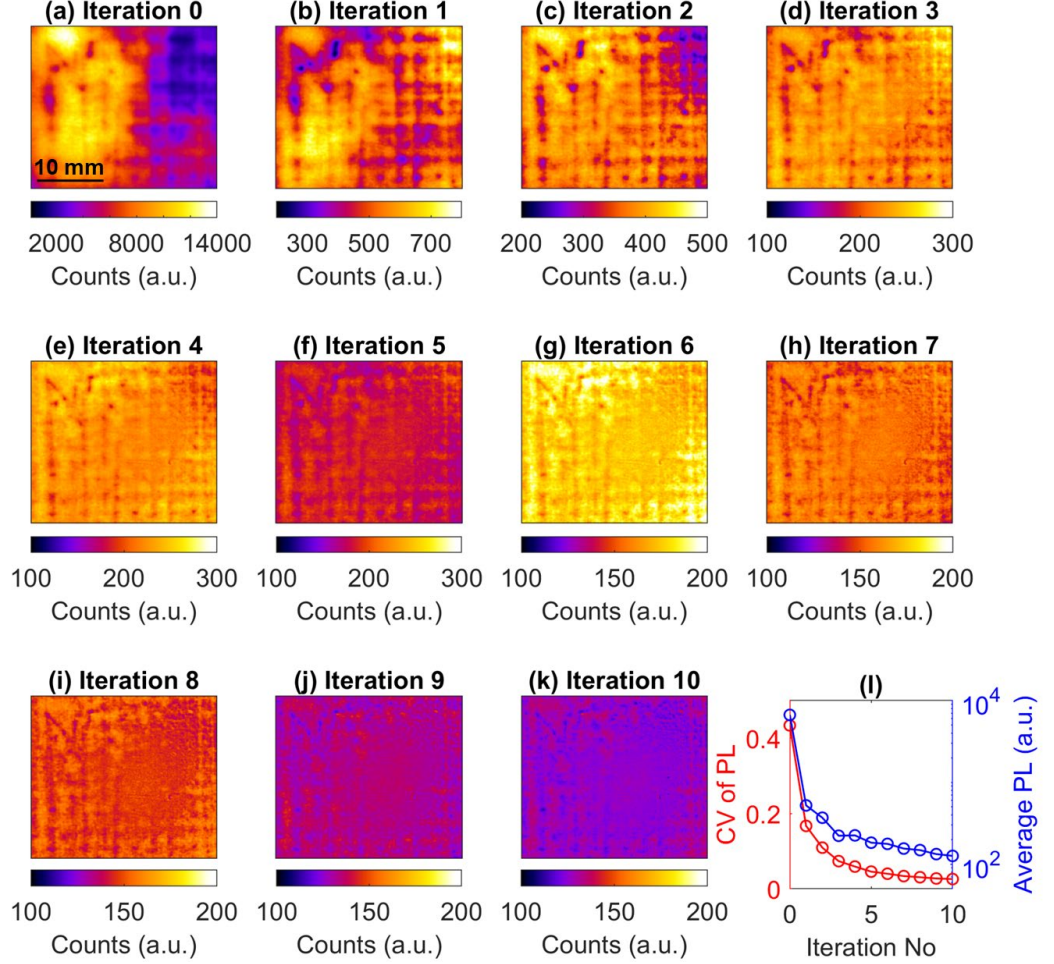


Figure 5.10 (a) Conventional PL image of an  $n$ -type non-diffused Cz wafer at 0.3 Suns illumination; (b)–(k) PL images using non-uniform excitation after 10 consecutive iterations; and (l) the average PL counts and CV of each of the images.

Figure 5.11(a) presents the minority carrier lifetime image extracted from the PL image measured with uniform excitation (Iteration 0). The lateral carrier flow smears the transition between high and low lifetime regions in this conventional lifetime image. This lifetime image was then numerically de-smearred using the method of Phang *et al.* [100], as shown in Figure 5.11(c). As expected, Figure 5.11(c) is sharper than Figure 5.11(a). The lifetime image obtained from the proposed non-uniform illumination method is given in Figure 5.11(e), where the non-uniformity of lifetime distribution is extracted from the excitation image after the last iteration. It is worth noting that the lifetime image extracted using the proposed method [Figure 5.11(e)] is comparable with the numerically de-smearred lifetime image [Figure 5.11(c)] but has a higher dynamic range.

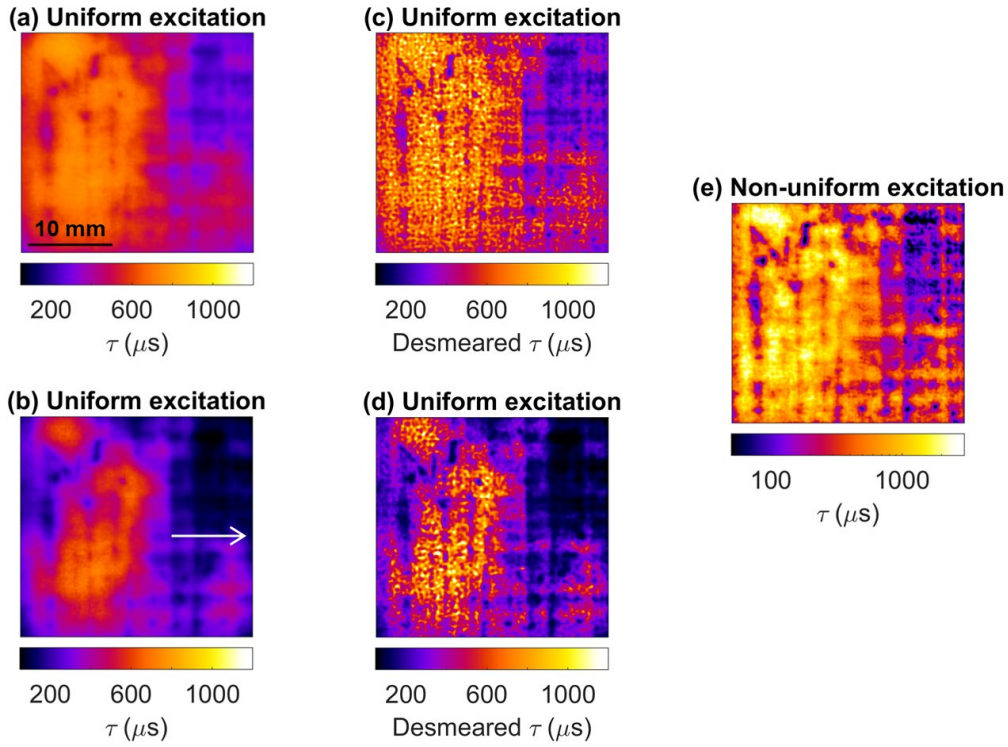


Figure 5.11 Lifetime images obtained from: (a)–(b) the conventional PL imaging method; (c)–(d) the corresponding de-smeared images; and (e) the proposed non-uniform excitation method at  $\Delta n = 1.5 \times 10^{14} \text{ cm}^{-3}$ . Note that (a) and (c) are obtained under 0.3 Suns illumination and have a global  $\Delta n$  of  $1.9 \times 10^{15} \text{ cm}^{-3}$ . (b) and (d) are obtained under 0.04 Suns illumination and have a global  $\Delta n$  of  $1.9 \times 10^{14} \text{ cm}^{-3}$ .

It is important to point out that lifetime images obtained from the conventional method represent the non-uniform lifetime distribution at spatially varying  $\Delta n$ , whereas the proposed method provides lifetime images at the same PL intensity, and thus, at spatially uniform  $\Delta n$ . Note that  $\Delta n$  across the lifetime image obtained from the proposed method is  $1.5 \times 10^{14} \text{ cm}^{-3}$ , whereas the average  $\Delta n$  in the conventional PL image [Figure 5.11(a) and (c)] is  $1.9 \times 10^{15} \text{ cm}^{-3}$ . Figure 5.11 also includes a lifetime image taken at uniform illumination with an average  $\Delta n$  of  $1.9 \times 10^{14} \text{ cm}^{-3}$  and its de-smeared image [Figure 5.11(b) and (d), respectively]. Its global  $\Delta n$  is closer to the  $\Delta n$  of the PL image obtained using the proposed method [Figure 5.11(e)]. Again, the lifetime image extracted from the proposed method is much sharper than the conventional PL image.

To provide a quantitative comparison, Figure 5.12 displays representative lifetime profiles [across the area highlighted with a white arrow in Figure 5.11(b)] obtained from the conventional method at (a) high and (b) low illumination intensity, (c) and (d) the de-smeared images, and from (e) the proposed method. In these figures, the marker colour

indicates the corresponding  $\Delta n$ . Since profile (e) is at a medium injection level, it is not surprising that the lifetime profile (e) is between the profiles obtained from (c) and (d). The profile (e) obtained from the proposed method has a significantly steeper profile, compared to the profiles of the conventional method and even the de-smear images. It is worth recalling that the de-smear method is less effective in high recombination areas and low signal-to-noise ratio regions [100, 101]. This highlights the improved capability of the proposed non-uniform excitation method for more accurate lifetime measurements of non-uniform samples.

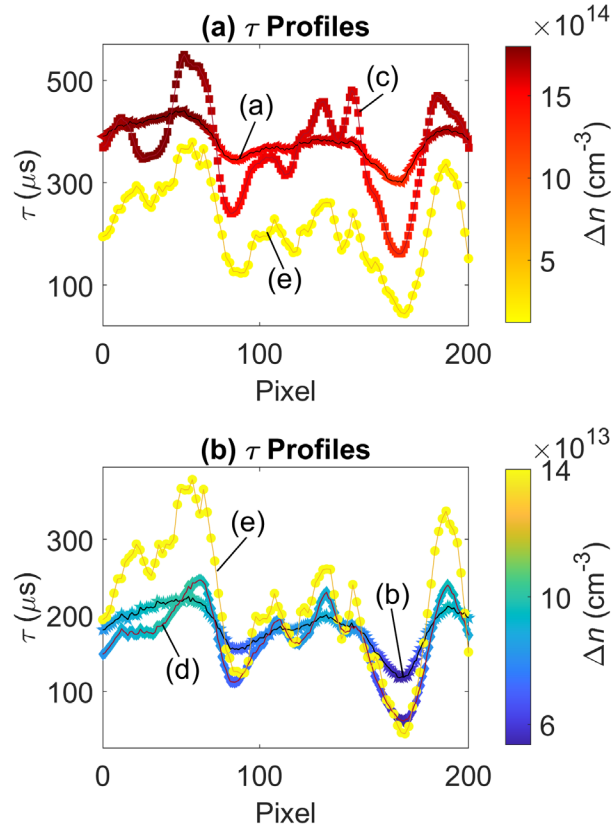


Figure 5.12 Horizontal lifetime profiles along the white arrow in Figure 5.11(b) where the trace colour is mapped to  $\Delta n$ . These profiles are extracted from Figure 5.11 and their corresponding sublabels (a)–(e).

### 5.3.2 Application to Diffused Sample

The advantages of the proposed method are demonstrated in this section using a diffused  $n$ -type Cz Si wafer with a resistivity of  $2.4 \, \Omega\cdot\text{cm}$  and a symmetric passivation stack of  $p$ -type polysilicon,  $\text{AlO}_x$ , and  $\text{SiN}_x$ . The sheet resistance of the diffused layer is  $\sim 100 \, \Omega/\text{sq}$ . The wafer is partially affected by striations (ring defect) [232], resulting in a spatially non-uniform lifetime distribution.

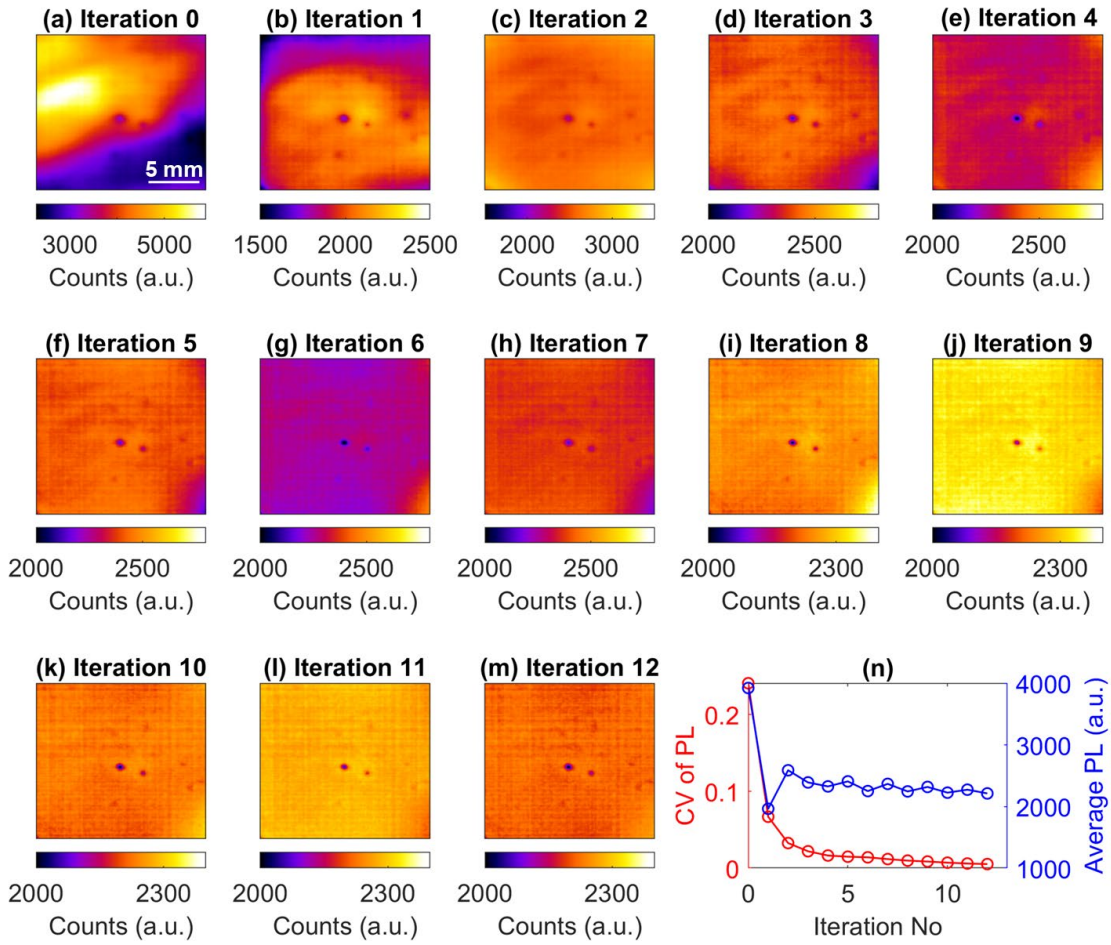


Figure 5.13 (a) Conventional PL image of a diffused *n*-type Cz wafer obtained under 1 Sun illumination; (b)–(m) PL images using non-uniform excitation after each iteration; and (n) average PL counts and CV of each of the images.

Figure 5.13 illustrates the PL images after the first 12 iterations. Figure 5.13(n) shows the average PL counts and CV after each iteration step. All PL images were normalised based on their respective exposure time to allow a direct comparison. The conventional PL image (Iteration 0) is obtained at an illumination equivalent to 1 Sun intensity. In the case of this diffused sample, a uniform PL image is achieved after only four iterations, with less than 2.5% relative deviation across the image. With more iterations, even better uniformity is achieved with only 0.5% relative deviation across the entire image [Figure 5.13(m)]. It is noticed that the convergence of this diffused sample happens much faster than the non-diffused sample. This can be attributed to the stronger injection dependence of the non-diffused sample's lifetime and its more complex non-uniform pattern.

The same iteration process was carried out to obtain a uniform PL image at lower  $\Delta n$  by reducing the laser intensity to the equivalent of 0.65 Suns. The average PL counts and CV after each iteration step are given in Figure 5.14, together with the PL images obtained under uniform illumination and after the last iteration. Compared to the measurements at 1 Sun, the convergence at lower  $\Delta n$  is much slower, as shown in Figure 5.14(c). The most likely explanation for this is the stronger impact of lateral carrier flow at low illumination intensity [74]. Nevertheless, after 17 iterations, a CV below 1% has been achieved.

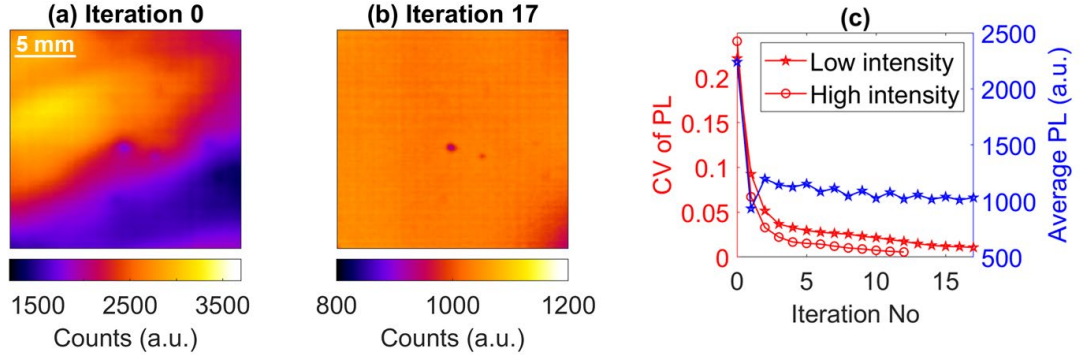


Figure 5.14 (a) Conventional PL image of a diffused *n*-type Cz wafer obtained under 0.65 Suns illumination; (b) PL image using non-uniform excitation after the 17<sup>th</sup> iteration; and (c) average PL counts and CV of each iteration. In (c), iteration 0 represents a uniform illumination of 0.65 Suns for low intensity and 1 Sun for high intensity, and the CV for the high intensity is the data from Figure 5.13(n).

Figure 5.15 compares the conventional lifetime images at average  $\Delta n$  of (a)  $5.6 \times 10^{15} \text{ cm}^{-3}$  and (b)  $3.5 \times 10^{15} \text{ cm}^{-3}$ , and the lifetime images extracted from the non-uniform excitation method at  $\Delta n$  of (c)  $4.0 \times 10^{15} \text{ cm}^{-3}$  and (d)  $2.2 \times 10^{15} \text{ cm}^{-3}$ . The images extracted using the proposed method are much sharper and have better contrast. A particularly clear demonstration of the superior image quality of the proposed method is marked with green rectangles in Figure 5.15. Several point-like defects with high recombination cannot clearly be distinguished in the conventional lifetime images, while they can be easily identified in Figure 5.15(c) and (d). This example illustrates the strong impact of the lateral carrier flow on conventional PL images, smearing local recombination activities and preventing accurate quantitative analysis. Since the de-smearing method [100] is not applicable to diffused samples for recovering the local recombination sites, this highlights the more general usability of the proposed method, leading to a significantly improved accuracy in the extraction of local recombination activities.

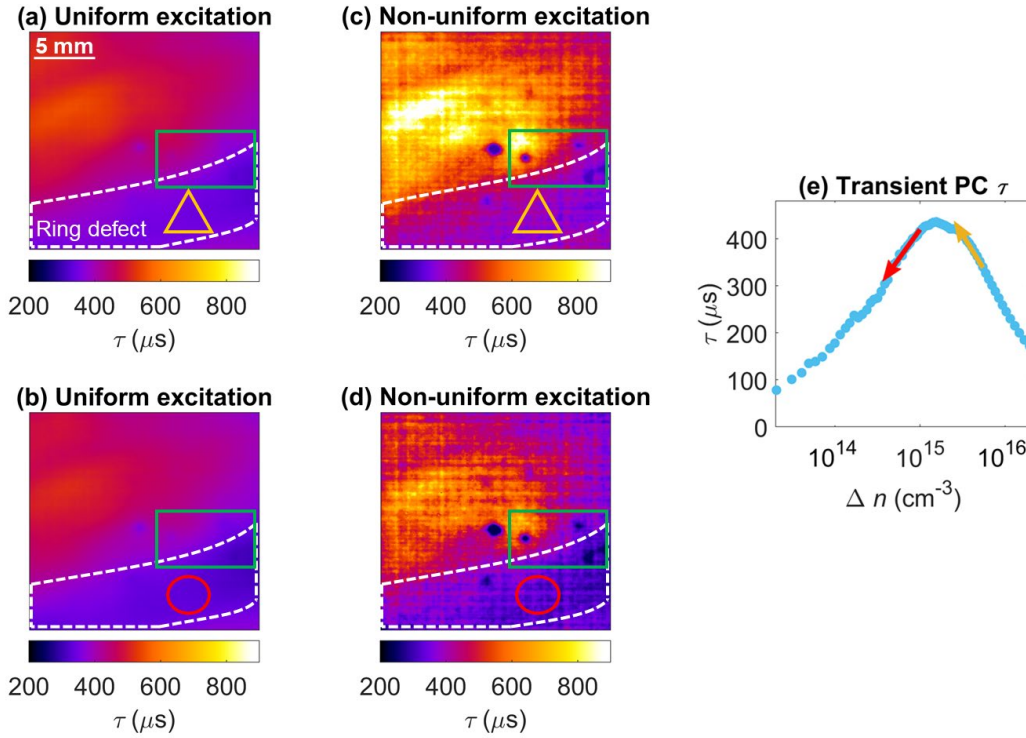


Figure 5.15 Lifetime images of the diffused sample obtained from the conventional PL imaging method at (a) 1 Sun and (b) 0.65 Suns, and lifetime images using the proposed non-uniform excitation method at (c)  $\Delta n = 4.0 \times 10^{15} \text{ cm}^{-3}$  and (d)  $2.2 \times 10^{15} \text{ cm}^{-3}$ . A corresponding injection-dependent lifetime measured by the PC-based lifetime tester is shown in (e).

By eliminating the impact of lateral carrier flow, the effective lifetime is expected to be lower at defected regions and higher at high-quality regions. However, it can be noticed that in the ring-defect region, the lifetime extracted using the proposed method is slightly higher compared to the corresponding lifetime obtained from the conventional method [see the representative area marked with yellow triangles in Figure 5.15(a) and (c)], while the opposite trend is observed in the images obtained under lower illumination [see the representative area marked with red circles in Figure 5.15(b) and (d)]. This result can be attributed to the injection-dependence of the lifetime that increases with decreasing  $\Delta n$  at higher injection ( $\Delta n > 3 \times 10^{15} \text{ cm}^{-3}$ ) and reduces with decreasing  $\Delta n$  at lower injection [see Figure 5.15(e)].

The grid pattern shown in the PL images and lifetime images [more obvious in Figure 5.15(c) and (d)] is not related to the samples. It is an artefact introduced by the camera. This can be eliminated by using a different camera, which was not available during my research.

## 5.4 Limitations and Future Improvements

### 5.4.1 Limitations

The above results experimentally demonstrate that using non-uniform excitation at the pixel-by-pixel level is an effective approach for eliminating the carrier smearing effect and, hence, providing more accurate lifetime images at constant  $\Delta n$ . However, there are some practical limitations to the current setup that should be addressed to make this method even more effective and generally applicable.

Currently, the contrast of the non-uniform excitation is one of the main limitations. The dynamic range of the chosen monochromic LCD is up to 1:300 at 808 nm illumination. Although this contrast allows a variation of the illumination intensity by more than two orders of magnitude, a fully uniform PL image cannot be achieved if the ratio between the non-uniform lifetime features is larger than the excitation contrast. It should be noted that the contrast ratio between two adjacent pixels can be lower than 1:300 in practice and the exact contrast ratio for each pixel depends on the pixel location and the optical aberrations of the illumination image.

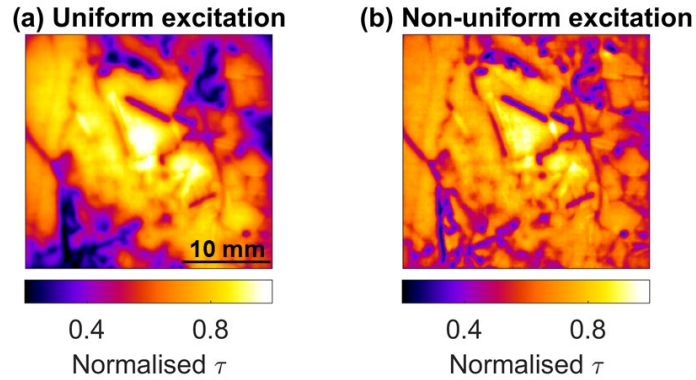


Figure 5.16 Normalised lifetime images of a mc-Si wafer using: (a) conventional method at 0.3 Suns; and (b) the proposed non-uniform excitation method. The lifetime images are normalised to their maximum counts.

An example is given by obtaining a uniform PL image of a mc-Si wafer using the non-uniform illumination (see Figure 5.16). Due to the large contrast ratio of its non-uniform features and the complex and small scale non-uniform distributions, a perfectly uniform PL image has not been achieved (CV of 7% obtained after the last iteration). Although a uniform  $\Delta n$  image of the mc-Si wafer cannot be obtained, the lifetime image extracted using the proposed method with the non-uniform illumination significantly reduces image

blurriness compared to the conventional method. The recombination activity of the grain boundaries appears much clearer in comparison to the conventional PL image.

Another limitation for acquiring accurate lifetime images at constant  $\Delta n$  for strongly inhomogeneous samples is the finite resolution of the LCD or camera, since in some instances, the pixel size can be larger than the feature size, for example, grain-boundaries or dislocation clusters. However, considering the current trend of the PV industry to shift to mono-crystalline Si wafers with a relatively larger scale of non-uniform distribution — like the ring defects presented in this chapter — it seems this constraint will be less critical for future applications.

At this stage, the lifetime images obtained by the non-uniform excitation setup are at medium- to low-injection levels, as the achievable illumination intensity is not sufficient to reach higher injection levels. Although a high-power laser is used, the highest illumination intensity at the sample plane is around  $0.1 \text{ W}\cdot\text{cm}^{-2}$ . This is due to the low overall transmission ( $\sim 13\%$ ) of the current setup as discussed in Section 5.2.1. As the lowest lifetime region restricts the achieved maximum injection level, a very strong local illumination is required for samples with low lifetime regions to achieve a uniform PL image at a relatively high-injection level.

#### **5.4.2 General Improvements**

Most of the above limitations can be addressed by using a LCD with a higher resolution, a higher fill factor, and a wider dynamic range. Currently, a commercially available LCD is used. However, this LCD is designed for visible light rather than NIR applications, thus clearly non-ideal for use with a high-power 808 nm laser illumination. A LCD specifically designed or optimised for infra-red illumination that has a higher fill factor is preferred for increasing the transmission. Another substantial increase in light intensity can be achieved if a polarised laser is used as an incoming light source which eliminates the need for the first polariser and increases the overall light throughput by a factor of  $\sim 2$ . Another solution is using a high-power laser in the visible range. This approach could potentially simplify the setup and improve the contrast of non-uniform excitation since a much larger range of LCD panels can be used. However, as mentioned in Section 5.2.1, short-wavelength illumination may cause a higher concentration of excess carriers generated near the illuminated surface of the sample.

### 5.4.3 Temperature-Dependent Measurements in Reflection Mode

The capabilities of the non-uniform excitation method have been extended to include temperature-dependent measurements, by modifying the configuration of the system from transmission to reflection mode. This modification allows the sample to be placed on a temperature-controlled stage and heated to the desired temperature. A schematic of the temperature-dependent PL imaging system using non-uniform excitation is shown in Figure 5.17. The generation of non-uniform illumination remains unchanged while the modifications on the imaging-side include: (a) a dichroic mirror used to reflect the non-uniform illumination to the sample and transmit the PL signal; (b) a temperature-controlled stage on which the sample is placed; and (c) the camera being placed above of the sample to collect the emitted PL signal transmitted through the dichroic mirror.

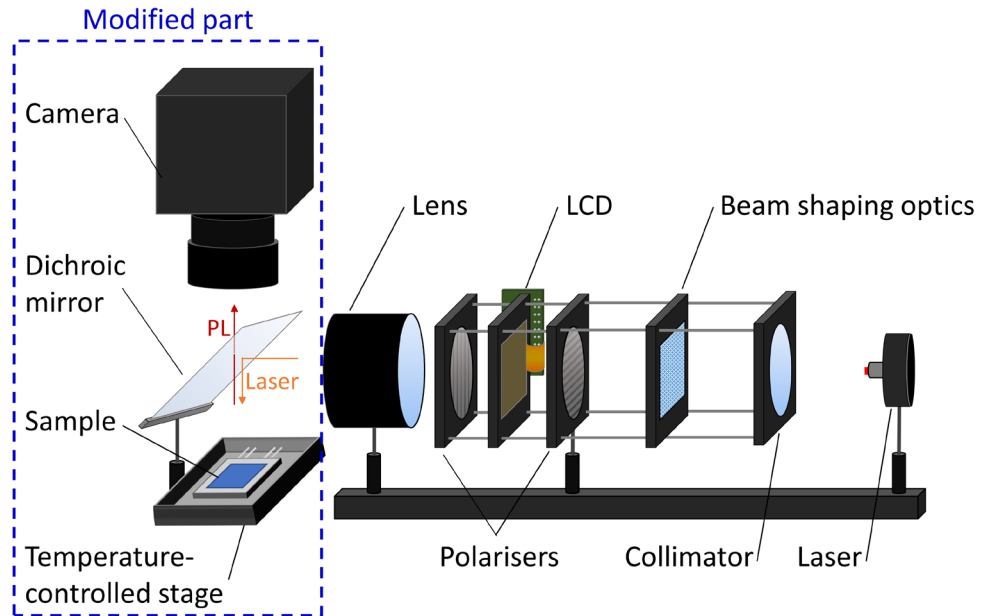


Figure 5.17 The temperature-dependent reflection-mode PL imaging system with a customised LCD-based non-uniform illumination setup.

As a proof of concept, measurements were conducted on an  $n$ -type diffused Cz wafer (with the ring defects) using a high-power light source. Figure 5.18 displays its temperature-dependent normalised lifetime images as well as the normalised lifetime image at 25 °C extracted using the conventional method. The lifetime images acquired by non-uniform excitation are much sharper than the image obtained under uniform excitation, where the highly recombination-active point-like defect can be identified. Moreover, temperature-dependent measurements reveal a beneficial thermal behaviour

of the region affected by the ring defect, owing to a lifetime improvement at higher temperatures.

This new capability of conducting temperature-dependent PL imaging measurements with non-uniform excitation enables a more accurate and comprehensive investigation of defects that are distributed non-uniformly within the sample. For example, by fitting the injection and temperature-dependent lifetime images (taken by the non-uniform excitation method) using the SRH statistics [44, 45, 97] for each pixel, the proposed method is expected to benefit local defect identification and defect parameter mapping. Moreover, by combining with the surface modelling method presented in Chapter 6, the impacts of surface recombination and bulk recombination can be separated from the obtained temperature-dependent lifetime images.

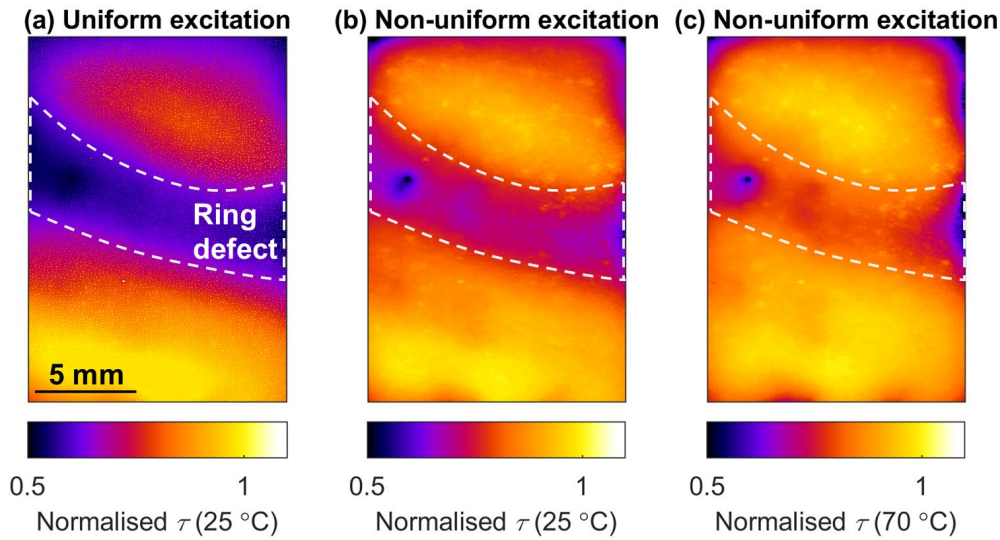


Figure 5.18 Normalised lifetime images of an *n*-type diffused wafer at: (a) 25 °C with uniform excitation; (b) 25 °C with non-uniform excitation; and (c) 70 °C with non-uniform excitation. Note that (b) and (c) represent lifetime images at a similar injection level.

## 5.5 Chapter Summary

In this chapter, a PL imaging method using spatially non-uniform excitation has been presented. It enables pixel-level adjustment of the illumination intensity to achieve a uniform luminescence distribution. The method allows the acquisition of images that are virtually unaffected by lateral carrier flows and the associated image smearing.

The proposed approach has successfully been applied to non-uniform Si wafers with and without diffusion to extract spatially non-uniform lifetime images. Compared with

the conventional lifetime images obtained under uniform illumination, the proposed method effectively removes artefacts introduced via lateral charge carrier drift and diffusion and the associated image blurring. This method, therefore, provides sharper and more accurate lifetime images with a larger dynamic range. For instance, local recombination sites which cannot be identified in lifetime images obtained using conventional PL images can be easily identified in images that are acquired with the proposed method. By modifying the configuration of the system from transmission to reflectance-mode PL measurements, the capability of the proposed method has been further extended to enable both injection- and temperature-dependent measurements. This new capability is expected to improve the understanding of materials' electrical properties, their temperature dependence at different operating temperatures and irradiation levels. Most importantly, the proposed method measures the samples under spatially uniform  $\Delta n$ , which allows more accurate extraction of recombination centre parameters across Si wafers, for example, in the context of interstitial iron imaging, as most PV electrical parameters (such as lifetime) are injection dependent.

The results presented in this chapter confirm and experimentally demonstrate significant advantages of PL imaging with non-uniform excitation. Thus, this proposed method is expected to benefit the quantitative investigation of non-uniform PV materials.



## Chapter 6

# Characterisation of the Silicon-Silicon Dioxide Interface under Various Operating Conditions<sup>§</sup>

In the previous chapter, a novel method to spatially resolve the effective lifetime of non-uniform samples was presented. However, effective lifetime quantifies the total recombination, occurring simultaneously within the bulk and at the surfaces. An in-depth investigation of the recombination within the device requires the separation of the bulk and surface components. In this chapter, a method to quantify surface recombination under different operating conditions and parameterise interface defect parameters is presented.

To demonstrate this method, SiO<sub>2</sub> was selected for surface passivation because of the critical role it has played in the development of high-efficiency Si-based solar cells. Although the electrical properties of the Si-SiO<sub>2</sub> interface have been extensively investigated in the past, the impact of temperature on the recombination at this interface remains less understood. As discussed in Chapter 3 and Chapter 4, the operating temperature significantly influences the field performance of PV devices. Therefore, this chapter investigates the recombination at the Si-SiO<sub>2</sub> interface by varying multiple parameters: temperature, excess carrier density, and dielectric fixed charge. This allows extraction of the Si-SiO<sub>2</sub> interface defect parameters and the temperature-dependence of the capture cross-sections. These results could be beneficial for the field-performance modelling of some high-efficiency PV devices that utilise SiO<sub>2</sub> passivation, such as polysilicon-based passivated contacts, IBC (Interdigitated Back Contact) devices, and others.

---

<sup>§</sup> This chapter is based on:

**S. Nie**, R. S. Bonilla, and Z. Hameiri, "Unravelling the silicon-silicon dioxide interface under different operating conditions," *Sol. Energy Mater. Sol. Cells*, vol. 224, pp. 111021, 2021.

**S. Nie**, R. S. Bonilla, and Z. Hameiri, "Temperature-dependent characterisation of Si-SiO<sub>2</sub> interface passivation for corona charged oxides," in *Asia-Pacific Solar Research Conference*, 2020.

Section 6.1 reviews previous findings regarding the Si-SiO<sub>2</sub> interface. Section 6.2 describes the experimental details and the proposed modelling method used in this investigation, while in Section 6.3 the temperature-dependent electrical characteristics of the Si-SiO<sub>2</sub> interface are summarised and discussed.

## 6.1 Characterisation of the Silicon-Silicon Dioxide Interface

The energy conversion efficiency of Si solar cells strongly depends on carrier recombination in the bulk and at their surfaces [17]. Extensive effort has been devoted to the improvement of the bulk quality via refined control of the crystallisation process [233], gettering [234], and hydrogenation [156]. Thus, the performance of many Si solar cells is now limited by the recombination at interfaces [235]. Furthermore, as the current PV industry tends towards thinner Si substrates and higher cell performance [236], investigating the surface passivation quality provided by various dielectrics is extremely important [237].

Silicon dioxide is the first and most studied dielectric for surface passivation of Si [238]. It has played a key role in PV development, leading to the first 20% efficient Si solar cells [51, 238]. Although the current industry standard surface passivation materials are silicon nitride [239, 240] and aluminium oxide [241], a thin SiO<sub>2</sub> or silicon oxide (SiO<sub>x</sub>) film is often included in the stack to enhance the passivation quality [238, 242]. Recently, SiO<sub>2</sub> is experiencing a renaissance as an indispensable component for various types of passivating contacts [238, 243].

The electrical properties of the Si-SiO<sub>2</sub> interface, usually described by  $D_{it}$ ,  $Q_f$ ,  $\sigma_{ns}$ , and  $\sigma_{ps}$ , have been studied extensively in the past [31, 244-251]. The majority of such measurements have been performed on metal-oxide-semiconductor (MOS) structures using deep level transient spectroscopy (DLTS), and capacitance-voltage measurements [31, 244-251]. A relatively low density of positive  $Q_f$  (in the range of  $10^{10}$ – $10^{11}$  q·cm<sup>-2</sup>, depending on the process) has been reported in as-grown SiO<sub>2</sub> films [18, 238]. Therefore, it appears that the passivation quality provided by SiO<sub>2</sub> mainly relies on reducing  $D_{it}$ . Although  $D_{it}$  strongly depends on the fabrication process [251], it seems to be above  $10^{11}$  cm<sup>-2</sup>eV<sup>-1</sup> for as-oxidised layers and can be further reduced by a forming gas anneal (FGA) [18]. Extremely low  $D_{it}$ , in the range of  $10^9$  cm<sup>-2</sup>eV<sup>-1</sup>, can be achieved by post-metallisation annealing, often referred to as ‘aneal’ [250]. Note that  $D_{it}$  has been found to be independent of the doping type and doping concentration of the Si wafers, for doping

concentrations below  $10^{16} \text{ cm}^{-3}$  [252]. Regarding  $\sigma_{\text{ns}}$  and  $\sigma_{\text{ps}}$ , there is a large uncertainty of 1–2 orders of magnitude in their values as determined by DLTS measurements [18, 253]. However, most studies have found  $\sigma_{\text{ns}}$  to be larger than  $\sigma_{\text{ps}}$  [254, 255].

Depositing corona charge can enhance the passivation quality of  $\text{SiO}_2$  via charge-assisted population control [256, 257]. The additional charge manipulates the surface potential and the interface band bending to reduce the surface recombination. Glunz *et al.* [258] used corona charge to study interface properties of Si-SiO<sub>2</sub> on both lifetime structures and solar cells. They found that the surface recombination is significantly reduced when the dielectric is highly charged either with negative or positive  $Q_{\text{f}}$ , with better results being obtained for positive charge since  $\sigma_{\text{ns}} > \sigma_{\text{ps}}$ . However, as the corona charge is unstable and dissipates with time, this method has not been utilised for industrial solar cells. Recently, Bonilla *et al.* [259] proposed a technique to stabilise the corona charge by a chemical treatment. SRV below 7 cm/s for three years with a decay time constant of 8.7 years has been demonstrated [259]. However, the stability of the charge has not been studied under realistic solar cell operating temperatures.

Despite numerous studies of the Si-SiO<sub>2</sub> interface, most of them provide information only at STC. As discussed in Chapter 3 and Chapter 4, it is increasingly necessary to characterise solar cells at various temperatures, as temperature critically impacts the electrical properties of solar cells. Therefore, the following sections investigate the recombination at the Si-SiO<sub>2</sub> interface under a wide range of variables, including temperature,  $\Delta n$ , and  $Q_{\text{f}}$ . Moreover, the stability of hydrogen passivation and corona charge at high operating temperatures are evaluated. A method to model and extract the interface defect parameters from temperature- and injection-dependent lifetime data is presented.

## 6.2 Method

### 6.2.1 Sample Preparation

Phosphorus (P)-doped, 4-inch *n*-type float zone (FZ) Si wafers (planar surfaces, crystal orientation [100]) with a resistivity of  $1 \pm 0.1 \text{ } \Omega \cdot \text{cm}$  and thickness of  $200 \pm 10 \text{ } \mu\text{m}$  are used in this chapter to fabricate symmetric lifetime structures. All wafers underwent Radio Corporation of America cleaning before thermal dry oxidation at  $1050 \text{ } ^\circ\text{C}$  (oxidation time: 80 minutes), producing 100 nm thick  $\text{SiO}_2$  on both sides. A subset of the wafers received

a forming gas (5% H<sub>2</sub> diluted in 95% N<sub>2</sub>) anneal (FGA) at 425 °C for 25 minutes. Chemical treatment was then used to produce a hydrophobic SiO<sub>2</sub> surface and stabilise the corona charge as reported in [259, 260]. Each wafer was then cleaved into four tokens. Corona charge was deposited using a custom-built corona discharge setup [259] on three tokens from each wafer (from both FGA and non-FGA groups) with charging time (CT) of 10, 20, and 40 sec. The corona rig has a point-to-plane configuration, with a single point electrode held at 30 kV placed at 20 cm above the sample.

This unique set of samples allows a more comprehensive understanding of the impacts of  $D_{it}$  (varied via FGA) and  $Q_f$  (varied via corona charge deposition) on the temperature- and injection-dependent electrical properties of Si-SiO<sub>2</sub> interfaces. Moreover, having a fixed bulk quality while varying  $D_{it}$  and  $Q_f$  allows the validation of the proposed method for extracting interface defect parameters. It should be noted that the bulk defects reported in [261], that may exist in high-quality FZ wafers, were eliminated by the thermal oxidation process.

### 6.2.2 Characterisation Setup

A modified lifetime tester based on the *Sinton WCT-120* instrument [47] is used in this chapter. In particular, a cryostat is used to vary the sample temperature in the range of 223 K to 473 K. The system is equipped with two different light sources: a Xenon flash and an 810 nm LED to allow lifetime measurements under a wide injection level range. The PC-based injection dependent  $\tau_{eff}$  is measured using both QSS and transient modes in the temperature range from 223 K to 473 K. The generation rate is calibrated by comparing the QSS and transient measurements at each temperature. The temperature-dependent carrier mobility model of Klaassen *et al.* [262] is used to calculate  $\Delta n$ .

### 6.2.3 Modelling

To gain insights into the recombination mechanisms at the Si-SiO<sub>2</sub> interface under different operating conditions, a modelling method is presented to determine the electrical characteristics of the interface via temperature- and injection-dependent lifetime data [263]. The method is based on previous frameworks [254, 255, 264] and has been extended to take the temperature dependence into consideration.

As discussed in Chapter 2, the experimentally obtained  $\tau_{eff}$  quantifies the recombination occurring simultaneously within the bulk and at the surfaces. It is

challenging to obtain  $\tau_{\text{SRH bulk}}$  and  $\tau_s$  individually from the measured  $\tau_{\text{eff}}$ . As shown in Section 6.3.1, comparing the same wafers with and without corona charge allows confirming that  $\tau_{\text{eff}}$  of the non-charged samples is dominated by the surface recombination (bulk lifetime  $\tau_{\text{bulk}}$  of the used wafers is above 3 ms). Hence, for the uncharged samples, it can be assumed that (with a relative error  $< 2\%$  for the non-FGA wafers and  $< 6\%$  for the FGA wafers):

$$\frac{1}{\tau_{\text{eff}}} \approx \frac{1}{\tau_s} + \frac{1}{\tau_{\text{Auger}}} + \frac{1}{\tau_{\text{rad}}} \quad 6.1$$

To extract the interface parameters,  $\tau_s$  are fitted using the SRH recombination model introduced by Grove and Fitzgerald [265] and later improved by Girisch *et al.* [255], Aberle *et al.* [254], and Bonilla *et al.* [264]. Recombination at the surface is described by a distribution of interface states:

$$U_s = \int_{E_v}^{E_c} \frac{(n_s p_s - n_i^2)}{\frac{[n_s + n_1(E)]}{v_{\text{thp}} D_{\text{it}}(E) \sigma_{\text{ps}}} + \frac{[p_s + p_1(E)]}{v_{\text{thn}} D_{\text{it}}(E) \sigma_{\text{ns}}}} dE \quad 6.2$$

$$n_1 = n_i e^{\frac{E_t - E_i}{k_B T}}, \quad p_1 = n_i e^{\frac{E_i - E_t}{k_B T}} \quad 6.3$$

$$n_s = (n_0 + \Delta n) e^{\frac{q \Psi_s}{k_B T}}, \quad p_s = (p_0 + \Delta n) e^{-\frac{q \Psi_s}{k_B T}} \quad 6.4$$

where  $\Psi_s$  denotes is the surface potential.  $E_c$  and  $E_v$  are the conduction and valence band edge. The thermal velocity is calculated based on Reference [112]. The intrinsic carrier concentration is calculated using Reference [116].

The exact solution of  $\Psi_s$  requires solving the Poisson and continuity equations for the electrons and holes dynamics imposed by the surface properties and the operating conditions [18]. In this chapter, an iterative approach proposed by Girisch *et al.* [255] is used to solve  $\Psi_s$  for any combination of  $\Delta n$ ,  $D_{\text{it}}$ ,  $Q_f$ ,  $\sigma_{\text{ns}}$  and  $\sigma_{\text{ps}}$ , assuming constant quasi-fermi energy levels throughout the surface space charge region. This approach is based on charge neutrality:

$$Q_{\text{Si}} + Q_{\text{it}} + Q_f + Q_g = 0 \quad 6.5$$

where  $Q_{\text{Si}}$  is the charge induced in the Si (see Equation 6.6),  $Q_{\text{it}}$  is the charge in the surface defect states (see Equation 6.7),  $Q_{\text{f}}$  is the fixed charge in the dielectric layer, and  $Q_{\text{g}}$  is the charge induced in the gate electrode (not relevant for this chapter).

$$Q_{\text{Si}} = -(2kTn_i\epsilon_0\epsilon_{\text{Si}})^{\frac{1}{2}} \left( e^{\frac{q}{k_{\text{B}}T}(\phi_{\text{p}} - \psi_{\text{s}})} - e^{\frac{q}{k_{\text{B}}T}\phi_{\text{p}}} + e^{\frac{q}{k_{\text{B}}T}(\psi_{\text{s}} - \phi_{\text{n}})} - e^{-\frac{q}{k_{\text{B}}T}\phi_{\text{n}}} + \frac{q}{k_{\text{B}}T} \psi_{\text{s}} \left( \frac{N_{\text{a}} - N_{\text{d}}}{n_{\text{i}}} \right) \right)^{\frac{1}{2}} \quad 6.6$$

where  $\epsilon_0$  is the vacuum permittivity,  $\epsilon_{\text{Si}}$  is the relative permittivity of Si,  $\phi_{\text{n}}$  ( $\phi_{\text{p}}$ ) is the quasi-Fermi potentials for electrons (holes), and  $N_{\text{a}}$  ( $N_{\text{d}}$ ) is acceptor (donor) concentration.

$$Q_{\text{it}} = q \int_{E_{\text{V}}}^{E_{\text{n}}} D_{\text{it,d}}(E) f_{\text{d}}(E) dE - q \int_{E_{\text{n}}}^{E_{\text{C}}} D_{\text{it,a}}(E) (1 - f_{\text{d}}(E)) dE \quad 6.7$$

$$f_{\text{d}} = \frac{\sigma_{\text{ns}}n_1 + \sigma_{\text{ps}}p_{\text{s}}}{\sigma_{\text{ns}}(n_{\text{s}} + n_1) + \sigma_{\text{ps}}(p_{\text{s}} + p_1)} \quad 6.8$$

where  $f_{\text{d}}$  is the trap occupation probability in donor states, and  $D_{\text{it,d}}$  ( $D_{\text{it,a}}$ ) is the density of the donor-like (acceptor-like) states. A neutral energy level  $E_{\text{n}}$  ( $E_{\text{n}} = E_{\text{g}}/2$ ) is used to separate acceptor-like and donor-like traps in the band-gap, as suggested in References [31, 264]. Here  $D_{\text{it}}$  is assumed to be temperature-independent but energy-dependent, as the band tail states are critical for determining the surface potential [266]. The energy dependence is described by [264]:

$$D_{\text{it}}(E) = D_{\text{it\_mg}} + D_{\text{it\_C}} e^{m_{\text{C}}E + E_{0\text{C}}} + D_{\text{it\_V}} e^{m_{\text{V}}E + E_{0\text{V}}} \quad 6.9$$

where  $D_{\text{it\_mg}}$  is the density of states at the middle of the bandgap,  $m_{\text{C}}$  ( $m_{\text{V}}$ ) and  $E_{0\text{C}}$  ( $E_{0\text{V}}$ ) determine the rate that the tail of states approaches  $D_{\text{it\_C}}$  ( $D_{\text{it\_V}}$ ) at the conduction (valence) band edge.

Energy-independent capture cross-sections are assumed since: (a) it has been demonstrated that the capture cross-sections are only weakly dependent on the energy [245, 267, 268], (b) Bonilla *et al.* [264] shows that the surface recombination is insensitive to the energy dependence of the surface recombination velocity of electrons and holes ( $S_{\text{n0}} = v_{\text{thn}}D_{\text{it}}\sigma_{\text{ns}}$  and  $S_{\text{p0}} = v_{\text{thp}}D_{\text{it}}\sigma_{\text{ps}}$ ), particularly when most of the recombination activity is mediated by deep-level defects, and (c) previous studies have demonstrated

that it is not required to include the energy dependence of the capture cross-sections into the model [269, 270].

The capture cross-sections' temperature dependence is considered using [271]:

$$\sigma_{ns/ps} = \sigma_{n_{s0}/p_{s0}} e^{-\frac{E_{\infty}}{k_B T}} \quad 6.10$$

where  $\sigma_{n_{s0}}$  ( $\sigma_{p_{s0}}$ ) are the temperature-independent pre-factors of the capture cross-section of electron (hole) and  $E_{\infty}$  is the thermal barrier that a free electron in the conduction band must overcome to be captured by the defect level. This temperature dependence is further discussed in Section 6.3.3.

The intrinsic lifetime parameterisation proposed by Richter *et al.* [42] is used, while the radiative recombination coefficient is taken from [22, 27]. Note that the temperature dependence of all the parameters in the intrinsic lifetime model [42] has been considered in this chapter, except for the temperature dependence of the Auger coefficients. Although Wang and MacDonald [38] have evaluated the ambipolar Auger coefficient at different temperatures (243–473 K), their parameterisation is valid only for the very high  $\Delta n$  of  $5 \times 10^{16} \text{ cm}^{-3}$  and is not suitable for the samples investigated here. Since temperature-independent Auger coefficients are assumed, the discrepancy is expected to be larger at a high  $\Delta n$  range.

The fit quality is evaluated using the residual:

$$Residual = \sum_{m=1}^m \sum_{j=1}^j \left( 1 - \frac{\tau_{\text{fitted},m,j}}{\tau_{\text{measured},m,j}} \right)^2, \quad \tau_{m,j} = \tau(\Delta n_m, T_j) \quad 6.11$$

where  $\tau_{\text{fitted}}$  is obtained from the discussed fitting procedure and  $\tau_{\text{measured}}$  is the experimentally obtained  $\tau_{\text{eff}}$ . The number of measured temperatures is represented by  $j$ , while  $m$  is the number of  $\Delta n$  points where the fit is evaluated.

Inspired by the defect parameter solution surface (DPSS) procedure [46], the values of  $\sigma_{n_{s0}}$  and  $Q_f$  are fixed, while the other parameters ( $\sigma_{p_{s0}}$ ,  $E_{\infty}$ ,  $D_{it\_mg}$ ,  $D_{it\_c}$ ,  $D_{it\_v}$ ) are fitted and the fit quality is recorded. By sweeping  $\sigma_{n_{s0}}$  and  $Q_f$  across the expected range of values and repeating the fitting, parameter sets that provide low fitting residuals are identified (see Figure 6.7). This procedure provides not only the interface defect parameters, but also the associated uncertainty by calculating the standard deviation of

all the fitting parameter sets that provide relatively good fits and low residual values ( $< 0.9$ ).

For corona-charged wafers, the assumption that  $\tau_{\text{eff}}$  is dominated by the surface recombination is no longer valid. The temperature- and injection-dependent  $\tau_{\text{SRH bulk}}$  impacts  $\tau_{\text{eff}}$ , especially when  $\tau_s$  is large (as for highly charged dielectrics). To eliminate the impact of  $\tau_{\text{SRH bulk}}$ , the lifetime difference ( $\Delta\tau_{\text{charge}}$ ) between charged and uncharged wafers is calculated:

$$\Delta\tau_{\text{charge}} = \frac{1}{\frac{1}{\tau_{\text{uncharged}}} - \frac{1}{\tau_{\text{charged}}}} \quad 6.12$$

where  $\tau_{\text{uncharged}}$  ( $\tau_{\text{charged}}$ ) is the measured lifetime of the uncharged (charged) wafer interpolated to the same  $\Delta n$ . Here, it is assumed that  $\Delta\tau_{\text{charge}}$  represents variation in  $\tau_s$  due to the increase of  $Q_f$ , while  $D_{\text{it}}$ ,  $\sigma_{\text{ns}}$ , and  $\sigma_{\text{ps}}$  are considered to remain unchanged during the corona charge deposition [260, 272]. Furthermore,  $\tau_{\text{SRH bulk}}$  of charged and uncharged samples are assumed to be identical, as these samples originate from the same wafer.  $\Delta\tau_{\text{charge}}$  is then fitted by the modelled  $\tau_s$  difference by varying  $Q_f$ .

In many cases, the decrease in recombination occurring at the Si-SiO<sub>2</sub> interface from corona charge reaches a plateau, in contradiction to theoretical expectations [258]. Glunz *et al.* [258] suggested surface potential fluctuations, originating from the inhomogeneous corona charge distribution, to explain this deviation between measurements and theory. Recently, Bonilla *et al.* [273] demonstrated that using a ‘charge fluctuations’ model rather than surface potential fluctuations provides a better fit. Although considered, spatial fluctuations of the surface charge (or potential) are not included in this chapter, due to: (a) both uncharged and charged samples having polished surfaces and demonstrating uniform PL images with relative deviation less than 5%; and (b) the sensed region (with a radius of 7 mm, see Figure 5.9) in the modified lifetime system being smaller than the standard system.

Note that accurate lifetime measurement is essential for determining accurate interface defect parameters. In this chapter, PC-based global lifetime measurements were conducted, as all the samples demonstrated uniform PL images. Moreover, these lifetime measurements are not affected by the wafer edges. The size of the wafers was selected such that the edges are at least three diffusion lengths long (considering the maximum

estimated diffusion length) from the PC coil sensing area (of a radius of 7 mm). For samples with a non-uniform lifetime distribution, the lifetime measurement method introduced in Chapter 5 is recommended, particularly for high-quality samples that have a large diffusion length.

## 6.3 Results and Discussion

### 6.3.1 Temperature- and Injection-Dependent Lifetime Measurements

Figure 6.1 shows temperature- and injection-dependent  $\tau_{\text{eff}}$  measurements of five representative wafers passivated with: (a)  $\text{SiO}_2$ ; (b)  $\text{SiO}_2 + \text{FGA}$ ; (c)  $\text{SiO}_2 + \text{FGA} + \text{corona charge (10 sec CT)}$ ; (d)  $\text{SiO}_2 + \text{FGA} + \text{corona charge (20 sec CT)}$ ; and (e)  $\text{SiO}_2 + \text{FGA} + \text{corona charge (40 sec CT)}$ , acquired as the temperature increases from 223 K to 473 K. Two methods are used for the presentation of  $\tau_{\text{eff}}$ : different ranges of the  $z$ -axis are used to optimise the display of each figure, while the same colour scale is used to demonstrate the different values. Across the entire temperature range,  $\tau_{\text{eff}}$  of the wafer passivated with  $\text{SiO}_2 + \text{FGA}$  is higher than  $\tau_{\text{eff}}$  of the wafer passivated with only  $\text{SiO}_2$ . As FGA leads to hydrogen passivation of the interface dangling Si bonds,  $D_{\text{it}}$  is expected to be reduced after this process [18].

The effectiveness of the corona charge for improving the passivation quality of  $\text{SiO}_2$  is clearly demonstrated in Figure 6.1(c)–(e). A significant increase of  $\tau_{\text{eff}}$ , by more than one order of magnitude, is observed after the corona charge deposition. An outstanding  $\tau_{\text{eff}}$  above 4 ms at  $\Delta n$  of  $1 \times 10^{15} \text{ cm}^{-3}$  (at room temperature) is achieved after 40 sec of corona charging. The improvement due to the additional charge is more visible at low  $\Delta n$  as  $\tau_{\text{eff}}$  at higher  $\Delta n$  is dominated by Auger recombination.

As illustrated in Figure 6.1(a) and (b), wafers without corona charge show a complex temperature dependence. At low temperature ranges (223–303 K),  $\tau_{\text{eff}}$  is found to decrease with increasing temperature at medium-to-high  $\Delta n$ , whereas the opposite trend is observed at low  $\Delta n$ . At higher temperatures (303–473 K),  $\tau_{\text{eff}}$  increases with increasing temperature for the entire  $\Delta n$  range. However, it is noticeable that  $\tau_{\text{eff}}$  of the wafer passivated with  $\text{SiO}_2 + \text{FGA}$  drops at temperatures above 373 K, as indicated by an arrow in Figure 6.1(b). This is likely due to  $\tau_s$  degradation at high temperatures, particularly due to the instability of the interface hydrogen passivation. This is evidenced by the reduction of  $\tau_{\text{eff}}$  remeasured at 303 K after the high-temperature measurements, shown in

Figure 6.2(b). The thermal instability of the Si-H bonds has also been reported by others [274]. Note that no variation of  $\tau_{\text{eff}}$  occurs after the completion of the temperature scan of the SiO<sub>2</sub>-only passivated wafer [see Figure 6.2(a)], indicating that the observed change in the FGA-passivated sample is not due to the loss of  $Q_f$  or bulk degradation (further discussed in Section 6.3.2).

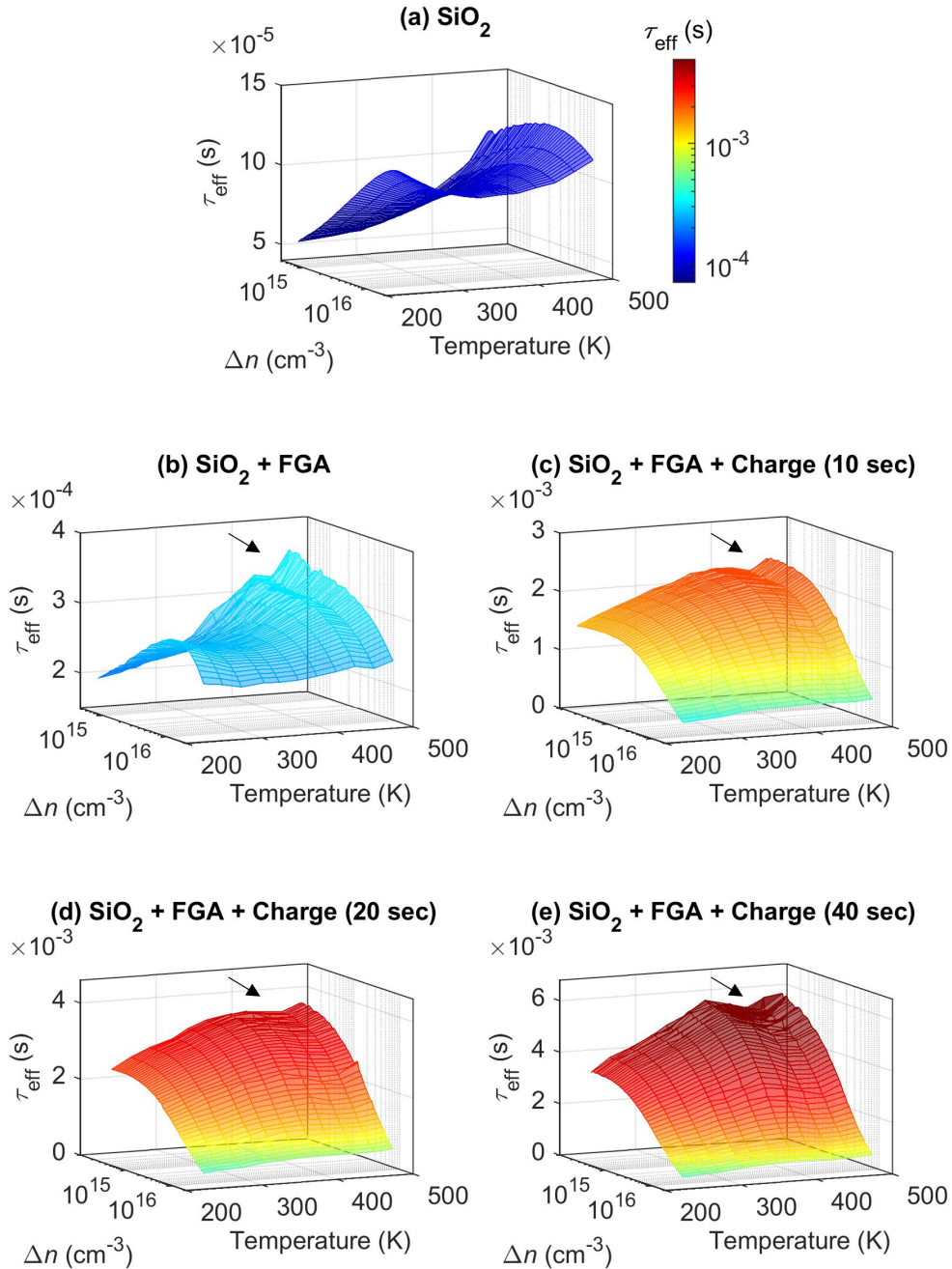


Figure 6.1 Temperature- and injection-dependent  $\tau_{\text{eff}}$  for *n*-type Si wafers passivated with: (a) SiO<sub>2</sub>; (b) SiO<sub>2</sub> + FGA; (c) SiO<sub>2</sub> + FGA + corona charge (10 sec CT); (d) SiO<sub>2</sub> + FGA + corona charge (20 sec CT); and (e) SiO<sub>2</sub> + FGA + corona charge (40 sec CT).

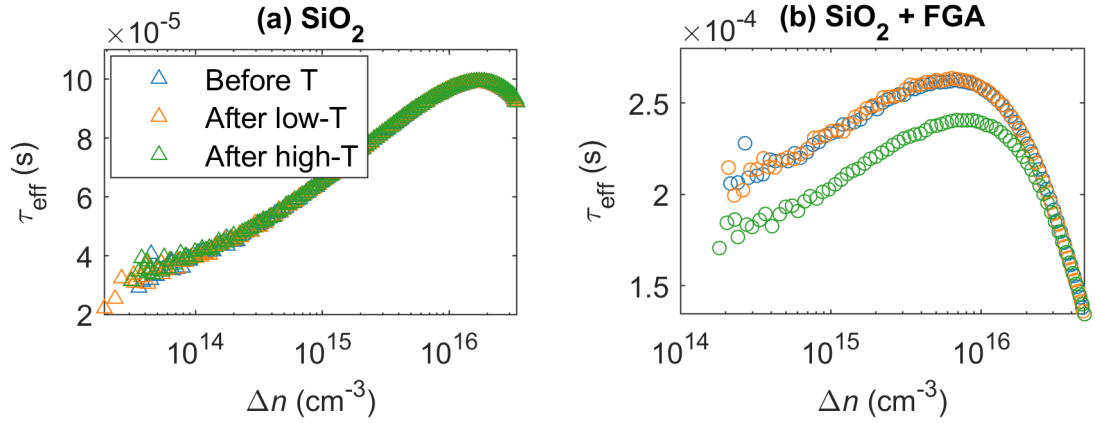


Figure 6.2  $\tau_{\text{eff}}$  at 303 K for  $n$ -type Si wafers passivated with: (a)  $\text{SiO}_2$ ; and (b)  $\text{SiO}_2 + \text{FGA}$ , measured before temperature-dependent measurements, after low temperature range measurements, and after high temperature range measurements.

In contrast to the uncharged wafers, all the corona-charged wafers show a consistent temperature behaviour for low-to-moderate temperatures, where  $\tau_{\text{eff}}$  is found to improve with increasing temperature for the entire  $\Delta n$  range. This temperature dependence appears to be much stronger at low  $\Delta n$ . However, the change of  $\tau_{\text{eff}}$  is not monotonic at higher temperatures, where a ‘valley’ (indicated by arrows) is observed in Figure 6.1(c)–(e). This can be assigned to the degradation of the interface hydrogen passivation, as discussed before, as well as the leakage of corona charge at high temperatures, as discussed in Section 6.3.2. Since the hydrogen-induced passivation degrades and corona charge leaks at high temperatures,  $\tau_{\text{eff}}$  is expected to drop continuously with increasing temperature. However, it is interesting to note that  $\tau_{\text{eff}}$  recovers and then peaks at the highest measured temperature of 473 K in Figure 6.1(b)–(e). This could be explained by a trade-off between the reduced recombination activity of the interface defects at higher temperatures, as discussed in Section 6.3.3, and the increase of  $D_{\text{it}}$  and reduction of  $Q_{\text{f}}$  at the same temperature range.

### 6.3.2 Stability of Hydrogen Passivation and Corona Charge at High Temperatures

In this section, the impact of high temperatures (323–423 K) on the  $\text{SiO}_2$  passivation quality is investigated. Wafers are dark annealed at different temperatures and monitored by in-situ lifetime measurements using a *Sinton WCT-120TS* lifetime tester. Figure 6.3 shows the normalised  $\tau_{\text{eff}}$  obtained at  $\Delta n$  of  $1 \times 10^{15} \text{ cm}^{-3}$  as a function of dark annealing duration at 373 K. The initial lifetime ( $\tau_0$ ) of each wafer at 373 K is given in the figure’s caption.

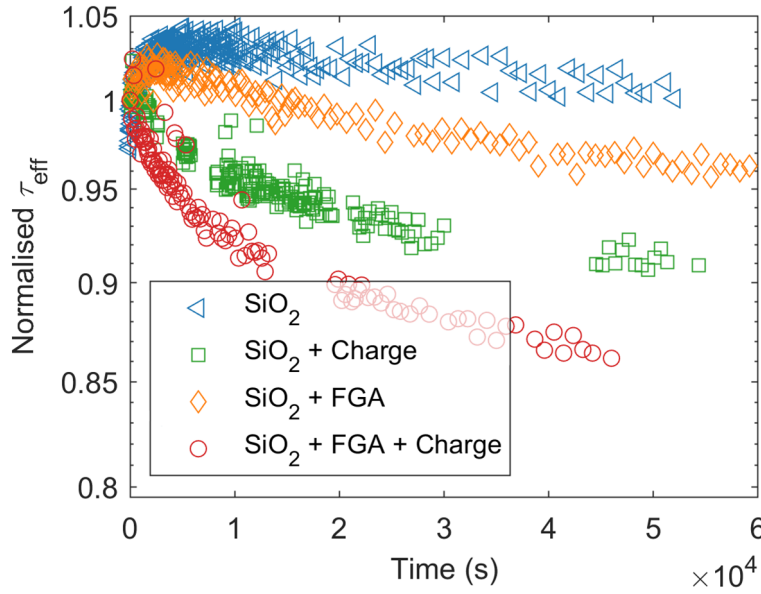


Figure 6.3 Evolution of  $\tau_{\text{eff}}$  as a function of the dark annealing (at 373 K) time for different wafers.  $\tau_0$  are  $78 \pm 3$ ,  $3150 \pm 126$ ,  $301 \pm 12$ , and  $5755 \pm 230$   $\mu\text{s}$  for wafers passivated with  $\text{SiO}_2$ ,  $\text{SiO}_2$  + charge (40 sec CT),  $\text{SiO}_2$  + FGA, and  $\text{SiO}_2$  + FGA + charge (40 sec CT), respectively.

As shown in Figure 6.3, no clear change in  $\tau_{\text{eff}}$  can be observed for the wafer passivated with only  $\text{SiO}_2$ , indicating that: (a) the intrinsic oxide charge is stable at these temperatures, and (b) no degradation in the chemical passivation quality (without FGA) occurs at high temperatures. Since  $\tau_{\text{eff}}$  of the wafer passivated with only  $\text{SiO}_2$  is limited by surface recombination, the bulk quality is then checked by comparing the lifetime of both annealed and un-annealed samples after a 40 sec deposition of corona charge. As shown in Figure 6.4, both annealed and un-annealed wafers passivated with  $\text{SiO}_2$  show identical lifetime before and after the 40 sec deposition of corona charge, confirming that the  $\tau_{\text{bulk}}$  does not degrade.

While examining the wafer that is passivated with  $\text{SiO}_2$  and corona charge (40 sec without FGA), a degradation is observed (in the range of 10%), see Figure 6.3, indicating a loss of charge at high temperatures. Worsening of the chemical passivation quality or the bulk quality is less likely as it has not been observed for the  $\text{SiO}_2$  passivated wafer.

A decrease of up to 5% of  $\tau_{\text{eff}}$  is observed during the dark annealing for the wafer passivated by  $\text{SiO}_2$  + FGA, as shown in Figure 6.3. This change of  $\tau_{\text{eff}}$  is due to the instability of hydrogen passivation at high temperatures that increases  $D_{\text{it}}$  and thus, enhances the surface recombination. It seems that the thermal instability of the corona charge at high temperatures has a stronger impact on the degradation compared to the

instability of the hydrogen passivation. As expected, the fastest degradation rate with the highest degradation extent is obtained for the wafer passivated with  $\text{SiO}_2$  + FGA + corona charge (40 sec), as it combines two instability mechanisms.

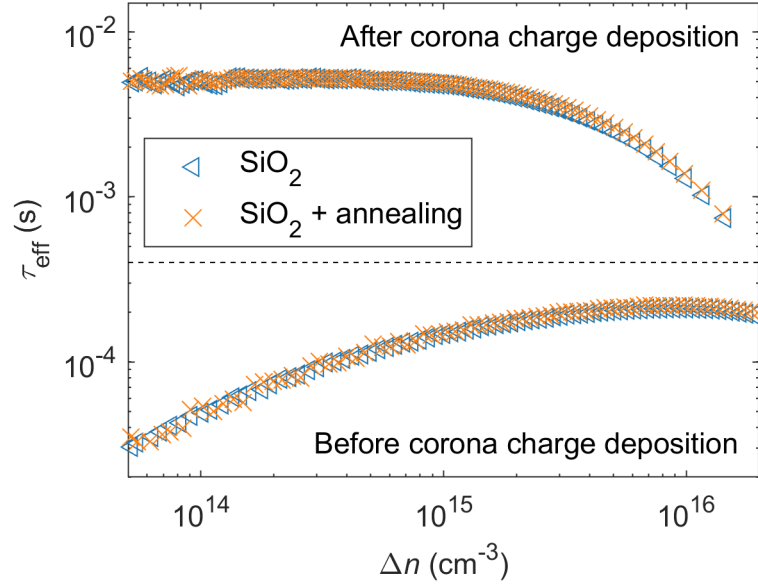


Figure 6.4  $\tau_{\text{eff}}$  as a function of  $\Delta n$  at 300 K of un-annealed and annealed wafers (annealing temperature 423 K) before and after depositing corona charges (40 sec CT).

Figure 6.5 displays the evolution of the normalised  $\tau_{\text{eff}}$ , extracted at  $\Delta n$  of  $1 \times 10^{15} \text{ cm}^{-3}$ , for identical wafers passivated with  $\text{SiO}_2$  + FGA + corona charge (40 sec) under dark annealing at different temperatures. The wafer had a  $\tau_{\text{eff}}$  of  $4300 \pm 243 \text{ } \mu\text{s}$  at 303 K. No significant degradation is observed at 323 K. The degradation extent is found to increase with increasing temperature. Moreover, the degradation rate shows a strong temperature dependence where a faster degradation rate is observed at high temperatures. This trend is observed on all the corona-charged wafers.

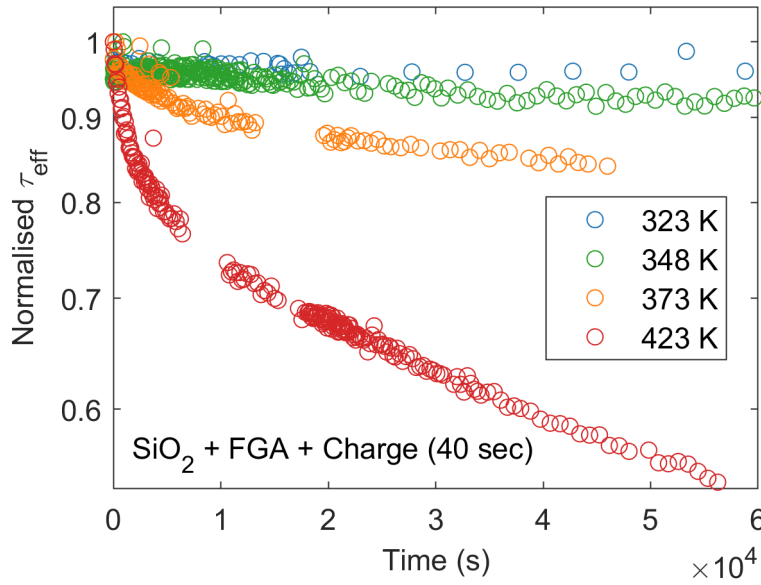


Figure 6.5 Evolution of  $\tau_{\text{eff}}$  for wafers passivated with  $\text{SiO}_2$  + FGA + corona charge (40 sec CT) under dark annealing at different temperatures.  $\tau_0$  are  $4303 \pm 172$ ,  $4627 \pm 185$ ,  $5755 \pm 230$ , and  $6188 \pm 247$   $\mu\text{s}$  at 323, 348, 373, and 423 K, respectively.

### 6.3.3 Modelling Lifetime Measurements

To extract the electrical parameters of the Si-SiO<sub>2</sub> interface defects, the temperature- and injection dependent lifetime measurements of the wafer passivated with only SiO<sub>2</sub> are fitted using the method introduced in Section 6.2.3. Figure 6.6 presents both measured and simulated temperature-dependent  $\tau_{\text{eff}}$ . The black error bars represent the measurement uncertainty calculated as the sum of the different uncertainties associated with lifetime measurements. For visibility reasons, the error bars are shown only for representative injection levels and one temperature.

The corresponding fitting residual map is shown in Figure 6.7. The residual is lower when both  $Q_f$  and  $\sigma_{n_{s0}}$  are low. The optimal fit can be identified by the lowest residual (marked by a red star with a residual of 0.3). Since multiple  $\tau_{\text{eff}}$  curves at different temperatures are fitted simultaneously to find the other four parameters for each combination of  $Q_f$  and  $\sigma_{n_{s0}}$ , the MATLAB global optimisation toolbox is used with 2000 different initial points generated for each free parameter:  $D_{\text{it\_mg}}$ ,  $D_{\text{it\_V}}$ ,  $D_{\text{it\_C}}$ ,  $\sigma_{p_{s0}}$ ,  $E_\infty$ . This procedure is assumed to reduce the risk of obtaining only a local minimum. Additionally, the fitting quality of all the parameter sets that provide relatively low residuals was visually inspected to confirm that the global minimum has been selected.

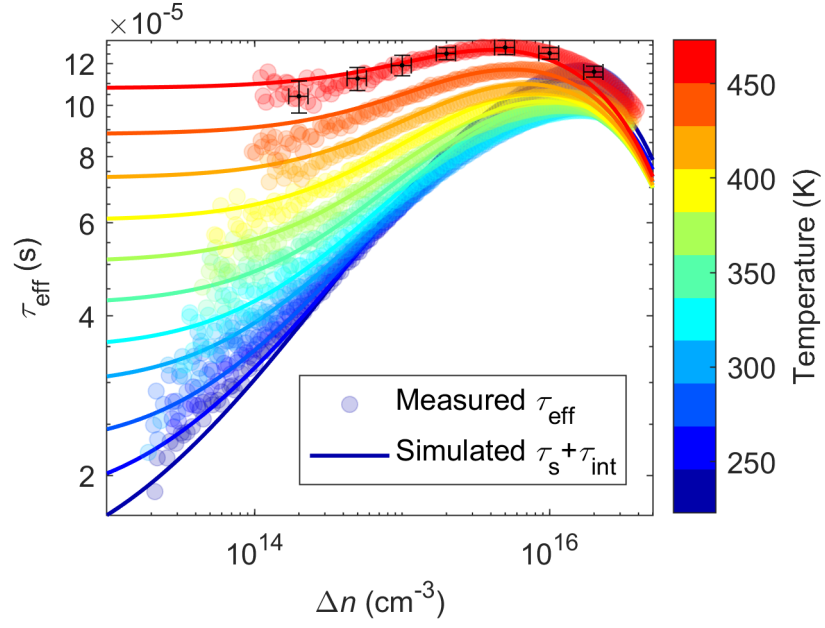


Figure 6.6 Measured (symbol) and simulated (solid line) temperature- and injection-dependent  $\tau_{\text{eff}}$  for wafers passivated with  $\text{SiO}_2$ .

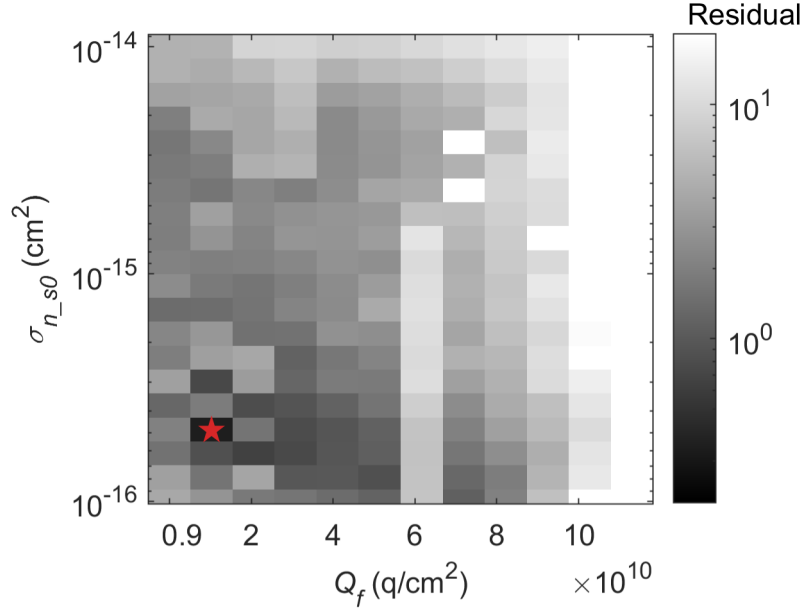


Figure 6.7 Fitting residual map obtained by fitting the temperature- and injection-dependent  $\tau_{\text{eff}}$  for the wafer passivated with only  $\text{SiO}_2$ . The red star indicates the minimum of this residual map.

From the fit, the Si-SiO<sub>2</sub> interface defect parameters are determined to be:  $Q_f = (1 \pm 0.5) \times 10^{10} \text{ q} \cdot \text{cm}^{-2}$ ,  $D_{\text{it\_mg}} = (1.3 \pm 0.2) \times 10^{11} \text{ cm}^{-2} \text{eV}^{-1}$ ,  $D_{\text{it\_V}} = (2.1 \pm 1.4) \times 10^{15} \text{ cm}^{-2} \text{eV}^{-1}$ ,  $D_{\text{it\_C}} = (2.6 \pm 1.8) \times 10^{15} \text{ cm}^{-2} \text{eV}^{-1}$ ,  $\sigma_{n\_s0} = (2 \pm 0.4) \times 10^{-16} \text{ cm}^2$ ,  $\sigma_{p\_s0} = (1 \pm 0.4) \times 10^{-16} \text{ cm}^2$  and  $E_\infty = (10 \pm 1) \text{ meV}$ .

The experimental data could not be satisfactorily reproduced if the temperature dependence of the capture cross-section is not considered. In this chapter, the lattice relaxation multi-phonon emission model [271] is used to describe the temperature dependence of  $\sigma_{ns}$  and  $\sigma_{ps}$ . A similar dependence has been suggested in the past for the interfaces of MOS devices [246, 268]. However, the determined values [ $\sigma_{n_{s0}} = (2 \pm 0.4) \times 10^{-16} \text{ cm}^2$  and  $E_{\infty} = (10 \pm 1) \text{ meV}$ ] are lower compared to the values obtained from DLTS measurements ( $\sigma_{n_{s0}} = 9 \times 10^{-14} \text{ cm}^2$  and  $E_{\infty} = 89 \text{ meV}$ ) of similar MOS devices [268]. The difference between the values can be explained by the different surface conditions, for example, the epitaxial Si wafers in Reference [268] compared to polished FZ wafers, or the oxide growth and post-oxidation annealing process. The finding regarding the temperature dependence of the capture cross-sections could also be relevant to other Si-SiO<sub>2</sub> interfaces, including tunnelling oxides used in state-of-the-art passivated contact devices. Despite different oxide growth conditions and post-growth annealing, previous studies reported similar Si-SiO<sub>2</sub> interface defect structural properties of thermally grown oxide, native oxide as well as oxides grown by wet chemistry [251, 275-277]. These findings may indicate that the fundamental temperature dependence can be similar for the same defect group, although the growth conditions are different.

At this stage, the same temperature dependence is assumed for both  $\sigma_{ps}$  and  $\sigma_{ns}$ . As these parameters are only rarely measured, this assumption cannot be confirmed, except for the good fit obtained. Further investigation is required to clarify this hypothesis.

To verify the model results,  $\tau_{\text{eff}}$  measurements of the wafer passivated with SiO<sub>2</sub> + FGA are fitted using the obtained set of interface parameters, modifying only  $D_{it}$  that is assumed to be changed by the FGA process. Since the hydrogen passivation is not stable at high temperatures as discussed in Section 6.3.2, the fits were done in the temperature range from 223 K to 323 K. No change of  $\tau_{\text{eff}}$  has been observed within this temperature range for the measurement duration. The good agreement between measurements and fitting, as shown in Figure 6.8, confirms previous conclusions and indicates that  $D_{it}$  is reduced to  $(4.5 \pm 1) \times 10^{10} \text{ cm}^2 \text{ eV}^{-1}$  for the middle of the bandgap [ $(7.0 \pm 1.4) \times 10^{14} \text{ cm}^2 \text{ eV}^{-1}$  for the valence band and  $(1.6 \pm 0.6) \times 10^{15} \text{ cm}^2 \text{ eV}^{-1}$  for the conduction band] after the FGA process. Note that these values are insensitive to the small variations in  $Q_f$ . The extracted parameters are still within the given uncertainty when  $Q_f$

varies by 30%. Moreover, the extracted  $D_{it}$  values are similar to previously reported values, as shown in Table 6-1.

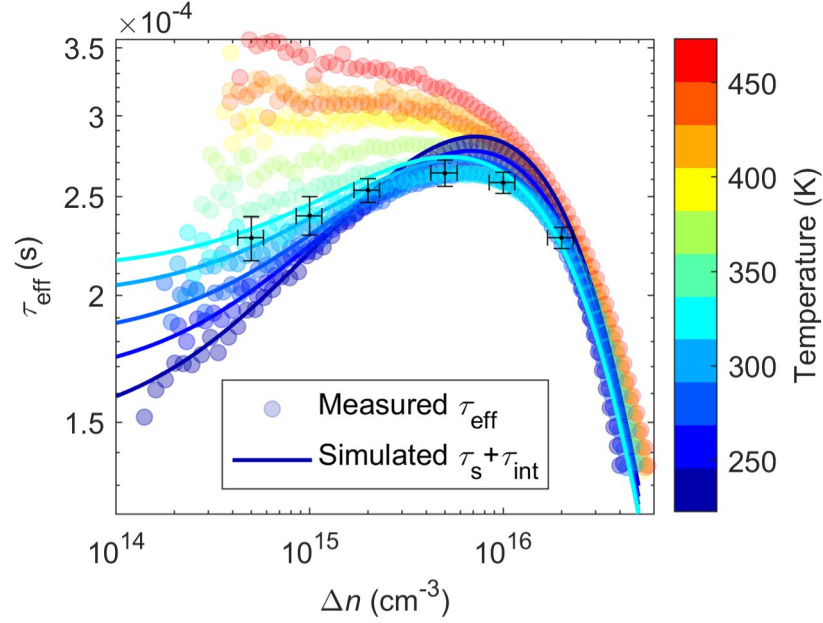


Figure 6.8 Measured (symbol) and simulated (line) temperature- and injection-dependent  $\tau_{eff}$  for wafers passivated with  $\text{SiO}_2 + \text{FGA}$ .

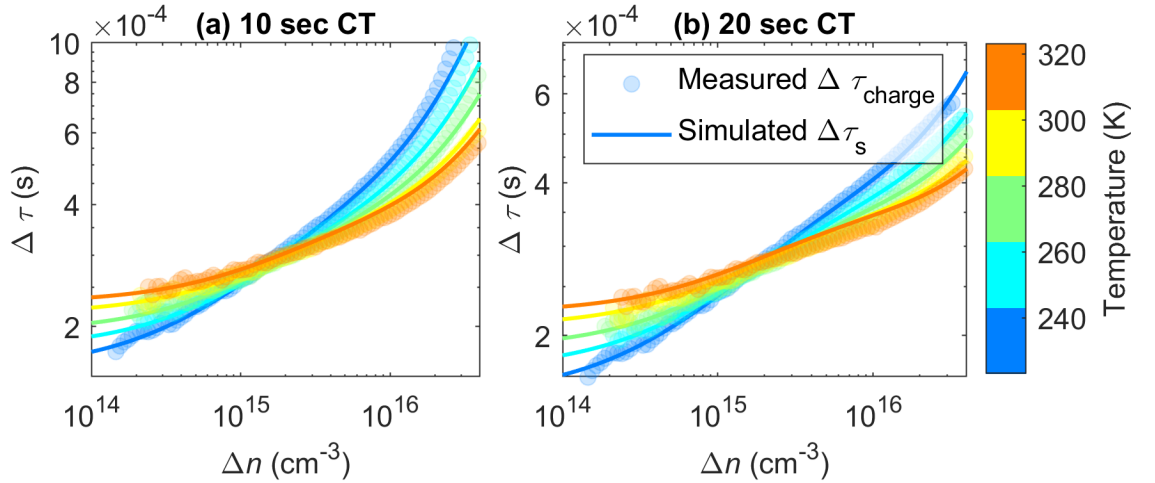


Figure 6.9 Measured (symbol) and fitted (line) lifetime difference between charge [ $\text{SiO}_2 + \text{FGA} + \text{Corona Charge}$ ] and uncharged [ $\text{SiO}_2 + \text{FGA}$ ] wafers.

These interface parameters are used to fit the FGA corona-charged wafers. As discussed in Section 6.2.3, for charged wafers  $\Delta\tau_{charge}$  is fitted to extract  $Q_f$ . All the other parameters are fixed and assumed to be similar to the  $\text{SiO}_2 + \text{FGA}$  wafers. Examples of the fitting results are given in Figure 6.9 for the wafers passivated with  $\text{SiO}_2 + \text{FGA} + \text{Corona Charge}$ : (a) 10 sec CT; and (b) 20 sec CT. As can be seen, a good fit is obtained

for the temperature range from 223 K to 323 K.  $Q_f$  are determined to be  $(2.8 \pm 0.1) \times 10^{11}$ ,  $(5.2 \pm 0.3) \times 10^{11}$ , and  $(1.2 \pm 0.2) \times 10^{12} \text{ q} \cdot \text{cm}^{-2}$  for 10, 20, 40 sec CT, respectively. These values agree well with the estimated charge deposition rate in the range of  $10^{11} \text{ q/sec}$ , as previously reported in [259, 278].

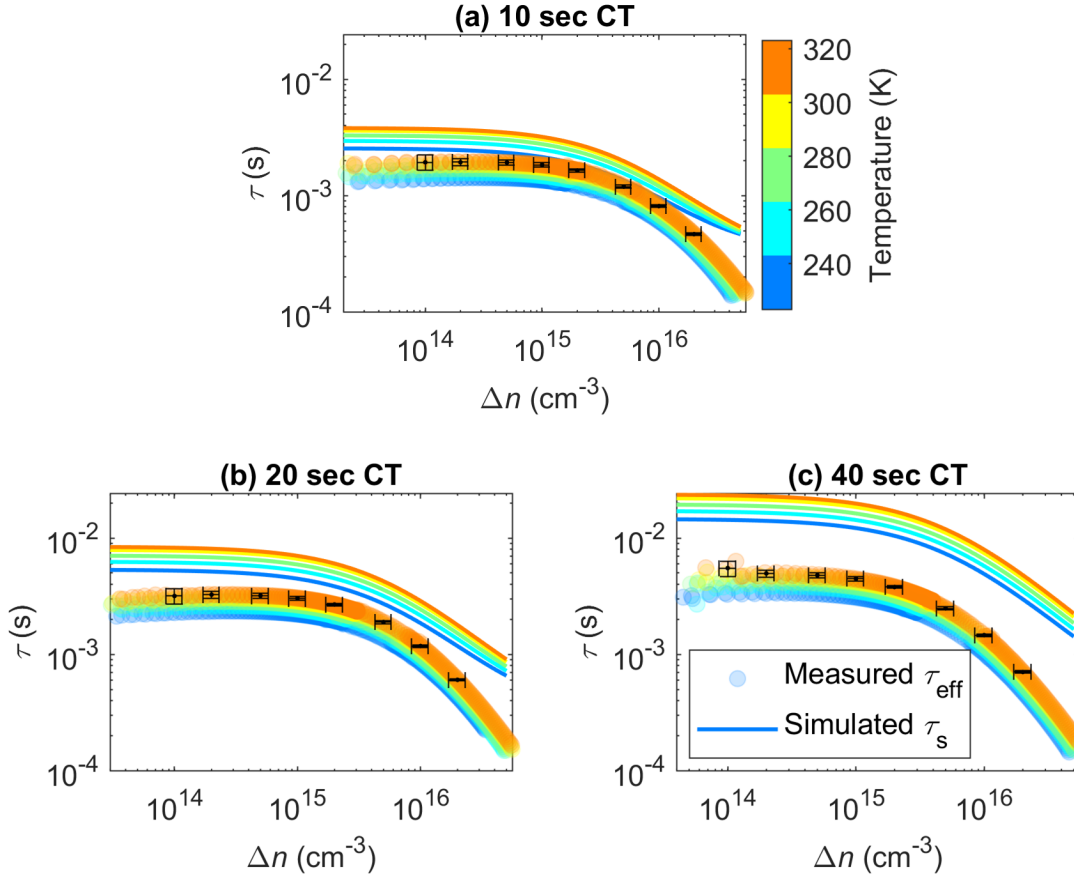


Figure 6.10 Measured (symbol)  $\tau_{\text{eff}}$  and simulated (line)  $\tau_s$  for corona charged wafers with CT: (a) 10 sec, (b) 20 sec; and (c) 40 sec.

Figure 6.10 compares the measured  $\tau_{\text{eff}}$  (symbol) and simulated  $\tau_s$  (line) based on the interface defect parameters obtained from the best fit for the charged wafers. It is interesting to note that  $\tau_s$  of the charged wafers increases with increasing temperature. Hence, the surface recombination decreases at higher temperatures, despite the increase of the capture-cross sections. This is due to the increasing surface potential with rising temperature, resulting in increased  $n_s$  and reduced  $p_s$  (see Equation 6.4). Therefore, the surface recombination is expected to be weaker at higher temperatures. It seems that this effect offsets the impact of the increased capture cross-sections. Moreover, this effect is more dominant when there is a strong band bending (larger  $\Psi_s$ ) due to a large  $Q_f$ , thus, the temperature-dependence of  $n_s$  and  $p_s$  are stronger. It is noticeable that the contribution

of the larger capture cross-sections with increasing temperatures to the overall surface recombination is relatively strong at the low-temperature range, for wafers with low  $Q_f$ .

The difference between  $\tau_{\text{eff}}$  and  $\tau_s$  (shown in Figure 6.10) is assumed to be  $\tau_{\text{bulk}}$ . Figure 6.11 presents  $\tau_{\text{bulk}}$  extracted by the inverse of  $(1/\text{measured } \tau_{\text{eff}} - 1/\text{simulated } \tau_s)$ . The good agreement between the extracted value, as indicated by the narrow distribution, confirms the proposed model as it appears the developed model provides a good fit for several wafers across a wide range of both  $\Delta n$  and temperature.

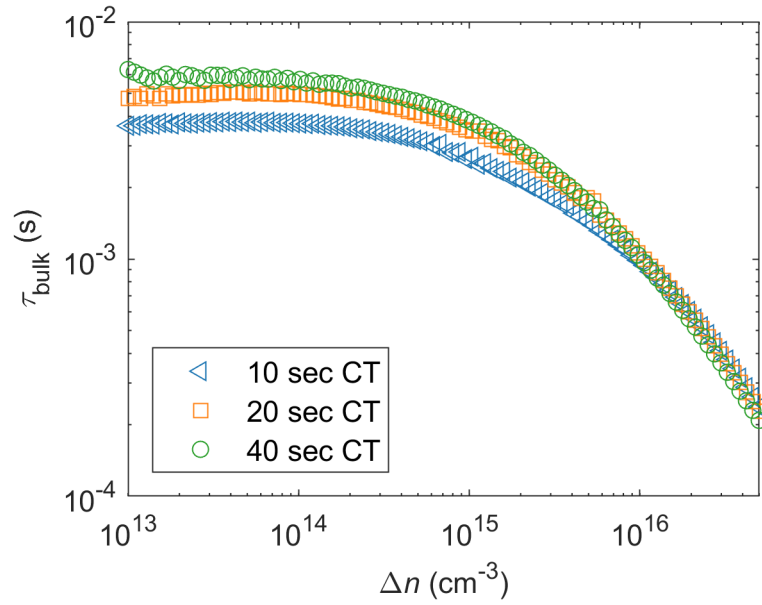


Figure 6.11 Extracted injection dependent  $\tau_{\text{bulk}}$  at 303 K for corona charged wafers with CT of 10, 20, and 40 sec.

Table 6-1 summarises the interface defect parameters obtained in this chapter and compares them to previously reported values. The attained  $Q_f$  is lower compared to other studies ( $6 \times 10^{10}$ – $3 \times 10^{11} \text{ q}\cdot\text{cm}^{-2}$ ). This could be due to the difference in the oxidation process. It has been suggested that  $Q_f$  reduces with increasing oxidation temperature [279]. The obtained  $D_{\text{it\_mg}}$  is within the reported range for cases with and without FGA treatment. It is important to note that  $D_{\text{it\_mg}}$  is impacted by the fabrication process, including the cleaning and the post oxidation steps. For example, the  $D_{\text{it\_mg}}$  reported by Aberle *et al.* [250] is much lower due to the additional post-metallisation annealing process.

The reported capture cross-sections from the literature have a wide range. Albohn *et al.* [275] found that the large  $\sigma_{\text{ns}}(E)$  can be assigned to the  $P_b$  centre, which originates from Si dangling bonds with three back-bonded silicon atoms, while the  $P_L$  defect that

originates from Si dangling bonds where one back-bond is substituted by oxygen, is commonly dominated by a lower  $\sigma_{\text{ns}}(E)$ . The determined values are within the expected range. Importantly, this method reduces the uncertainty range of extracting interface defect parameters and provides a temperature dependency that has not been reported previously.

Table 6-1 Interface defect parameters used to fit empirical data in this chapter (highlighted in grey) and parameters from previous reports.

	$Q_{\text{f}}$ ( $\text{q}\cdot\text{cm}^{-2}$ )	$D_{\text{it\_mg}}$ ( $\text{cm}^{-2}\text{eV}^{-1}$ )	$\sigma_{\text{ns}}$ ( $\text{cm}^2$ )	$k$ ( $\sigma_{\text{ns}}/\sigma_{\text{ps}}$ )
<i>n</i> -type + SiO <sub>2</sub>	$(1\pm0.5) \times 10^{10}$	$(1.3\pm0.2) \times 10^{11}$	$(1.4\pm0.4) \times 10^{-16}$ at 300 K	$2\pm0.4$
<sup>a</sup> <i>n</i> -type + SiO <sub>2</sub>	$2.2 \times 10^{11}$	$1 \times 10^{11}$	$8.7 \times 10^{-16}$	7.9
<sup>b</sup> <i>n</i> -type + SiO <sub>2</sub>	$(2.4\text{--}2.6) \times 10^{11}$	$1.2 \times 10^{11}$	$7.5 \times 10^{-15}$	2.3
<i>n</i> -type + SiO <sub>2</sub> + FGA	$(1\pm0.5) \times 10^{10}$	$(4.5\pm1) \times 10^{10}$	$(1.4\pm0.4) \times 10^{-16}$ at 300 K	$2\pm0.4$
<sup>a</sup> <i>n</i> -type + SiO <sub>2</sub> + FGA	$2.2 \times 10^{11}$	$5 \times 10^{10}$	$7.7 \times 10^{-16}$	13.4
<sup>b</sup> <i>p</i> -type + SiO <sub>2</sub> + FGA	$(2.7\text{--}3) \times 10^{11}$	$2.6 \times 10^{10}$	$1.5 \times 10^{-14}$	5.2
<sup>c</sup> SiO <sub>2</sub> + post-metallisation anneal	$(6\text{--}8) \times 10^{10}$	$(3\text{--}5) \times 10^9$	n/a	50–70
<sup>d</sup> <i>n</i> -type + P-doped poly-Si/SiO <sub>2</sub> /c-Si	$2.4 \times 10^{12}$	$1 \times 10^{11}$	$5 \times 10^{-15}$	1

<sup>a</sup>[273]: Room temperature PC decay measurements (the surface carrier population of Si wafer are controlled during measurement by using a semi-transparent PEDOT:PSS gate).

<sup>b</sup>[270]: Room temperature PL imaging with applied bias over the rear side passivation layer.

<sup>c</sup>[250]: DLTS and capacitance-voltage measurements on MOS samples.

<sup>d</sup>[280]: Room temperature PC decay measurements and capacitance-voltage measurements.

## 6.4 Chapter Summary

In this chapter, a comprehensive, non-destructive, and contactless method is presented to determine temperature- and injection-dependent surface recombination. It allows the extraction of  $Q_{\text{f}}$ ,  $D_{\text{it}}$ , capture cross-sections, and electron and hole surface recombination velocities without the need for DLTS or capacitance-voltage measurements that require complicated sample preparation. The method significantly reduces the uncertainty

associated with the extracted interface defect parameters since the fitting is performed on a large dataset taken at different temperatures and  $\Delta n$ .

To demonstrate this method, the characteristics of SiO<sub>2</sub> under different operating conditions were investigated (i.e., temperature,  $\Delta n$ , annealing, and corona charge). It has been concluded that the SiO<sub>2</sub> layer is expected to benefit from high operational temperatures due to increasing lifetime at temperatures above 303 K, possibly yielding some advantages to the overall device performance in the field and contributing to the superior temperature coefficients of high-efficiency devices that utilise SiO<sub>2</sub> passivation layers. Moreover, the Si-SiO<sub>2</sub> interface defect parameters were extracted.  $Q_f$  and  $D_{it\_mg}$ , are determined to be  $(1 \pm 0.5) \times 10^{10} \text{ q} \cdot \text{cm}^{-2}$  and  $(1.3 \pm 0.2) \times 10^{11} \text{ cm}^{-2} \text{ eV}^{-1}$ , respectively. FGA effectively reduces  $D_{it\_mg}$  to  $(4.5 \pm 1) \times 10^{10} \text{ cm}^{-2} \text{ eV}^{-1}$ . Importantly, the temperature-dependent capture cross-sections for electrons and holes were determined to be  $(2 \pm 0.4) \times 10^{-16} \exp[(-10 \pm 1) \times 10^{-3}/k_B T]$  and  $(1 \pm 0.4) \times 10^{-16} \exp[(-10 \pm 1) \times 10^{-3}/k_B T] \text{ cm}^2$ , respectively. The suggested lattice relaxation multi-phonon emission capture process has a relatively large impact on the surface passivation at the low-temperature range when a low amount of  $Q_f$  is present in the dielectric. However, for large  $Q_f$ , the temperature dependence of the surface recombination has been found to be strongly influenced by carrier concentration at the surface and by their temperature dependence.

With SiO<sub>2</sub> being used in commercial high-efficiency devices (i.e., polysilicon-based passivated contacts), such information is highly beneficial for improving the understanding of surface recombination in realistic operating conditions outside of STC, as well as temperature-dependent device modelling for predicting and optimising the field operation of solar cells. The proposed method can also be used in future work to study the temperature- and injection-dependent performance of other dielectrics commonly used in solar cell fabrication (e.g., SiN<sub>x</sub> and AlO<sub>x</sub>) and extract their interface defect parameters.



## Chapter 7

### Summary and Future Work

This thesis aims to improve the temperature- and injection-dependent characterisation of PV devices. In Chapter 3, a novel, non-destructive method for measuring the temperature-dependent  $iV_{OC}$  images of both metallised and non-metallised samples was developed. The advantages of the proposed method have been demonstrated by investigating  $TC(iV_{OC})$  of mc-Si (Chapter 3) and cast-mono Si (Chapter 4) wafers and cells. Using this method, it is feasible to intuitively examine the local temperature-dependent behaviours of regions with varying quality, and visually compare them at different ingot heights between different materials, and after different fabrication processes. This method further allows understanding and distinguishing the local versus global effects of the material-, defect-, and process-related factors on  $iV_{OC}$  and  $TC(iV_{OC})$  metrics, which cannot be inferred from global measurements (such as  $I-V$ ). Therefore, this method can lead to a more comprehensive understanding of different PV performances at various operating temperatures.

In Chapter 5, an advanced approach was introduced for accurately imaging the carrier lifetime of PV devices with non-uniformly distributed defects. Therefore, the actual local recombination activities, unaffected by the inherent presence of lateral carrier drift and diffusion within the sample, can be revealed. Since this approach can accurately measure the sample's lifetime distribution under spatially uniform  $\Delta n$ , at different operating temperatures, and different irradiance levels, it is an ideal quantitative characterisation technique for local defects in Si wafers and solar cells. This, for instance, enables a more accurate extraction of the recombination centre parameters across the sample.

In Chapter 6, an innovative analysis of temperature- and injection-dependent lifetime data was established to extract the surface recombination under different operating conditions, and, subsequently, determine the associated interface defect parameters. Such information can provide valuable insights into the electrical properties of the dielectric layer and associated interface recombination under realistic operating conditions.

Additionally, it helps to distinguish the impacts of surface and bulk recombination, which then benefits the separate investigation of the bulk defects via TIDLS and assessment of surface passivation quality, hence, enabling targeted improvement of PV devices' efficiency.

Overall, the work presented in this thesis contributes to the growing PV characterisation knowledge-base and builds a comprehensive understanding of PV electrical performance under different operating conditions. The original contributions in each chapter are detailed in the next section followed by the proposed future work.

## 7.1 Summary of Contributions

### Chapter 3 Spatially resolved temperature-dependent characterisation of Si wafers and cells:

- A contactless method was developed to spatially quantify the  $TC(iV_{OC})$  of Si wafers and cells under different operating conditions by combining temperature-dependent PL imaging and QSS PL front detection measurements. The primary advantages of this method include (a) enabling both local and global assessment of temperature-dependent  $iV_{OC}$ , (b) allowing measuring both metallised and non-metallised samples, and (c) being resilient to the effects of carrier trapping and DRM.
- The associated system for determining  $TC(iV_{OC})$  maps of Si wafers and cells was constructed. This system incorporated an 808 nm laser for optical excitation of the sample, a temperature-controlled stage for altering the sample's temperature, a Si CCD camera for acquiring PL images, and an InGaAs photodiode for detecting QSS PL signal.
- The temperature sensitivity of mc-Si wafers and cells from different ingot heights were investigated using the newly developed technique. A correction between reduced temperature sensitivity and the increasing ingot height is realised and demonstrated by both wafers and cells. Furthermore, the wafers from the top of the ingots show a larger spread of local  $TC(iV_{OC})$  towards less negative values which is particularly evident at a medium to low  $iV_{OC}$  range, likely due to the presence of less temperature-sensitive dislocation clusters.

- Dislocated areas on mc-Si wafers were found to have both high and low temperature sensitivity, depending partly on the ingot position.  $\mu$ PL measurements were performed at the dislocated regions with different TC values, which suggests that different impurities occupy these regions, thereby resulting in different TC values.

#### **Chapter 4 Impacts of gettering and hydrogenation on Si wafer temperature sensitivity:**

- The spatially resolved temperature-dependent electrical performance of cast-mono Si wafers was investigated after different processes such as gettering, firing, and advanced hydrogenation. The variations in  $TC(iV_{OC})$  in response to different processes cannot be simply explained by Si intrinsic parameters. It is also significantly affected by the temperature dependence of the recombination, as parameterised by  $\gamma$ . Gettering was found to lower  $\gamma$ , resulting in more favourable temperature sensitivity. However, the subsequent firing process does not have a significant impact on  $TC(iV_{OC})$ , due to a trade-off between improving  $iV_{OC}$  and increasing  $\gamma$ . Interestingly, performing an advanced hydrogenation process can further reduce the temperature sensitivity, more than expected solely from the improvement in  $iV_{OC}$ .
- Contrary to the commonly-held belief of more negative  $TC(iV_{OC})$  with lower  $iV_{OC}$ , most regions containing crystallographic defects have the lowest temperature sensitivity, following the processing steps. This suggested that although the crystallographic defects are the efficiency-limiting factor for cast-mono Si samples from the top of the ingot, their detrimental impact is reduced at higher operating temperatures. The lower temperature sensitivity of crystallographic defects was further investigated using hyperspectral PL imaging measurements and APT. It has been suggested that the reduced temperature sensitivity is due to impurities decorating the crystallographic defects. A significant excess of C, O, and Ni was detected at the regions containing crystallographic defects, suggesting that these impurities play important roles both in causing the recombination as well as the less negative  $TC(iV_{OC})$  at these regions.

**Chapter 5 Advanced PL imaging using non-uniform excitation:**

- A PL imaging method using spatially non-uniform excitation was developed. By adaptively adjusting the illumination intensity at each pixel to counterbalance the lateral carrier flows within the sample, PL images with uniform  $\Delta n$  can be obtained. The non-uniform carrier lifetime images can then be extracted from the spatial inverse of the illumination intensity. The required calibration procedure was introduced in detail as well.
- The first transmission-mode PL imaging system with a customised LCD-based laser illumination setup was built. This system was optimised to maximise the achievable illumination intensity and contrast at the sample plane and to minimise the optical aberrations of the illumination image. Furthermore, by modifying the configuration of the PL imaging system from transmission mode to reflectance mode, the capability of the developed technique has been further extended to enable temperature-dependent measurements.
- The proposed approach has been successfully applied to both inhomogeneous non-diffused and diffused Si samples to accurately extract the spatially non-uniform lifetime images. Compared with the conventional lifetime images obtained under uniform illumination, the proposed method can effectively remove artefacts introduced via lateral carrier drift and diffusion, and the associated image blurring. For the first time, it has been experimentally demonstrated that using non-uniform excitation at the pixel-to-pixel level is a powerful approach to eliminate the carrier smearing effect, hence providing more accurate lifetime images at spatially constant  $\Delta n$ .

**Chapter 6 Characterisation of the Si-SiO<sub>2</sub> interface under various operating conditions:**

- A comprehensive method was presented to determine temperature- and injection-dependent surface recombination, based on simultaneous fitting of multiple lifetime measurements. It allows the extraction of the interface defect parameters without the need for techniques such as DLTS or capacitance-voltage measurements that often involve complicated sample preparation steps. Importantly, the uncertainty associated with the extracted interface defect

parameters can be reduced with this method, as the fitting was performed on a large dataset obtained over a broad range of temperatures and  $\Delta n$ .

- To demonstrate this method, the electrical characteristics of SiO<sub>2</sub> were investigated, for the first time, considering a wide range of variables, including temperature,  $\Delta n$ , and  $Q_f$ . The defect parameters and the temperature dependence of the capture cross-sections associated with the Si-SiO<sub>2</sub> interface were determined with a thorough analysis. It has been concluded that improved SiO<sub>2</sub> surface passivation is expected at high operating temperatures, potentially yielding some benefits to the overall PV performance in the field.

In this thesis, the objectives established in Chapter 1 have been accomplished. The developed techniques allow for the characterisation of PV devices under various operating conditions. Furthermore, the spatially resolved feature of the developed methods is greatly beneficial considering the localised design of many PV devices such as selectively diffused emitters and local contacts as well as the non-uniformly distributed detrimental defects that they are often suffered from. Taken together, this thesis significantly contributes to a better understanding of the electrical properties of PV devices under different operating conditions and the identification of performance implications arising from specific device layers and defects. This is of paramount importance for improving PV device efficiencies and as a result, lowering the cost-per-watt. Particularly promising is the applications of the developed characterisation methods to evaluate and predict PV devices' field performance prior to deployment, providing a path for innovative device optimisation of specific operating conditions. Looking forward, in a wider perspective, the work presented in this thesis is expected to be immensely valuable for improving the energy conversion efficiency of PV technologies and promoting the growth of PV deployment.

## 7.2 Future Work

The several opportunities for further research resulting from this thesis are discussed below.

In Chapter 3, the proposed method was used for resolving TC( $iV_{oc}$ ) map at 0.5 Suns which is the maximum intensity achieved for 6-inch samples with the current system. By upgrading the illumination source, this system can also be used to investigate the

illumination intensity dependence of the spatially resolved TC( $iV_{OC}$ ). Moreover, this method can be extended to study the  $iV_{OC}$  images at low temperatures ( $< 298$  K). Also, it will be interesting to explore spatially resolved TC( $iV_{OC}$ ) at the module level, in which the effects of performance variation between different interconnected cells on the TC( $iV_{OC}$ ) can be evaluated. In addition, this spatially resolved TC concept can be extended to properly study non-Si-based devices.

A thorough investigation of low TC( $iV_{OC}$ ) at the regions containing crystallographic defects has been conducted in Chapter 4. However, there remains a few aspects that can be further improved. Although APT measurements presented in Chapter 4 helped to narrow down the candidates responsible for the low temperature sensitivity of regions containing crystallographic defects, it is necessary to conduct complementary APT measurements at different regions and after different fabrication processes to reduce the speculations. Moreover, using the lifetime imaging method proposed in Chapter 5, it can be useful to conduct a TIDLS study for the localised crystallographic defects, so to establish potential correlations with the APT results.

In Chapter 5, great effort has been made to develop and optimise the LCD-based laser illumination setup to achieve PL images at constant  $\Delta n$ . However, there are still some practical limitations of the setup, which were outlined in Chapter 5 together with suggestions for further improving the system. Meanwhile, this system can be used for spatially resolved IDLS or TIDLS studies of non-uniformly distributed bulk defects. It can also be applied to investigate edge recombination, which can severely affect half cells performance. Moreover, this technique can be extended to study large-area perovskite devices where process-induced defects may form.

In Chapter 6, a modelling approach was developed to investigate surface recombination under different operating conditions. While this approach was only demonstrated on the  $\text{SiO}_2$ , in the future, its applications can be extended to investigate other dielectric layers, such as  $\text{SiN}_x$ ,  $\text{AlO}_x$ , and amorphous Si. In addition, this concept can be extended to study the interfaces of non-Si-based technologies, such as perovskite solar cells.

## Appendix A

Based on the blue-shift (2–3 meV) of the defect PL peaks as the light intensity (carrier injection) is increased, the observed recombination mechanism can be identified as donor-acceptor pair recombination [152]. Using Reference [152], the donor-acceptor pair recombination rate ( $U_{\text{DAP}}$ ) for a  $p$ -type semiconductor can be expressed as:

$$U_{\text{DAP}} = \frac{pN_{\text{t}}C_{\text{p2}}t'}{\left(p + p'_{\frac{3}{2}}\right)C_{\text{p2}} + t'} \quad \text{A.1}$$

where  $C_{\text{p2}}$  is the capture probability of holes to the acceptors when the donor-acceptor is in the charge state of TWO,  $t'$  is the interlevel transition rate between donor and acceptor levels, and  $p'_{\frac{3}{2}}$  is a carrier density term containing the acceptor energy level.

Assuming  $\left(p + p'_{\frac{3}{2}}\right)C_{\text{p2}} \gg t'$ , Equation A.1 can be re-arranged as:

$$U_{\text{DAP}} = \frac{N_{\text{t}}t'}{\left(1 + \frac{p'_{\frac{3}{2}}}{p}\right)} \quad \text{A.2}$$

where  $p_{3/2}'$  is given by

$$p'_{\frac{3}{2}} = CT^{1.5}e^{-\frac{E_{\text{a}}}{k_{\text{B}}T}} \quad \text{A.3}$$

By combining Equations A.2 and A.3, Equation 3.4 is obtained and can be used to determine  $E_{\text{a}}$ .



## Reference

- [1] "Vital signs of the planet: Global climate change " <https://climate.nasa.gov/vital-signs/carbon-dioxide/> (accessed 2021/12).
- [2] D. Lüthi *et al.*, "High-resolution carbon dioxide concentration record 650,000–800,000 years before present," *Nature*, vol. 453, pp. 379-382, 2008.
- [3] "United States Environmental Protection Agency, Global greenhouse gas emissions data." <https://www.epa.gov/ghgemissions/global-greenhouse-gas-emissions-data> (accessed 2021/12).
- [4] R. Perez and M. Perez, "A fundamental look at supply side energy reserves for the planet," *The International Energy Agency SHC Programme Solar Update*, vol. 62, pp. 4-6, 2015.
- [5] M. Tao, H. Hamada, T. Druffel, J.-J. Lee, and K. Rajeshwar, "Review—Research needs for photovoltaics in the 21st century," *ECS J. Solid State Sci. Technol.*, vol. 9, pp. 125010, 2020.
- [6] "International energy agency: Data and statistics." <https://www.iea.org/data-and-statistics> (accessed 2021/12).
- [7] C. Breyer *et al.*, "On the role of solar photovoltaics in global energy transition scenarios," *Prog. Photovoltaics Res. Appl.*, vol. 25, pp. 727-745, 2017.
- [8] M. Haegel Nancy *et al.*, "Terawatt-scale photovoltaics: Transform global energy," *Science*, vol. 364, pp. 836-838, 2019.
- [9] "International technology roadmap for photovoltaic (ITRPV): 2020 Results," 2021.
- [10] M. A. Green, "How did solar cells get so cheap?," *Joule*, vol. 3, pp. 631-633, 2019.
- [11] "Lazard's levelized cost of energy analysis—version 14.0." <https://www.lazard.com/perspective/lcoe2020> (accessed 2021/12).
- [12] P. J. Verlinden, "Future challenges for photovoltaic manufacturing at the terawatt level," *J. Renew. Sustain. Energy*, vol. 12, pp. 053505, 2020.
- [13] G. M. Wilson *et al.*, "The 2020 photovoltaic technologies roadmap," *J. Phys. D: Appl. Phys.*, vol. 53, pp. 493001, 2020.
- [14] "Photovoltaic Devices—Part 1–10," IEC-60904, 2009.
- [15] O. Dupré, R. Vaillon, and M. A. Green, *Thermal behavior of photovoltaic devices*. Switzerland: Springer, 2017.
- [16] K. Kawajiri, T. Oozeki, and Y. Genchi, "Effect of temperature on PV potential in the world," *Environ. Sci. Technol.*, vol. 45, pp. 9030-9035, 2011.
- [17] M. A. Green, *Solar cells : operating principles, technology and system applications*. Englewood Cliffs: Prentice-Hall, 1992.
- [18] A. G. Aberle, *Crystalline silicon solar cells : advanced surface passivation and analysis*. Sydney: Centre for Photovoltaic Engineering, University of New South Wales, 1999.
- [19] P. Würfel and U. Würfel, *Physics of solar cells: From basic principles to advanced concepts*. Wiley, 2016.

- [20] Y. P. Varshni, "Band-to-band radiative recombination in groups IV, VI, and III-V semiconductors (I)," *Phys. Status Solidi B*, vol. 19, pp. 459-514, 1967.
- [21] P. Auger, "Sur les rayons  $\beta$  secondaires produits dans un gaz par des rayons X," *C.R.A.S.*, vol. 177, pp. 169-171, 1923.
- [22] P. P. Altermatt, F. Geelhaar, T. Trupke, X. Dai, A. Neisser, and E. Daub, "Injection dependence of spontaneous radiative recombination in c-Si: experiment, theoretical analysis, and simulation," in *5<sup>th</sup> International Conference on Numerical Simulation of Optoelectronic Devices*, pp. 47-48, 2005.
- [23] A. Fell, T. Niewelt, B. Steinhauser, F. D. Heinz, M. C. Schubert, and S. W. Glunz, "Radiative recombination in silicon photovoltaics: Modeling the influence of charge carrier densities and photon recycling," *Sol. Energy Mater. Sol. Cells*, vol. 230, pp. 111198, 2021.
- [24] W. Michaelis and M. H. Pilkuhn, "Radiative recombination in silicon p-n junctions," *Phys. Status Solidi B*, vol. 36, pp. 311-319, 1969.
- [25] H. T. Nguyen, S. C. Baker-Finch, and D. Macdonald, "Temperature dependence of the radiative recombination coefficient in crystalline silicon from spectral photoluminescence," *Appl. Phys. Lett.*, vol. 104, pp. 112105, 2014.
- [26] H. Schlangenotto, H. Maeder, and W. Gerlach, "Temperature dependence of the radiative recombination coefficient in silicon," *Phys. Status Solidi A*, vol. 21, pp. 357-367, 1974.
- [27] T. Trupke *et al.*, "Temperature dependence of the radiative recombination coefficient of intrinsic crystalline silicon," *J. Appl. Phys.*, vol. 94, pp. 4930-4937, 2003.
- [28] A. R. Beattie, P. T. Landsberg, and H. Fröhlich, "Auger effect in semiconductors," *Proc. R. Soc. Lond. A*, vol. 249, pp. 16-29, 1959.
- [29] A. R. Beattie, P. T. Landsberg, and H. Fröhlich, "One-dimensional overlap functions and their application to Auger recombination in semiconductors," *Proc. R. Soc. Lond. A*, vol. 258, pp. 486-495, 1960.
- [30] L. Huldt, "Band-to-band Auger recombination in indirect gap semiconductors," *Phys. Status Solidi A*, vol. 8, pp. 173-187, 1971.
- [31] S. M. Sze and K. K. Ng, *Physics of Semiconductor Devices*. New York: Wiley, 1981.
- [32] A. Hangleiter and R. Häcker, "Enhancement of band-to-band Auger recombination by electron-hole correlations," *Phys. Rev. Lett.*, vol. 65, pp. 215-218, 1990.
- [33] J. Dziewior and W. Schmid, "Auger coefficients for highly doped and highly excited silicon," *Appl. Phys. Lett.*, vol. 31, pp. 346-348, 1977.
- [34] P. P. Altermatt, J. Schmidt, G. Heiser, and A. G. Aberle, "Assessment and parameterisation of Coulomb-enhanced Auger recombination coefficients in lowly injected crystalline silicon," *J. Appl. Phys.*, vol. 82, pp. 4938-4944, 1997.
- [35] P. T. Landsberg, "Trap-Augur recombination in silicon of low carrier densities," *Appl. Phys. Lett.*, vol. 50, pp. 745-747, 1987.
- [36] D. B. Laks, G. F. Neumark, and S. T. Pantelides, "Accurate interband-Augur recombination rates in silicon," *Phys. Rev. B*, vol. 42, pp. 5176-5185, 1990.
- [37] M. Govoni, I. Marri, and S. Ossicini, "Augur recombination in Si and GaAs semiconductors: Ab initio results," *Phys. Rev. B*, vol. 84, pp. 075215, 2011.
- [38] S. Wang and D. Macdonald, "Temperature dependence of Augur recombination in highly injected crystalline silicon," *J. Appl. Phys.*, vol. 112, pp. 113708, 2012.
- [39] M. J. Kerr and A. Cuevas, "General parameterization of Augur recombination in crystalline silicon," *J. Appl. Phys.*, vol. 91, pp. 2473-2480, 2002.

- [40] B. A. Veith-Wolf, S. Schäfer, R. Brendel, and J. Schmidt, "Reassessment of intrinsic lifetime limit in n-type crystalline silicon and implication on maximum solar cell efficiency," *Sol. Energy Mater. Sol. Cells*, vol. 186, pp. 194-199, 2018.
- [41] T. Niewelt *et al.*, "Reassessment of the intrinsic bulk recombination in crystalline silicon," *Sol. Energy Mater. Sol. Cells*, vol. 235, pp. 111467, 2022.
- [42] A. Richter, S. W. Glunz, F. Werner, J. Schmidt, and A. Cuevas, "Improved quantitative description of Auger recombination in crystalline silicon," *Phys. Rev. B*, vol. 86, pp. 165202, 2012.
- [43] R. Lee Chin, "Applications of photoluminescence microscopy for probing bulk defects in silicon," PhD, University of New South Wales, Australia, 2020.
- [44] W. Shockley and W. T. Read, "Statistics of the recombinations of holes and electrons," *Phys. Rev.*, vol. 87, pp. 835-842, 1952.
- [45] R. N. Hall, "Electron-hole recombination in germanium," *Phys. Rev.*, vol. 87, pp. 387-387, 1952.
- [46] S. Rein, *Lifetime spectroscopy : A method of defect characterization in silicon for photovoltaic applications*. New York: Springer, 2005.
- [47] Y. Zhu, "Advanced characterization of defects in silicon wafers and solar cells," PhD, University of New South Wales, Australia, 2019.
- [48] C.-T. Sah and W. Shockley, "Electron-hole recombination statistics in semiconductors through flaws with many charge conditions," *Phys. Rev.*, vol. 109, pp. 1103-1115, 1958.
- [49] D. Macdonald and A. Cuevas, "Validity of simplified Shockley-Read-Hall statistics for modeling carrier lifetimes in crystalline silicon," *Phys. Rev. B*, vol. 67, pp. 075203, 2003.
- [50] J. D. Murphy, K. Bothe, R. Krain, V. V. Voronkov, and R. J. Falster, "Parameterisation of injection-dependent lifetime measurements in semiconductors in terms of Shockley-Read-Hall statistics: An application to oxide precipitates in silicon," *J. Appl. Phys*, vol. 111, pp. 113709, 2012.
- [51] A. G. Aberle, "Surface passivation of crystalline silicon solar cells: a review," *Prog. Photovoltaics Res. Appl.*, vol. 8, pp. 473-487, 2000.
- [52] A. Cuevas, T. Allen, J. Bullock, W. Yimao, Y. Di, and Z. Xinyu, "Skin care for healthy silicon solar cells," in *42<sup>nd</sup> IEEE Photovoltaic Specialist Conference (PVSC)*, pp. 1-6, 2015.
- [53] A. Cuevas and D. Yan, "Misconceptions and misnomers in solar cells," *IEEE J. Photovoltaics*, vol. 3, pp. 916-923, 2013.
- [54] E. Yablonovitch and T. Gmitter, "Auger recombination in silicon at low carrier densities," *Appl. Phys. Lett.*, vol. 49, pp. 587-589, 1986.
- [55] M. J. Kerr, "Surface, emitter and bulk recombination in silicon and development of silicon nitride passivated solar cells," PhD, Australian National University, Australia, 2002.
- [56] D. K. Schroder, *Semiconductor material and device characterization*. Wiley, 2005.
- [57] A. B. Sproul, "Dimensionless solution of the equation describing the effect of surface recombination on carrier decay in semiconductors," *J. Appl. Phys*, vol. 76, pp. 2851-2854, 1994.
- [58] H. Nagel, C. Berge, and A. G. Aberle, "Generalized analysis of quasi-steady-state and quasi-transient measurements of carrier lifetimes in semiconductors," *J. Appl. Phys*, vol. 86, pp. 6218-6221, 1999.
- [59] "Sinton Instruments WCT-120 photoconductance lifetime tester: User manual," 2011.

- [60] K. R. McIntosh and R. A. Sinton, "Uncertainty in photoconductance lifetime measurements that use an inductive-coil detector," in *23<sup>rd</sup> European Photovoltaic Solar Energy Conference*, pp. 77-82, 2008.
- [61] R. A. Sinton and A. Cuevas, "Contactless determination of current–voltage characteristics and minority-carrier lifetimes in semiconductors from quasi-steady-state photoconductance data," *Appl. Phys. Lett.*, vol. 69, pp. 2510-2512, 1996.
- [62] R. A. Sinton, A. Cuevas, and M. Stuckings, "Quasi-steady-state photoconductance, a new method for solar cell material and device characterization," in *25<sup>th</sup> IEEE Photovoltaic Specialists Conference*, pp. 457-460, 1996.
- [63] "Sinton Instruments." <https://www.sintoninstruments.com/> (accessed 2021/11).
- [64] J. Tan, D. Macdonald, F. Rougieux, and A. Cuevas, "Accurate measurement of the formation rate of iron–boron pairs in silicon," *Semicond. Sci. Technol.*, vol. 26, pp. 055019, 2011.
- [65] R. A. Bardos, T. Trupke, M. C. Schubert, and T. Roth, "Trapping artifacts in quasi-steady-state photoluminescence and photoconductance lifetime measurements on silicon wafers," *Appl. Phys. Lett.*, vol. 88, pp. 053504, 2006.
- [66] D. Macdonald and A. Cuevas, "Trapping of minority carriers in multicrystalline silicon," *Appl. Phys. Lett.*, vol. 74, pp. 1710-1712, 1999.
- [67] D. H. Neuhaus, P. J. Cousins, and A. G. Aberle, "Trapping and junction-related perturbations of the effective excess carrier lifetime," in *3<sup>rd</sup> World Conference on Photovoltaic Energy Conversion*, pp. 91-94, 2003.
- [68] T. Trupke and R. A. Bardos, "Self-consistent determination of the generation rate from photoconductance measurements," *Appl. Phys. Lett.*, vol. 85, pp. 3611-3613, 2004.
- [69] T. Trupke, R. A. Bardos, and M. D. Abbott, "Self-consistent calibration of photoluminescence and photoconductance lifetime measurements," *Appl. Phys. Lett.*, vol. 87, pp. 184102, 2005.
- [70] J. A. Giesecke, M. C. Schubert, and W. Warta, "Self-sufficient minority carrier lifetime in silicon from quasi-steady-state photoluminescence," *Phys. Status Solidi A*, vol. 209, pp. 2286-2290, 2012.
- [71] J. A. Giesecke, M. C. Schubert, and W. Warta, "Measurement of net dopant concentration via dynamic photoluminescence," *J. Appl. Phys.*, vol. 112, pp. 063704, 2012.
- [72] J. A. Giesecke and W. Warta, "Microsecond carrier lifetime measurements in silicon via quasi-steady-state photoluminescence," *Prog. Photovoltaics Res. Appl.*, vol. 20, pp. 238-245, 2012.
- [73] T. Roth, P. Rosenits, M. Rudiger, W. Warta, and S. W. Glunz, "Comparison of photoconductance- and photo-luminescence-based lifetime measurement techniques," in *Conference on Optoelectronic and Microelectronic Materials and Devices*, pp. 249-252, 2008.
- [74] T. Trupke, R. A. Bardos, M. C. Schubert, and W. Warta, "Photoluminescence imaging of silicon wafers," *Appl. Phys. Lett.*, vol. 89, pp. 044107, 2006.
- [75] B. Mitchell, J. W. Weber, M. Juhl, D. Macdonald, and T. Trupke, "Photoluminescence imaging of silicon bricks," *Solid State Phenom.*, vol. 205-206, pp. 118-127, 2014.
- [76] S. Herlufsen *et al.*, "Dynamic photoluminescence lifetime imaging for the characterisation of silicon wafers," *Phys. Status Solidi RRL*, vol. 5, pp. 25-27, 2011.

- [77] S. T. Kristensen, S. Nie, C. Berthod, R. Strandberg, J. O. Odden, and Z. Hameiri, "Temperature coefficients of crystal defects in multicrystalline silicon wafers," *IEEE J. Photovoltaics*, vol. 10, pp. 449-457, 2020.
- [78] S. Nie, S. T. Kristensen, A. Gu, R. L. Chin, T. Trupke, and Z. Hameiri, "Photoluminescence-based spatially resolved temperature coefficient maps of silicon wafers and solar cells," *IEEE J. Photovoltaics*, vol. 10, pp. 585-594, 2020.
- [79] O. Breitenstein, H. Höffler, and J. Haunschild, "Photoluminescence image evaluation of solar cells based on implied voltage distribution," *Sol. Energy Mater. Sol. Cells*, vol. 128, pp. 296-299, 2014.
- [80] Z. Hameiri and P. Chaturvedi, "Spatially resolved electrical parameters of silicon wafers and solar cells by contactless photoluminescence imaging," *Appl. Phys. Lett.*, vol. 102, pp. 073502, 2013.
- [81] R. Bhoopathy, O. Kunz, M. Juhl, T. Trupke, and Z. Hameiri, "Outdoor photoluminescence imaging of photovoltaic modules with sunlight excitation," *Prog. Photovoltaics Res. Appl.*, vol. 26, pp. 69-73, 2018.
- [82] I. Zafirovska, M. K. Juhl, J. W. Weber, J. Wong, and T. Trupke, "Detection of finger interruptions in silicon solar cells using line scan photoluminescence imaging," *IEEE J. Photovoltaics*, vol. 7, pp. 1496-1502, 2017.
- [83] H. C. Sio, S. P. Phang, T. Trupke, and D. Macdonald, "An accurate method for calibrating photoluminescence-based lifetime images on multi-crystalline silicon wafers," *Sol. Energy Mater. Sol. Cells*, vol. 131, pp. 77-84, 2014.
- [84] C. Shen, H. Kampwerth, and M. A. Green, "Photoluminescence based open circuit voltage and effective lifetime images re-interpretation for solar cells: The influence of horizontal balancing currents," *Sol. Energy Mater. Sol. Cells*, vol. 130, pp. 393-396, 2014.
- [85] S. Nie, S. T. Kristensen, A. Gu, T. Trupke, and Z. Hameiri, "A novel method for characterizing temperature sensitivity of silicon wafers and cells," in *46<sup>th</sup> IEEE Photovoltaic Specialists Conference*, pp. 0813-0816, 2019.
- [86] B. Michl, D. Impera, M. Bivour, W. Warta, and M. C. Schubert, "Suns-PLI as a powerful tool for spatially resolved fill factor analysis of solar cells," *Prog. Photovoltaics Res. Appl.*, vol. 22, pp. 581-586, 2014.
- [87] M. Glatthaar, J. Haunschild, M. Kasemann, J. Giesecke, W. Warta, and S. Rein, "Spatially resolved determination of dark saturation current and series resistance of silicon solar cells," *Phys. Status Solidi RRL*, vol. 4, pp. 13-15, 2010.
- [88] Z. Hameiri, P. Chaturvedi, and K. R. McIntosh, "Imaging the local ideality factor by contactless photoluminescence measurement," *Appl. Phys. Lett.*, vol. 103, pp. 023501, 2013.
- [89] H. Kampwerth, T. Trupke, J. W. Weber, and Y. Augarten, "Advanced luminescence based effective series resistance imaging of silicon solar cells," *Appl. Phys. Lett.*, vol. 93, pp. 202102, 2008.
- [90] T. Trupke, B. Mitchell, J. W. Weber, W. McMillan, R. A. Bardos, and R. Kroeze, "Photoluminescence imaging for photovoltaic applications," *Energy Procedia*, vol. 15, pp. 135-146, 2012.
- [91] P. Würfel, T. Trupke, T. Puzzer, E. Schäffer, W. Warta, and S. W. Glunz, "Diffusion lengths of silicon solar cells from luminescence images," *J. Appl. Phys.*, vol. 101, pp. 123110, 2007.
- [92] D. Walter, A. Fell, E. Franklin, D. Macdonald, B. Mitchell, and T. Trupke, "The impact of silicon CCD photon spread on quantitative analyses of luminescence images," *IEEE J. Photovoltaics*, vol. 4, pp. 368-373, 2014.

- [93] D. Walter, A. Liu, E. Franklin, D. Macdonald, B. Mitchell, and T. Trupke, "Contrast enhancement of luminescence images via point-spread deconvolution," in *38<sup>th</sup> IEEE Photovoltaic Specialists Conference*, pp. 000307-000312, 2012.
- [94] S. Herlufsen, J. Schmidt, D. Hinken, K. Bothe, and R. Brendel, "Photoconductance-calibrated photoluminescence lifetime imaging of crystalline silicon," *Phys. Status Solidi RRL*, vol. 2, pp. 245-247, 2008.
- [95] J. A. Giesecke, M. C. Schubert, B. Michl, F. Schindler, and W. Warta, "Minority carrier lifetime imaging of silicon wafers calibrated by quasi-steady-state photoluminescence," *Sol. Energy Mater. Sol. Cells*, vol. 95, pp. 1011-1018, 2011.
- [96] S. T. Kristensen *et al.*, "A high-accuracy calibration method for temperature dependent photoluminescence imaging," *AIP Conference Proceedings*, vol. 2147, pp. 020007, 2019.
- [97] H. Haug, R. Søndena, A. Berg, and M. S. Wiig, "Lifetime spectroscopy with high spatial resolution based on temperature- and injection dependent photoluminescence imaging," *Sol. Energy Mater. Sol. Cells*, vol. 200, pp. 109994, 2019.
- [98] D. Macdonald, J. Tan, and T. Trupke, "Imaging interstitial iron concentrations in boron-doped crystalline silicon using photoluminescence," *J. Appl. Phys.*, vol. 103, pp. 073710, 2008.
- [99] L. E. Mundt *et al.*, "Spatially resolved impurity identification via temperature- and injection-dependent photoluminescence imaging," *IEEE J. Photovoltaics*, vol. 5, pp. 1503-1509, 2015.
- [100] S. P. Phang, H. C. Sio, and D. Macdonald, "Carrier de-smearing of photoluminescence images on silicon wafers using the continuity equation," *Appl. Phys. Lett.*, vol. 103, pp. 192112, 2013.
- [101] S. P. Phang, H. C. Sio, and D. Macdonald, "Applications of carrier de-smearing of photoluminescence images on silicon wafers," *Prog. Photovoltaics Res. Appl.*, vol. 24, pp. 1547-1553, 2016.
- [102] H. Steinkemper, I. Geisemeyer, M. Schubert, W. Warta, and S. Glunz, "Temperature-dependent modeling of silicon solar cells  $E_g$ ,  $n_i$ , recombination, and  $V_{oc}$ ," *IEEE J. Photovoltaics*, vol. 7, pp. 450-457, 2017.
- [103] R. Pässler, "Dispersion-related description of temperature dependencies of band gaps in semiconductors," *Phys. Rev. B*, vol. 66, pp. 085201, 2002.
- [104] V. Alex, S. Finkbeiner, and J. Weber, "Temperature dependence of the indirect energy gap in crystalline silicon," *J. Appl. Phys.*, vol. 79, pp. 6943-6946, 1996.
- [105] M. A. Green, "General temperature dependence of solar cell performance and implications for device modelling," *Prog. Photovoltaics Res. Appl.*, vol. 11, pp. 333-340, 2003.
- [106] Y. P. Varshni, "Temperature dependence of the energy gap in semiconductors," *Physica*, vol. 34, pp. 149-154, 1967.
- [107] W. Bludau, A. Onton, and W. Heinke, "Temperature dependence of the band gap of silicon," *J. Appl. Phys.*, vol. 45, pp. 1846-1848, 1974.
- [108] G. G. Macfarlane, T. P. McLean, J. E. Quarrington, and V. Roberts, "Fine structure in the absorption-edge spectrum of Si," *Phys. Rev.*, vol. 111, pp. 1245-1254, 1958.
- [109] C. D. Thurmond, "The standard thermodynamic functions for the formation of electrons and holes in Ge, Si, GaAs, and GaP," *J. Electrochem. Soc.*, vol. 122, pp. 1133-1141, 1975.

- [110] R. Pässler, "Parameter sets due to fittings of the temperature dependencies of fundamental bandgaps in semiconductors," *Phys. Status Solidi B*, vol. 216, pp. 975-1007, 1999.
- [111] R. Pässler, "Semi-empirical descriptions of temperature dependences of band gaps in semiconductors," *Phys. Status Solidi B*, vol. 236, pp. 710-728, 2003.
- [112] M. A. Green, "Intrinsic concentration, effective densities of states, and effective mass in silicon," *J. Appl. Phys*, vol. 67, pp. 2944-2954, 1990.
- [113] A. B. Sproul and M. A. Green, "Improved value for the silicon intrinsic carrier concentration from 275 to 375 K," *J. Appl. Phys*, vol. 70, pp. 846-854, 1991.
- [114] A. B. Sproul and M. A. Green, "Intrinsic carrier concentration and minority-carrier mobility of silicon from 77 to 300 K," *J. Appl. Phys*, vol. 73, pp. 1214-1225, 1993.
- [115] K. Misiakos and D. Tsamakis, "Accurate measurements of the silicon intrinsic carrier density from 78 to 340 K," *J. Appl. Phys*, vol. 74, pp. 3293-3297, 1993.
- [116] R. Couderc, M. Amara, and M. Lemiti, "Reassessment of the intrinsic carrier density temperature dependence in crystalline silicon," *J. Appl. Phys*, vol. 115, pp. 093705, 2014.
- [117] A. Schenk, "Finite-temperature full random-phase approximation model of band gap narrowing for silicon device simulation," *J. Appl. Phys*, vol. 84, pp. 3684-3695, 1998.
- [118] R. Dumbrell, M. K. Juhl, T. Trupke, and Z. Hameiri, "Extracting metal contact recombination parameters from effective lifetime data," *IEEE J. Photovoltaics*, vol. 8, pp. 1413-1420, 2018.
- [119] D. Faiman, "Assessing the outdoor operating temperature of photovoltaic modules," *Prog. Photovoltaics Res. Appl.*, vol. 16, pp. 307-315, 2008.
- [120] M. A. Green, K. Emery, and A. W. Blakers, "Silicon solar cells with reduced temperature sensitivity," *Electron. Lett.*, vol. 18, no. 2, pp. 97-98doi: 10.1049/el:19820066.
- [121] P. Singh and N. M. Ravindra, "Temperature dependence of solar cell performance—an analysis," *Sol. Energy Mater. Sol. Cells*, vol. 101, pp. 36-45, 2012.
- [122] T. Moot *et al.*, "Temperature coefficients of perovskite photovoltaics for energy yield calculations," *ACS Energy Lett.*, vol. 6, pp. 2038-2047, 2021.
- [123] M. Piliougine, A. Oukaja, M. Sidrach-de-Cardona, and G. Spagnuolo, "Temperature coefficients of degraded crystalline silicon photovoltaic modules at outdoor conditions," *Prog. Photovoltaics Res. Appl.*, vol. 29, pp. 558-570, 2021.
- [124] T. Ishii, K. Otani, and T. Takashima, "Effects of solar spectrum and module temperature on outdoor performance of photovoltaic modules in round-robin measurements in Japan," *Prog. Photovoltaics Res. Appl.*, vol. 19, pp. 141-148, 2011.
- [125] J. C. C. Fan, "Theoretical temperature dependence of solar cell parameters," *Solar Cells*, vol. 17, pp. 309-315, 1986.
- [126] S. M. F. Zhang *et al.*, "Temperature- and illumination-dependent characterization of solar cells using Suns- $V_{oc}(T)$  and  $I-V(T)$ ," in *48<sup>th</sup> IEEE Photovoltaic Specialists Conference*, pp. 0737-0740, 2021.
- [127] C. Berthod, R. Strandberg, and J. O. Odden, "Temperature coefficients of compensated silicon solar cells – Influence of ingot position and blend-in-ratio," *Energy Procedia*, vol. 77, pp. 15-20, 2015.
- [128] P. Löper *et al.*, "Analysis of the temperature dependence of the open-circuit voltage," *Energy Procedia*, vol. 27, pp. 135-142, 2012.

- [129] C. Berthod *et al.*, "Temperature sensitivity of multicrystalline silicon solar cells," *IEEE J. Photovoltaics*, vol. 9, pp. 957-964, 2019.
- [130] O. Dupré, R. Vaillon, and M. A. Green, "Experimental assessment of temperature coefficient theories for silicon solar cells," *IEEE J. Photovoltaics*, vol. 6, pp. 56-60, 2016.
- [131] C. Berthod, R. Strandberg, J. O. Odden, and T. O. Saetre, "Reduced temperature sensitivity of multicrystalline silicon solar cells with low ingot resistivity," in *43<sup>rd</sup> IEEE Photovoltaic Specialists Conference*, pp. 2398-2402, 2016.
- [132] A. H. Tuan Le *et al.*, "Temperature-dependent performance of silicon solar cells with polysilicon passivating contacts," *Sol. Energy Mater. Sol. Cells*, vol. 225, pp. 111020, 2021.
- [133] H. Haug, C. Berthod, Å. Skomedal, J. O. Odden, E. S. Marstein, and R. Søndenå, "Simulated and measured temperature coefficients in compensated silicon wafers and solar cells," *Sol. Energy Mater. Sol. Cells*, vol. 200, pp. 109921, 2019.
- [134] R. Eberle, S. T. Haag, I. Geisemeyer, M. Padilla, and M. C. Schubert, "Temperature coefficient imaging for silicon solar cells," *IEEE J. Photovoltaics*, vol. 8, pp. 930-936, 2018.
- [135] Z. Hameiri, M. K. Juhl, R. Carlaw, and T. Trupke, "Spatially resolved lifetime spectroscopy from temperature-dependent photoluminescence imaging," in *42<sup>nd</sup> IEEE Photovoltaic Specialist Conference*, pp. 1-3, 2015.
- [136] H. Haug, R. Søndenå, M. S. Wiig, and E. S. Marstein, "Temperature dependent photoluminescence imaging calibrated by photoconductance measurements," *Energy Procedia*, vol. 124, pp. 47-52, 2017.
- [137] R. Eberle, A. Fell, S. Mägdefessel, F. Schindler, and M. C. Schubert, "Prediction of local temperature-dependent performance of silicon solar cells," *Prog. Photovoltaics Res. Appl.*, vol. 27, pp. 999-1006, 2019.
- [138] M. A. Green, "Radiative efficiency of state-of-the-art photovoltaic cells," *Prog. Photovoltaics Res. Appl.*, vol. 20, pp. 472-476, 2012.
- [139] R. A. Sinton, "Predicting multi-crystalline solar cell efficiency from life-time measured during cell fabrication," *3<sup>rd</sup> World Conference on Photovoltaic Energy Conversion*, vol. 2, pp. 1028-1031, 2003.
- [140] J. Isenberg, J. Dicker, and W. Warta, "Averaging of laterally inhomogeneous lifetimes for one-dimensional modeling of solar cells," *J. Appl. Phys*, vol. 94, pp. 4122-4130, 2003.
- [141] D. Macdonald, A. Cuevas, A. Kinomura, Y. Nakano, and L. J. Geerligs, "Transition-metal profiles in a multicrystalline silicon ingot," *J. Appl. Phys*, vol. 97, pp. 033523, 2005.
- [142] H. C. Sio *et al.*, "Recombination sources in p-type high performance multicrystalline silicon," *Jpn. J. Appl. Phys.*, vol. 56, pp. 08MB16, 2017.
- [143] L. J. Geerligs, Y. Komatsu, I. Röver, K. Wambach, I. Yamaga, and T. Saitoh, "Precipitates and hydrogen passivation at crystal defects in n- and p-type multicrystalline silicon," *J. Appl. Phys*, vol. 102, pp. 093702, 2007.
- [144] H. C. Sio *et al.*, "The electrical properties of high performance multicrystalline silicon and mono-like silicon: Material limitations and cell potential," *Sol. Energy Mater. Sol. Cells*, vol. 201, pp. 110059, 2019.
- [145] D. H. Macdonald, A. Liu, H. T. Nguyen, S. Y. Lim, and F. E. Rougieux, "Physical modelling of luminescence spectra from crystalline silicon," in *31<sup>st</sup> European Photovoltaic Solar Energy Conference and Exhibition*, pp. 440 - 443, 2015.

- [146] A. T. Blumenau, R. Jones, S. Öberg, P. R. Briddon, and T. Frauenheim, "Dislocation related photoluminescence in silicon," *Phys. Rev. Lett.*, vol. 87, pp. 187404, 2001.
- [147] M. Suezawa, Y. Sasaki, and K. Sumino, "Dependence of photoluminescence on temperature in dislocated silicon crystals," *Phys. Status Solidi A*, vol. 79, pp. 173-181, 1983.
- [148] H. T. Nguyen *et al.*, "Microscopic distributions of defect luminescence from subgrain boundaries in multicrystalline silicon wafers," *IEEE J. Photovoltaics*, vol. 7, pp. 772-780, 2017.
- [149] H. T. Nguyen, F. E. Rougieux, F. Wang, H. Tan, and D. Macdonald, "Micrometer-scale deep-level spectral photoluminescence from dislocations in multicrystalline silicon," *IEEE J. Photovoltaics*, vol. 5, pp. 799-804, 2015.
- [150] M. Tajima, Y. Iwata, F. Okayama, H. Toyota, H. Onodera, and T. Sekiguchi, "Deep-level photoluminescence due to dislocations and oxygen precipitates in multicrystalline Si," *J. Appl. Phys*, vol. 111, pp. 113523, 2012.
- [151] J. F. Kielkopf, "New approximation to the Voigt function with applications to spectral-line profile analysis," *J. Opt. Soc. Am.*, vol. 63, pp. 987-995, 1973.
- [152] L. W. Aukerman and M. F. Millea, "Steady-State Recombination via Donor-Acceptor Pairs," *Phys. Rev.*, vol. 148, pp. 759-765, 1966.
- [153] P. P. Altermatt, A. Schenk, B. Schmithüsen, and G. Heiser, "A simulation model for the density of states and for incomplete ionization in crystalline silicon. II. Investigation of Si:As and Si:B and usage in device simulation," *J. Appl. Phys*, vol. 100, pp. 113715, 2006.
- [154] D. A. Clugston and P. A. Basore, "PC1D version 5: 32-bit solar cell modeling on personal computers," in *26<sup>th</sup> IEEE Photovoltaic Specialists Conference*, pp. 207-210, 1997.
- [155] S. T. Kristensen, S. Nie, C. Berthod, R. Strandberg, J. O. Odden, and Z. Hameiri, "How gettering affects the temperature sensitivity of the implied open circuit voltage of multicrystalline silicon wafers," in *46<sup>th</sup> IEEE Photovoltaic Specialists Conference*, pp. 0061-0067, 2019.
- [156] B. J. Hallam, P. G. Hamer, A. M. Ciesla née Wenham, C. E. Chan, B. Vicari Stefani, and S. Wenham, "Development of advanced hydrogenation processes for silicon solar cells via an improved understanding of the behaviour of hydrogen in silicon," *Prog. Photovoltaics Res. Appl.*, vol. 28, pp. 1217-1238, 2020.
- [157] A. Liu, S. P. Phang, and D. Macdonald, "Gettering in silicon photovoltaics: A review," *Sol. Energy Mater. Sol. Cells*, vol. 234, pp. 111447, 2022.
- [158] M. Seibt, A. Sattler, C. Rudolf, O. Voß, V. Kveder, and W. Schröter, "Gettering in silicon photovoltaics: current state and future perspectives," *Phys. Status Solidi A*, vol. 203, pp. 696-713, 2006.
- [159] J. S. Kang and D. K. Schroder, "Gettering in silicon," *J. Appl. Phys*, vol. 65, pp. 2974-2985, 1989.
- [160] A. Liu, C. Sun, H. C. Sio, X. Zhang, H. Jin, and D. Macdonald, "Gettering of transition metals in high-performance multicrystalline silicon by silicon nitride films and phosphorus diffusion," *J. Appl. Phys*, vol. 125, pp. 043103, 2019.
- [161] R. L. Meek, T. E. Seidel, and A. G. Cullis, "Diffusion gettering of Au and Cu in silicon," *J. Electrochem. Soc.*, vol. 122, pp. 786-796, 1975.
- [162] M. Apel, I. Hanke, R. Schindler, and W. Schröter, "Aluminum gettering of cobalt in silicon," *J. Appl. Phys*, vol. 76, pp. 4432-4433, 1994.

- [163] A. Liu, D. Yan, S. P. Phang, A. Cuevas, and D. Macdonald, "Effective impurity gettering by phosphorus- and boron-diffused polysilicon passivating contacts for silicon solar cells," *Sol. Energy Mater. Sol. Cells*, vol. 179, pp. 136-141, 2018.
- [164] T. Buonassisi *et al.*, "Synchrotron-based investigations of the nature and impact of iron contamination in multicrystalline silicon solar cells," *J. Appl. Phys*, vol. 97, pp. 074901, 2005.
- [165] G. Stokkan *et al.*, "Impurity control in high performance multicrystalline silicon," *Phys. Status Solidi A*, vol. 214, pp. 1700319, 2017.
- [166] T. Buonassisi *et al.*, "Chemical natures and distributions of metal impurities in multicrystalline silicon materials," *Prog. Photovoltaics Res. Appl.*, vol. 14, pp. 513-531, 2006.
- [167] E. R. Weber, "Transition metals in silicon," *Appl. Phys. A*, vol. 30, pp. 1-22, 1983.
- [168] D. Macdonald, A. Cuevas, A. Kinomura, and Y. Nakano, "Phosphorus gettering in multicrystalline silicon studied by neutron activation analysis," in *29<sup>th</sup> IEEE Photovoltaic Specialists Conference*, pp. 285-288, 2002.
- [169] M. Seibt and V. Kveder, "Gettering processes and the role of extended defects," in *Advanced Silicon Materials for Photovoltaic Applications*, 2012, pp. 127-188.
- [170] Y. Boulfrad, A. Haarahiltunen, H. Savin, E. J. Øvrelid, and L. Arnberg, "Enhanced performance in the deteriorated area of multicrystalline silicon wafers by internal gettering," *Prog. Photovoltaics Res. Appl.*, vol. 23, pp. 30-36, 2015.
- [171] V. Osinniy *et al.*, "Gettering improvements of minority-carrier lifetimes in solar grade silicon," *Sol. Energy Mater. Sol. Cells*, vol. 101, pp. 123-130, 2012.
- [172] P. S. Plekhanov, R. Gafiteanu, U. M. Gösele, and T. Y. Tan, "Modeling of gettering of precipitated impurities from Si for carrier lifetime improvement in solar cell applications," *J. Appl. Phys*, vol. 86, pp. 2453-2458, 1999.
- [173] P. Manshanden and L. J. Geerligs, "Improved phosphorous gettering of multicrystalline silicon," *Sol. Energy Mater. Sol. Cells*, vol. 90, pp. 998-1012, 2006.
- [174] A. Cuevas, M. J. Kerr, C. Samundsett, F. Ferrazza, and G. Coletti, "Millisecond minority carrier lifetimes in n-type multicrystalline silicon," *Appl. Phys. Lett.*, vol. 81, pp. 4952-4954, 2002.
- [175] A. Cuevas, M. Stocks, S. Armand, M. Stuckings, A. Blakers, and F. Ferrazza, "High minority carrier lifetime in phosphorus-gettered multicrystalline silicon," *Appl. Phys. Lett.*, vol. 70, pp. 1017-1019, 1997.
- [176] M. Acciarri *et al.*, "Effect of P-induced gettering on extended defects in n-type multicrystalline silicon," *Prog. Photovoltaics Res. Appl.*, vol. 15, pp. 375-386, 2007.
- [177] A. Bentzen, A. Holt, R. Kopecek, G. Stokkan, J. S. Christensen, and B. G. Svensson, "Gettering of transition metal impurities during phosphorus emitter diffusion in multicrystalline silicon solar cell processing," *J. Appl. Phys*, vol. 99, pp. 093509, 2006.
- [178] D. P. Fenning, A. S. Zuschlag, M. I. Bertoni, B. Lai, G. Hahn, and T. Buonassisi, "Improved iron gettering of contaminated multicrystalline silicon by high-temperature phosphorus diffusion," *J. Appl. Phys*, vol. 113, pp. 214504, 2013.
- [179] H. Talvitie, V. Vähänissi, A. Haarahiltunen, M. Yli-Koski, and H. Savin, "Phosphorus and boron diffusion gettering of iron in monocrystalline silicon," *J. Appl. Phys*, vol. 109, pp. 093505, 2011.
- [180] T. Buonassisi *et al.*, "Impact of metal silicide precipitate dissolution during rapid thermal processing of multicrystalline silicon solar cells," *Appl. Phys. Lett.*, vol. 87, pp. 121918, 2005.

- [181] J. F. Lelièvre, E. Fourmond, A. Kaminski, O. Palais, D. Ballutaud, and M. Lemiti, "Study of the composition of hydrogenated silicon nitride SiN<sub>x</sub>:H for efficient surface and bulk passivation of silicon," *Sol. Energy Mater. Sol. Cells*, vol. 93, pp. 1281-1289, 2009.
- [182] H. C. Sio, S. P. Phang, H. T. Nguyen, Z. Hameiri, and D. Macdonald, "Hydrogenation in multicrystalline silicon: The impact of dielectric film properties and firing conditions," *Prog. Photovoltaics Res. Appl.*, vol. 28, pp. 493-502, 2020.
- [183] S. Martinuzzi, I. Périchaud, and F. Warchol, "Hydrogen passivation of defects in multicrystalline silicon solar cells," *Sol. Energy Mater. Sol. Cells*, vol. 80, pp. 343-353, 2003.
- [184] J. Hong, W. M. M. Kessels, W. J. Soppe, A. W. Weeber, W. M. Arnoldbik, and M. C. M. van de Sanden, "Influence of the high-temperature "firing" step on high-rate plasma deposited silicon nitride films used as bulk passivating antireflection coatings on silicon solar cells," *J. Vac. Sci. Technol. B*, vol. 21, pp. 2123-2132, 2003.
- [185] H. F. W. Dekkers, G. Beaucarne, M. Hiller, H. Charifi, and A. Slaoui, "Molecular hydrogen formation in hydrogenated silicon nitride," *Appl. Phys. Lett.*, vol. 89, pp. 211914, 2006.
- [186] D. Mathiot, "Modeling of hydrogen diffusion in n- and p-type silicon," *Phys. Rev. B*, vol. 40, pp. 5867-5870, 1989.
- [187] C. H. Seager and R. A. Anderson, "Real-time observations of hydrogen drift and diffusion in silicon," *Appl. Phys. Lett.*, vol. 53, pp. 1181-1183, 1988.
- [188] J. Zhu, N. M. Johnson, and C. Herring, "Negative-charge state of hydrogen in silicon," *Phys. Rev. B*, vol. 41, pp. 12354-12357, 1990.
- [189] R. Job, W. R. Fahrner, N. M. Kazuchits, and A. G. Ulyashin, "Two-step low-temperature process for a p-n junction formation due to hydrogen enhanced thermal donor formation in p-type Czochralski silicon," in *Materials Research Society Symposium - Proceedings*, pp. 337-342, 1998.
- [190] R. Rizk, P. De Mierry, D. Ballutaud, M. Aucouturier, and D. Mathiot, "Hydrogen diffusion and passivation processes in p- and n-type crystalline silicon," *Phys. Rev. B*, vol. 44, pp. 6141-6151, 1991.
- [191] C. Herring, N. M. Johnson, and C. G. Van de Walle, "Energy levels of isolated interstitial hydrogen in silicon," *Phys. Rev. B*, vol. 64, pp. 125209, 2001.
- [192] P. Hamer, B. Hallam, S. Wenham, and M. Abbott, "Manipulation of Hydrogen Charge States for Passivation of P-Type Wafers in Photovoltaics," *IEEE J. Photovoltaics*, vol. 4, pp. 1252-1260, 2014.
- [193] P. Hamer, "Hydrogen charge states and dopant interactions in crystalline silicon solar cells," PhD, University of New South Wales, Australia, 2014.
- [194] R. Einhaus *et al.*, "Hydrogen passivation of newly developed EMC-multicrystalline silicon," *Mater. Sci. Eng. B*, vol. 58, pp. 81-85, 1999.
- [195] S. J. Pearton, J. W. Corbett, and T. S. Shi, "Hydrogen in crystalline semiconductors," *Appl. Phys. A*, vol. 43, pp. 153-195, 1987.
- [196] L. J. Geerligs, A. Azzizi, D. H. Macdonald, and P. Manshanden, "Hydrogen passivation of iron in multicrystalline silicon," *Energy Research Centre of the Netherlands*, 2003.
- [197] A. Liu, C. Sun, and D. Macdonald, "Hydrogen passivation of interstitial iron in boron-doped multicrystalline silicon during annealing," *J. Appl. Phys.*, vol. 116, pp. 194902, 2014.

- [198] C. Sun, A. Liu, S. P. Phang, F. E. Rougieux, and D. Macdonald, "Charge states of the reactants in the hydrogen passivation of interstitial iron in P-type crystalline silicon," *J. Appl. Phys.*, vol. 118, pp. 085709, 2015.
- [199] H. C. Sio *et al.*, "3-D modeling of multicrystalline silicon materials and solar cells," *IEEE J. Photovoltaics*, vol. 9, pp. 965-973, 2019.
- [200] F. Jiang *et al.*, "Hydrogenation of Si from SiN<sub>x</sub>(H) films: Characterization of H introduced into the Si," *Appl. Phys. Lett.*, vol. 83, pp. 931-933, 2003.
- [201] A. Y. Liu, C. Sun, V. P. Markevich, A. R. Peaker, J. D. Murphy, and D. Macdonald, "Gettering of interstitial iron in silicon by plasma-enhanced chemical vapour deposited silicon nitride films," *J. Appl. Phys.*, vol. 120, pp. 193103, 2016.
- [202] J. Tan, A. Cuevas, D. Macdonald, T. Trupke, R. Bardos, and K. Roth, "On the electronic improvement of multi-crystalline silicon via gettering and hydrogenation," *Prog. Photovoltaics Res. Appl.*, vol. 16, pp. 129-134, 2008.
- [203] M. I. Bertoni *et al.*, "Influence of defect type on hydrogen passivation efficacy in multicrystalline silicon solar cells," *Prog. Photovoltaics Res. Appl.*, vol. 19, pp. 187-191, 2011.
- [204] O. F. Vyvenko, O. Krüger, and M. Kittler, "Cross-sectional electron-beam-induced current analysis of the passivation of extended defects in cast multicrystalline silicon by remote hydrogen plasma treatment," *Appl. Phys. Lett.*, vol. 76, pp. 697-699, 2000.
- [205] P. Hamer *et al.*, "Laser illumination for manipulation of hydrogen charge states in silicon solar cells," *Phys. Status Solidi RRL*, vol. 9, pp. 111-114, 2015.
- [206] S. H. Lee, M. F. Bhopal, D. W. Lee, and S. H. Lee, "Review of advanced hydrogen passivation for high efficient crystalline silicon solar cells," *Mater. Sci. Semicond. Process.*, vol. 79, pp. 66-73, 2018.
- [207] B. Lim, K. Bothe, and J. Schmidt, "Deactivation of the boron-oxygen recombination center in silicon by illumination at elevated temperature," *Phys. Status Solidi RRL*, vol. 2, pp. 93-95, 2008.
- [208] B. J. Hallam *et al.*, "Rapid mitigation of carrier-induced degradation in commercial silicon solar cells," *Jpn. J. Appl. Phys.*, vol. 56, pp. 08MB13, 2017.
- [209] L. Song *et al.*, "Laser Enhanced Hydrogen Passivation of Silicon Wafers," *Int. J. Photoenergy*, vol. 2015, pp. 1-13, 2015.
- [210] A. Wenham *et al.*, "Defect passivation on cast-mono crystalline screen-printed cells," *Front. Energy*, vol. 11, pp. 60-66, 2017.
- [211] I. Burud, T. Mehl, A. Flo, D. Lausch, and E. Olsen, "Hyperspectral photoluminescence imaging of defects in solar cells," *J. Spectral Imaging*, vol. 5, pp. 1-5, 2016.
- [212] L. Gong, F. Wang, Q. Cai, D. You, and B. Dai, "Characterization of defects in mono-like silicon wafers and their effects on solar cell efficiency," *Sol. Energy Mater. Sol. Cells*, vol. 120, pp. 289-294, 2014.
- [213] L. Song and X. Yu, "Defect engineering in cast mono-like silicon: A review," *Prog. Photovoltaics Res. Appl.*, vol. 29, pp. 294-314, 2021.
- [214] Y. Ohno *et al.*, "Recombination activity of nickel, copper, and oxygen atoms segregating at grain boundaries in mono-like silicon crystals," *Appl. Phys. Lett.*, vol. 109, pp. 142105, 2016.
- [215] P. Wang, C. Cui, D. Yang, and X. Yu, "Seed-assisted growth of cast-mono silicon for photovoltaic application: challenges and strategies," *Solar RRL*, vol. 4, pp. 1900486, 2020.
- [216] F. Frühauf, P. P. Altermatt, T. Luka, T. Mehl, H. Deniz, and O. Breitenstein, "Injection intensity-dependent recombination at various grain boundary types in

- multicrystalline silicon solar cells," *Sol. Energy Mater. Sol. Cells*, vol. 180, pp. 130-137, 2018.
- [217] R. Tauler, "Multivariate curve resolution applied to second order data," *Chemometrics and Intelligent Laboratory Systems*, vol. 30, pp. 133-146, 1995.
- [218] C. Sun, A. Liu, A. Samadi, C. Chan, A. Ciesla, and D. Macdonald, "Transition metals in a cast-monocrystalline silicon ingot studied by silicon nitride gettering," *Phys. Status Solidi RRL*, vol. 13, pp. 1900456, 2019.
- [219] D. Tweddle *et al.*, "Atom probe tomography study of gettering in high-performance multicrystalline silicon," *IEEE J. Photovoltaics*, vol. 10, pp. 863-871, 2020.
- [220] J. Colwell, "Copper and silicon: Implications for the long-term stability of plated contacts for silicon solar cells," PhD, University of New South Wales, Australia, 2018.
- [221] A. Inglese, J. Lindroos, H. Vahlman, and H. Savin, "Recombination activity of light-activated copper defects in p-type silicon studied by injection- and temperature-dependent lifetime spectroscopy," *J. Appl. Phys*, vol. 120, pp. 125703, 2016.
- [222] D. Macdonald, A. Cuevas, S. Rein, P. Lichtner, and S. W. Glunz, "Temperature- and injection-dependent lifetime spectroscopy of copper-related defects in silicon," in *3rd World Conference on Photovoltaic Energy Conversion, 2003. Proceedings of*, pp. 87-90 Vol.1, 2003.
- [223] C. Sun, F. E. Rougieux, and D. Macdonald, "Reassessment of the recombination parameters of chromium in n- and p-type crystalline silicon and chromium-boron pairs in p-type crystalline silicon," *J. Appl. Phys*, vol. 115, pp. 214907, 2014.
- [224] F. E. Rougieux, C. Sun, and D. Macdonald, "Determining the charge states and capture mechanisms of defects in silicon through accurate recombination analyses: A review," *Sol. Energy Mater. Sol. Cells*, vol. 187, pp. 263-272, 2018.
- [225] F. D. Heinz, Y. Zhu, Z. Hameiri, M. Juhl, T. Trupke, and M. C. Schubert, "The principle of adaptive excitation for photoluminescence imaging of silicon: Theory," *Phys. Status Solidi RRL*, vol. 12, pp. 1800137, 2018.
- [226] Y. Zhu, F. D. Heinz, M. Juhl, M. C. Schubert, T. Trupke, and Z. Hameiri, "Photoluminescence imaging at uniform excess carrier density using adaptive nonuniform excitation," *IEEE J. Photovoltaics*, vol. 8, pp. 1787-1792, 2018.
- [227] S. Nie, Y. Zhu, O. Kunz, H. Kampwerth, T. Trupke, and Z. Hameiri, "Temperature-dependent photoluminescence imaging using non-uniform excitation," in *47<sup>th</sup> IEEE Photovoltaic Specialists Conference*, pp. 0789-0792, 2020.
- [228] F. Wippermann, U.-D. Zeitner, P. Dannberg, A. Bräuer, and S. Sinzinger, "Beam homogenizers based on chirped microlens arrays," *Opt. Express*, vol. 15, pp. 6218-6231, 2007.
- [229] E. L. Dereniak and T. D. Dereniak, *Geometrical and Trigonometric Optics*. Cambridge: Cambridge University Press, 2008.
- [230] D. N. R. Payne, M. K. Juhl, M. E. Pollard, A. Teal, and D. M. Bagnall, "Evaluating the accuracy of point spread function deconvolutions applied to luminescence images," in *43<sup>rd</sup> IEEE Photovoltaic Specialists Conference*, pp. 1585-1589, 2016.
- [231] S. Nie, Y. Zhu, O. Kunz, T. Trupke, and Z. Hameiri, "Advanced photoluminescence imaging using non-uniform excitation," *Prog. Photovoltaics Res. Appl.*, 2021.
- [232] G. Coletti *et al.*, "Removing the effect of striations in n-type silicon solar cells," *Sol. Energy Mater. Sol. Cells*, vol. 130, pp. 647-651, 2014.

- [233] Y. M. Yang, A. Yu, B. Hsu, W. C. Hsu, A. Yang, and C. W. Lan, "Development of high-performance multicrystalline silicon for photovoltaic industry," *Prog. Photovoltaics Res. Appl.*, vol. 23, pp. 340-351, 2015.
- [234] M. B. Shabani, T. Yamashita, and E. Morita, "Study of gettering mechanisms in silicon: competitive gettering between phosphorus diffusion gettering and other gettering sites," *Solid State Phenom.*, vol. 131-133, pp. 399-404, 2008.
- [235] C. Battaglia, A. Cuevas, and S. De Wolf, "High-efficiency crystalline silicon solar cells: status and perspectives," *Energy Environ. Sci.*, vol. 9, pp. 1552-1576, 2016.
- [236] ITRPV, "International Technology Roadmap for Photovoltaic," pp. 1-76, 2019.
- [237] R. S. Bonilla, B. Hoex, P. Hamer, and P. R. Wilshaw, "Dielectric surface passivation for silicon solar cells: A review," *Phys. Status Solidi A*, vol. 214, pp. 1700293, 2017.
- [238] S. W. Glunz and F. Feldmann, "SiO<sub>2</sub> surface passivation layers – a key technology for silicon solar cells," *Sol. Energy Mater. Sol. Cells*, vol. 185, pp. 260-269, 2018.
- [239] R. Hezel and R. Schörner, "Plasma Si nitride—A promising dielectric to achieve high-quality silicon MIS/IL solar cells," *J. Appl. Phys.*, vol. 52, pp. 3076-3079, 1981.
- [240] A. G. Aberle, "Overview on SiN surface passivation of crystalline silicon solar cells," *Sol. Energy Mater. Sol. Cells*, vol. 65, pp. 239-248, 2001.
- [241] G. Dingemans and W. M. M. Kessels, "Status and prospects of Al<sub>2</sub>O<sub>3</sub>-based surface passivation schemes for silicon solar cells," *J. Vac. Sci. Technol., A*, vol. 30, pp. 040802, 2012.
- [242] W. Soppe, H. Rieffe, and A. Weeber, "Bulk and surface passivation of silicon solar cells accomplished by silicon nitride deposited on industrial scale by microwave PECVD," *Prog. Photovoltaics Res. Appl.*, vol. 13, pp. 551-569, 2005.
- [243] A. Cuevas, T. Allen, J. Bullock, W. Yimao, Y. Di, and Z. Xinyu, "Skin care for healthy silicon solar cells," in *42<sup>nd</sup> IEEE Photovoltaic Specialist Conference*, pp. 1-6, 2015.
- [244] E. H. Nicollian and A. Goetzberger, "MOS conductance technique for measuring surface state parameters," *Appl. Phys. Lett.*, vol. 7, pp. 216-219, 1965.
- [245] H. Deuling, E. Klausmann, and A. Goetzberger, "Interface states in Si-SiO<sub>2</sub> interfaces," *Solid-State Electron.*, vol. 15, pp. 559-571, 1972.
- [246] T. J. Tredwell and C. R. Viswanathan, "Determination of interface-state parameters in a MOS capacitor by DLTS," *Solid-State Electron.*, vol. 23, pp. 1171-1178, 1980.
- [247] E. H. Nicollian and J. R. Brews, *MOS (Metal Oxide Semiconductor) Physics and Technology*. New York: Wiley, 1982.
- [248] W. D. Eades and R. M. Swanson, "Improvements in the determination of interface state density using deep level transient spectroscopy," *J. Appl. Phys.*, vol. 56, pp. 1744-1751, 1984.
- [249] W. D. Eades and R. M. Swanson, "Determination of the capture cross section and degeneracy factor of Si-SiO<sub>2</sub> interface states," *Appl. Phys. Lett.*, vol. 44, pp. 988-990, 1984.
- [250] A. G. Aberle, S. W. Glunz, A. W. Stephens, and M. A. Green, "High-efficiency silicon solar cells: Si/SiO<sub>2</sub>, interface parameters and their impact on device performance," *Prog. Photovoltaics Res. Appl.*, vol. 2, pp. 265-273, 1994.
- [251] W. Füssel, M. Schmidt, H. Angermann, G. Mende, and H. Flietner, "Defects at the Si/SiO<sub>2</sub> interface: Their nature and behaviour in technological processes and stress," *Nucl. Instrum. Methods Phys. Res., Sect. A*, vol. 377, pp. 177-183, 1996.

- [252] J. Snel, "The doped Si/SiO<sub>2</sub> interface," *Solid-State Electron.*, vol. 24, pp. 135-139, 1981.
- [253] J. T. Ryan, A. Matsuda, J. P. Campbell, and K. P. Cheung, "Interface-state capture cross section—Why does it vary so much?," *Appl. Phys. Lett.*, vol. 106, pp. 163503, 2015.
- [254] A. G. Aberle, S. Glunz, and W. Warta, "Impact of illumination level and oxide parameters on Shockley–Read–Hall recombination at the Si-SiO<sub>2</sub> interface," *J. Appl. Phys.*, vol. 71, pp. 4422-4431, 1992.
- [255] R. B. M. Girisch, R. P. Mertens, and R. F. D. Keersmaecker, "Determination of Si-SiO<sub>2</sub> interface recombination parameters using a gate-controlled point-junction diode under illumination," *IEEE Trans. Electron Devices*, vol. 35, pp. 203-222, 1988.
- [256] M. Schoffthaler, R. Brendel, G. Langguth, and J. H. Werner, "High-quality surface passivation by corona-charged oxides for semiconductor surface characterization," in *1<sup>st</sup> IEEE World Conference on Photovoltaic Energy Conversion*, pp. 1509-1512, 1994.
- [257] J. Schmidt and A. G. Aberle, "Easy-to-use surface passivation technique for bulk carrier lifetime measurements on silicon wafers," *Prog. Photovoltaics Res. Appl.*, vol. 6, pp. 259-263, 1998.
- [258] S. W. Glunz, D. Biro, S. Rein, and W. Warta, "Field-effect passivation of the SiO<sub>2</sub>/Si interface," *J. Appl. Phys.*, vol. 86, pp. 683-691, 1999.
- [259] R. S. Bonilla, C. Reichel, M. Hermle, P. Hamer, and P. R. Wilshaw, "Long term stability of c-Si surface passivation using corona charged SiO<sub>2</sub>," *Appl. Surf. Sci.*, vol. 412, pp. 657-667, 2017.
- [260] R. S. Bonilla and P. R. Wilshaw, "Stable field effect surface passivation of *n*-type Cz silicon," *Energy Procedia*, vol. 38, pp. 816-822, 2013.
- [261] N. E. Grant, V. P. Markevich, J. Mullins, A. R. Peaker, F. Rougieux, and D. Macdonald, "Thermal activation and deactivation of grown-in defects limiting the lifetime of float-zone silicon," *Phys. Status Solidi RRL*, vol. 10, pp. 443-447, 2016.
- [262] D. B. M. Klaassen, "A unified mobility model for device simulation—II. Temperature dependence of carrier mobility and lifetime," *Solid-State Electron.*, vol. 35, pp. 961-967, 1992.
- [263] S. Nie, R. S. Bonilla, and Z. Hameiri, "Unravelling the silicon-silicon dioxide interface under different operating conditions," *Sol. Energy Mater. Sol. Cells*, vol. 224, pp. 111021, 2021.
- [264] R. S. Bonilla and P. R. Wilshaw, "On the c-Si/SiO<sub>2</sub> interface recombination parameters from photo-conductance decay measurements," *J. Appl. Phys.*, vol. 121, pp. 135301, 2017.
- [265] A. S. Grove and D. J. Fitzgerald, "Surface effects on p-n junctions: Characteristics of surface space-charge regions under non-equilibrium conditions," *Solid-State Electron.*, vol. 9, pp. 783-806, 1966.
- [266] Z. Xin *et al.*, "An Improved Methodology for Extracting the Interface Defect Density of Passivated Silicon Solar Cells," *IEEE J. Photovoltaics*, vol. 6, pp. 1080-1089, 2016.
- [267] J. A. Cooper and R. J. Schwartz, "Electrical characteristics of the SiO<sub>2</sub>-Si interface near midgap and in weak inversion," *Solid-State Electron.*, vol. 17, pp. 641-654, 1974.
- [268] M. Schulz and N. M. Johnson, "Evidence for multiphonon emission from interface states in MOS structures," *Solid State Commun.*, vol. 25, pp. 481-484, 1978.

- [269] L. E. Black and K. R. McIntosh, "Modeling recombination at the Si–Al<sub>2</sub>O<sub>3</sub> interface," *IEEE J. Photovoltaics*, vol. 3, pp. 936-943, 2013.
- [270] H. Haug, S. Olibet, Ø. Nordseth, and E. Stensrud Marstein, "Modulating the field-effect passivation at the SiO<sub>2</sub>/c-Si interface: Analysis and verification of the photoluminescence imaging under applied bias method," *J. Appl. Phys*, vol. 114, pp. 174502, 2013.
- [271] C. H. Henry and D. V. Lang, "Nonradiative capture and recombination by multiphonon emission in GaAs and GaP," *Phys. Rev. B*, vol. 15, pp. 989-1016, 1977.
- [272] R. S. Bonilla, F. Woodcock, and P. R. Wilshaw, "Very low surface recombination velocity in n-type c-Si using extrinsic field effect passivation," *J. Appl. Phys*, vol. 116, pp. 054102, 2014.
- [273] R. S. Bonilla, I. Al-Dhahir, M. Yu, P. Hamer, and P. P. Altermatt, "Charge fluctuations at the Si–SiO<sub>2</sub> interface and its effect on surface recombination in solar cells," *Sol. Energy Mater. Sol. Cells*, vol. 215, pp. 110649, 2020.
- [274] A. Goetzberger, E. Klausmann, and M. J. Schulz, "Interface states on semiconductor/insulator surfaces," *Crit. Rev. Solid State Sci.*, vol. 6, pp. 1-43, 1976.
- [275] J. Albohn, W. Füssel, N. D. Sinh, K. Kliefoth, and W. Fuhs, "Capture cross sections of defect states at the Si/SiO<sub>2</sub> interface," *J. Appl. Phys*, vol. 88, pp. 842-849, 2000.
- [276] F. J. Himpsel, F. R. McFeely, A. Taleb-Ibrahimi, J. A. Yarmoff, and G. Hollinger, "Microscopic structure of the SiO<sub>2</sub>/Si interface," *Phys. Rev. B*, vol. 38, pp. 6084-6096, 1988.
- [277] M. L. Reed and J. D. Plummer, "Chemistry of Si-SiO<sub>2</sub> interface trap annealing," *J. Appl. Phys*, vol. 63, pp. 5776-5793, 1988.
- [278] R. S. Bonilla, N. Jennison, D. Clayton-Warwick, K. A. Collett, L. Rands, and P. R. Wilshaw, "Corona charge in SiO<sub>2</sub>: Kinetics and surface passivation for high efficiency silicon solar cells," *Energy Procedia*, vol. 92, pp. 326-335, 2016.
- [279] B. E. Deal, M. Sklar, A. S. Grove, and E. H. Snow, "Characteristics of the surface-state charge (Q<sub>ss</sub>) of thermally oxidized silicon," *J. Electrochem. Soc.*, vol. 114, pp. 266-273, 1967.
- [280] S. Choi *et al.*, "Interface analysis of ultrathin SiO<sub>2</sub> layers between c-Si substrates and phosphorus-doped poly-Si by theoretical surface potential analysis using the injection-dependent lifetime," *Prog. Photovoltaics Res. Appl.*, vol. 29, pp. 32-46, 2021.